Constitutive Modeling of Rock Salt with Application to Energy Storage Caverns

Dissertation

as a requirement of the degree of
Doktor-Ingenieur (Dr.-Ing.)

at the Faculty of
Civil and Environmental Engineering
Ruhr-Universität Bochum

submitted by
Kavan Khaledi

Reviewers:
Prof. Dr.-Ing. habil. Tom Schanz
Dr. Maria Datcheva
Prof. Dr. Janos L. Urai

Bochum, November 2017

Vorwort des Herausgebers

Die vorliegende Promotion von Herrn Dr.-Ing. Kavan Khaledi ist im Bereich der Grundlagenforschung in der Felsmechanik angesiedelt. Sie entstammt aus einem Verbundforschungsvorhaben im Geotechnologie-2-Programm der DFG und des BMBF's. In diesem Forschungsvorhaben wurde die Speicherung von erneuerbarer Energie in Salzkavernen untersucht. Dies dient dazu, die unterschiedlichen zeitlichen Verläufe von Energieangebot und Energiebedarf im täglichen Rhythmus auszugleichen. Die Energie wird in Form von komprimierter Luft bzw. komprimierten Wasserstoffs in die Salzkaverne eingepresst. Die damit verbundenen Druckschwankungen im Speicher gehen mit entsprechenden Temperaturschwankungen einher. Beide zusammen induzieren komplexe, thermisch mechanisch gekoppelte Belastungspfade im Umfeld der Kaverne. Diese Kavernen weisen zudem außerordentlich große Geometrien auf. Das Wirtsgestein Steinsalz hat auf Grund seiner kristallinen Mikrostruktur ein sehr komplexes Materialverhalten. Von besonderer Bedeutung sind die unterschiedlichen Phasen und die damit verbundenen Zeitskalen des Kriechens, der damit einhergehenden Schädigung und die Ermüdung unter zyklischer Beanspruchung. Im Unterschied zu gebräuchlichen saisonalen Energiespeichern von fossilen Brennstoffen in Salzkavernen handelt es sich im vorliegenden Forschungsvorhaben um eine zyklische Beanspruchung alle ein bis zwei Tage. Des Weiteren ist der realitätsnahen Abbildung des Primärspannungszustands durch das ursprüngliche Auffahren der Kaverne durch Auslaugen besondere Beachtung zu schenken. Die Arbeit beinhaltet mit Kapitel 2 einen hervorragenden überblick über das Materialverhalten von Steinsalz. Korrekterweise wird bereits hier ein Mehrskalen-Konzept verfolgt, dass sich durch die gesamte Arbeit zieht: Verständnis des phänomenologischen Verhaltens von Steinsalz auf der makroskopischen Skala durch Analyse der Mikrostruktur und deren Veränderung durch die Beanspruchungen. Auf Ebene des Makro-Verhaltens wird zwischen den Belastungsarten Mechanik und Temperatur und der Belastungsdauer kurz oder lang unterschieden. Detailliert diskutiert wird die Bedeutung der Dilatanzgrenze, der induzierten Schädigung und des Ermüdungsverhalten unter zyklischer Beanspruchung. Ausführlich werden existierende Materialmodelle für Steinsalz diskutiert, die in ihrer Mehrzahl jeweils jedoch nur Einze-

laspekte des Gesamtverhaltens physikalisch korrekt wiedergeben. Ausführlich werden die Initial- und Randbedingungen einer TM-Analyse einer Salzkaverne diskutiert. Dabei kommt dem Auffahrprozess einer Kaverne, der mehrere Jahre dauert, eine besondere Bedeutung zu, um den Initialzustand möglichst realistisch zu beschreiben. Bei der angestrebten probabilistischen Zuverlässigkeitsanalyse kommt dem Bewertungskriterium eine besondere Bedeutung zu. Detailliert werden unterschiedliche Möglichkeiten dazu bezüglich des Versagens und der Gebrauchstauglichkeit diskutiert. In Kapitel 3 wird ein hieraischer Modellansatz zur Beschreibung des Materialverhaltens von Steinsalz unter den oben genannten Randbedingungen formuliert. Ausgehend von einem empirischen Kriechmodell wird als komplexeste Stufe ein visko-plastisches Kriechmodell mit Schädigung formuliert. In Kapitel 6 werden die von Herrn Khaledi verwendeten und mehrheitlich selbst implementierten mathematischen Methoden zur anschließenden Systemanalyse eingeführt. Besonders bei der verwendeten Metamodellstrategie und der damit verbundenen Sampling-Strategie handelt es sich um einen originären Vorschlag von Herrn Khaledi. Daneben werden Methoden der inversen Analyse und der globalen und lokalen Sensitivitätsanalyse behandelt. Bei diesen Methoden ist ein präzises und effizientes Metamodell unabdingliche Voraussetzung. Einen weiteren originären Beitrag in diesem Kapitel stellt die thermodynamisch konsistente Herleitung der TM-Randbedingungen unter zyklischem Betrieb an der Kontur der Kaverne dar. Die Arbeit von Herrn Khaledi bewegt sich international auf höchstem Niveau der theoretischen und numerischen Felsmechanik. Die von ihm vorgelegten Untersuchungen zum gekoppelten thermisch-mechanischen Konstitutivverhalten von Steinsalz unter hochfrequenter (täglicher) zyklischer Beanspruchung sind in diesem Umfang und in dieser Qualität nach Wissen des Gutachters einzigartig.

Bochum, September 2017 Tom Schanz

Dedicated to my parents, brother and

my beloved wife Aran

For their endless love and support

Acknowledgements

It is Monday 16.01.2017, 8 p.m. I am sitting alone in my office recalling all the good memories that I had during the last four years. When I look back and compare myself to the time that I started my PhD, I can easily see a lot of positive changes in my personal and academic life. Regardless of my destiny in future, I am feeling happy and blissful at this moment. Obviously, I owe many people in my life for giving me this feeling, and this is an opportunity for me to thank them.

First and foremost, I would like to thank my first supervisor Prof. Tom Schanz for trusting me and giving me the opportunity to work in his group at the chair of foundation engineering, soil and rock mechanics, Ruhr-Universität Bochum. His supports and advices showed me the right way to proceed in my PhD path. Moreover, he is a wonderful human being who understands the problems of his colleagues. I will never forget those days that my father was suffering from illness and I was not emotionally in a good condition. When I informed Prof. Schanz on this issue, he wrote me back: "when and if your father is not doing well, if you may improve his suffering, you have to do your utmost to change this situation". This sort of behavior which I saw from him several times was always soothing to me.

I also have to thank Dr. Maria Datcheva from Institute of Mechanics, Bulgarian Academy of Sciences. She is very friendly and helpful, and of course accurate in her work. I appreciate all her contributions of time and ideas to make my PhD experience more productive and stimulating. Furthermore, I would like to thank Prof. Janos L. Urai from chair of Structural Geology, Tectonics and Geomechanics at RWTH Aachen University for the effort and the time that he spent on reviewing this thesis.

My colleagues at the chair of foundation engineering, soil and rock mechanics have contributed extremely to my personal and professional time. The group has been a source of friendships as well as good collaborations. Among them, I especially thank my friends in ANGUS+ project, Elham and Achim and Dr. König for the stimulating discussions we had together, and also for the efforts we made together before deadlines. I also thank all other friends Arash, Nina, Meisam, Thomas, Chenyang, Raoul, Wolfgang and Christoph

for all the fun we had in the last four years (in our trips, coffee time, lunch time, Sommerfest, Weinachtsfest, ...).
Last but not least, I would like to thank my family for all their love and encouragement. For my parents who raised me with love and supported me in all steps of my life. For the friendship of my brother Kamyar. And most of all for my loving, supportive, encouraging, and patient wife Aran whose support during the final stages of this PhD is so appreciated. Thank you.

Kavan Khaledi
Bochum, 16.01.2017

Abstract

Underground storage of crude oil, liquid hydrocarbons and natural gas in salt formations has relatively a long history. Nowadays, rock salt caverns integrated with renewable energy sources have attracted wide attention as suitable places for storing compressed air and hydrogen. Unlike the seasonal storage caverns, these caverns are subjected to thermo-mechanical cyclic loads with relatively short periods. Therefore, it is essential to investigate their stability and serviceability through adequate numerical simulations. To achieve this goal, proper constitutive models are required to describe the material behavior of rock salt under different loading conditions. In this thesis, an elasto-viscoplastic-creep model is employed to predict the stress-strain relation around salt caverns during the construction and the cyclic operation phases. The employed viscoplastic model is based on a non-associated flow rule which accounts for compressibility, dilatancy and failure in short-term experiments. To describe the long-term behavior of rock salt, the Norton-Hoff creep model is modified by introducing a new creep potential surface. This modification yields to a better description for the volumetric strain in long-term creep tests. On the other hand, an energy-dependent damage parameter is added to the model to describe the brittle behavior of rock salt in dilatancy domain. To accomplish this, the relationship between stresses in the undamaged material and the damaged material is defined based on the continuum damage mechanics definition of the effective area. This formulation allows us to describe the strain softening in triaxial strength test, the tertiary creep in long-term creep tests and the failure in cyclic loading tests. In the following, the material parameters of the employed model are determined using the relevant experimental existing in the literature. Then, in the numerical section, a number of examples illustrating the simulation of salt caverns are presented. In these examples, several design criteria related to the stability and the serviceability of salt caverns are discussed. Finally, based on the performed investigations, conclusions regarding the performance of the storage caverns are drawn, and some suggestions for future studies are given.

Zusammenfassung

Die untertägige Speicherung von Rohöl, flüssigem Kohlenwasserstoff und Erdgas in Steinsalzformationen hat bereits eine verhältnismäßig lange Historie. Heutzutage weckt aber zunehmend auch die Nutzung von Salzkavernen zur Speicherung erneuerbarer Energien in Form von Druckluft und Kohlenwasserstoff eine große Aufmerksamkeit. Im Unterschied zu saisonalen Speicherkavernen sind diese Kavernen einer zyklischen thermo-mechanischen Belastung bei vergleichsweise kurzen Intervallen ausgesetzt. Es ist daher von zentraler Bedeutung, die Stabilität und Gebrauchstauglichkeit mittels angemessener numerischer Simulationen zu untersuchen. Um dieses Ziel zu erreichen, ist es erforderlich, das Materialverhalten von Steinsalz bei unterschiedlichen Belastungsbedingungen durch geeignete Stoffgesetze zu beschreiben. Im Rahmen dieser Arbeit wurde ein elasto-viskoplastisches Modell verwendet, um die Spannungs-Dehnungs-Beziehungen im Kavernenumfeld während des Herstellungsprozesses sowie während der zyklischen Betriebsphasen vorherzusagen. Das verwendete Stoffgesetz basiert auf einer nicht-assoziierten Fließregel, welche Kompressibilität, Dilatanz und Kurzzeitfestigkeit berücksichtigt. Um das Langzeitverhalten von Steinsalz zu beschreiben, wurde das Norton-Hoff Kriechgesetz durch die Einführung einer neuen Kriechpotentialfläche modifiziert, sodass die Volumendehnung von Langzeit-Kriechversuchen besser abgebildet werden kann. Außerdem wurde das Stoffgesetz um einen energieabhängigen Schädigungsparameter ergänzt, um das spröde Verhalten von Steinsalz im Dilatanzbereich beschreiben zu können. Diese Formulierung ermöglicht es, das Entfestigungsverhalten in triaxialen Festigkeitversuchen, tertiäres Kriechen in Langzeit-Kriechversuchen sowie das Materialversagen in zyklischen Belastungsversuchen abzubilden. Im Folgenden werden die Materialparameter des verwendeten Stoffgesetzes auf Grundlage relevanter, bereits existierender Versuchsdaten aus der Literatur ermittelt. Im numerischen Abschnitt werden einige Beispiele dargestellt, die die Simulation von Salzkavernen veranschaulichen. Anhand dieser Beispiele werden unterschiedliche Designkriterien bezüglich der Stabilität und der Gebrauchstauglichkeit von Salzkavernen diskutiert. Abschließend werden, basierend auf den durchgeführten Untersuchungen, Schlussfolgerungen zur Leistungsfähigkeit der Speicherkavernen getroffen und einige Ansätze für zukünftige Forschungsschwerpunkte vorgeschlagen.

Contents

List of Figures

List of Tables

List of Symbols

UC ..... Utilization criterion

SFR ..... Short-term failure ratio

LFR ..... Long-term failure ratio

FOS ..... Factor of safety

VL ..... Volume loss of cavern

TC ..... Triaxial compression test

SS ..... Simple shear test

TE ..... Triaxial extension test

POD ..... Proper orthogonal decomposition

RBF ..... Radial basis function

COV ..... Coefficient of variance

EE ..... Elementary effect

NRMSE ..... Normalized root mean square error

σ_{ij} ..... Stress tensor

$\boldsymbol{\sigma}$ ..... Stress tensor

s_{ij} ..... Deviatoric stress tensor

$\mathbf{s}$ ..... Deviatoric stress tensor

σ_1 ..... First principal stress

σ_2 ..... Second principal stress

σ_3 ..... Third principal stress, confining pressure in triaxial compression tests

σ_v ..... Vertical stress

σ_h ..... Horizontal stress

τ ..... Octahedral shear stress $\tau = \sqrt{\frac{1}{3}\mathbf{s} : \mathbf{s}}$

q ..... Deviatoric stress $q = \sqrt{\frac{3}{2}\mathbf{s} : \mathbf{s}}$

p ..... Mean stress

p_p ..... Pore fluid pressure

$\sigma_{ij}^{\mathbf{eff}}$ ..... Effective stress tensor in the presence of pore fluid

$\bar{\boldsymbol{\sigma}}$ ..... Effective stress tensor in the presence of damage

I_1 ..... First invariant of stress tensor

J_2 ..... Second invariant of deviatoric stress tensor

J_3 ..... Third invariant of deviatoric stress tensor

θ ..... Lode's angle

F^{vp} ..... Viscoplastic yield function

F^{cr} ..... Creep yield function

Q^{vp} ..... Viscoplastic potential function

Q^{cr} ..... Creep potential function

I_1^{ss} ..... Intersection of creep potential function and dilatancy boundary

$\boldsymbol{\sigma}_{t+\Delta t}$ ..... Stress tensor at time $t + \Delta t$

$\boldsymbol{\sigma}_t$ ..... Stress tensor at time t

p_g^{max} ..... Maximum gas pressure in cavern during cyclic loading

p_g^{min} ..... Minimum gas pressure in cavern during cyclic loading

ε_{ij} ..... Total strain tensor

$\boldsymbol{\varepsilon}$ ..... Total strain tensor

ε_{ij}^{ss} ..... Steady-state creep strain tensor

ε_{ij}^{tr} ..... Transient creep strain tensor

ε_{ij}^{el} ..... Elastic strain tensor

ε_{ij}^{ie} ..... Inelastic strain tensor

ε_{ij}^{cr} ..... Creep strain tensor

ε_{ij}^{ve} ..... Viscoelastic strain tensor

ε_{ij}^{vp} ..... Viscoplastic strain tensor

ε_{vol} ..... Volumetric strain

ε_{vol}^{ie} ..... Inelastic volumetric strain

$\Delta\boldsymbol{\varepsilon}$ ..... Total strain increment

$\Delta\boldsymbol{\varepsilon}^{vp}$ ..... Viscoplastic strain increment

$\Delta\boldsymbol{\varepsilon}^{cr}$ ..... Creep strain increment

ξ ..... Accumulated total viscoplastic strain

ξ_{vol} ..... Accumulated viscoplastic volumetric strain

w_{vol} ..... Released volumetric strain energy per unit volume

w_f ..... Released volumetric strain energy per unit volume at failure

q_f ..... Ultimate deviatoric stress in triaxial quasi-static experiments

q_{max} ..... Maximum deviatoric stress in cyclic experiments

q_{min} ..... Minimum deviatoric stress in cyclic experiments

G ..... Elastic shear modulus

K ..... Elastic bulk modulus

v_s ..... Velocity of transverse S-wave

v_p ..... Velocity of longitudinal P-wave

δ_{ij} ..... Kronecker delta

ϕ ..... Porosity of salt

k ..... Permeability of salt

k_{tr} ..... Fluidity parameter for transient creep in Cristescu model

k_{ss} ..... Fluidity parameter for steady-state creep in Cristescu model

A_c ..... Material parameter in BGRa model

Q_c ..... Material parameter in BGRa model, activation energy

n_c ..... Material parameter in BGRa model, stress exponent

$\bar{\eta_m}$ ..... Maxwell dashpot coefficient

$\bar{\eta_k}$ ..... Kelvin dashpot coefficient

$\bar{G_k}$ ..... Kelvin spring coefficient

η_k ..... LUBBY2 parameter related to Kelvin dashpot coefficient

k_2 ..... LUBBY2 parameter related to Kelvin dashpot coefficient

G_k ..... LUBBY2 parameter related to Kelvin spring coefficient

k_1 ..... LUBBY2 parameter related to Kelvin spring coefficient

η_m ..... LUBBY2 parameter related to Maxwell dashpot coefficient

m ..... LUBBY2 parameter related to Maxwell dashpot coefficient

l ..... LUBBY2 parameter related to Maxwell dashpot coefficient

μ_1 ..... Fluidity coefficient for Desai viscoplastic model

μ_2 ..... Fluidity coefficient for the creep model

μ_0 ..... Reference fluidity coefficient for the creep model

N_1 ..... Flow rule exponent for Desai viscoplastic model

N_2 ..... Flow rule exponent for the creep model

β_1 ..... Constitutive model parameter for Desai viscoplastic model

β ..... Constitutive model parameter for Desai viscoplastic model

n ..... Constitutive model parameter for Desai viscoplastic model

m_v ..... Constitutive model parameter for Desai viscoplastic model

k_v ..... Constitutive model parameter for Desai viscoplastic model

α ..... Hardening parameter in Desai viscoplastic model

α_q ..... Hardening parameter for potential function in Desai viscoplastic model

α_{ss} ..... Hardening parameter for creep potential function

k_{cr} ..... Constitutive model parameter for the creep model

d ..... Damage parameter

ΔT ..... Temperature increment

T_m ..... Salt melting temperature

T_a ..... Air temperature

p_a ..... Air pressure

$T,\ T_s$ ..... Salt temperature

α_s ..... Heat expansion coefficient

k_s ..... Heat conductivity coefficient

ρ_a ..... Air density

V ..... Total volume of cavern

$\dot{m}_{in}$ ..... Mass inflow rate in cavern during charge process

$\dot{m}_{out}$ ..... Mass outflow rate in cavern during discharge process

h_{in} ..... Specific enthalpy of the air during charge process

u_a ..... Specific internal energy of air

h_c ..... Heat transfer coefficient for cavern

A_c ..... Heat transferring area for cavern

c_a ..... Specific heat capacity of air

c_s ..... Specific heat capacity of salt

$\mathbf{X}$ ..... Matrix of sample points

$\mathbf{U}$ ..... Matrix of outputs, snapshot matrix

$\mathbf{x}$ ..... Vector of sample point

$\mathbf{u}$ ..... Vector of observations

$\mathbf{u}^m$ ..... Vector of measurement data

$\mathbf{u}^c$ ..... Vector of computed data through forward model

$\bar{\mathbf{u}}$ ..... Vector of computed data through metamodel

n_p ..... Number of sample points

$\mathbf{\Phi}$ ..... Proper orthogonal decomposition basis vectors

1 Introduction

1.1 Background

Rock salt formations can be found in large volumes in different parts of the world. Moreover, rock salt has some unique features such as low permeability, solubility in water and adequate thermal and mechanical properties which make it distinguished from other rock materials. Because of these reasons, rock salt caverns have been recognized since almost seven decades as ideal places for storing energy carriers such as crude oil, light hydrocarbons and natural gas. Salt caverns are created using the solution-mining technique. In this technique, fresh water is continuously injected into the rock salt medium through leaching pipes and the mixture of salt and water (brine) is transferred to the ground surface. In this way, an underground cavity with the desired shape and storage volume can be formed. The first salt caverns were constructed in Canada during World War II. Later, in the early 1950's, the cavern construction became more popular in North America and several European countries. Nowadays, hundreds of such caverns exist in different parts of the world such as United States, Canada, France, Germany and China Thomas & Gehle (2000). For example, about 554 caverns were used to store natural gas around the world by the end of 2012 Yang et al. (2015). Fig. 1.1 depicts the distribution of salt caverns in Germany which are used to store crude oil, light hydrocarbons and natural gas. On the other hand, during the recent years, renewable energy sources such as wind and solar energy have gained wide attention because of their low pollutant and greenhouse gas emissions. However, these sources have an uncontrollable nature and produce electricity intermittently. Due to this fact, the integration of renewable energy sources into the electricity power grid has become a new technical challenge in the energy sector. Storing energy in the form of compressed air and hydrogen inside the underground caverns is a promising technique to overcome this problem and also to meet the energy demand fluctuations in electricity power grids. The two operational Compressed Air Storage Systems (CAES) i.e. the 290 MW Huntorf plant in Germany with a total storage volume of 300000 m^3 and the 110 MW MacIntash plant in USA with a storage space

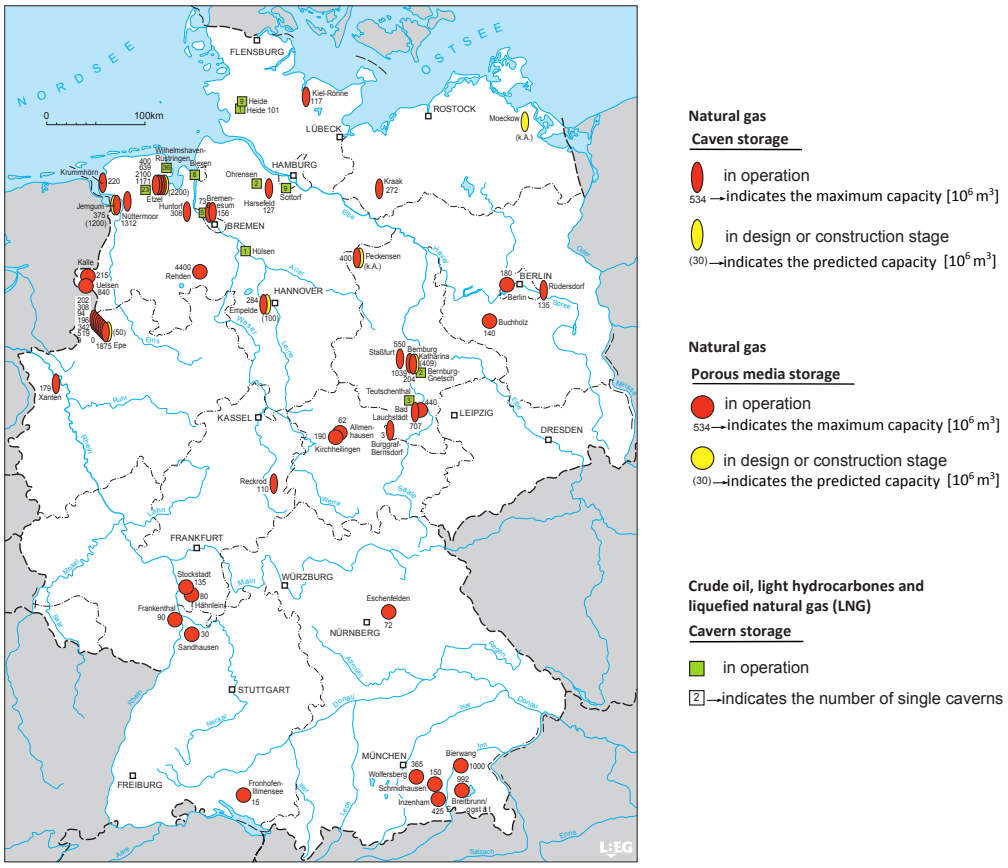

Figure 1.1: Distribution of crude oil, light hydrocarbons and natural gas storage caverns in Germany (status 31.12.2015) *Erdöl und Erdgas in der Bundesrepublik Deutschland 2015* (2016)

of 500000 m^3 have both used the solution-mining technique to construct their caverns Cortogino et al. (2001). Fig. 1.2 is a schematic representation of a salt cavern in a CAES plant. In general, a CAES plant consists of several components, i.e. (1) motor (2) compressor (3) after-cooler (4) underground compressed air storage cavern (5) recuperator (6) gas turbine and (7) generator. As depicted in this figure, the electrical power from the renewable sources is used by a motor to run the compressor and compress the air to a certain level. The compressed air is then cooled via after-cooler and its temperature reaches to a predefined value prior to storage. Thereafter, the air is injected to the underground salt cavern for storage purposes. During peak periods, when the electricity demand exceeds the supply, the pre-compressed air from the storage cavern is preheated trough a heat recuperator, then mixed with natural gas in a combustion chamber and expanded through a coupled turbine-generator to generate electricity. A typical salt cavern can be subjected to different loading conditions during the operation time. In other words, the thermo-mechanical loads applied to the rock salt cavern have various changes throughout

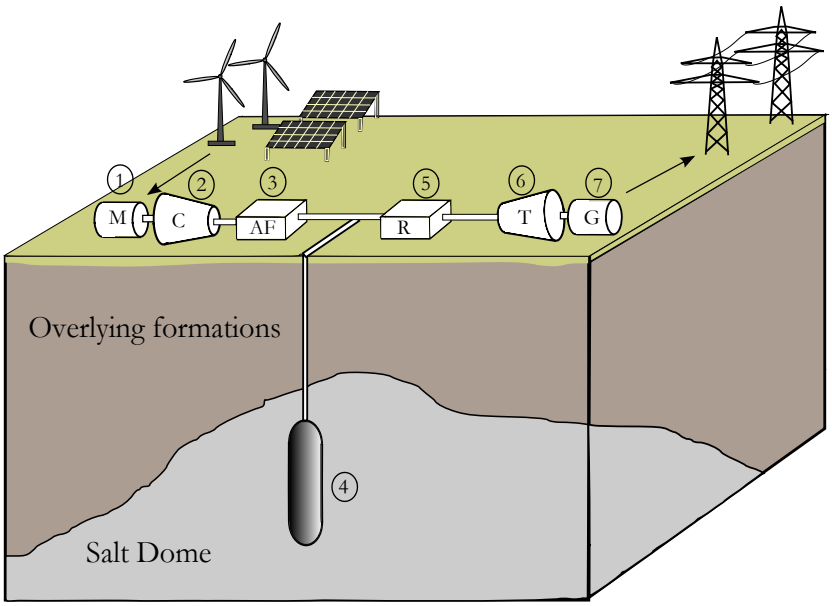

Figure 1.2: The main components of a compressed air energy storage plant: (1) motor (2) compressor (3) after-cooler (4) underground compressed air storage cavern (5) recuperator (6) gas turbine and (7) generator

the cavern's operating life. Additionally, depending on the storage product, salt caverns can operate with daily, monthly or yearly cyclic periods. Therefore, it is essential to investigate the stability and the serviceability of underground storage systems. Obviously, accurate design of these underground cavities requires adequate numerical simulations which take into account the most important processes that could affect the performance of the system.

1.2 Motivation and objectives

As mentioned, in a CAES plant, the extra electricity during off-peak periods of consumption is used to store the air into an underground cavern excavated in rock salt. Later, during the peak of energy demand, the cavern is discharged to generate electricity through a gas turbine. During this process, the rock salt surrounding the cavern is subjected to different loading conditions. In other words, the thermo-mechanical loads applied to the rock salt cavern have various changes throughout the cavern's operating life. Moreover, these types of caverns may operate with daily or hourly cyclic periods. That means, the pressure and temperature applied to the inner boundary of salt cavern have relatively rapid changes in comparison to the seasonal storage caverns which are used for storing

natural gas. In order to achieve a reliable geotechnical design, the stress-strain response of rock salt under such loading condition has to be identified and predicted. For this reason, it is essential to investigate the effect of thermo-mechanical cyclic loading on the stability and the serviceability of storage systems. Obviously, accurate design of these underground cavities requires adequate numerical simulations which take into account the most important processes that could affect the performance of the system. Furthermore, the computational model relies primarily on the governing constitutive model for predicting the behavior of rock salt.
The objectives of the investigation are:

- To review studies and models related to the rock salt and its applications summarizing the progresses and deficiencies.. The thesis also intends to define key terms, definitions and terminology related to this field of study and provide an overview for existing findings and recent major advances.
- To develop/adopt/modify a proper constitutive model for rock salt which is able to describe the short/long-term behavior of rock salt in different loading conditions such as constant loading, monotonic loading and cyclic loading.
- To integrate the employed constitutive model into the finite element program CodeBright.
- To identify the required material/model parameters using existing experimental data in literature.
- To develop mathematical and numerical models for the simulation of cyclic operation in underground storage caverns with relatively short loading and unloading periods.
- To investigate the stability and the serviceability of salt caverns under different loading scenarios.

1.3 Layout of the thesis

The thesis is composed of eight chapters. After the introductory chapter, the literature review is presented in Chapter. 2. The review begins with the studies related to the experimental observations including the micro-structure and the phenomenological behavior of rock salt. Then, it continues with the constitutive modeling of rock salt and the numerical simulation of salt caverns.
Chapter. 3 introduces the structure of three employed constitutive models for modeling of

rock salt behavior. This chapter is divided into three sections. The explanation regarding the constitutive modeling of rock salt begins with the BGRa creep model in Section. 3.2. Then, it follows by the viscoelastic model LUBBY2 in Section. 3.3. The explanations regarding the employed viscoplastic-creep-damage model are given in Section. 3.4. In Chapter 4, the general procedure to implement the viscoplastic-creep-damage model in a standard finite element code is presented. The main objective in this chapter is to provide an implicit scheme to update the stress tensor and other constitutive variables. In Chapter. 5, the material parameters related to the implemented constitutive models are identified using existing experimental data in literature. Moreover, a parametric study is carried out in this chapter to assess the performance of the employed viscoplastic-creep-damage model in different loading conditions. In addition to this, some of the key factors influencing the model responses are introduced and their effects are qualitatively represented. To achieve this goal, the performance of the viscoplastic-creep-damage model in triaxial quasi-static tests, long-term creep tests and cyclic loading tests is numerically investigated. Chapter. 6 introduces the applied computational tools in this thesis. A number of investigations including thermodynamic of gas inside the cavern, metamodeling, global sensitivity analysis and parameter identification have been conducted in this thesis. These studies are not directly related to the previous chapters. However, they have been used as computational tools to analyze the results obtained from numerical simulations. Therefore, they have been briefly introduced in Chapter. 6. Then, in Chapter. 7, the numerical simulation of salt caverns is carried out. Three numerical examples have been included in this chapter. The first example is related to the modeling of salt cavern under constant mechanical loading. While, the second and the third examples deal with the modeling of cyclic loading condition. The stability and the serviceability of underground storage caverns are discussed in these numerical examples. Finally, the last chapter i.e. Chapter. 8 presents the conclusions drawn based on the results obtained in the the foregoing chapters, and suggestions and recommendations for further studies in this field are given.

2 State of the art

The overall structure of this review has been summarized in Fig. 2.1. As shown in this figure, the review begins with experimental observations which include the micro-structure and the phenomenological behavior of rock salt. The micro-structural behavior of rock salt is explained in Section. 2.1. The dominant deformation mechanisms in the lattice structure of rock salt are explained in this section as well. Then, in Section. 2.2, the phenomenological behavior of rock salt under different loading conditions is described. That means, the influencing factors on the stress-strain relation in different testing conditions such as quasi-static triaxial test, long-term creep test and cyclic loading test are discussed. Beside the experimental investigations, constitutive modeling of rock salt and predicting material behavior with sufficient accuracy and confidence have been the subject of research for many years. Therefore, some of the existing constitutive models and their features are listed in Section. 2.3. Finally, in Section. 2.4, the design requirements and the important issues related to the modeling of salt caverns are outlined.

2.1 Micro-structure of rock salt

Natural rock salt is a polycrystalline material with an average density around 2000 kg/m^3. Each crystal grain of salt is made of several smaller parts known as sub-grains Hunsche & Hampel (1999). The grain size may range from less than 1 mm to several dm. Salt grains are connected to each other via grain boundaries (i.e. high-angle boundaries) while the sub-grains are distinguished from each other by sub-grain boundaries (i.e. low angle boundaries). Microscopic observations show that rock salt consists of grains of halite (NACL) which contain impurities, secondary mineral phases and fluid inclusions trapped in grain boundaries or in pores Urai & Spiers (2007). In this section, the main processes involved in the deformation mechanism and the effect of micro-structure changes on the macroscopic behavior are explained as discussed in literature (state of the art).

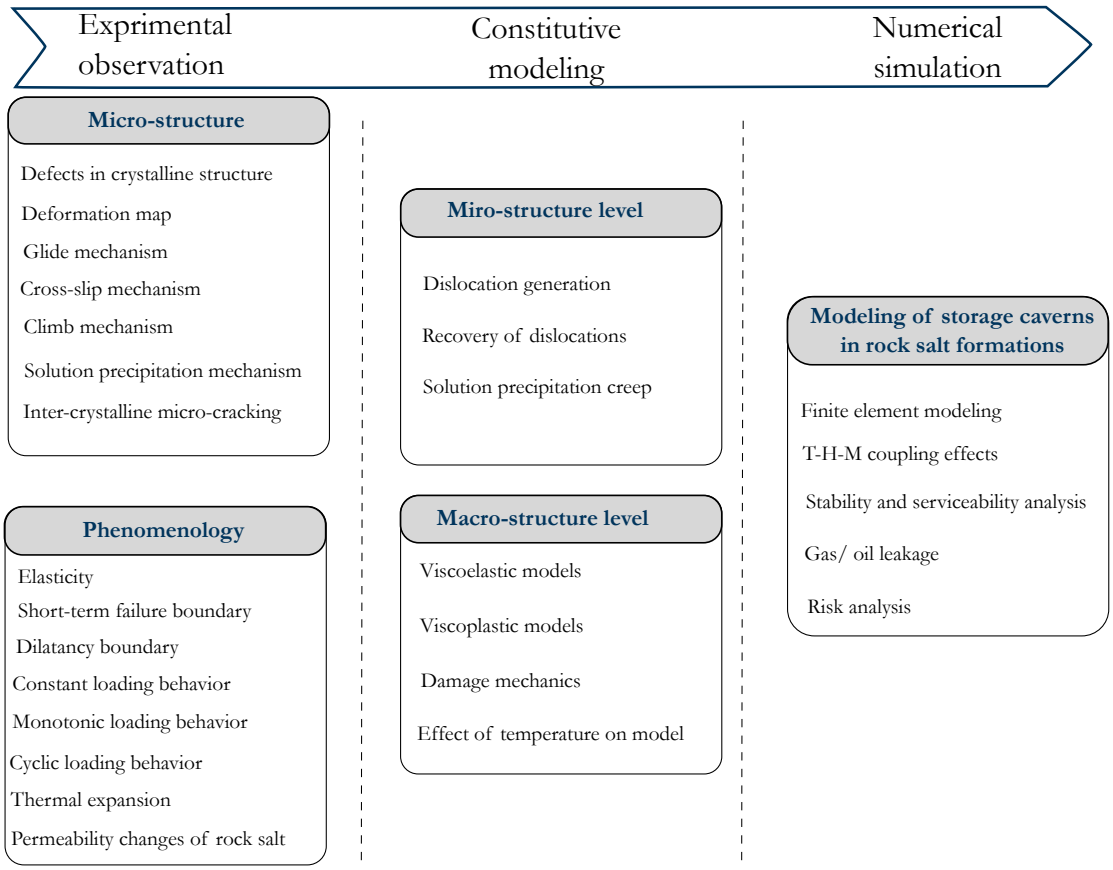

Figure 2.1: Three main steps to analyze the energy storage caverns

2.1.1 Defects in crystalline structure

A lattice is a periodic arrangement of atoms in a crystal. Fig. 2.2a is a schematic representation of an ideal crystal without any defect. In contrary to the ideal crystals, the lattice structure of natural rock salt contains imperfections or defects. A defect is defined as any disturbance in the regular arrangement of the lattice. Lattice defects have a large influence on the inelastic behavior and they contribute to the mechanical properties of rock salt. Depending on their dimensions, the following defects may be presented in a lattice structure Hirth & Lothe (1982):

- Point defects (0-dimensional defects): these types of defects are related to the lack of individual atoms (vacancies) or the existence of foreign atoms (impurity) in the lattice structure (see Fig. 2.2b).
- Linear defects (1-dimensional defects): these defects are commonly known as "dislocations". Generally, the term "dislocation" refers to the one dimensional disruptions in the regular arrangement of the atoms in a real crystal. There are two basic types

of linear defects i.e. (1) edge dislocations and (2) screw dislocations. In fact, many linear defects in lattice structure are a combination of both edge and screw dislocations (i.e. mixed dislocations). Edge dislocations are generated if an extra half layer of atoms lies between two parallel layers. Fig. 2.2c shows how the inter-atomic bonds are affected by an extra half layer of atoms. On the other hand, screw dislocations are formed when the lattice itself is sheared. Then, a part of lattice is offset relative to other parts. Fig. 2.2d is a simple visualization of screw dislocation generated by shear stress. Within the creep process, edge dislocations move in directions parallel to their dislocation line, but the screw dislocations move in directions perpendicular to their dislocation lines. It has been well accepted that the creep deformation of rock salt in a wide range of stress and temperature is carried by moving dislocations. It should be noted here, that existence of point defects such as impurities and vacancies in lattice structure can significantly change the resistance of the material against the creep deformation. Depending on the type of the impurity atoms, the point defects can slow down or even stop the movement of free dislocations and, in this way, play an important role within the creep process.

- Planar defects (2-dimensional defects): which are interfaces between homogeneous regions of the rock salt. Planar defects include grain boundaries and external surfaces (see Fig. 2.2e).
- Bulk defects (3-dimensional defects): these types of defects have bigger scales than the above-mentioned imperfections. The term "bulk defect" refers to a spatial disorder in the lattice volume which results in the creation of pores and micro-cracks (see Fig. 2.2e).

  Figs. 2.3a and 2.3b demonstrate the Scanning Electron Microscope (SEM) images of grain boundaries, sub-grain boundaries and free dislocations.

2.1.2 Deformation map

Rock salt exhibits different microscopic responses under the influence of stress and temperature. The effect of these influencing factors cannot be well understood without considering the relevant deformation mechanisms. The dominant creep mechanisms under different stress and temperature conditions can be represented by using a deformation map. In this map, the important processes acting during the creep deformation are classified and the governing mechanisms are depicted. Although the interaction between these mechanisms is complicated, in most cases it is assumed that one mechanism is dominating.

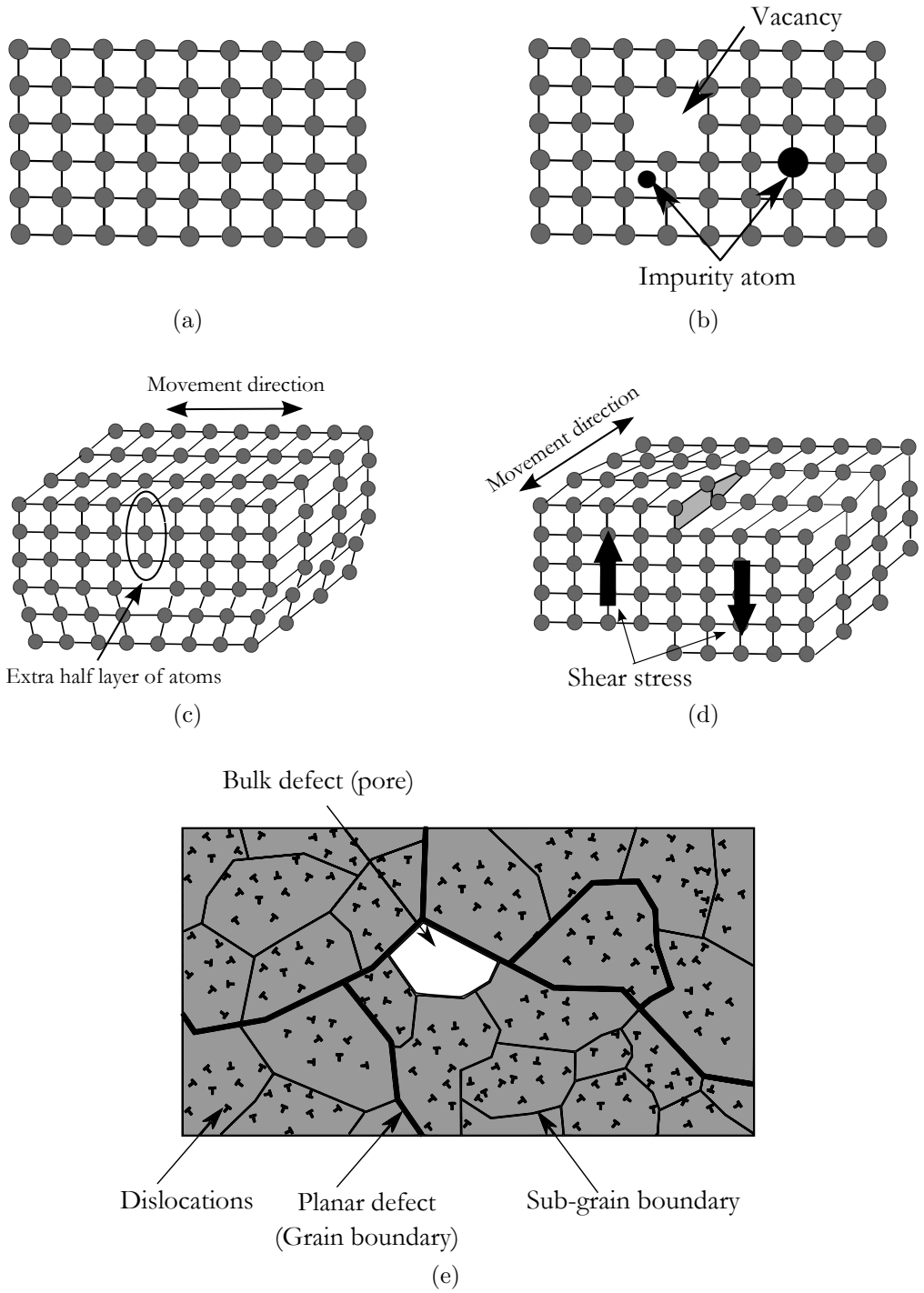

Figure 2.2: Schematic representation of (a) ideal crystal; (b) point defects; (c) linear defect, edge dislocation; (d) linear defect, screw dislocation; (e) planar defect (e.g. grain boundary) and bulk defect (e.g pores)

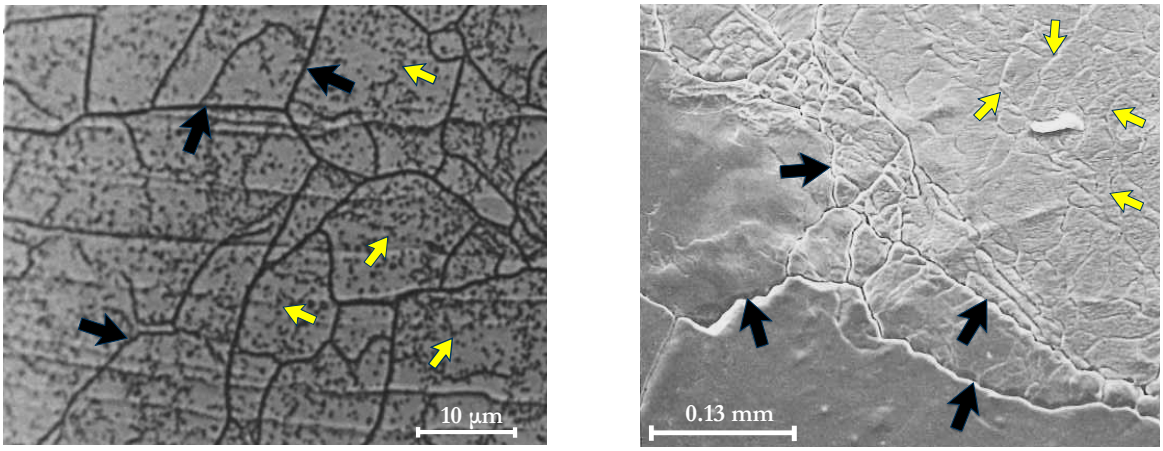

(a) (b)

Figure 2.3: The Scanning Electron Microscope (SEM) images of the micro-structure of rock salt; (a) sub-grain boundaries (black arrows) versus free dislocations (yellow arrows) Senseny et al. (1992); (b) grain boundaries (black arrows) versus sub-grain boundaries (yellow arrows) Friedman et al. (1984)

Essentially, such deformation maps (normalized shear stress vs. homologous temperature) are derived from experimental observations. The first attempts to prepare a deformation map for the creep of rock salt were carried out by Heard (1972) followed by the work of Verrall et al. (1977). In the same framework, Munson (1979) presented a deformation mechanism map for the natural rock salt from Waste Isolation Pilot Plant (WIPP) site located in New Mexico. Fig. 2.4 shows the obtained map by Munson for a temperature range less than half of the melting temperature which is the probable working condition in the energy storage applications. The rectangle 25-200 °C by 5-20 MPa in this figure shows the feasible domain inside which the laboratory tests can be performed. In this domain, the creep deformation is mainly carried by the movement of dislocations. In other words, the creep deformation rate in this range depends on the rate of the dislocation generation and the dislocation recovery. Munson did not provide any definition for the active mechanisms in low stress ranges (i.e. less than 5 MPa). Later, Urai et al. (1986) introduced another creep mechanism which plays the governing role in this range of stress. According to his findings, the solution-precipitation creep is the most important mechanism which controls the creep deformation in very small strain rates. Another terminologies can be found in the literature for this mechanism such as recrystallization process Senseny et al. (1992), pressure solution Urai & Spiers (2007); Hickman & Evans (1991); Li et al. (2012), fluid-assisted grain boundary migration Carter & Hansen (1983); Desbois et al. (2012), fluid-assisted creep Olivella & Gens (2002) and water-enhanced creep Cristescu & Hun-

sche (1998). The following sections explain the above-mentioned mechanisms more in detail.

2.1.3 Deformation induced by dislocation movement

When rock salt has an adequate confining pressure and it is subjected to a constant load, the existing dislocations in lattice start moving with a certain velocity. The movement of dislocations results in a time–dependent ductile deformation in the rock sample. This time-dependent deformation is called "creep" and it is strongly dependent on the environmental factors such as temperature and humidity. Depending on the magnitude of the applied stresses and the temperature, creep in the rock salt may occur under different mechanisms. If the stress and the temperature are in the feasible range of laboratory conditions shown in Fig. 2.4, the creep deformation is predominantly carried by free dislocations. In contrary to the solution precipitation mechanism in which the deformation occurs along the grain boundaries, the dislocation creep process take place inside the crystal lattice of salt grains without any visible change in the grain orientation. Immediately after applying the load, the shear stresses created inside the lattice generate new dislocations or force them to move inside the grain through "glide mechanism". That means, the edge and screw dislocations move on certain crystallographic planes which do not bring together ions with the same charge. Subsequently, the density of free dislocations increases inside the grains. Figs. 2.5a and 2.5b illustrate the glide mechanism for edge and screw dislocations, respectively. However, the movement of dislocations can be stopped when they encounter the existing obstacles in the lattice structure. Impurities, dislocation pile-ups and grain boundaries are the obstacles which can retard the movement of dislocations. At this situation, the density of dislocations increases in sub-grain structure and the resulting dislocation network causes that the average velocity of moving dislocations decreases Cristescu & Hunsche (1998). The increase of dislocation density produces an increasing resistance against deformation which is known as "strain hardening". Due to the strain hardening, the creep deformation rate reduces and forms the "transient" part of creep. At the same time, rearrangement of sub-grain structure leads to the recovery of dislocations in other parts of the sub-grain. The recovery process in rock salt is associated with "cross slip" and "climb" processes. During the recovery process, the increasing strain energy caused by dislocation pile-ups is released. Cross slip mechanism is a process in which two screw dislocations join each other in order to skip an obstacle. In this way, the gliding dislocations find a new path for movement. Cross slip mechanism can occur in a wide range of temperature and it is the dominant recovery mechanism at

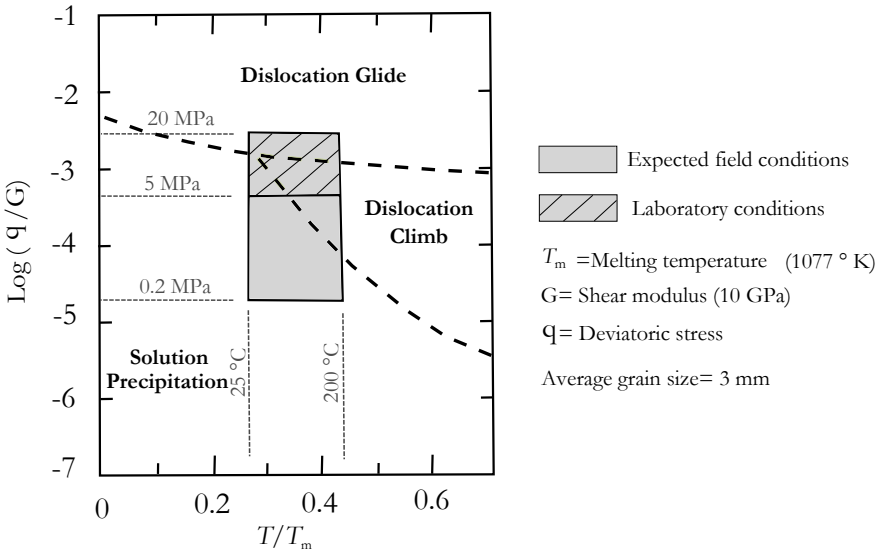

Figure 2.4: Deformation map of rock salt after Munson (1979), the solution precipitation creep was added later to this map by Urai et al. (1986)

relatively low temperatures. However, it has been found that it does not depend strongly on temperature Senseny et al. (1992). Fig. 2.6a is a schematic representation of cross slip mechanism which yields to the dislocation recovery. For high temperatures, the climb mechanism is the important recovery mechanism. As explained, the mobility of gliding dislocations is retarded when they encounter obstacles. Climb is a recovery process by which two edge dislocations can move perpendicular to their gliding plane and connect each other. This process has been shown in Fig. 2.6b. During the dislocation creep process, new sub-grains may form in the halite grain. The average diameter of the generated sub-grains is correlated with deviatoric stress Urai & Spiers (2007); Carter et al. (1993). If the loading conditions are kept constant, the number of dislocations which are recovered increases and finally an equilibrium state is reached between the dislocation generation and the dislocation recovery. Afterward, the rate of deformation remains constant and the "steady-state" creep is developed. The steady-state creep rate is dependent on stress state and temperature, if the structure is not changed, i.e. by dilatancy, impurities or recrystallization Cristescu & Hunsche (1998).

2.1.4 Deformation induced by solution precipitation

As shown in Fig. 2.4, the creep deformation in very low deviatoric stresses (i.e. 1-5 MPa) is controlled by solution precipitation process. Under such condition, deformation occurs

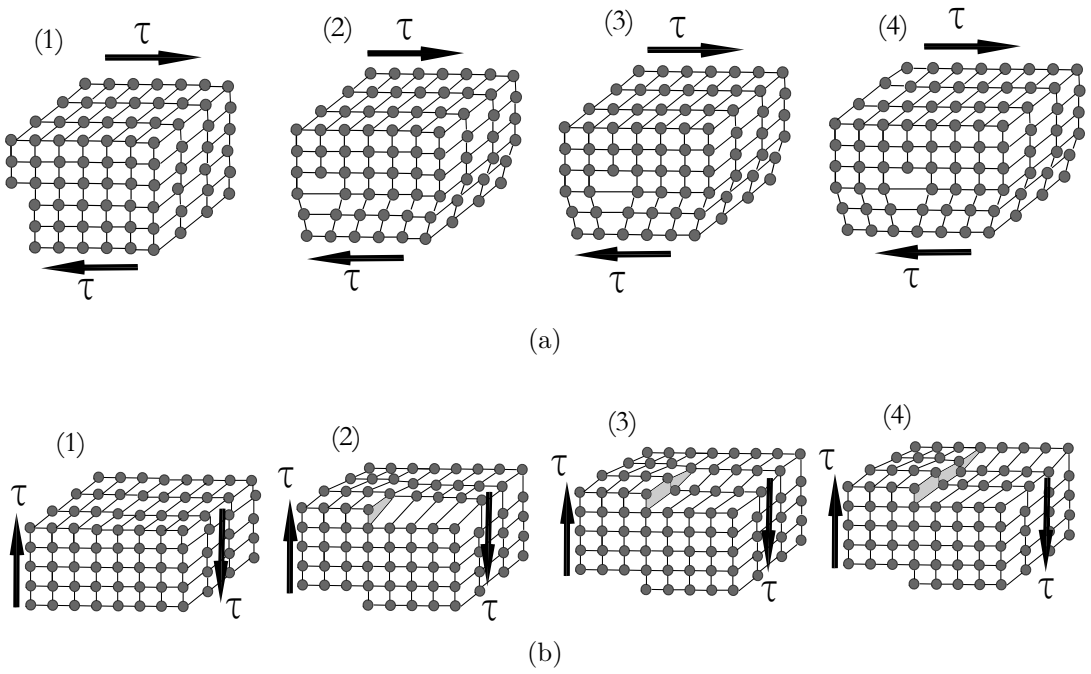

Figure 2.5: Schematic representation of dislocation generation and glide processes for (a) edge dislocation (b) screw dislocation

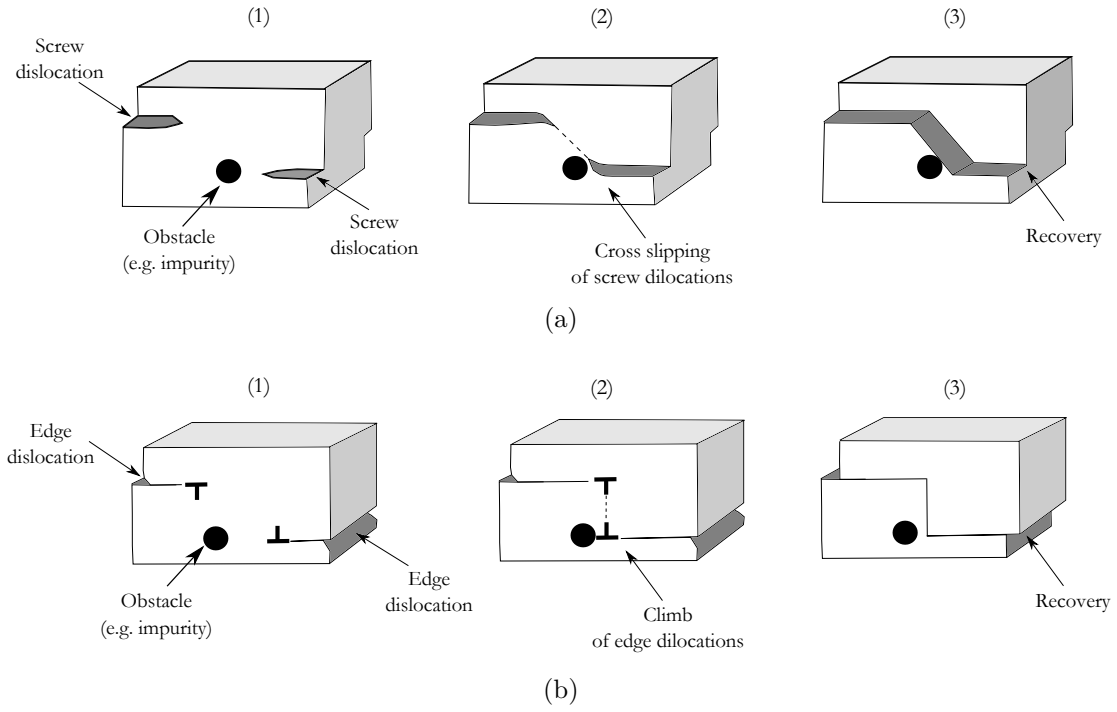

Figure 2.6: Schematic representation of recovery processes (a) cross slipping of screw dislocations (b) climb of edge dislocations

along the grain boundaries (not inside the grain). In this mechanism, salt is dissolved in the liquid phase existing at grain boundaries and it migrates from zones of stress concentration to zones of lower stress level. Finally, precipitation of salt in low stress zones results in a macroscopic deformation. The solution precipitation mechanism has been schematically shown in Fig. 2.7. This mechanism has been extensively investigated by Spiers et al. (1986, 1988). The following factors are considered as prerequisite for this mechanism to take place:

- Rock salt should be subjected to very low deviatoric stresses. Otherwise, other mechanisms which cause inter-granular deformation are activated.

- This process takes place along the grain boundaries. Therefore, existence of enough brine at the boundaries is necessary. The driving force of this mechanism is the difference of chemical potential across grain boundaries Urai & Spiers (2007).

- Another important factor for this mechanism is time. The strain rate caused by solution precipitation mechanism is less than $10^{-10}\ s^{-1}$. Therefore, its effect on deformation becomes more significant in long time scales.

The long-term deformation of rock salt would be underestimated if the governing equations which describe other creep mechanisms (i.e. dislocation creep) are extrapolated in this range of stress Urai et al. (1986). Solution precipitation creep can be also considered as a recovery process because it contributes to the reduction of stored energy of dislocations at grain boundaries.

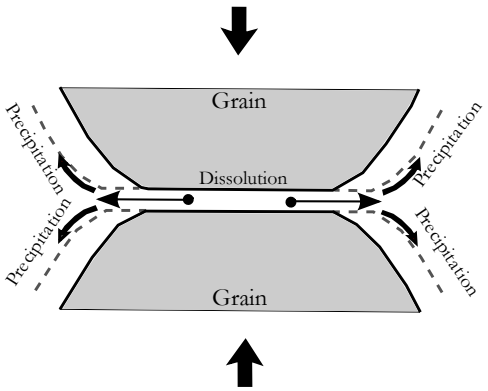

Figure 2.7: Schematic representation of solution precipitation creep Olivella & Gens (2002)

2.1.5 Deformation induced by inter-crystalline micro-cracking

At low confining pressures and high deviatoric stresses, rock salt exhibits a transition from ductile to brittle behavior. In this range of loading, the inter-crystalline micro-cracking, grain rotation and inter-granular slip are important deformation processes (see Fig. 2.8). Opening of micro-cracks results in volume increase or dilatation of rock salt. Under such conditions, the "tertiary creep" may occur due to the inter-crystalline micro-cracking. Numerous experiments on rock salt samples performed by several researchers show that there exist a zone in stress space whose boundary separates the ductile behavior from the brittle response. More details regarding the consequences of transition from the ductile to the brittle behavior are presented in Section. 2.2.2.2.

2.2 Phenomenological behavior of rock salt

The macroscopic behavior of rock salt in laboratory has been the subject of research for many years. The main focus of these types of studies lies on the observation and the interpretation of material response of rock salt under different thermo-mechanical conditions. The current section presents a review on different phenomenological aspects related to the rock salt behavior.

2.2.1 Elastic behavior

Rock salt has been considered as an isotropic material by most researchers. For example, Wawersik & Hanuum (1980) performed a hydrostatic test to investigate the isotropic

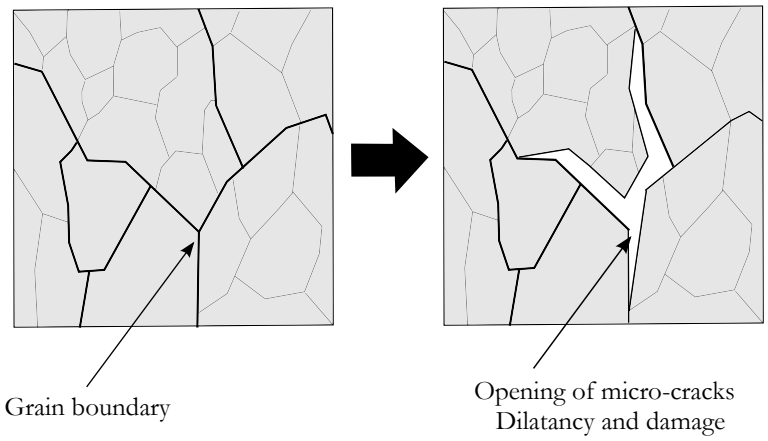

Figure 2.8: Schematic representation of inter-crystalline micro-cracking

behavior of rock salt. The volumetric strain obtained in this test was 3 times the axial and the lateral strains (i.e. $\varepsilon_{vol} = 3\varepsilon_1 = 3\varepsilon_3$). The agreement of $3\varepsilon_1$ and $3\varepsilon_3$ indicates that the rock salt is mechanically isotropic. With this assumption, the instantaneous reversible response can be described by two elastic parameters using Hooke's law:

$$\dot{\varepsilon}_{ij}^{el} = \frac{1}{2G}\dot{\sigma}_{ij} + \left(\frac{1}{9K} - \frac{1}{6G}\right)\dot{I}_1\delta_{ij}, \tag{2.1}$$

where σ_{ij} is the ij^{th} component of the stress tensor and I_1 denotes the first stress invariant. δ_{ij} is the Kronecker delta. In addition, K and G are bulk and shear moduli, respectively. There are two common ways to determine the elastic parameters, i.e. (1) dynamic method and (2) static method. In the dynamic method, the travel time of the longitudinal P-wave and the transverse S-wave propagating through the rock salt sample are measured. Accordingly, the bulk modulus K and shear modulus G are back calculated using the following equations Matei & Cristescu (2000):

$$K = \rho\left(v_p^2 - \frac{4}{3}v_s^2\right), \qquad G = \rho v_s^2 \tag{2.2}$$

where, ρ is the density of salt; v_p and v_s denote the velocity of the P- and S-waves, receptively. With the aid of this technique, the structural changes in rock salt sample due to micro-cracking, dilatancy can be detected as well (e.g see Popp & Kern (1998)). The elastic parameters may change when micro-cracks are generated in rock sample. In other words, the elastic parameters for damaged rock salt may depend on a damage parameter which describes the micro-cracking history evolution Cristescu & Gioda (1994). In the static method, the slopes of the stress-strain curves during unloading/reloading cycles are determined. Having these slopes, the elastic parameters and their variations can be obtained. However, the two methods do not necessary lead to same values for the elastic parameters Matei & Cristescu (2000). The dependency of elastic parameters on confining pressure was investigated by Hansen et al. (1984). They determined the elastic parameters of ten different rock salt samples taken from different sites and different depths. Obtained results from reloading/unloading cycles in the stress-strain curves showed that the elastic parameters were site independent (i.e. independent of applied confining pressure). Similar conclusions regarding the independent relation between the elastic parameters and the confining pressure were reported before in Höfer & Thoma (1968). However, the dependency of elastic parameters on stress state is a subject which has not been extensively investigated. Likewise, rare investigations have been conducted to understand the relation between temperature and elastic parameters. Wawersik & Hanuum (1980) reported

that the pressure and the temperature do not alter the elastic parameters. In contrary, Sriapai et al. (2012) showed that, the elastic shear and bulk moduli decrease linearly with increasing temperature and Poisson's ratio tends to remain constant. The loading rate is another factor which may influence the elastic parameters. Fuenkajorn et al. (2012) performed a series of triaxial tests on specimens from Maha Sarakham formation considering different loading rates (ranging from 0.001 to 10 MPa/s). The elasticity parameters in these tests were obtained using the tangent of the stress-strain curves at 40% of failure stress. As reported in Fuenkajorn et al. (2012), the elastic modulus (E) of salt shows slightly increase with increasing the loading rate and Poisson's ratio tends to be independent of the loading rate. Similar results have been reported by Liang et al. (2011).

2.2.2 Rock salt behavior in short-term triaxial strength tests

The main objective of this section is to explain the mechanical behavior of rock salt in short-term triaxial strength tests (i.e. quasi-static tests). The quasi-static tests can be performed in two ways; i.e. (1) strain-controlled (2) load-controlled. When a rock salt sample is tested under a short-term conventional triaxial loading (either compression; $\sigma_1 > \sigma_2 = \sigma_3$ or extension; $\sigma_1 < \sigma_2 = \sigma_3$) with constant strain rate, the obtained stress-strain curve indicates five regions of deformation behavior. Fig. 2.9 represents a typical stress-strain curve obtained for rock salt in a triaxial strength test. The changes of volumetric strain versus axial strain has been shown in this figure, as well. The first region (i.e. O-A) shows a steep linear curve, which corresponds to the elastic regime. According to Alkan et al. (2007) and Liang et al. (2011), two types of deformation are expected in this range of loading. The first one is due to the closure of pre-existing micro-cracks and the second is the purely elastic deformation which is completely recoverable. The second region (i.e. A-B) exhibits the transition from elastic to plastic deformation. Point B, in this figure, indicates the onset of dilation. That means, the volume of rock salt sample gradually increases due to the propagation of micro-cracks. Additionally, a slow transition from ductile to brittle behavior takes place in this range of loading. In the third region (i.e. B-C), the ductile-brittle transition and the micro-crack generation continue up to point C. As seen, in this region, the curvature of the stress-strain curve increases with deformation, which is due to the strain hardening mechanism (i.e. increasing the density of dislocations) explained in Section. 2.1.3. At about 80% of peak stress, i.e. at point C, a critical stress condition is reached Liang et al. (2011). Because, at this level of loading, the opening of micro-cracks accelerate significantly and the damage growth

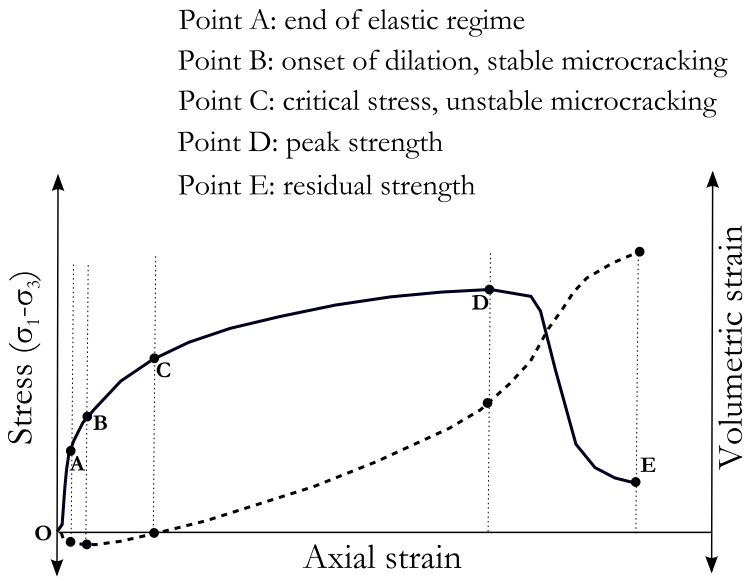

Figure 2.9: Typical responses observed in short-term strength tests; stress vs. strain (solid line) and volumetric strain vs. axial strain (dashed line)

becomes significant. Finally, at the end of fourth region (i.e. C-D), the peak strength is reached. At this point, the rock salt sample cannot withstand loading and exhibits brittle failure accompanied by strain softening behavior. Therefore, the fifth region starts to develop and the stress drops down from the peak value to the residual strength at point E.

2.2.2.1 Short-term failure boundary

Studying the short-term failure conditions obtained in quasi-static loadings is essential for characterizing the properties of rock salt and to develop the required constitutive models. The mechanical behavior of rock salt in short-term triaxial strength tests has been investigated by several researchers (e.g. Senseny et al. (1992); Cristescu & Hunsche (1998); Wawersik & Hanuum (1980); Höfer & Thoma (1968); Liang et al. (2007); Langer (1982); Fuenkajorn & Phueakphum (2010); Hunsche (1992); Sriapai et al. (2013)). Generally, in these experiments, different confining pressures have been applied to rock salt samples in a triaxial conventional testing apparatus. Then, the axial load/strain changes with a certain rate until the peak strength is reached. The strain rate in strain-controlled tests is commonly more than $10^{-6}\ s^{-1}$. Having the peak stresses for different values of confining pressures, a short-term failure boundary can be defined in the stress space as illustrated

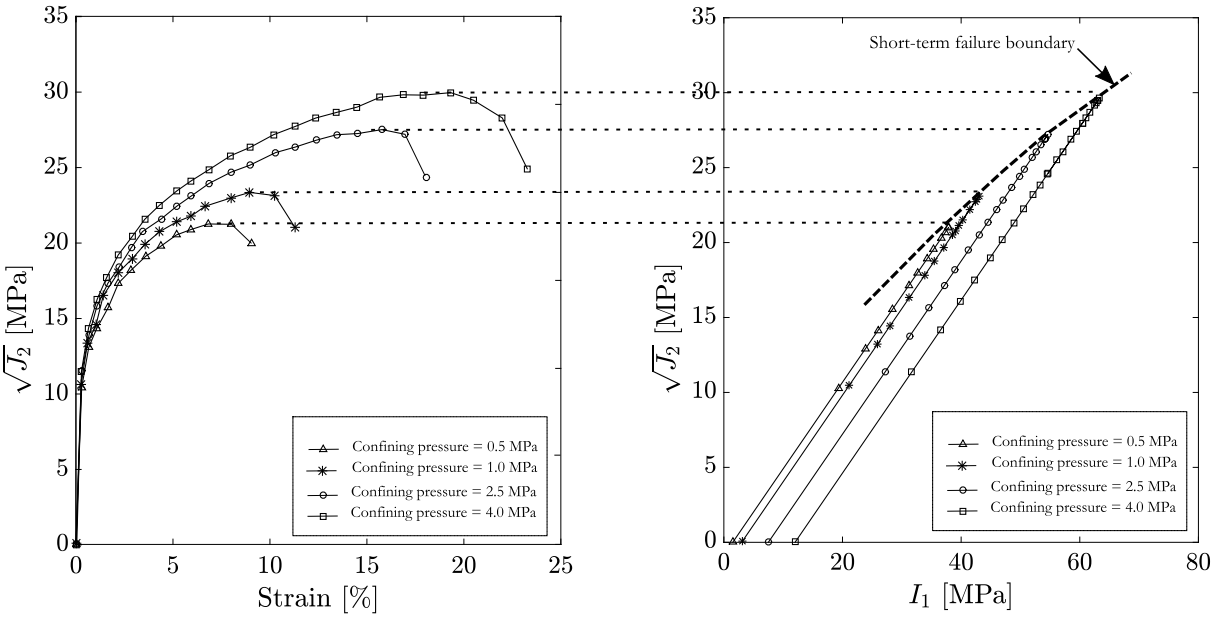

Figure 2.10: Stress-strain curves for different confining pressures (left); stress-paths in triaxial compression experiment and the short-term failure boundary (right); experimental data from Günther & Salzer (2007)

in Fig. 2.10. As seen, the failure boundary of rock salt is highly dependent on the applied confining pressure. In other words, the compressive strength of rocks generally increases with increasing confining pressure. For low confining pressures, rock salt becomes more brittle and the peak strength is reached faster. The pressure dependence of rock strength has been experimentally studied by many researchers and different failure boundaries have been defined for rock salt in the literature. Some of the existing failure boundaries are listed in Table 2.1. Fig. 2.11a is an illustration for some of the rock salt failure boundaries in $I_1 - \sqrt{J_2}$ space. The test data for rock salt strength in triaxial compression test obtained by Hunsche (1992) has been shown in this figure as well. Beside confining pressure, several important factors such as temperature, stress path, load/strain rate may influence the behavior of rock salt in short-term tests. These influencing factors are discussed in the following sections.

2.2.2.2 Long-term failure boundary/ dilatancy boundary

As shown in Fig. 2.9, the plastic volumetric strain curve has a turnover point at which the compression changes to dilation. Numerous experimental investigations performed by many scholars show that there is a band in the stress space which separates the com-

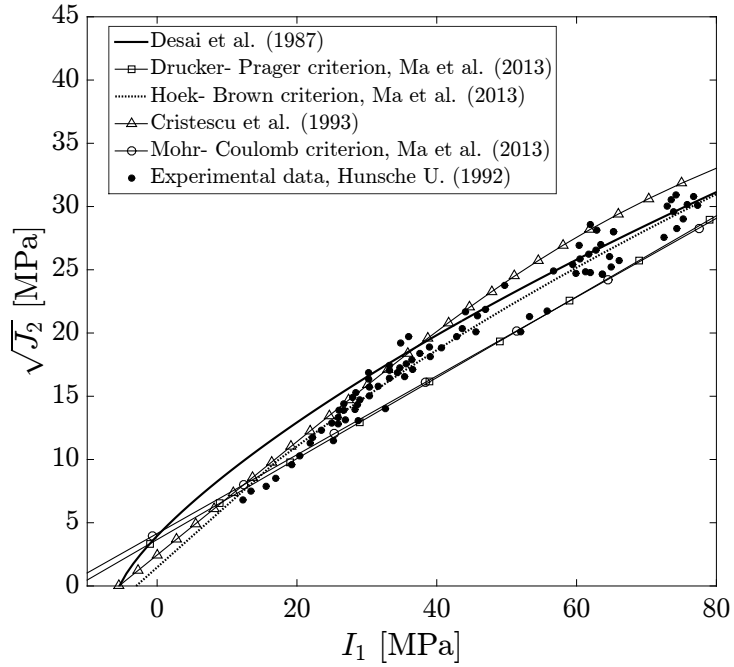

(a)

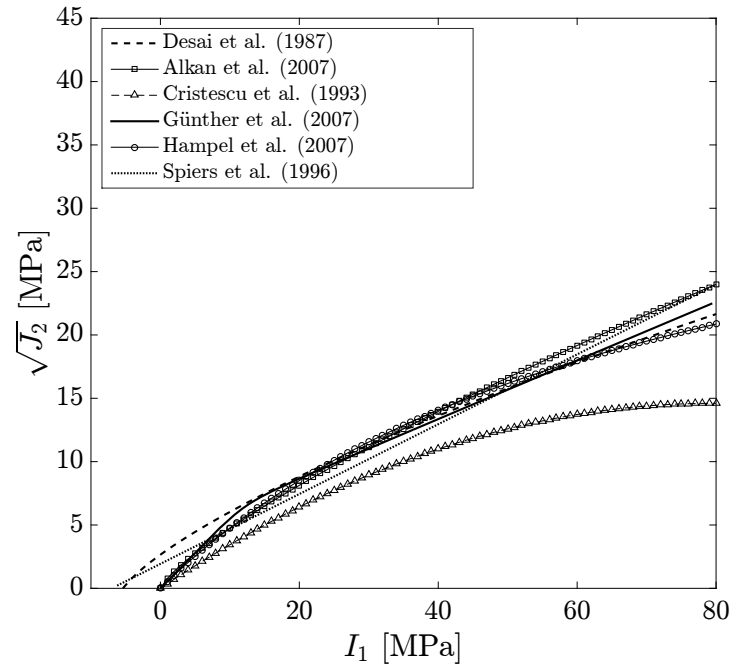

(b)

Figure 2.11: (a) Different short-term failure boundaries defined for rock salt in $I_1 - \sqrt{J_2}$ plane; (a) Different dilatancy boundaries defined for rock salt in $I_1 - \sqrt{J_2}$ plane

Table 2.1: Some of the existing short-term failure boundaries of rock salt in the literature

Model	Equation	Description
Mohr-Columb	$\tau = c + p\tan\varphi$	τ and p are the octahedral shear stress and the mean stress, respectively. c is the cohesion and φ is the friction angle Liang et al. (2007); Ma, Liu, Fang, Xu, Xia, Li, Yang & Li (2013).
Modified Mohr-Columb	$\sigma_1 = \sigma_c + \left(1 + \frac{\sigma_m - \sigma_c}{\sigma_\phi - \sigma_3}\right)\sigma_3$	σ_1 and σ_3 are the first and the third principal stresses, respectively. σ_c is the uniaxial compression strength. σ_m and σ_ϕ are two model parameters which determine the maximum possible strength and the curvature of the failure boundary, respectively Minkley & Muehlbauer (2007).
Hoek-Brown	$\sigma_1 = \sigma_3 + \sigma_c\sqrt{m\frac{\sigma_3}{\sigma_c} + s}$	σ_1 and σ_3 are the first and the third principal stresses, respectively. σ_c is the uniaxial compression strength. m and s are two dimensionless parameters related to the characteristic of the rock Ma, Liu, Fang, Xu, Xia, Li, Yang & Li (2013).
Generalized Hoek-Brown	$\sigma_1 = \sigma_3 + \sigma_c\left(m_b\frac{\sigma_3}{\sigma_c} + s_b\right)^a$	This is an improved version of Hoek-Brown criterion. Parameters m_b, s_b and a are not constant anymore. These parameters can change as a function of damage parameter d. Parameter d is a factor which reflects the degree of disturbance of rock masses, varying from 0 for undisturbed insitu rock masses to 1 for severely disturbed rock masses Ma, Liu, Fang, Xu, Xia, Li, Yang & Li (2013).
Drucker-Prager	$\sqrt{J_2} = \alpha I_1 + k$	J_2 is the second invariant of deviatoric stress tensor and I_1 is the first invariant of stress tensor. α and k are model parameters Ma, Liu, Fang, Xu, Xia, Li, Yang & Li (2013).
Cristescu et al.	$p = r\tau + s\tau^6 - \tau_0$	τ and p are the octahedral shear stress and the mean stress, respectively. m, r and τ_0 are model parameters Cristescu & Hunsche (1998); Cristescu (1987); Cristescu & Gioda (1994).
Desai et al.	$\sqrt{J_2} = \sqrt{\gamma\left(\exp\left(\beta_1 I_1\right) - \beta\cos\left(3\theta\right)\right)^{m_v}}I_1$	J_2 is the second invariant of deviatoric stress tensor. I_1 is the first invariant of stress tensor. θ is the Lode's angle. γ, β_1 and β are model parameters Desai & Zhang (1987); Desai & Varadarajan (1987).
Hou/Lux	$q = a_0\beta^{\mathrm{TC}}(\sigma_3)k_\beta(\sigma_3,\theta)$	q is the deviatoric stress i.e. , $q = \sqrt{3J_2}$. a_0 is model parameter. $\beta^{\mathrm{TC}}(\sigma_3)$ and $k_\beta(\sigma_3,\theta)$ are two functions dependent on the minimum principal stress σ_3 and the Lode's angle θ Hou & Lux (1998); Hou (2003).
Fuenkajorn	$\tau = ap^b(\dot{\tau})^{cp^d}$	This model describes the dependecy of failure boundary on the loading rate. τ and p are the octahedral shear stress and the mean stress, respectively. a, b, c and d are model parameters. $\dot{\tau}$ is the shear stress rate Fuenkajorn & Phueakphum (2010).

pressive behavior of rock salt from the dilative response (e.g. see Cristescu & Hunsche (1998); Alkan et al. (2007); Hunsche (1992); Sambeek et al. (1993); DeVries et al. (2000); Czaikowski (2011)). Accordingly, under a given confining pressure, the plastic volumetric strain shows a transition from compression to dilation with the increase of applied deviatoric stress. Although the compression and dilatancy zones are separated though a band, it is common to use a boundary to describe this transition. This boundary is known as "dilatancy boundary" or "long-term failure boundary". When the stress states is in the compressibility zone (i.e., below the dilatancy boundary), a time-dependent ductile deformation without any visible macroscopic cracking is observed. For this reason, critical conditions such as crack propagation and brittle failure do not occur below the dilatancy boundary. In contrary, with reducing the confining pressur or increasing the deviatoric stress, the stress state may lie in the dilatancy zone (i.e., beyond the dilatancy boundary). In this case, inter-crystalline micro-cracking, grain rotation and inter-granular slip become the dominate deformation mechanisms. These processes result in dilatancy or volume increase of salt. Dilatation and interconnection of micro-cracks have a number of consequences such as: rapid increase in permeability, tertiary creep or long-term failure Hunsche & Hampel (1999). For this reason, the onset of salt dilation is regarded as a crucial factor for the long-term design of storage caverns. However, accurate determination of dilatancy boundary in experiments is technically a challenging task. The following methods are normally used to obtain the onset of dilatancy in experiments.

- The axial and lateral strains are directly measured during the test. Having the strain components, the volumetric strain is obtained as $\varepsilon_{vol} = \varepsilon_1 + \varepsilon_2 + \varepsilon_3$.

- In some triaxial test devices, the lateral stress is produced through the hydraulic pressure of a confining fluid. In this case, a dilatometer system is used to measure the volumetric strain of rock salt sample based on the changes of fluid level in the triaxial cell (e.g see Wawersik & Hanuum (1980); Roberts et al. (2015))

- The onset of dilatancy and the growth of micro-cracks can be detected by the passive "Acoustic Emission" technique (AE). At the onset of dilatancy, the inter-granular slip takes place. As a consequence, the acoustic waves (sound) are generated due to the opening of micro-cracks. Then, the acoustic waves travel through the sample, and they are sensed and recorded by appropriate devices. In this way, the onset of dilatancy can be identified. This method is called passive, because it only detects events naturally occurring within the specimen Bauer et al. (2011); Zhang, Liang, Li, Xu & Zhao (2015).

- The onset of dilatancy and the micro-cracking can be measured by an active technique known as "Ultrasonic Wave Velocity". In this technique, a source (located out of the sample) is used to generate the waves. Then, the longitudinal P-wave or the transverse S-wave propagating through the rock salt sample are sensed and recorded. In this way, the changes of rock salt structure, the development of damage and the growth of cracks can be monitored Popp & Kern (1998); Popp et al. (2001); Schulze et al. (2001).

Fig. 2.11b shows some of the dilatancy boundaries defined for rock salt in $I_1 - \sqrt{J_2}$ space. As it is seen, the dilatancy boundary of rock salt has a significant dependency on the applied confining pressure. That means, the gain boundary sliding and the opening of micro-cracks are more likely in low confining pressures.

2.2.2.3 Effect of stress-path on the short-term behavior of rock salt

In a number of studies, the effect of stress path on the short-term failure boundary of rock salt has been discussed (e.g. Cristescu & Hunsche (1998); Wawersik & Hanuum (1980); Langer (1982); Desai & Varadarajan (1987); Hunsche (1984)). Fig. 2.12a shows the obtained failure stresses from conventional compression, simple shear and conventional extension tests. As it is observed, the stress path plays an important role in the definition of failure boundary in triaxial experiments. The rock salt strength in extension tests is clearly smaller than the strength obtained in compression tests. For this reason, a number of researchers have taken into account the influence of the intermediate stress component on the mechanical behavior of rock salt. Consequently, they have defined Lode's angle dependent failure boundaries in order to consider the effect of stress path on short-term behavior of rock salt (e.g. see Langer (1982); Hunsche (1992); Ma, Liu, Fang, Xu, Xia, Li, Yang & Li (2013); Desai & Zhang (1987); Hou (2003)). Fig. 2.12b illustrates a Lode's angle dependent failure boundary in $\pi-$plane introduced by Desai & Zhang (1987). As seen, the dependency of failure boundary on the Lode's angle θ results in different peak strengths in triaxial compression ($\theta = 60°$), shear ($\theta = 30°$) and extension ($\theta = 0°$) tests.

2.2.2.4 Effect of load/strain rate on the mechanical behavior

As explained earlier, the short-term failure boundary is determined through triaxial quasi-static tests with certain load/strain rates. However, the applied deformation rates in these tests are relatively high in comparison to the field condition. Therefore, it is important to investigate the effect of load/deformation rate on the mechanical behavior of rock salt. In

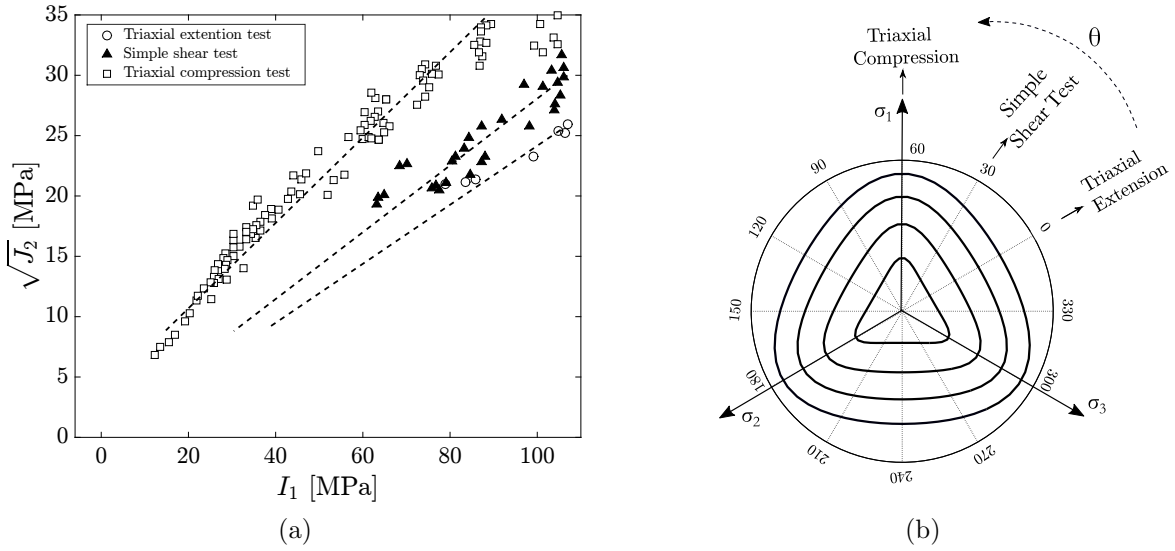

(a) (b)

Figure 2.12: (a) Dependency of failure boundary on stress-path in short-term triaxial experiments (test data from Cristescu & Hunsche (1998)); (b) The Lode's angle dependent failure surface defined by Desai & Varadarajan (1987)

contrary to other rock materials, rare attempts have been made up to now to understand the rate-dependent behavior of rock salt Liang et al. (2011). In addition, the reported results are not consistent in some cases. For example, Hunsche (1994) performed a series of triaxial compression tests on cylindrical specimens from Asse mine located in Germany. Different confining pressures (ranging from 0 to 20 MPa) and various strain rates (from 10^{-2} to $10^{-6}s^{-1}$) were considered in these tests to determine the peak strength of the rock salt. Fig. 2.13a shows the obtained ultimate stresses in these tests for the considered confining pressures and strain rates. The obtained values show that, for a constant confining pressure, the ultimate strength of rock salt is only slightly dependent on strain rate $\dot{\varepsilon}$. As discussed by Cristescu & Gioda (1994), unlike the brittle rocks, the peak strength of rock salt does not change significantly with the strain rate. However, because of ductility, the value of strain at failure increases by decreasing the deformation rate. Furthermore, if the test is carried out at a sufficiently low value of strain rate then the experiment becomes finally a creep test with constant stress state without short-term failure (but perhaps with tertiary creep after a long time if the stress state is in the dilatancy zone Cristescu & Gioda (1994)). Similar results regarding the independent relation between failure boundary and strain rate have been reported by Senseny et al. (1992) and Liang et al. (2011). However, Fuenkajorn et al. (2012) performed a series of load-controlled triaxial tests on cubic samples from Maha Sarakham mine in Thailand. The obtained results for different confining pressures (i.e. ranging from 0 to 20 MPa) and the different

loading rates (i.e. from 0.001 to 10 MPa/s) have been represented in Fig. 2.13b. As seen, the ultimate strength of rock salt increases considerably with increasing the loading rate, in particular for high confining pressures. Fuenkajorn and his coworkers described the dependency between the failure boundary and the loading rate through a power function (see Table 2.1). On the other hand, they showed that the strain value at failure decreases with increasing the loading rate. Earlier, similar results were reported by Langer (1982) and Farmer & Gilbert (1984). They also concluded that the ultimate strength of rock salt reduces with decreasing the strain rate.

2.2.2.5 Effect of temperature on the short-term strength

Depending on the type of the storage product (i.e. crude oil, natural gas, compressed air or hydrogen), the temperature of the surrounding rock salt in a cavern may have considerable variations (e.g. typically between 25 to 200 °C). Temperature affects the material properties of rock salt. For example, Wawersik & Hanuum (1980) showed that the ultimate stress reduces in high temperature condition while the rock salt ductility increases. They also showed that the ratio of volumetric strain to deviatoric strain in quasi-static experiments increases significantly with increasing temperature. The weakening of rock salt at elevated temperatures has been reported by Langer (1982) and Sriapai et al. (2012), as well. Fig. 2.14 shows the degradation of short-term failure boundary of rock salt in high temperature condition reported in Langer (1982).

2.2.2.6 Permeability changes and the effect of pore pressure

The low permeability of rock salt is an important factor to guarantee the tightness of the underground storage cavities. Generally, rock salt in undisturbed state can be considered as an impermeable material because of its extremely low permeability (i.e. less than 10^{-20} m^2 Peach (1991)). Volume increase of rock salt in dilatancy domain is expected to increase the permeability because of the new porosity created during the micro-cracking process. Numerous experimental investigations have been conducted during the past decades in order to understand the effect of permeability changes on the mechanical behavior of rock salt (e.g. see Popp & Kern (1998); Popp et al. (2001); Schulze et al. (2001); Peach (1991); Pfeifle et al. (1998); Alkan (2009); Fokker et al. (1993)). Since the permeability of rock salt changes above the dilatancy boundary, its evolution can be described through either the porosity or the volumetric inelastic strain. In a number

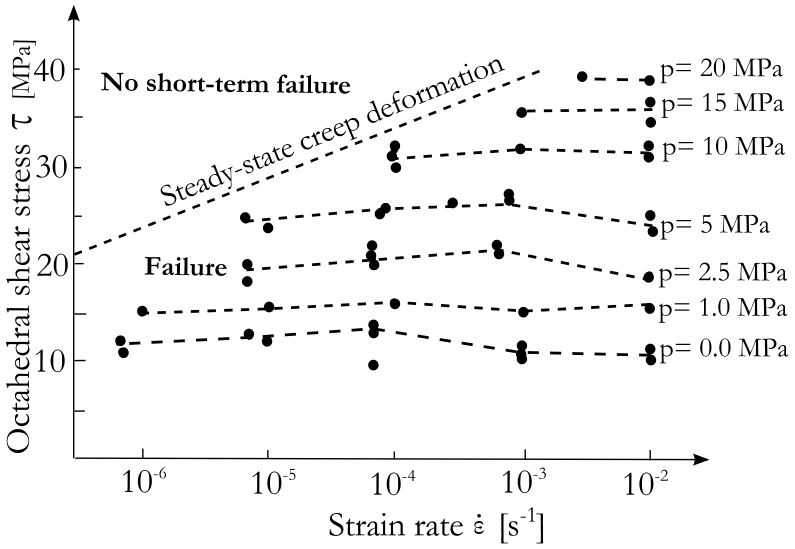

(a)

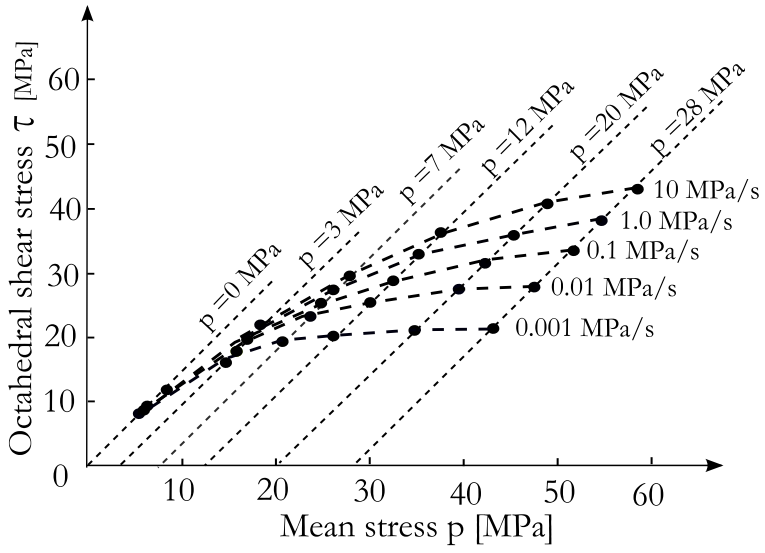

(b)

Figure 2.13: (a) Strength of rock salt determined from triaxial compression tests at a great number of confining pressures and strain rates Hunsche (1994); (b) Strength of rock salt determined from triaxial compression tests for various confining pressures and loading rates Fuenkajorn et al. (2012)

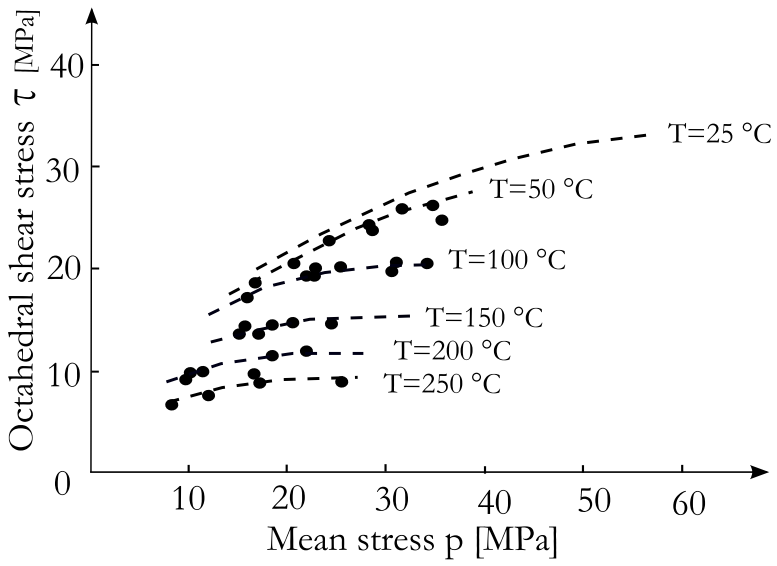

Figure 2.14: Degradation of short-term failure boundary of rock salt in high temperature condition Langer (1982)

Table 2.2: Some of the existing models to describe the permeability changes of rock salt

Model	Equation	Description
Stormont et al.	$k = \frac{m^2}{b}\phi^s$	This equation has been developed based on the equivalent channel concept. m, b and s are model parameters and ϕ is the porosity Stormont (1997).
Peach	$k = a\varepsilon_{vol}^b$	The permeability is related to the dilatant volumetric strain through a power function. a, b are model parameters and ε_{vol} is the inelastic volumetric stain Peach & Spiers (1996).
Stormont et al.	$k = a\sigma_3^{(b+c\sigma_3)}\varepsilon_{vol}^{(m+n\sigma_3)}$	The influence of minimum principal stress on the permeability changes has been taken into account in this model. a, b, c, m and n are model parameters. ε_{vol} and σ_3 denote the inelastic volumetric stain and the minimum principal stress, respectively Stormont et al. (1992).
Heemann and Heusermann	$k = \frac{k_{\mathrm{tp}}}{\left(\frac{\phi_{\mathrm{tp}}}{\phi}\right)^{n_1} + \left(\frac{\phi_{\mathrm{tp}}}{\phi}\right)^{n_2}}$	n_1, n_2 are model parameters. k_{tp} and ϕ_{tp} are both exponential functions of minimum principal stress, i.e. $k_{\mathrm{tp}} = a_k \exp(b_k\sigma_3)$ and $\phi_{\mathrm{tp}} = a_\phi \exp(b_\phi\sigma_3)$ Heemann & Heusermann (2004); Popp et al. (2007).

of studies, the effect of minimum principal stress on the permeability changes has been taken into account as well. Table 2.2 shows some of the existing models to describe the permeability changes of rock salt.
Fokker et al. (1993) investigated the effect of pore pressure on the peak strength and the permeability of salt and showed that strength reduces and permeability increases with increasing the pore pressure. When damage occurs in dilatancy domain, new pathways may be generated for the gas/liquid to penetrate into the rock salt. Because of this reason, the pore pressure increase can influence the strength and the mechanical behavior. The presence of a fluid (liquid or gas) in the pores of a damaged rock salt creates an effective pore pressure. The effect of pore pressure can be explained with the effective stress concept Alkan et al. (2007); Schulze et al. (2001), which is given by:

$$\sigma_{ij}^{\text{eff}} = \sigma_{ij} - \alpha_b p_p \delta_{ij} \tag{2.3}$$

where α_b is the Biot coefficient and p_p is the pore pressure. The Biot coefficient $\alpha_b < 1$ indicates that only a part of the rock salt is affected by the fluid pressure. Alkan et al. (2007) performed a series of tests on the Asse rock salt to determine the Biot coefficient. The results obtained in these tests showed that the Biot coefficient is around 0.25 in the vicinity of dilatancy boundary.

2.2.2.7 Tensile strength of rock salt

Tensile strength of rock material is normally defined by the ultimate strength in tension. Rock salt generally has a low tensile strength (typically ranging from 0.2 to 3 MPa). The tensile strength of rock salt can be determined either by the Brazilian test or the direct tensile test. However, the tensile strength values obtained from the direct tensile test may differ from the values determined from Brazilian test. This difference is due to the testing procedure and the nature of salt itself Jeremic (1994). The low tensile strength is due to the existence of micro-cracks in the rock. When the rock sample is under tension, the pre-existing micro-cracks can propagate faster. The existence of micro-cracks may also result in rupture in tension with a small strain. It should be noted that the tensile strength is an important factor in design process of underground storage system. Therefore, all the points at the vicinity of underground storage caverns should not experience a tensile stress higher that the tensile strength.

2.2.3 Rock salt behavior in long-term creep tests

2.2.3.1 Transient, steady-state and tertiary creep

When a rock salt sample is subjected to a constant load and temperature, a time-dependent deformation known as "creep" takes place. Fig. 2.15 demonstrates how the strain and the strain rate are developed during a creep test. Depending on the magnitude of the applied load and the temperature, the following creep phases can be observed in long-term experiments:

- Transient creep: after applying the load a transient deformation occurs. This type of deformation is known as "transient creep" or "primary creep". During the transient creep, the creep strain rate reduces significantly due to the strain hardening.
- Steady-state creep: when the creep strain rate approaches to a constant value, a steady-state deformation starts to develop. This phase of deformation is known as "steady-state creep", "secondary creep" or "stationary creep".
- Tertiary creep: this is the third phase of creep deformation which is also known as "accelerated creep". In this phase, the creep strain rate shows a rapid increase due to the crack growth and the damage propagation in the sample. When the damage reaches to a certain threshold, the creep rupture or long-term failure takes place. As already explained in Section. 2.2.2.2, the long-term failure or creep rupture occurs only in dilatancy domain. Therefore, for the stress conditions below the dilatancy boundary, this phase of creep is not experienced.

2.2.3.2 Effect of temperature on creep behavior

Studying the effect of temperature on creep behavior has a long history, in particular, with regard to the storage of waste material in salt formations. In that case, the considerable increase of temperature due to the radiation processes of nuclear waste deposited in salt formations can significantly affect the creep behavior. Similarly, in the energy storage caverns, the pressure fluctuations of the storage product (i.e. compressed air or hydrogen) results in the temperature variation of surrounding rock. It is well accepted that the rock salt ductility increases with increasing temperature. Due to this fact, the steady-state strain rate in creep tests increases considerably at elevated temperatures. Fig. 2.16 shows a double logarithmic chart representing the changes of steady-state strain rate with respect to the applied stresses (i.e. deviatoric stress q) and the temperature. As seen, for a given

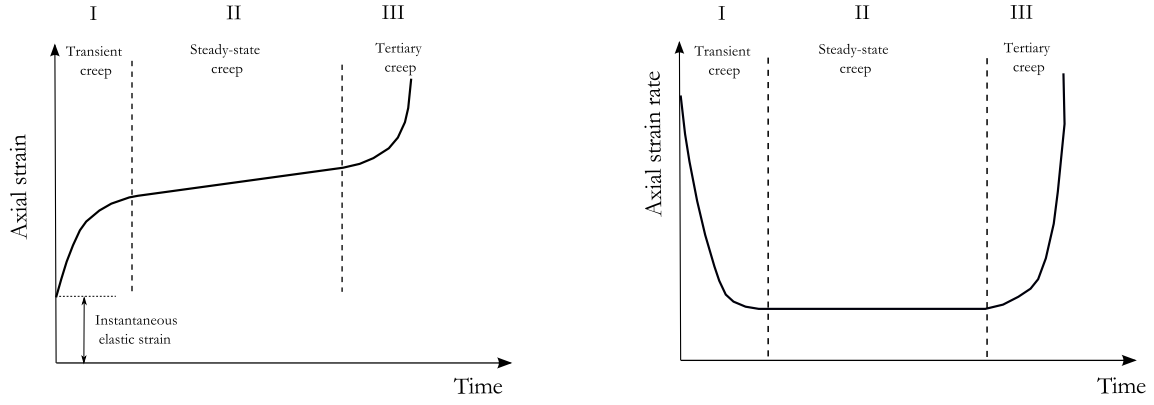

Figure 2.15: Typical responses observed in long-term creep tests, (a) axial strain vs. time; (b) axial strain rate vs. time

stress, the steady-state rate shows a remarkable increase at the elevated temperatures. For this reason, the maximum allowable temperature in a energy storage cavern is one of the most important design factors, because it can accelerate the cavern convergence and endanger the long-term serviceability of the storage system.

2.2.4 Rock salt behavior under cyclic loading

In the past, rare investigations have been made to understand the behavior of rock salt under cyclic loading conditions. Therefore, the modeling of salt caverns that work under cyclic loading conditions is still a challenging task. During the recent years, a limited number of experimental studies have been performed to assess the effect of cyclic loading on the mechanical behavior of rock salt with main focus on the fatigue failure and cyclic damage progress (e.g. Fuenkajorn & Phueakphum (2010); Ma, Liu, Fang, Xu, Xia, Li, Yang & Li (2013); Liu et al. (2014); Guo et al. (2012); Liang et al. (2012); Roberts et al. (2015); Bauer et al. (2011)). Fig. 2.17a shows a typical stress-strain curve which can be observed in the cyclic loading tests. This test has been performed by Guo et al. (2012) on Jintan rock salt under uniaxial cyclic loading. As shown in this figure, the axial stress monotonically increases from 0 to 22.5 MPa (90% of compressive strength), then, it varies between 11.25 and 22.5 MPa. On the other hand, the plotted axial strain versus time in Fig. 2.17 shows that the whole cyclic loading process can be divided into three stages that is similar to the conventional static creep tests. In the first stage, the axial strain increases rapidly and there is a large accumulation of strain. Then, in the second stage, the axial

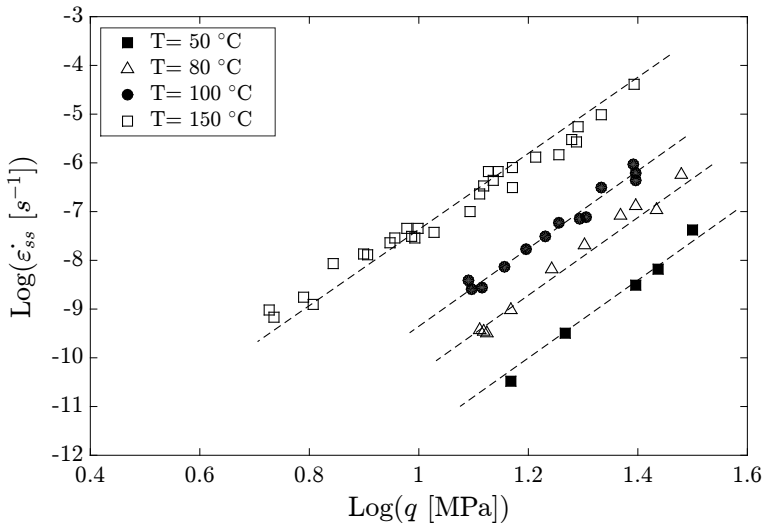

Figure 2.16: Effect of temperature on creep deformation; $\dot{\varepsilon}_{ss}$ is the steady-state creep rate and q represents the deviatoric stress, i.e. $q = \sigma_1 - \sigma_3$; test data from Hunsche & Hampel (1997)

strain accumulates slowly with a relatively constant rate and finally, after a number of cycles, the axial strain increases considerably and the specimen reaches the fatigue failure. Fatigue failure occurs when the strain energy exceeds a critical energy level equivalent to failure under non-cyclic load Ma, Liu, Wang, Xu, Hua, Fan, Jiang, Wang & Yi (2013); Attewell & Farmer (1973). The following items summarize the most important findings related to the mechanical behavior of rock salt in cyclic loading condition.

- The failure in cyclic tests (or fatigue failure) can not be observed when the maximum applied stress is below a threshold. Ma, Liu, Wang, Xu, Hua, Fan, Jiang, Wang & Yi (2013) observed the fatigue failure for stresses in the range of 80-89 % of the triaxial compressive strength of rock salt. Guo et al. (2012) reported a series of uniaxial cyclic tests. Based on their observations, the suggested threshold value of fatigue is between 75-80% of uniaxial strength. Song et al. (2013) suggest that the fatigue limit of salt rock is equal to 75% of the compression strength. Liang et al. (2012) indicate that, under cyclic loading, rock salt fails at a stress close to 65-70% of the ultimate strength. However, all the suggested values are beyond the dilatancy boundary which is approximately 65% of the compression strength. Therefore, it can be concluded that fatigue failure is only expected above dilatancy boundary. The damage accumulation will accelerate beyond the point of volume expansion (Point B in Fig. 2.9). Afterward, with increasing the stress level, the rock salt will quickly yield and fail under cyclic loading Liu et al. (2014).

- The rock salt viscoplasticity decreases with increasing loading frequency. That means, for lower loading frequencies, the rock salt ductility increases. Therefore, the fast cyclic loads results in less strain accumulations Fuenkajorn & Phueakphum (2010); Guo et al. (2012). However, the loading frequency conducted in most of the experimental studies is much higher than those induced by the charge and discharge processes of rock salt cavern (e.g., daily, monthly or annually).
- The maximum stress during the cyclic loading has more influence than the minimum stress on the deformation behavior of rock salt. When the maximum stress increases, the strain accumulation becomes more significant compared with those obtained from increasing of minimum stress Ma, Liu, Wang, Xu, Hua, Fan, Jiang, Wang & Yi (2013).
- The effect of temperature on cyclic loading behavior is still an open question. Song et al. (2013) performed three uniaxial cyclic tests with different constant temperatures (i.e. 13 °C, 30 °C and 60 °C). The obtained results showed that the fatigue life increases with increasing temperature. This phenomenon may be caused by the increase in the viscosity and ductility of rock salt.

2.3 Existing constitutive models for rock salt

2.3.1 Classification of the existing models

The phenomenological and micro-structural studies provide a basis for developing the rock salt constitutive models. Underground storage of energy carriers in the form of crude oil, liquid hydrocarbons or natural gas inside the rock salt caverns has been the topic of research for many years. Therefore, a large number of investigations have focused only on the modeling of transient and steady-state creep deformation. These models have been specifically derived to predict long-term creep deformations in caverns with relatively constant internal pressures (e.g. for seasonal or annual storage caverns). Of the main concern in these groups of studies is to describe the ductile behavior of rock salt observed in the long time experiments. These types of constitutive models are only applicable for the stress states below the dilatancy boundary. In this case, dilatation effects such as damage propagation, failure, permeability changes are not important. Table 2.3 provides a list of some existing models which have been merely developed for the creep behavior of rock salt without considering damage and dilatancy effects. However, the design process of

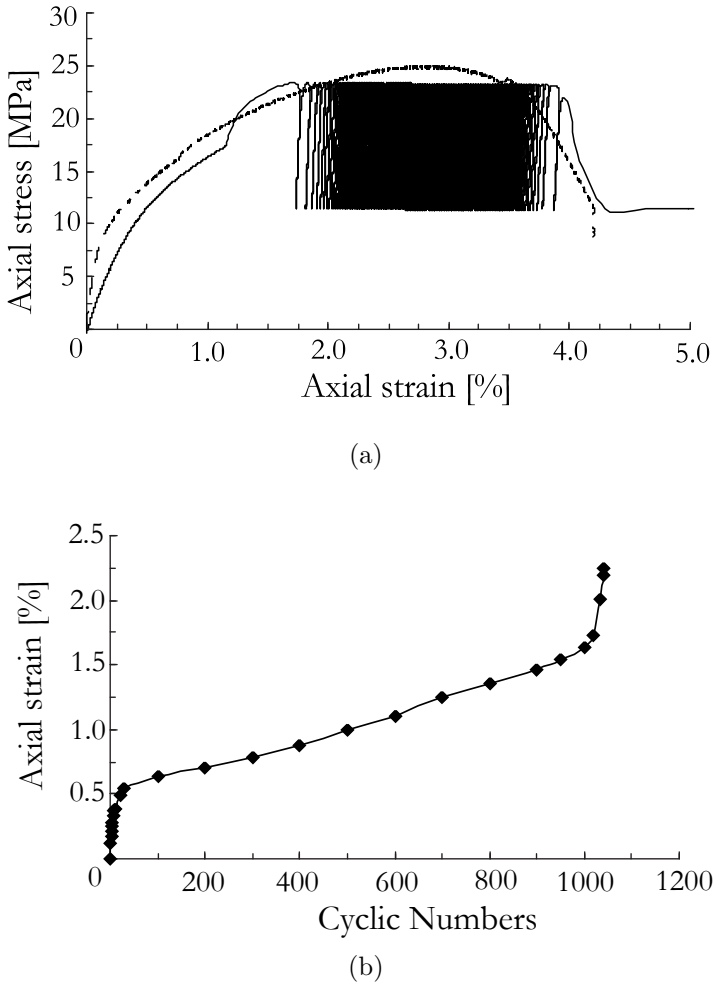

Figure 2.17: Typical responses observed in cyclic loading tests, (a) axial stress vs. axial strain, the red curve is the uniaxial quasi-static curve ; (b) axial strain vs. time; test data from Guo et al. (2012)

caverns, in particular those operating under the cyclic thermo-mechanical loadings, becomes more reliable if the models cover all experimentally observed features. With this motivation, more elaborate constitutive models have been developed during the recent decade in an attempt to predict the rock salt behavior in the brittle domain (i.e. beyond the dilatancy boundary). These groups of models provide the possibility to describe both short-term and long-term behavior of rock salt. Table 2.4 lists a number of existing models which have been developed to predict the damage propagation and dilatancy effects around the caverns. In another classification, the models can be divided into two groups concerning their modeling approach, i.e. (1) macro-structural models (2) micro-structural models. Basically, the macro-structural models employ the continuum mechanical concepts such as viscoelasticity, viscoplasticity or continuum damage mechanics to describe

the phenomenological behavior of rock salt under different conditions. Depending on the model assumptions and the number of model parameters, different levels of complexity exist among these types of models. However, these models have a general form as:

$$\dot{\varepsilon}_{ij}^{ie} = f\left(\sigma_{ij}, T, t, d, \alpha_1, \alpha_2, \cdots, \alpha_n\right) \tag{2.4}$$

where, $\dot{\varepsilon}_{ij}^{ie}$ denotes the inelastic strain rate. The inelastic behavior can be also described as an additive superposition of several terms with the same format as Equtaion. 2.4. In general, the inelastic strain rate can be a function of stress tensor σ_{ij}, temperature T, time t, damage parameter d or a number of internal variables $\alpha_1, \alpha_2, \cdots, \alpha_n$. Essentially, the internal variables are defined to control the development of inelastic strain within the hardening and softening processes. These constitutive models may also have some model parameters without any physical meaning (i.e. curve fitting parameters). Generally, Eq. 2.4 can be expanded as:

$$\dot{\varepsilon}_{ij}^{ie} = F\left(\sigma_{ij}, T, t, d, \alpha_1, \alpha_2, \cdots, \alpha_n\right) \frac{\partial Q\left(\sigma_{ij}, T, t, d, \acute{\alpha_1}, \acute{\alpha_2}, \cdots, \acute{\alpha_n}\right)}{\partial \sigma_{ij}} \tag{2.5}$$

here, function F is a scalar function which describes the magnitude of inelastic strain rate tensor and function Q corresponds to the potential surface. The derivation of potential surface with respect to the stress tensor (i.e. $\dfrac{\partial Q}{\partial \sigma_{ij}}$) describes the direction of strain. Both functions F and Q may include temperature dependent parameters (e.g. temperature dependent viscosity). In this way, the effect of temperature on the mechanical behavior is taken into account. Time is another important factor in constructing the constitutive model. Some constitutive models directly include the time as a variable in the model (time hardening models). Damage parameter can be another variable in a constitutive model. Depending on the experimental observations, different definitions exist in the literature for describing the damage of rock salt. For example, Hou (2003) and Ma, Liu, Fang, Xu, Xia, Li, Yang & Li (2013) used a stress-dependent damage function to describe the tertiary creep of rock salt. According to this definition, the rate of damage progress during creep test is dependent on the magnitude of stresses applied to the rock sample as well as of the current accumulated damage. Liu et al. (2014) showed that the released energy during loading–unloading cycles increases exponentially above the dilatancy boundary. They also concluded that, with the onset of volume dilation, the damage development accelerates. Therefore, they proposed an exponential function for the damage evolution which increases with the released strain energy. In the same line of thought, Hampel & Schulze (2007) introduced a damage parameter whose value grows

exponentially with the released volumetric strain energy in the dilatancy domain. On the other hand, the micro-structural models intend to give a physical meaning to the internal model variables. In other words, some model variables which affect the response of the model in macro-level are defined based on the micro-level observations such as the average grain size or the density of dislocations. In this way, a consistent description between the micro-level changes and the macro-level observations is achieved. It should be noted, in most cases, the micro-structural models apply one single equation to describe different deformation mechanisms. In other words, the transition from one mechanism to another in theses models is controlled by the internal variables associated with the micro-sturctural (not through superpositioning). In order to highlight the differences between these modeling approaches, two well accepted and approved constitutive models for rock salt (in particular within the German research community) are explained more in detail in the following sections.

Table 2.3: The transient and steady-state creep models without damage and dilatancy effects

Model	Type	Description
BGRa/BGRb	Macro-structure	These models were introduced by Hunsche & Schulze (1994) to describe the steady-state creep deformation of rock salt as a function of temperature and deviatoric stress. More explanations in Section. 3.2
LUBBY2	Macro-structure	LUBBY2 is a viscoelastic model to describe transient and steady-state creep deformations. More explanations in Section. 3.3
Composite model	Micro-structure	Composite Model (CM) describes the transient and the steady-state creep deformations using one single equation. Based on the model assumptions, the sub-grain structure consists of: (1) the sub-grain boundary which is formed by dislocations with high density (hard zone), and (2) the sub-grain interior with a lower dislocation density (soft zone). Therefore, similar to the composite material, the interior part is more ductile than the boundaries and it shows a different deformation behavior. The strain rate is defined based on the Orowan's equation which relates the creep rate to the average microscopic velocity and the density of free dislocations in the crystalline materials. The creep strain rate in this model, is a function of the deviatoric stress, temperature and three internal state variables i.e. (1) the mean distance between dislocations, (2) the average width of sub-grain walls and (3) the average diameter of sub-grains. The dependency of the creep rate on temperature has been expressed by an exponential term while a hyperbolic sine term describes the stress dependency. In the isothermal condition, only the internal state variables change during the transient creep. Therefore, the creep strain rate can be adjusted by varying these variables within a predefined range using suitable evolution functions. On the other hand, when the internal variables reach to their maximum values, the creep strain rate remains constant and the steady-state creep starts to develop. Under this condition, a balance state between the dislocation generation and the dislocation recovery is obtained within the creep process Weidinger et al. (1997); Sedláček & Blum (2002).

Table 2.3 Continued: The transient and steady-state creep models without damage and dilatancy effects

MD model	Micro-structure	The Multi-mechanism Deformation (MD) model was developed by Munson and Dawson to describe the transient and steady-state creep deformations. The total creep strain rate in this model is a summation of three terms. Each term is associated with a specific creep deformation mechanism. The three mechanisms represent (1) dislocation climb controlled creep (2) the micro-mechanistically undefined mechanism for low stresses (this mechanism was introduced in Section 2.1.4), and (3) dislocation glide mechanism. The model includes two internal variables to model the strain hardening and the recovery process during the transient creep. However, the model has no description for dilatancy and damage evolution. Therefore, it is mainly used to model creep deformation below the dilatancy boundary Munson & Dawson (1981); Munson (1997, 1998); Senseny & Fossum (1998) .
SUVIC model	Micro-structure	The SUVIC model (Strain rate history-dependent Unified Viscoplastic model with Internal variables for Crystalline materials) is a unified model with internal state variables (ISV) to describe the ductile deformation of rock salt. Similar to the composite model (CM), one single equation is used to describe the strain rate during the transient and the steady-state creeps. This equation has some internal state variables which can evolve during hardening and recovery processes. When theses variables reach to their saturation value, the transient creep terminates and the steady-state creep develops. Since its first version (Aubertin et al. (1991)), several modifications have been applied to the model, e.g. see Aubertin et al. (1991, 1999); Yahya et al. (2000); Aubertin et al. (1993).
Olivella et al.	Micro-structure	This model has been basically developed for crushed salt which is used as the back-fill material in nuclear waste disposal systems. In constant loading applications, the inelastic strain rate in this model consists of two terms; i.e. (1) the fluid-assisted diffusional transfer rate $\dot{\varepsilon}^{\mathrm{FADT}}$ and (2) the dislocation creep rate $\dot{\varepsilon}^{\mathrm{DC}}$. As earlier discussed in Section. 2.1.4, the fluid-assisted diffusional transfer creep is related to the deformation at very low stress ranges. Olivella and Gens (2002) theoretically obtained a function for $\dot{\varepsilon}^{\mathrm{FADT}}$ which describes the deformation based on several factors such as stress, temperature, void ratio, average grain size and degree of saturation. on the other hand, the dislocation creep term is associated with the movement of free dislocations. This term is only dependent on stress, temperature and void ratio Olivella & Gens (2002).

Table 2.3 Continued: The transient and steady-state creep models without damage and dilatancy effects

Urai et al. model	Micro-structure	This model describes the steady-state creep at low stress conditions. As discussed earlier, the deformation at low stress ranges is governed by solution precipitation creep. Under such condition, the creep strain rate has a linear relation with the deviatoric stress, i.e. $\dot{\varepsilon} \propto q$. Moreover, the creep rate is a function of temperature and the average diameter of the grains. According to Urai et al. (1986), the long-term deformation of rock salt would be underestimated if the governing equations which describe other creep mechanisms are extrapolated to this range of stress. For example, Fig. 2.18 shows the experimental data for the steady-state creep rates at different temperatures and stresses. As seen, the BGRa model can adequately represent the creep behavior within the feasible range of the experimental studies (i.e. green box). However, for the low stress range (i.e. less than 5 MPa), the solution precipitation creep is the governing mechanism. Therefore, extrapolation of the BGRa model to the low stress range may result in large errors in long time Urai & Spiers (2007); Urai et al. (1986, 1987).
Wawersik and Zeuch. (1984)	Macro-structural	This is a steady-state creep model obtained based on theoretical and experimental studies. The model is suitable for describing the steady-state creep deformation controlled by cross slip mechanism Wawersik & Zeuch (1984).

Table 2.4: List of existing constitutive models of rock salt with damage and dilatancy effects

Model	Type	Description
Cristescu et al.	Macro-structural	More explanations in Section. 2.3.2
IfG/GS	Micro-structural	More explanations in Section. 2.3.3.
IfG/Minkley	Macro-structural	This is a viscoelastic-plastic model to describe the short-term and long-term behavior of rock salt. Similar to the LUBBY2 model, the viscoelastic part of the model describes the transient and the steady-state creep deformations using the Kelvin and the Maxwell models, respectively. While, the plastic component of the model accounts for the short-term behavior in quasi-static tests. A modified Mohr-Columb failure boundary has been used to predict the short-term failure. Moreover, the post-failure softening can be described by including damage into the model. The elastic parameters in this model are functions of inelastic volumetric strain. Therefore, in dilatancy domain where damage and micro-cracking occur, the elastic parameters are degraded with increasing the volumetric strain Minkley & Muehlbauer (2007) .
Desai et al.	Macro-structural	The Desai model is based on a single-surface plasticity. The non-associated flow rule in this model yields to better description of the volumetric plastic strain. The dependency of yield surface on Lode's angle results in different material responses in triaxial compression, shear and extension tests. The model takes into account the material dilatancy and compressibility which enhances the modeling of the volumetric behavior and improves the fit to the experimental data. In addition, the failure boundary allows the model to account for the short-term failure of the rock salt in quasi-static strength tests. Furthermore, the rate dependency described via the viscoplasticity formulation explains the rate dependent behavior of rock salt. As shown in Desai & Varadarajan (1987), the model can be extended to a viscoplastic model using Perzyna viscoplasticity concept Desai & Zhang (1987); Desai & Varadarajan (1987); Desai & Salami (1987); Desai (2016).

Table 2.4 Continued: List of existing constitutive models of rock salt with damage and dilatancy effects

Composite Dilatancy Model	Micro-structural	Composite Dilatancy Model (CDM) is an extended version of Composite model (CM) which accounts for damage evolution, humidity effects and short-term failure. Based on this model, the non-dilatant strain rate obtained by the Composite Model is modified using three correction factors. The functions F_h, δ_{dam} and P_F are the correction factors which refer to the effects of humidity, damage and post failure, respectively. The dilatancy boundary defined by Hunsche et al. (2003) is used in the CDM to characterize the onset of dilatancy and damage. Humidity increases the creep rate above the dilatancy boundary. The function $F_h(\Phi, \sigma_3, \tau)$ applies the effect of relative humidity Φ on the creep rate if the minimum principal stress σ_3 and the octahedral shear stress τ ensure that the stress state is above the dilatancy boundary. The function $\delta_{\mathrm{dam}}(d, \sigma_3)$ defines the dependency of creep rate on damage parameter d. In this model, the damage evolution is formulated through the inelastic strain work performed in dilatancy zone. This function results in material weakening and failure. The correction factor P_F describes the post failure behavior in quasi-static strength tests. Recently, an extended version of CDM was introduced in Hampel (2015) that takes into account the damage reduction and the healing process below the dilatancy boundary Hampel & Schulze (2007); Schulze et al. (2007); Hampel (2012, 2015).
FZK-INE	Macro-structural	The total inelastic strain rate in this model has two terms; i.e. (1) the constant volume term and (2) non-constant volume term. The constant volume term describes the transient and the steady-state creeps as a function of deviatoric stress and temperature. The volume increase of rock salt above the dilatancy boundary is described by a Perzyna type viscoplastic model. The model was originally developed for crushed salt by Hein (1991). An associated flow rule is used in this model to described the dilatancy and compressibility of the rock salt. The size of yield surface in stress space changes as a function of plastic volumetric strain. The defined dilatancy boundary by Hunsche (1993) has been used in this model to characterize the onset of dilatancy. Moreover, the short-term failure boundary of Cristecu Cristescu & Gioda (1994) has been utilized to predict the peak strength in quasi-static tests Hein (1991); Pudewills & Krauss (1999); Pudewills & Droste (2003); Pudewills (2007*a*,*b*).

Table 2.4 Continued: List of existing constitutive models of rock salt with damage and dilatancy effects

MDCF	Micro-structural	This is an extended version of MD model which accounts for damage evolution and damage healing during creep deformation. The Multi-mechanism Deformation Coupled Fracture (MDCF) model was formed by adding three terms to MD model. These terms describe the strain rates caused by shear damage, tensile damage and damage healing. Furthermore, a continuum, isotropic damage parameter has been included in the model to enhance the stress influence by reduction of the effective area and contributes directly to the creep strain rate. Therefore, tertiary creep or long-term failure can be described by this model Chan et al. (1994, 1997); Fossum et al. (1998). Some modified versions of MDCF model such as IUB-MDCF and LUBBY-MDCF have been suggested in Schulze et al. (2007); Leuger et al. (2010); Hampel et al. (2010).
Hou/Lux model	Macro-structural	The total inelastic strain rate in this model is the result of the additive superposition of three parts (1) viscoelstic strain rate with constant volume $\dot{\varepsilon}_{ij}^{ve}$ (2) viscoplastic strain rate induced by damage $\dot{\varepsilon}_{ij}^{d}$ (3) viscoplastic strain rate induced by healing $\dot{\varepsilon}_{ij}^{h}$. The viscoelastic term with constant volume is based on the LUBBY 2 model. Hou and Lux have defined a dilatancy zone in the stress space. In this zone, micro-cracking takes place and damage grows up. Because of this reason, other relevant factors such as permeability and creep rate have an upward trend. The dilatancy damage strain rate $\dot{\varepsilon}_{ij}^{d}$ consists of two terms: the $\dot{\varepsilon}_{ij}^{ds}$ term, as a result of shear induced damage and the $\dot{\varepsilon}_{ij}^{dz}$ term which is the damage strain rate under a tensile stress. Hou and Lux defined another boundary below the dilatancy boundary called as healing boundary. The term healing is used for the overall process of the damage decreasing. Within the healing zone (i.e. below the healing boundary), the closing of micro-cracks takes place and the damage heals. There exists also a transient area between the healing and the dilatancy boundaries which is called "constant volume zone". In this zone, the volumetric deformation and the damage remain constant. Similar to the dilatancy damage strain ε_{ij}^{d}, the healing damage strain ε_{ij}^{h} is expressed through the plasticity theory Hou (2003); Hou & Lux (1998); Lux (2009).

Table 2.4 Continued: List of existing constitutive models of rock salt with damage and dilatancy effects

Ma et al.	Macro-structural	The inelastic strain in this model has two terms, (1) the creep strain consisting of transient, steady-state and tertiary terms, and (2) the instantaneous plastic strain with generalized Hoek-Brown failure boundary. The plastic term can describe the short-term behavior of rock salt in quasi-static tests, while the creep term represents the long-term behavior. Additionally, an isotropic damage parameter has been included in the model to predict the tertiary creep and the long-term failure. The evolution of damage parameter in this model is dependent on the stress state and the current damage value Ma, Liu, Fang, Xu, Xia, Li, Yang & Li (2013).
Deng et al.	Macro-structural	The inelastic strain in this model is a superposition of (1) a viscoelastic term based on the Kelvin model; and (2) a viscoplastic term based on the Duvaut-Lions model Duvant & Lions (2012) with Drucker-Prager yield function. Moreover, based on the continuum damage mechanics definition of the effective area, the relationship between stresses in the undamaged material and the damaged material has been defined. The evolution of damage in this model is related to the effective inelastic strain. In this way, the tertiary creep in long-term experiments and the softening in strain-controlled quasi-static tests can be modeled. The model is capable to simulate the time-dependent deformation and quantitatively evaluate the long-term stability of salt caverns Deng et al. (2014).

2.3.2 A macro-structural constitutive model: Cristescu et al. model

In this section, one of the macro-structural models is introduced more in detail. Cristescu formulated an elasto-viscoplastic model in order to model the transient and the steady-state creep of rock salt considering the volumetric dilatation and compressibility (see Cristescu & Hunsche (1998); Cristescu & Gioda (1994); Cristescu (1987, 1993); Nicolae (1999)). Based on this model, the total inelastic strain rate is obtained using Eq. 2.6. $\dot{\varepsilon}_{ij}^{tr}$ and $\dot{\varepsilon}_{ij}^{ss}$ represent the transient and the steady-state creep rates, respectively. In the following, these quantities are explained in detail.

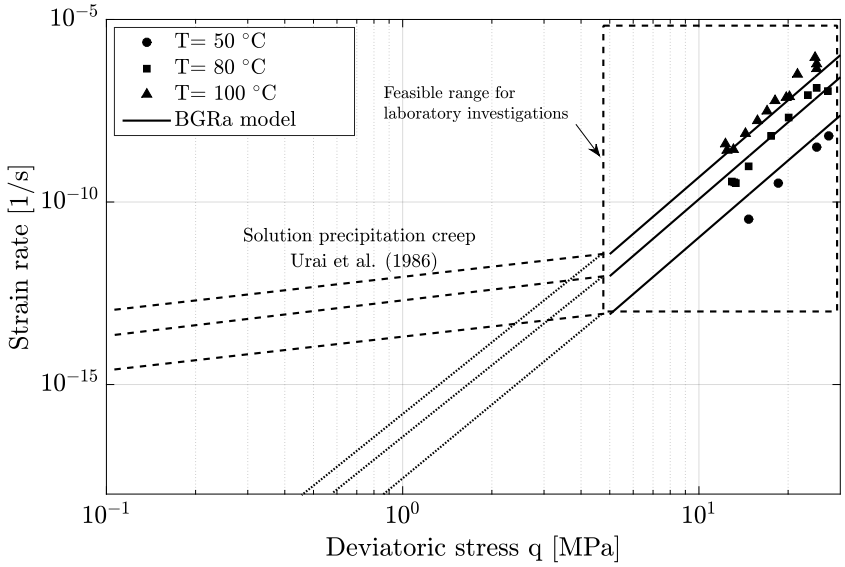

Figure 2.18: Deviatoric stress q versus steady-state strain rate diagram including the BGR laboratory data Hunsche & Hampel (1999). Applying these data in the low stress range requires extrapolation. Dotted lines are extrapolation of the BGRa creep model. Red dashed lines are the solution- precipitation creep model. As seen, the extrapolated BGRa model may result in large errors in the long-term predictions

$$\begin{cases} \dot{\varepsilon}_{ij}^{ie} = \dot{\varepsilon}_{ij}^{tr} + \dot{\varepsilon}_{ij}^{ss} \\ \dot{\varepsilon}_{ij}^{tr} = k_{_{tr}} \left\langle 1 - \dfrac{w(t)}{H(p,\tau)} \right\rangle \dfrac{\partial Q^{tr}(p,\tau)}{\partial \sigma_{ij}} \\ \dot{\varepsilon}_{ij}^{ss} = k_{_{ss}} \dfrac{\partial Q^{ss}(p,\tau)}{\partial \sigma_{ij}} \end{cases} \tag{2.6}$$

The term $\dot{\varepsilon}_{ij}^{tr}$ represents a non-associated viscoplastic equation which describes the transient part of the creep strain. Q^{tr} and H are the viscoplastic potential and yield functions for the transient creep, respectively. Cristescu assumed that both functions depend on two stress invariants only: the mean stress p and the octahedral shear stress τ. That means, the effect of intermediate stress has not been taken into account in this model. The viscosity coefficient $k_{_{tr}}$ is a constant value (however, this parameter can be defined as a function of temperature). w is the irreversible work per unit volume which is used as a work hardening parameter or internal state variable. The brackets $\langle\rangle$ return always the positive part of the function. The dilatancy and the short-term failure boundaries defined by Cristescu and his coworkers have been shown in Fig. 2.11. Function Q^{tr} has the key

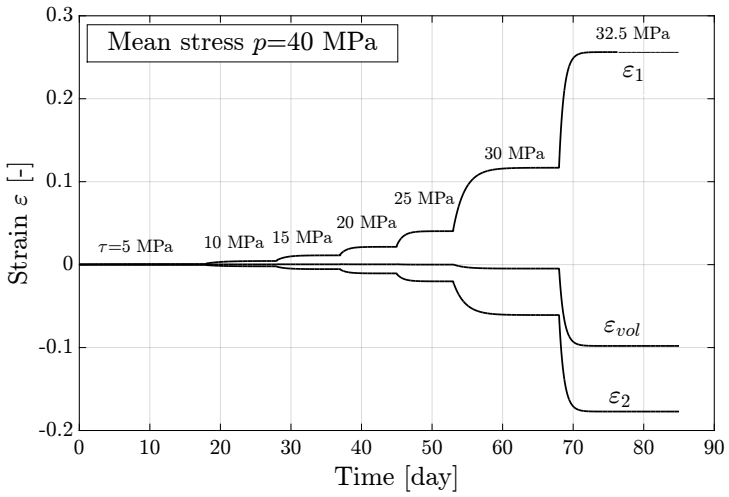

(a) Transient creep curves in triaxial deviatoric tests

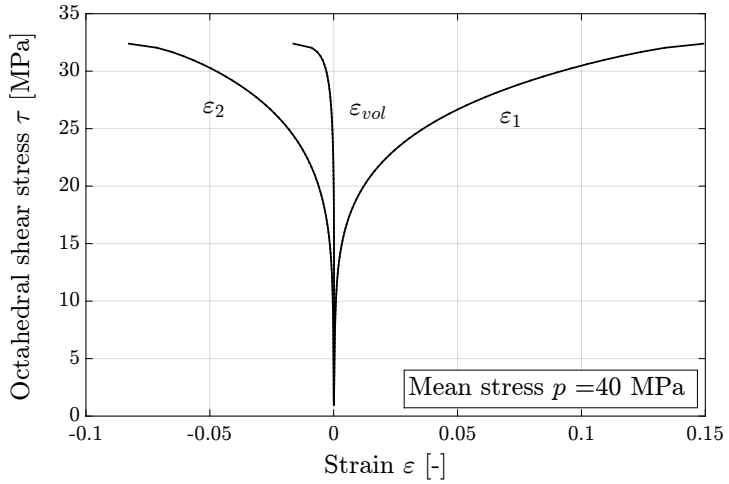

(b) True triaxial strain- stress curves for salt rock

Figure 2.19: Modeling of creep and true triaxial tests for rock salt using Cristescu et al. model

role in describing the volumetric deformation during transient creep. This function has been defined in a way that the following conditions are fulfilled Cristescu (1993):

$$\begin{cases} \text{Below dilatancy boundary} \Rightarrow \dfrac{\partial Q^{tr}(p,\tau)}{\partial p} > 0 \Rightarrow \dot{\varepsilon}^{tr}_{\text{vol}} < 0 \\ \text{Dilatancy boundary} \Rightarrow \dfrac{\partial Q^{tr}(p,\tau)}{\partial p} = 0 \Rightarrow \dot{\varepsilon}^{tr}_{\text{vol}} = 0 \\ \text{Beyond dilatancy boundary} \Rightarrow \dfrac{\partial Q^{tr}(p,\tau)}{\partial p} < 0 \Rightarrow \dot{\varepsilon}^{tr}_{\text{vol}} > 0 \end{cases} \tag{2.7}$$

The term $\dot{\varepsilon}_{ij}^{tr}$ can be also used to describe the quasi-static strength tests. Two typical examples of applying the Cristescu model for salt rock have been shown in Fig. 2.19. In the first example, the transient creep of the salt rock has been modeled. A constant mean pressure ($p = 40$ MPa) has been applied to the salt rock specimen while the deviatoric part increases in seven steps ($\tau = 5, 10, 15, 20, 25, 30, 32.5$ MPa). The duration of each step is between 10-15 days. Therefore, the change of strain has been calculated using the transient creep term. The second example describes the short-term strain-stress behavior of the salt rock in a triaxial experiment. The mean stress is kept constant (p=40 MPa) and the deviatoric part increases with a constant rate ($\dot{\tau} = 21.4$ MPa/min). As shown, the volume increase (dilatation) and the failure can be described using this model.
The term $\dot{\varepsilon}_{ij}^{ss}$ in Eq. 2.6 corresponds to the steady-state creep deformation. k_{ss} is the steady-state viscosity coefficient and $Q^{ss}(p, \tau)$ is the steady-state potential function. This function has been obtained by Cristescu in Cristescu & Gioda (1994); Cristescu & Hunsche (1998). Based on the model assumptions, the volumetric changes inside the compressibility zone is assumed to be zero for the steady-state creep because the volume can not shrink to zero when time goes to infinity. Therefore, the steady-state potential function has been defined considering the following conditions:

$$\begin{cases} \text{Below dilatancy boundary} \Rightarrow \dfrac{\partial Q^{ss}(p,\tau)}{\partial p} = 0 \Rightarrow \dot{\varepsilon}_{\text{vol}}^{ss} = 0 \\ \text{Compressibility/dilatancy boundary} \Rightarrow \dfrac{\partial Q^{ss}(p,\tau)}{\partial p} = 0 \Rightarrow \dot{\varepsilon}_{\text{vol}}^{ss} = 0 \\ \text{Beyond dilatancy boundary} \Rightarrow \dfrac{\partial Q^{ss}(p,\tau)}{\partial p} < 0 \Rightarrow \dot{\varepsilon}_{\text{vol}}^{ss} > 0 \end{cases} \tag{2.8}$$

Two typical creep curves have been depicted in Fig. 2.20a which show the transient and the stationary creep responses using the Cristescu model. Moreover, a scalar damage parameter d has been defined by Cristescu in Eq. 2.9 to determine the amount of energy released due to the micro-cracking. $w_{vol}(t)$ denotes the volumetric viscoplastic strain work per unit volume and w_{vol}^{max} is its maximum value which is reached at the dilatancy boundary. The critical value of damage d_f for characterizing the creep failure is obtained empirically. Therefore, the long-term failure or creep rupture occurs when $d(t)$ is equal to its ultimate value d_f.

$$d(t) = w_{vol}^{max} - w_{vol}(t) \tag{2.9}$$

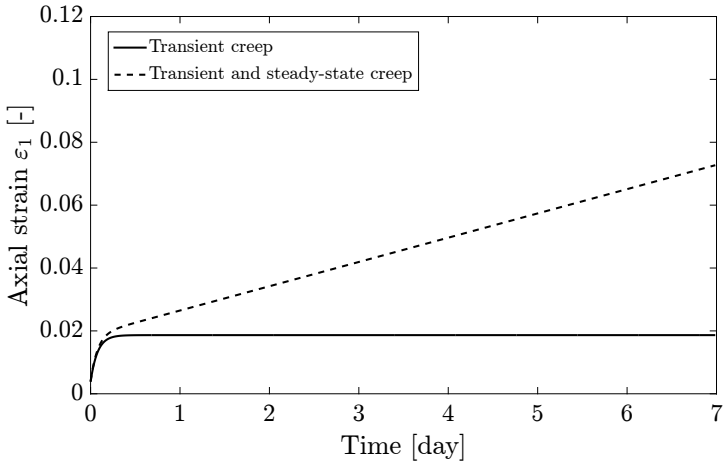

(a) Cristescu's model

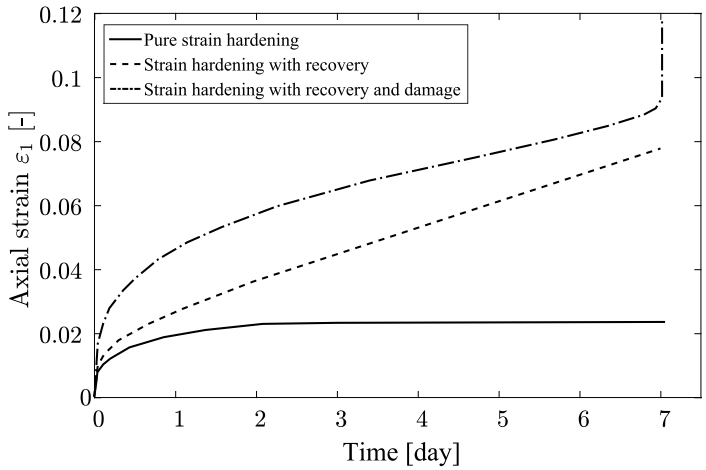

(b) Günther/Salzer's model

Figure 2.20: Typical creep response of salt rock obtained by (a) Günther/Salzer's model (b) Cristescu's model

2.3.3 A micro-structural constitutive model: Günther/Salzer model

In this section, one of the micro-structural models is introduced more in detail. This constitutive model has been developed based on the physical processes which take place at the microscopic level Günther & Salzer (2007); Günther (2009); Günther et al. (2015). Accordingly, the three phases of creep are described in the scope of a single equation. Based on this model, the inelastic strain rate is equal to:

$$\dot{\varepsilon}_{ij}^{ie} = A_{_p} \frac{q^{n_p}}{\left(\varepsilon_{\text{eff}}^{V}\right)^{\mu}} \frac{\partial Q^{cr}}{\partial \sigma_{ij}} \tag{2.10}$$

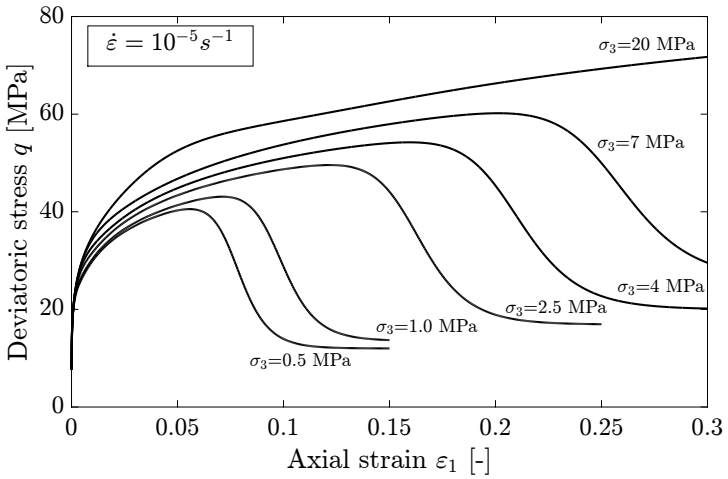

(a) Constant deformation rate

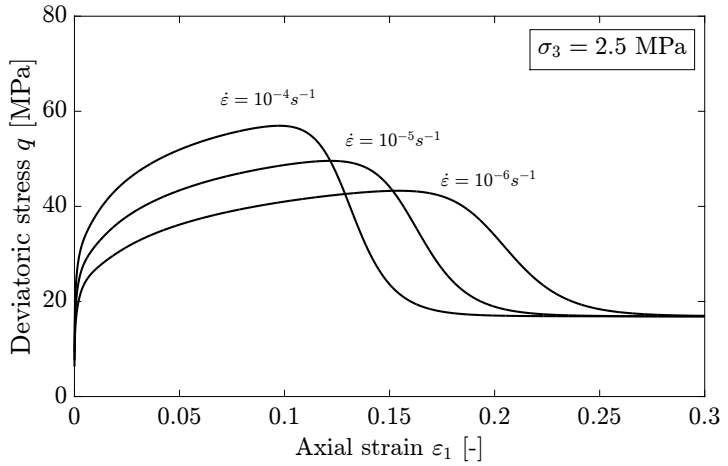

(b) Constant confining pressure

Figure 2.21: Triaxial short-term strength test modeling using Günther/Salzer's model

where A_p, n_p and μ are material parameters and q is the deviatoric stress. $\varepsilon_{\text{eff}}^{V}$ is an internal state variable which governs the hardening, recovery and damage behavior. The potential function Q^{cr} in this equation is only dependent on the second invariant of deviatoric stress tensor, i.e. $Q^{cr} = q = \sqrt{3J_2}$. Initially, the deformation rate depends on the dislocations presented in the natural crystal of the salt rock which is shown as $\varepsilon_{\text{eff}}^{V0}$. As deformation continues , new dislocations are generated and the density of dislocations increases. Therefore, the value of $\varepsilon_{\text{eff}}^{V}$ goes up and this leads to a reduction in the inelastic strain rate $\dot{\varepsilon}^{ie}$. This step can be considered as the transient part of creep for the salt rock. With further deformation, the recovery processes become active. With the growing density of dislocations, or hardening, also the recovery rate increases. When the rate of the recovery and the generation of dislocations are equal, the value of $\varepsilon_{\text{eff}}^{V}$ becomes

constant and the creeping passes into the steady-state phase. For the stresses beyond the dilatancy boundary, the local stresses resulting from the generation of micro-cracks lead to the long-term failure. Under such condition, the propagation of damage results in softening behavior. Therefore, the generated damage counteracts the hardening and the value of $\varepsilon^{V}_{\text{eff}}$ decreases rapidly and the tertiary creep occurs. Considering these micro-level processes, Günther and Salzer proposed the following equation for the evolution of the state variable $\varepsilon^{V}_{\text{eff}}$:

$$\dot{\varepsilon}^{V}_{\text{eff}} = \sqrt{\frac{2}{3}\dot{\varepsilon}^{ie}_{ij} : \dot{\varepsilon}^{ie}_{ij}} - \frac{\varepsilon^{V}_{\text{eff}}}{t_c \exp\left(Q/RT\right)} - \dot{\varepsilon}_{\text{vol}} \tag{2.11}$$

The term $t_c \exp\left(Q/RT\right)$ defines the time at which the steady-state creep starts to develop. The dependency of the creep rate on the temperature is captured by this term. The parameter t_c is determined experimentally. The last term in the right side of Eq. 2.11 shows the effect of damage on the strain rate. Accordingly, the damage evolution rate is equal to the volumetric strain rate $\dot{\varepsilon}_{vol}$. Günther and Salzer developed a function for describing volumetric strain rate. This function is dependent on the inelastic strain work performed above the dilatancy boundary w_{dil} and the minimum principle stress σ_3. During the creep test, the term $\dot{\varepsilon}^{V}_{\text{eff}}$ is positive in the transient creep domain and converges to zero in case of steady-sate creep. If damage is considered, the term $\dot{\varepsilon}^{V}_{\text{eff}}$ decreases and becomes negative. Therefore the creep rate accelerates and the tertiary creep occurs. Fig. 2.20b represents the typical creep curves obtained by the Günther/Salzer's model.
The Günther/Salzer's model can be used for modeling the triaxial short-term strength test. In this case, the parameter $n_{_p}$ in Eq. 2.11 is not constant anymore. Instead, this parameter changes with the volumetric strain ε_{vol} and the minimum principal stress σ_3 as follows:

$$n_{_p} = \frac{n_{p0} + n_1 \exp\left(n_2\sigma_3\right)\left(1 - \exp\left(-n_3\varepsilon_{\text{vol}}\right)\right)}{\left(1 - \varepsilon_{\text{vol}}\right)^{n_4}} \tag{2.12}$$

where n_0 denotes the stress exponent for the non damaged salt rock. σ_3 is the confining pressure and n_1,..., n_4 are the model parameters. Fig. 2.21 represents two examples of triaxial test modeling using Günther/Salzer's model.

2.4 Modeling of storage systems in rock salt formations

Beside the material modeling investigations, a large number of studies deal with the numerical simulation of salt caverns for different applications. Depending on the storage product, the modeling considerations such as the time scale of the simulation, the loading rate and the magnitude of the thermo-hydro-mechanical loads applied to the rock salt may be different from one application to another. For example, in a crude oil storage cavern, the loading rate is very slow and the time scale of the storage is very long in comparison to the compressed air storage caverns. A large number of investigations have been specifically performed to predict the long-term behavior of salt caverns under creep deformation with relatively constant internal pressures (e.g. natural gas storage caverns). However, it has to be pointed that, up to now, rare investigations have been made to model the behavior of rock salt in compressed air storage caverns considering both cyclic mechanical and cyclic thermal loading. The main objective in this section is to review the most important issues related to the modeling of salt caverns.

2.4.1 Solution-mining process

A typical salt cavern is subjected to different loading conditions during the construction and operation time. In other words, the magnitude and rate of loading applied to the rock salt medium may have various changes throughout the cavern's life. As schematically represented in Fig. 2.22, the solution mining process is carried out in different phases which are explained as follows:

Initial phase: a bore hole is drilled from the ground surface down to a level equal to the bottom of the cavern. Then, two leaching pipes which are concentrically suspended into each other are run into the bore hole. Depending on the storage product and the geological formations, the depth of excavation may vary between 300 to 2000 m Bérest et al. (2007). Some of the existing caverns and their excavation depths have been shown in Fig. 2.23. After drilling the well, the bore hole is cemented from the ground surface to the casing-shoe which indicates the top of the cavern.

Leaching phase: in this phase, fresh water is continuously injected into the rock salt medium through the leaching pipes. The salt is dissolved by the water and the mixture of salt and water (brine) is transferred to the ground surface. Two different operational modes are used to ensure a controlled development of the cavern shape. The leaching modes are defined as: (1) the direct leaching process in which the fresh water runs through

the inner leaching pipe and the produced brine is transferred to the ground surface via the outer pipe and (2) the indirect leaching process in which the brine runs through the inner leaching pipe and the fresh water is injected to the rock salt medium via the outer pipe. By applying these two leaching modes and by shifting leaching pipes, the cavern is shaped. Leaching phase is relatively a long-term process. That means, depending on the volume of the cavern, the leaching time could range from one year to a few years Bérest & Brouard (2003).

Debrining phase: debrining process is performed after leaching phase. In this phase, the brine remaining in the cavern is displaced by injecting the storage product (i.e. such as compressed air or hydrogen) into the cavern. The storage product is injected through the outer pipe while the brine is extracted via the inner leaching pipe. The duration of this phase is less than leaching phase and it may take a few months to extract the brine from the cavern.

2.4.2 Finite element simulation of storage systems in rock salt

A number of studies can be found in the literature that suggest analytical solutions to investigate the performance of rock salt caverns (e.g. analytical solutions for predicting the cavern convergence Brouard et al. (2013); Li et al. (2015); Wei et al. (2016) or calculating the failure and the dilatancy around caverns Cristescu & Paraschiv (1995)). However, these types of studies are not applicable for more complicated scenarios in terms of geometry, loading condition and material model. In this case, Finite Element Modeling (FEM) can be considered as a powerful tool to solve the boundary value problems which govern the behavior of the model. Obviously, a finite element model should be constructed based on appropriate assumptions. In the following, some of the required assumptions for the finite element modeling of salt caverns are reviewed.

2.4.2.1 In-situ condition

The initial or the in-situ stresses before excavation are called "primary stresses". In most studies, the primary stresses have been assumed to be isotropic (i.e. $\frac{\sigma_h}{\sigma_v} = 1$). The in-situ measurement performed by BGR for the Gorleben salt dome located in Germany showed that the maximum and minimum in-situ stresses at the measuring points differ by only a small amount, which justifies the isotropic stress assumption Bräuer et al. (2011). However, Cristescu reported that, depending on several factors such as pore pressure,

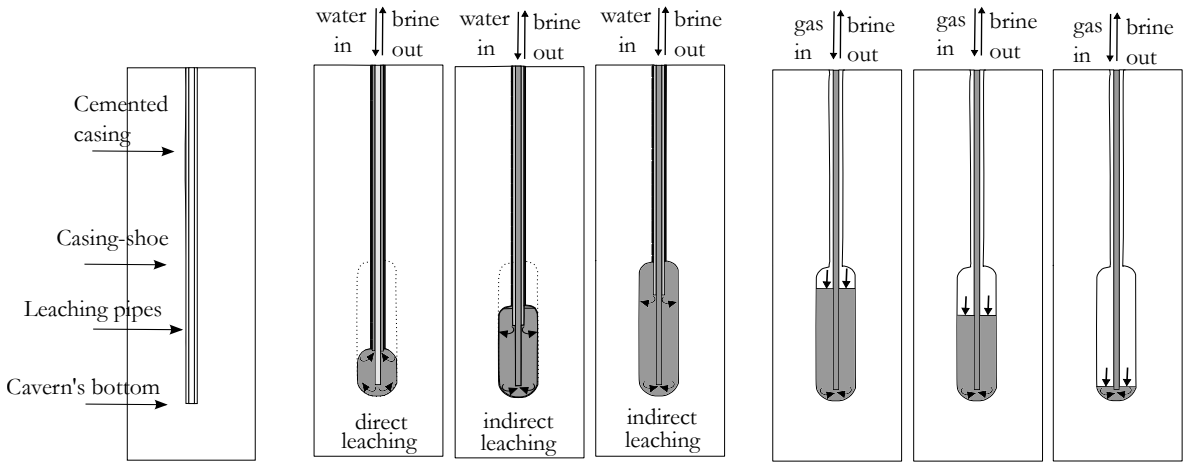

Figure 2.22: Schematic representation of salt cavern excavation process including leaching and debrining phases

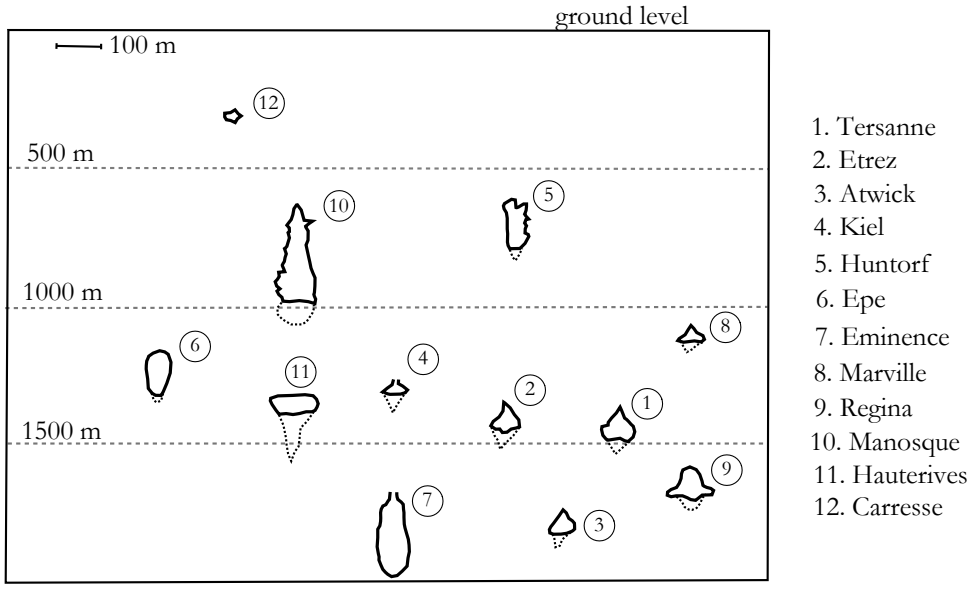

Figure 2.23: Some of the existing caverns and their excavation depths Bérest & Brouard (2003)

lithology, geologic structure and tectonic setting, the ratio between horizontal primary stress and the vertical primary stress can range between 0.3 to 3. Despite of the fact, very rare investigations have been performed up to now to understand the effect of primary stresses on the modeling predictions. In general, with the isotropic stress assumption, the vertical and horizontal stresses at depth h are calculated through the overburden pressure (i.e. $\sigma_v = \sigma_h = \rho g h$).
Regarding the initial temperature, the initial rock mass temperature increases linearly with depth with a temperature gradient of $\approx 0.03\ ^\circ\mathrm{C}/m$ Serbin et al. (2015). Therefore, the temperature at the depth of h is approximately equal to $T(h) = T(h_0) + 0.03h$. Here, $T(h_0)$ is the above ground temperature. Similar equations can be found in the literature that describe the changes of temperature with depth. For example, Düsterloh (2010) applied the following equation:

$$T(h) = T(h_0) + 0.04h_{\text{cap}} + 0.02h_{\text{salt}} \tag{2.13}$$

where, h_{cap} indicates the thickness of overlaying formation above the salt dome and h_{salt} denotes the thickness of salt formation above the cavern.

2.4.2.2 Thermodynamic of gas in the cavern

The temperature variation resulted from the injection and withdrawal processes is an important issue which should be considered in the numerical simulation. In particular, the effects of temperature variation can be more significant in the compressed air or hydrogen storage caverns which have relatively rapid charge/discharge cycles. However, accurate prediction of temperature inside the cavern is a challenging task. A lot of factors may influence the temperature of gas inside the cavern such as properties the storage gas (e.g. specific heat capacity), density of the gas, volume of the cavern, rate of charge/discharge processes, heat transfer between gas and rock mass, inflow/outflow temperature and surrounding rock temperature. Practically, some of these factors (e.g. the heat transfer between the gas and the surrounding rock mass) cannot be easily measured. Therefore, the existing models have simplified the process by different assumptions such as uniform distribution of temperature inside the cavern, constant volume for the cavern, constant rock mass temperature or even adiabatic condition (for example see Serbin et al. (2015); Lestringant et al. (2010); Kushnir et al. (2012); Raju & Khaitan (2012); Maton et al. (2013); Xia et al. (2015); Guo et al. (2016)). In these types studies, the calculation of gas

temperature and pressure inside the cavern is carried out by solving the mass and energy balance equations analytically.

2.4.2.3 Geometry of the cavern

For the sake of simplicity, the cavern geometry is normally idealized. In general, the simplified salt caverns have typically cylindrical, spherical or oval shapes. Fig. 2.24 is an illustration for a simplified cavern model. The most important geometrical parameters which can affect the mechanical behavior of cavern are: the cavern diameter, the height, the shape of the roof (i.e. flat or with curvature), the distance to the neighboring caverns and the distance to the neighboring formations (e.g cap rock) Staudtmeister & Rokahr (1997). The effect of geometrical parameters on the stability of the cavern have been investigated in a number of studies; for example in Cristescu & Paraschiv (1995); Wang et al. (2013); Sharifzadeh & Ghasr (2006); Moghadam et al. (2015); Wang, Yang, Ma, Daemen & Wu (2015); Yang et al. (2016); Wang et al. (2016).

2.4.2.4 Boundary conditions and time scale of the simulation

The boundary conditions and time scale of the simulation are strongly dependent on the storage product and the storage requirements. For example, the pressure variations in natural gas storage caverns takes place in a seasonal basis, while the compressed air storage caverns may experience daily cycles. Due to this fact, the selected time steps for the FE simulation should be much smaller in salt caverns with high frequency cycles than the seasonal or annual storage caverns. In addition, because of different storage requirements, the magnitude of the operating pressure and temperature differs from one application to another.

2.4.2.5 Thermo-Hydro-Mechanical coupling

Obviously, the safety assessment of rock salt caverns requires careful consideration of thermo–hydro–mechanical (and chemical) processes. These processes interact and influence each other in a complex manner. Additionally, they do not necessarily have the same spatial and temporal scales Martín et al. (2015). For example, the flow pathways created by the damage increase the permeability of rock and represent the potential risk for gas leakage around the cavern. Subsequently, if the pore pressure locally exceeds the minimum principal stress, the fluid infiltration in rock salt takes place and the local widening

of grain boundaries occurs Schulze et al. (2001). Under such conditions, the mechanical behavior of the rock salt is affected by the gas and liquid phases. On the other hand, the temperature of rock salt around the cavern may change due to the gas injection and withdrawal processes. This temperature change introduces additional stresses in a narrow zone around the cavern due to the thermal expansion and contraction Bérest et al. (2007); Brouard et al. (2011). Moreover, the temperature variation affects the rate of creep deformation and changes the cavern closure rate Pudewills & Droste (2003); Serbin et al. (2015).

2.4.3 Design criteria for salt caverns

Rock salt caverns are widely recognized as secure storage places for storing energy. However, some accidents have been reported in the past (e.g. see Yang et al. (2013); Bérest & Brouard (2003); Evans et al. (2006)) which show the necessity of careful engineering designs. It should be noted that the numerical simulations are always accompanied by different types of uncertainties. These uncertainties can be associated with both the input variables of the model and the numerical approximation itself. During the recent years, a number of studies have been performed to evaluate the performance of the storage systems considering uncertainties (for example see probabilistic study of failure Mahmoudi et al. (n.d.), risk analysis associated with storage caverns Yang et al. (2013); Zhang et al. (2017)). Although various factors such as excessive loading conditions, equipment failure or human error may endanger the performance of a storage system, only the geomechanical design criteria which cause major failure are discussed in this thesis. This type of failure can have disastrous consequences such as huge economical loss, destructive environmental impacts or even casualties. As shown in Fig. 2.25, the most important geomechanical design criteria are mechanical stability, serviceability and oil/gas leakage. These factors are explained in the following sections.

2.4.3.1 No-dilatancy criterion

As explained earlier, the rock salt shows a transition from ductile to brittle behavior in the dilatancy zone. Subsequently, the increasing damage in dilatancy zone results in the opening of micro-cracks and the increasing of permeability. For these reasons, the dilatancy boundary can be considered as a threshold to ensure the long-term integrity and tightness of the cavern. In general, a conservative utilization criterion is defined as shown in Eq. 2.14 to check whether the stress state is in the dilatancy zone or not (e.g.

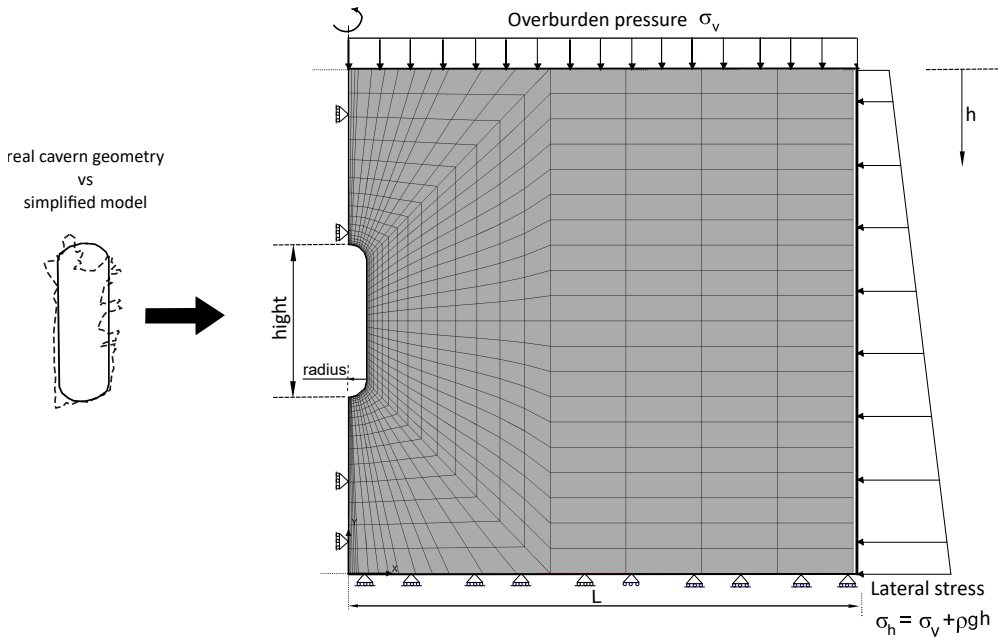

Figure 2.24: The finite element mesh and the boundary conditions for a simplified salt cavern Khaledi, Mahmoudi, Datcheva & Schanz (2016*a*)

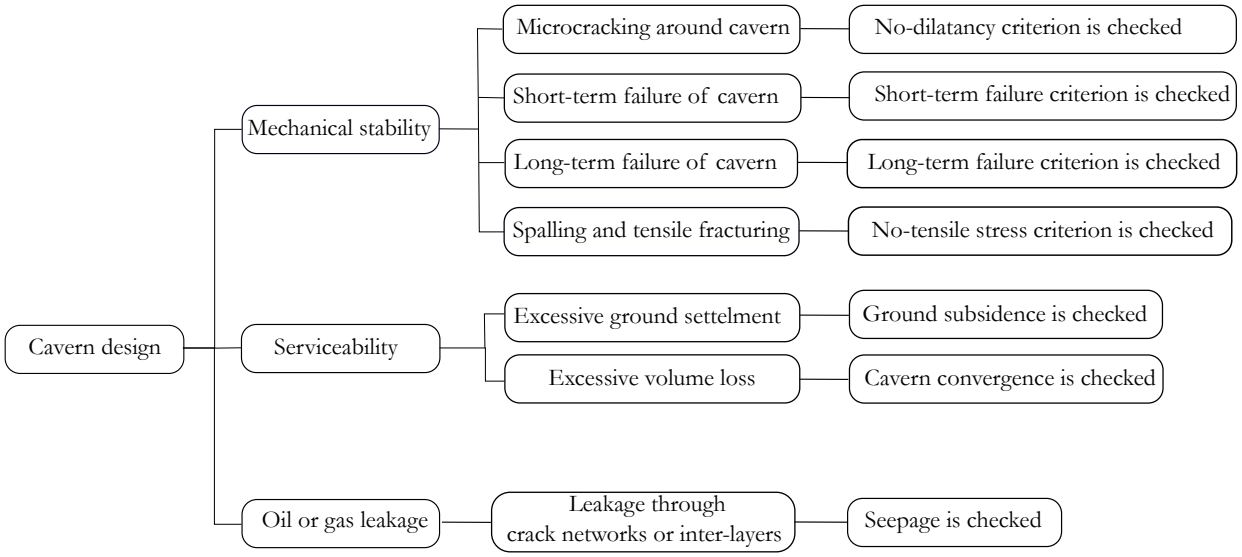

Figure 2.25: The most important geomechanical design criteria for energy storage salt caverns

see Yang et al. (2016); Wang et al. (2016); DeVries et al. (2005); Asgari et al. (2012); Ma et al. (2015)).

$$\mathrm{UC} = \frac{\sqrt{J_2^{\mathrm{dil}}}}{\sqrt{J_2}} \tag{2.14}$$

where J_2 is the second invariant of deviatoric stress and J_2^{dil} is its value at the dilatancy boundary. When UC < 1, the stress state locates beyond the dilatancy boundary. Thus, the operating condition of the cavern is not safe and cavern may experience long-time failure due to the damage progress.

2.4.3.2 Short-term failure ratio (SFR)

The ratio between the ultimate shear stress and the current shear stress is a quantity to show the failure zones around the cavern subjected to the extreme loading conditions Fuenkajorn et al. (2012); Nazary et al. (2013). The short-term failure ratio is defined as follows:

$$\mathrm{SFR} = \frac{\tau_f}{\tau} \tag{2.15}$$

where τ is the octahedral shear stress and τ_f denotes the ultimate octahedral shear stress. When SFR $= 1$, the stress state has reached to the short-term failure boundary. Thus, the failure zone around the cavern can not carry the load anymore and it may collapse.

2.4.3.3 Long-term failure ratio (LFR)

In a number of studies, the long-term stability of rock salt caverns has been investigated. If the operating conditions in a cavern are not selected appropriately, the stress state around the cavern may lie in the dilatancy zone. Therefore, some points around the cavern experience dilatancy and damage. Under such condition, the damage accumulates with time at the boundary of cavern. When the accumulated damage is equal to a critical value obtained from experiments, the long-term failure of the cavern is reached Cristescu & Gioda (1994); Nazary et al. (2013); Fuenkajorn et al. (2012). Based on this explanation, the long-term failure ratio (LFR) is defined as follows:

$$\mathrm{LFR} = \frac{d(t)}{d_f} \tag{2.16}$$

Where $d(t)$ is the damage value at time t and d_f is the ultimate damage value. The long-term failure ratio can be considered as quantity to predict the tertiary creep or the long-term cyclic failure. Creep deformation and long-term integrity of salt caverns have been investigated in Yang et al. (2015); Hou (2003); Deng et al. (2014); Nazary et al. (2013); Martín et al. (2015).

2.4.3.4 Tensile failure

Rock salt has a poor tensile strength. The thermo–mechanical loading conditions have to be defined in a way that no tensile stress is experienced around the cavern. The tensile failure may have different sources. The operating pressure of the cavern can cause tensile failure if it exceeds the overburden pressure. Therefore, based on an empirical approach, the maximum admissible pressure in the cavern should be set to 80-85 % of the overburden pressure Bérest et al. (2015). The thermal contractions around the cavern may lead to tensile failure as well. According to Bérest et al. (2007); Jafari et al. (2011); Brouard et al. (2011), the temperature of rock salt around the cavern changes due to the gas injection and withdrawal processes. This temperature change introduces additional stresses in a narrow zone around the cavern due to the thermal expansion and contraction. In other words, the temperature decrease resulted from rapid depressurization induces significant thermal stresses at the boundary of cavern Bérest et al. (2013). These additional thermal stresses can lead to tensile fracturing. Therefore, to obtain the maximum depressurization rate and the minimum admissible temperature, the tensile failure criterion have to be checked. Accordingly, the minimum principal stress σ_3 in the surrounding rock should not exceed the tensile strength of rock salt σ_{tensile}, that is:

$$\sigma_3 < \sigma_{\text{tensile}} \tag{2.17}$$

2.4.3.5 Cavern convergence

The serviceability of the system is affected if a significant reduction in the storage capacity of the cavern occurs. For this reason, it is important to control the factors which may increase the rate of cavern closure. The volume loss of the cavern (VL) during its operation time is evaluated using the following equation:

$$\text{VL} = \frac{V_0 - V_t}{V_0}. \tag{2.18}$$

here, V_0 is the initial volume of cavern and V_t denotes the volume after time t. As explained before creep deformation of rock salt is a function of deviatoric stress and temperature. Therefore, when the internal pressure of the cavern drops down , the rate of volume convergence increases because the cavern is subjected to the higher deviatoric stresses. Similarly, the cavern closure rate can accelerate if the temperature inside the cavern rises up Pudewills & Droste (2003); Serbin et al. (2015). However, the rate of cavern volume loss typically is limited to 1% per year Asgari et al. (2012) (or not more than 30% for the whole design lifetime Wang et al. (2016)).

2.4.3.6 Ground subsidence

Up to now, rare major accidents at the ground level resulting from the convergence of deep caverns has been experienced. For instance, Yang et al. (2013) listed five subsidence accidents which occured between 1970 to 1999. Because of large cavern convergence, the amount of subsidence was between 20 to 90 mm/a in these caverns. However, the ground subsidence in shallow rock salt caverns (i.e. less than 500 m deep) can be relatively higher. Beside the depth of cavern, other factors such as internal pressure, material properties of salt, cavern diameter, running time and excavation rate may affect the surface settlement Zhang, Wu, Wang, Zhang, Daemen & Liu (2015). If the operating conditions of an existing cavern are not appropriate, the creep deformation around storage caverns becomes significant. Under such condition, the surface subsidence induced by the excessive volume loss may cause huge environmental and economical losses. Therefore, the prediction of surface settlement is essential to ensure the long-term serviceability of salt caverns. During the recent years, numerous studies have been performed by many scholars to predict the surface settlement above the storage cavern. Among them, the following studies are worth to be mentioned:

- Subsidence prediction model for cylindrical caverns with stiff roof Karimi-Jafari et al. (2008)
- Time-dependent subsidence prediction model for spherical caverns in bedded rock salt Zhang, Wu, Wang, Zhang, Daemen & Liu (2015)
- Subsidence prediction model for cylindrical caverns Eickemeier (2005)
- Semi-analytic model for subsidence prediction caused by hydrocarbon extractionFokker & Orlic (2006)
- Subsidence prediction model for cylindrical and spherical caverns with constant or cyclic internal pressures Li et al. (2015)

- Subsidence prediction model for caverns excavated in bedded rock salt Wei et al. (2016)

2.4.3.7 Gas/oil leakage

The storage product in the cavern gas/oil may find different path ways for leakage. The potential leakage pathways are (1) through the cemented shaft, (2) through the casing, (3) through the space between cemented shaft and the casing and (4) through the fractures and cracks in the rock salt Bai et al. (2014). For the later case, it is essential to take into account the permeability changes of rock salt under the influence of damage. Another important pathway for leakage is the high permeable layers existing in bedded rock salt formations. Modeling of gas seepage and the tightness of cavern excavated in bedded rock salt have been investigated in Cosenza & Ghoreychi (1999); Huang & Xiong (2011); Kim et al. (2012); Wang, Ma, Yang, Shi & Daemen (2015); Xiong et al. (2015).

2.5 Summary

In this chapter, the state of the art and the advances related to the micro-structure and the phenomenological behavior of rock salt were presented. In addition, the most important design factors in numerical modeling of storage caverns excavated in rock salt formations were outlined. Accordingly, the following conclusions can be drawn based on the presented discussions :

- Rock salt is a ductile material with very low permeability in its undamaged state. Moreover, rock salt formations can be found in different parts of the world in sufficient depth and volume. These properties make the rock salt caverns suitable places for storing gaseous or liquid energy carriers.
- Mechanical properties of rock salt are governed by deformation mechanisms occurring in the crystal structure. In other words, many experimental observations such as creep, strain hardening, volume changes or failure can be explained through micro-structural deformations. In general, stress state, temperature and time are the variables which determine the dominant deformation mechanisms in the structure of salt. For example, depending on the applied stress and temperature, creep deformation in rock salt can be due to the movement of free dislocations or the precipitation of salt along grain boundaries.

- Rock salt shows a transition from ductile to brittle behavior. This transition is commonly represented in stress space through the dilatancy boundary. Beyond the dilatancy boundary, i.e. in the brittle domain, microscopic cracking takes place. Subsequently, because of grain rotation and inter-granular slip, the volume of salt increases. The volume increase and the interconnection of micro-cracks have unfavorable consequences such as rapid increase of permeability, mechanical weakening, tertiary creep and long-term failure. This fact should be taken into account in all steps of cavern design.
- Many rock salt constitutive models with different orders of complexity can be found in the literature. However, depending on the storage product and the storage requirements, the governing variables at field such as stress, temperature and deformation rate (time) may significantly differ from one application to another. Therefore, for each application, it is important to select a model which can represents the most relevant deformation mechanisms at field.
- Stability and serviceability of salt caverns have to be investigated through adequate numerical simulations constructed based on appropriate assumptions. Geometry of the cavern, in-situ condition, time scale of the simulation and thermo-hydro-mechanical coupling are the most important modeling factors which should be carefully selected. Additionally, rock salt dilatation, damage propagation, tensile failure, permeability changes and volume loss are the most important criteria to check the safety of caverns.

Some recommendations concerning enhancing reliability in modeling and the possible future developments are:

- Obviously, a fundamental understanding of micro-mechanism processes is essential to describe the rheological behavior of rock salt. However, a quick survey of existing literature reveals that the number of contributions related to the microscopic behavior of rock salt are much less than those in macro-level. Therefore, more elaboration in this regard is needed.
- The damage healing process, in particular during cyclic loading, is still an unknown process. More laboratory experiments are required to set up a reliable model to predict healing process.
- A few experimental studies can be found in literature regarding the cyclic loading behavior of rock salt. Recently, a number of studies have investigated the fatigue failure under the influence of loading amplitude or frequency. However, there are

still open questions regarding the cyclic response of rock salt. For example, the effect of cyclic loading on the onset of dilatancy or the effect of cyclic temperature on mechanical behavior are still not clear.

- In a majority of studies, the thermo-mechanical loads applied to the rock salt sample in the experiment do not necessarily represent the field condition. Consequently, the calibration of constitutive model and the predictions made by the numerical simulations may involve a significant amount of uncertainties. Due to this fact, the field conditions have to be taken into account in conducting the experimental investigations.
- Although, the increasing of permeability caused by dilatancy has been investigated since many years, the development of effective stress in rock salt in the presence of pore fluid pressure needs still more research efforts.
- Validation of constitutive models using in-situ measurement data is an important issue. All introduced approaches need to be validated against real data or/and representative laboratory tests that may be considered as a challenging task for future. Since the solution-mined caverns are very deep structures, conducting the field measurements which might help us to understand the real response of the host rock are practically very difficult. Therefore, it is needed to development new in-situ investigatory methods for determining rheological material parameters.
- It is common to simplify the salt cavern finite element model in terms of its geometry and boundary conditions. In this regard, the 3D modeling of cavern with non-simplified geometries or modeling of non-salt layers may improve the predictions.
- Accurate prediction of thermodynamics of gas/air in caverns can be considered as an interesting research topic. Advanced numerical techniques such as CFD modeling (computational fluid dynamics) can be applied to achieve this goal.
- The deformation mechanism under low stress and temperature has not been fully understood and it may affect the long-term predictions. More studies regarding the effect of this mechanism on the long-term response of underground storage systems are needed.

3 Structure of the implemented constitutive models

3.1 General

The basic governing field equations in the framework of Newtonian mechanics are (1) conservation of mass, (2) conservation of momentum, (3) conservation of angular momentum, (4) conservation of energy, and (5) thermodynamic laws. Independent of the internal constitution of the material, these principles have to be valid for all engineering boundary value problems. In addition to the these basic principles, a solution to a boundary value problem in continuum mechanics requires constitutive equations. A constitutive equation is a mathematical function which describes the observed deformations in a continuous medium. In this chapter, the structure of three employed constitutive models for modeling of rock salt behavior are explained. The models can be ordered based on their complexity and their capabilities in modeling of observed deformation responses as follows:

- Model I: it is an empirical model to describe the steady-state creep deformation without dilatancy and damage.
- Model II: it is a viscoelastic model to describe the transient and the steady-state creep deformations without dilatancy and damage.
- Model III: it is a viscoplastic-creep-damage model to describe the short-/long-term behavior of rock salt considering dilatancy and damage.

It should be noted that these models have been implemented in the finite element code Code-Bright and they have been used in this thesis for modeling of salt caverns. The following sections describe the structure of the models more in detail.

3.2 Model I: an empirical creep model

This model is known as BGRa model and it has been introduced by Hunsche & Schulze (1994) to describe the steady-state creep deformation of rock salt as a function of temperature and stress. In fact, this model has been developed based on the Norton-Hoff power law model which is a well-known creep model for metals Norton (1929). According to this model, the total strain rate is a sum of two parts, i.e. the elastic strain rate $\dot{\varepsilon}_{ij}^{el}$ and the steady-state creep strain rate $\dot{\varepsilon}_{ij}^{cr}$. That is:

$$\begin{cases} \dot{\varepsilon}_{ij} = \dot{\varepsilon}_{ij}^{el} + \dot{\varepsilon}_{ij}^{cr}, \\ \dot{\varepsilon}_{ij}^{el} = \frac{1}{2G}\dot{s}_{ij} + \frac{1}{9K}\dot{I}_1\delta_{ij}, \\ \dot{\varepsilon}_{ij}^{cr} = \left\{ A_c \exp\left(\frac{Q_c}{RT}\right) q^{n_c} \right\} \frac{\partial q}{\partial \sigma_{ij}} = \frac{3}{2}\left\{ A_c \exp\left(\frac{Q_c}{RT}\right) q^{n_c-1} \right\} s_{ij}. \end{cases} \tag{3.1}$$

As seen, the elastic strain is simply described using Hooke's law. As explained earlier, K and G are the bulk and shear moduli respectively and s_{ij} denotes the ij^{th} component of deviatoric stress tensor. On the other hand, the creep strain rate $\dot{\varepsilon}_{ij}^{cr}$ is a function of two variables i.e. temperature T and the equivalent deviatoric stress q (where $q = \sqrt{\frac{3}{2}s_{ij}s_{ij}}$). Since the potential function of the model is of von-Mises type, the changes in volumetric strain (i.e. dilation or compression) during the creep deformation cannot be represented by this model. Therefore, it is more suitable for applications with constant loading below the dilatancy boundary (e.g. for nuclear waste disposal) Hunsche & Hampel (1999); Hunsche (1994); Hunsche & Schulze (1994). Moreover, the model has three material parameters i.e. A_c, Q_c and n_c, which have to be determined using long-term creep tests. It should be noted that R is the gas constant which is equal to 8.314 J/mol. The determination of material parameters for BGRa model is explained in Section. 5.1.

3.3 Model II: a viscoelastic model

This model is known as LUBBY2 model. The model is a viscoelastic model to describe transient and steady-state creep deformations in ductile regime Heusermann et al. (2003). The transient creep is represented by Kelvin viscoelastic model consisting of a dashpot element parallel to a spring. Both dashpot and spring elements in this model are assumed to be exponential functions of the deviatoric stress q. On the other hand, the steady-state creep is described by Maxwell viscoelastic model. The Maxwell dashpot element of the

model has also an exponential dependency on temperature and deviatoric stress. The model can describe the creep deformation in both constant loading and stepwise loading (similar to the loading condition in seasonal storage caverns). Similar to the BGRa model, the changes of inelastic volumetric strain cannot be described by this model. Therefore, the model does not provide any description regarding dilatancy and damage evolution. Fig. 3.1 shows the rheological sketch of the model. Where, $\bar{\eta}_k$ and $\bar{\eta}_m$ denote the Kelvin and the Maxwell dashpot coefficients, respectively and $\bar{G}_k$ represents the Kelvin spring module Heusermann et al. (2003, 1983). This model considers the strain rate as a sum of two parts, i.e. elastic strain rate $\dot{\varepsilon}_{ij}^{el}$ and the visco-elastic strain rate $\dot{\varepsilon}_{ij}^{ve}$.

$$\dot{\varepsilon}_{ij} = \dot{\varepsilon}_{ij}^{el} + \dot{\varepsilon}_{ij}^{ve}. \tag{3.2}$$

The elastic strain is obtained using the generalized Hooke's law. The material characteristic of the dashpots and springs in this model are stress dependent. The visco-elastic strain rate in this model is divided into two parts: (1) the transient phase ε^{tr} (2) the steady–state phase ε^{ss}. The following equations define the visco-elastic strain rate:

$$\begin{cases} \dot{\varepsilon}_{ij}^{ve} = \dot{\varepsilon}_{ij}^{tr} + \dot{\varepsilon}_{ij}^{ss}, \\ \dot{\varepsilon}_{ij}^{tr} = \left(\dfrac{q - \bar{G}_k \varepsilon^{tr}}{\bar{\eta}_k} \right) \dfrac{\partial q}{\partial \sigma_{ij}} = \dfrac{3}{2} \dfrac{1}{\bar{\eta}_k} \left(1 - \dfrac{\bar{G}_k \varepsilon^{tr}}{q} \right) s_{ij}, \\ \dot{\varepsilon}_{ij}^{ss} = \dfrac{q}{\bar{\eta}_m} \dfrac{\partial q}{\partial \sigma_{ij}} = \dfrac{3}{2} \dfrac{1}{\bar{\eta}_m} s_{ij}. \end{cases} \tag{3.3}$$

Where s_{ij} is the $(ij)^{th}$ element of the deviatoric stress tensor and ε^{tr} represents the equivalent transient strain (i.e. $\dot{\varepsilon}^{tr} = \sqrt{\dfrac{2}{3} \dot{\varepsilon}_{ij}^{tr} \dot{\varepsilon}_{ij}^{tr}}$). The stress dependency of the viscoelstic coefficients is described through the following equations.

$$\bar{\eta}_k = \eta_k \exp\left(k_2 q\right), \ \bar{\eta}_m = \eta_m \exp\left(mq\right) \exp\left(lq\right), \ \bar{G}_k = G_k \exp\left(k_1 q\right). \tag{3.4}$$

Where η_k, η_m, G_k, k_1, k_2, m and l are material parameters. These parameters are determined through stepwise creep tests with different stress levels. The determination of material parameters for LUBBY2 model is explained in Section. 5.2.

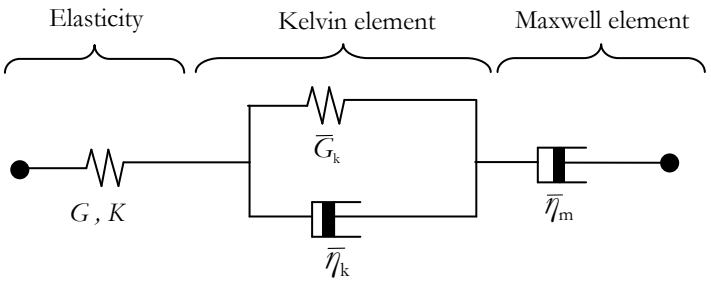

Figure 3.1: The rheological sketch of LUBBY2 constitutive model

3.4 Model III: a viscoplastic-creep-damage model

This section is largely taken from Khaledi, Mahmoudi, Datcheva & Schanz (2016*b*). As explained in the previous chapter, rock salt exhibits different macro/microscopic behaviors above and below the dilatancy boundary. When the stress state is in the compressibility domain (i.e. below the dilatancy boundary), a time-dependent ductile deformation without any visible macroscopic fracture is observed. This time-dependent behavior is highly affected by the magnitude of the applied load as well as the environmental factors like temperature. In case the stress state goes above the dilatancy boundary, micro-cracking and inter-granular slip occur Hunsche & Hampel (1999). Thus, the irreversible volumetric strain increases due to the opening of micro-cracks, and other relevant factors such as damage, permeability increase and long-term failure become significant in this zone.
To take into account the above-mentioned mechanical properties of rock salt, an elasto-viscoplastic-creep model combined with damage is introduced in this chapter. Under the small strain and strain additive assumptions, the total strain rate is defined using the equation below.

$$\dot{\varepsilon}_{ij} = \dot{\varepsilon}^{el}_{ij} + \dot{\varepsilon}^{ie}_{ij} = \dot{\varepsilon}^{el}_{ij} + \dot{\varepsilon}^{vp}_{ij} + \dot{\varepsilon}^{cr}_{ij}. \tag{3.5}$$

Where $\dot{\varepsilon}^{el}_{ij}$, $\dot{\varepsilon}^{ie}_{ij}$ are the elastic and inelastic parts of the total strain rate, respectively. The reversible instantaneous strain ε^{el}_{ij} is obtained using the generalized Hooke's law. While, the inelastic strain rate is the result of additive superposition of two parts i.e. the viscoplastic strain rate $\dot{\varepsilon}^{vp}_{ij}$ and the creep strain rate $\dot{\varepsilon}^{cr}_{ij}$. These components of strain rate are explained in the following subsections .

3.4.1 Viscoplastic deformation

In this thesis, the viscoplastic model introduced by Desai in Desai & Varadarajan (1987); Desai & Zhang (1987) is employed to describe the irreversible rate-dependent deformation

considering the volumetric dilation and compression. This model which is based on the classical Perzyna's viscoplasticity model Perzyna (1966) has the general form as below:

$$\dot{\varepsilon}_{ij}^{vp} = \mu_1 \left\langle \frac{F^{vp}}{F_0} \right\rangle^{N_1} \frac{\partial Q^{vp}}{\partial \sigma_{ij}}. \tag{3.6}$$

Where $\langle x \rangle = (x + |x|)/2$ is the Macauley bracket. The fluidity coefficient μ_1 and the stress exponent N_1 are material parameters, and F_0 is a reference value with dimension of the squared stress. F^{vp} and Q^{vp} are the viscoplastic yield and potential functions, respectively, defined similarly like in Desai & Varadarajan (1987); Desai & Zhang (1987). That is:

$$F^{vp} = J_2 - \left(-\alpha I_1^n + \gamma I_1^2\right) \left[\exp\left(\beta_1 I_1\right) - \beta \cos\left(3\theta\right)\right]^{m_v}, \tag{3.7}$$

$$Q^{vp} = J_2 - \left(-\alpha_{_q} I_1^n + \gamma I_1^2\right) \left[\exp\left(\beta_1 I_1\right) - \beta \cos\left(3\theta\right)\right]^{m_v}, \tag{3.8}$$

$$\theta = \frac{1}{3}\cos^{-1}\left(\frac{-\sqrt{27}J_3}{2J_2^{1.5}}\right), \quad I_1 = -\sigma_{ii} \quad J_2 = \frac{1}{2}s_{ij}s_{ij}, \quad J_3 = det(s_{ij}). \tag{3.9}$$

Where γ, β_1, β, n and m_v are material parameters. Both functions F^{vp} and Q^{vp} are dependent on three stress invariants i.e. the first invariant of stress tensor I_1, the second invariant of deviatoric stress tensor J_2 and the Lode's angle θ. To allow for cohesion and tensile strength, the functions in Eqs. 3.7 and 3.8, are expressed in terms of transformed stress coordinates such that $I_1^* = I_1 + 3\sigma_{_{\text{tensile}}}$, where $\sigma_{_{\text{tensile}}}$ denotes the tensile strength. Eqs. 3.7 and 3.8 correspond to an oval-shaped surface illustrated in Figs. 3.2a and 3.2b. Additionally, two hardening parameters α and $\alpha_{_q}$ have been included in these equations to control the size of viscoplastic yield and potential surfaces in the stress space. The hardening parameter α which determines the size of yield surface F^{vp} is a function of accumulated viscoplastic strain ξ defined in Eq. 3.10. In general, the size of viscoplastic potential surface Q^{vp} could differ from the yield surface F^{vp} by defining $\alpha_{_q}$ according to Eq. 3.11. Applying Eq. 3.11, the viscoplastic strain rate defined in Eq. 3.6 is obtained through a non-associated flow rule.

$$\alpha = \frac{a_1}{\xi^{\eta}} \qquad \xi = \int_0^t \sqrt{\dot{\varepsilon}_{ij}^{vp} : \dot{\varepsilon}_{ij}^{vp}}\, dt, \tag{3.10}$$

$$\alpha_{_q} = \alpha + k_v \left(\alpha_0 - \alpha\right)\left(1 - \xi_{vol}/\xi\right). \tag{3.11}$$

Where a_1, η are material parameters and ξ_{vol} denotes the accumulated volumetric viscoplastic strain. Parameter k_v in Eq. 3.11 can be a constant value or a stress dependent function Desai & Zhang (1987). Figs. 3.2c and 3.2d demonstrate how the viscoplastic

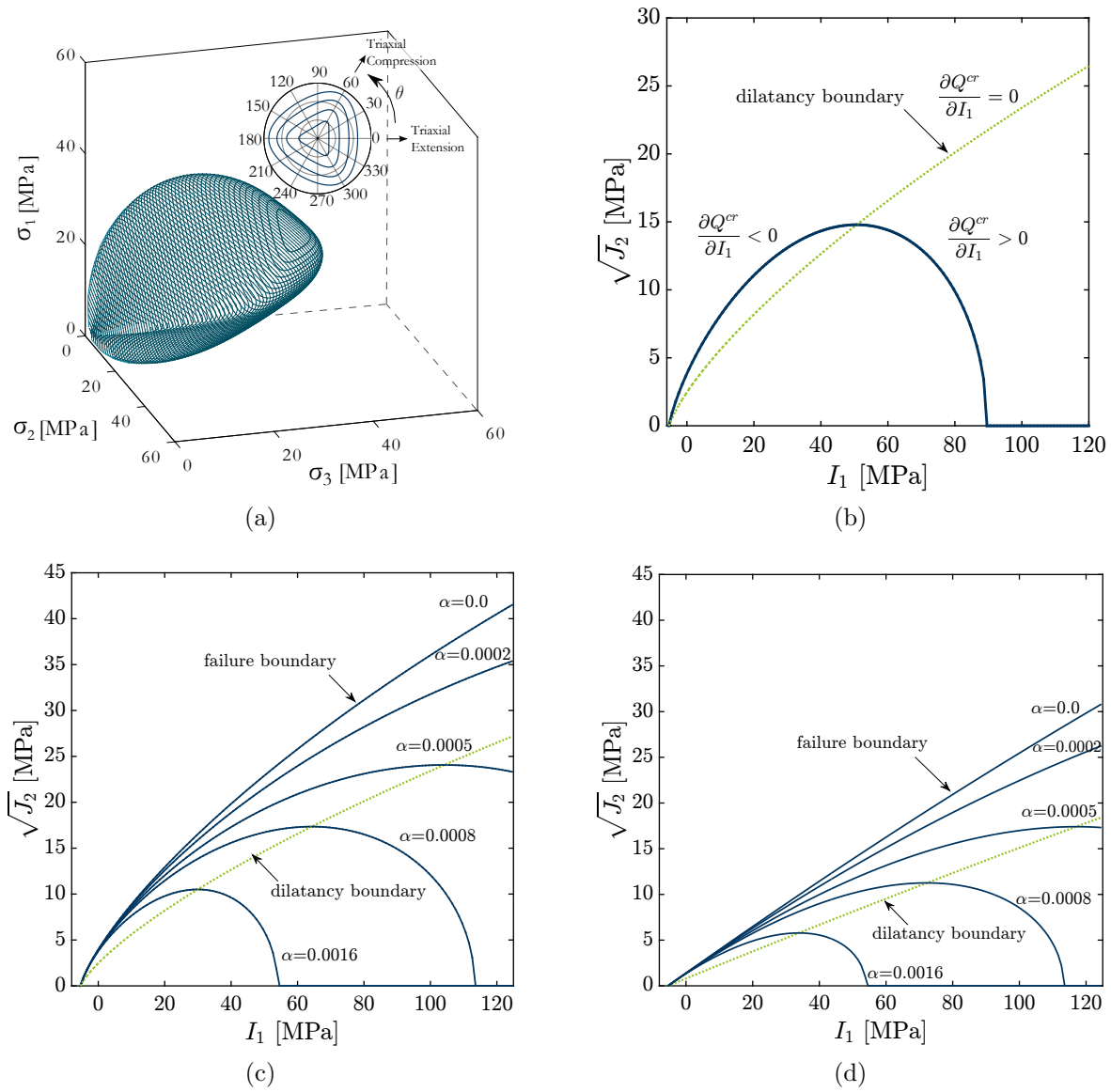

Figure 3.2: Viscoplastic potential and yield functions in the stress space; (a) Viscoplastic potential function Q^{vp} in the principal stress coordinate; (b) Viscoplastic potential function Q^{vp} in $I_1 - \sqrt{J_2}$ plane for $\theta = 60°$, the compression and the dilation behaviors are separated by dilatancy boundary; (c) Evolution of viscoplastic yield function F^{vp} in $I_1 - \sqrt{J_2}$ plane for $\theta = 60°$, the size of the surfaces is controlled by hardening parameter α. It has to be noted that $\alpha = 0$ corresponds to the ultimate envelope or the short-term failure boundary; (d) Evolution of viscoplastic yield function F^{vp} in $I_1 - \sqrt{J_2}$ plane for $\theta = 0°$.

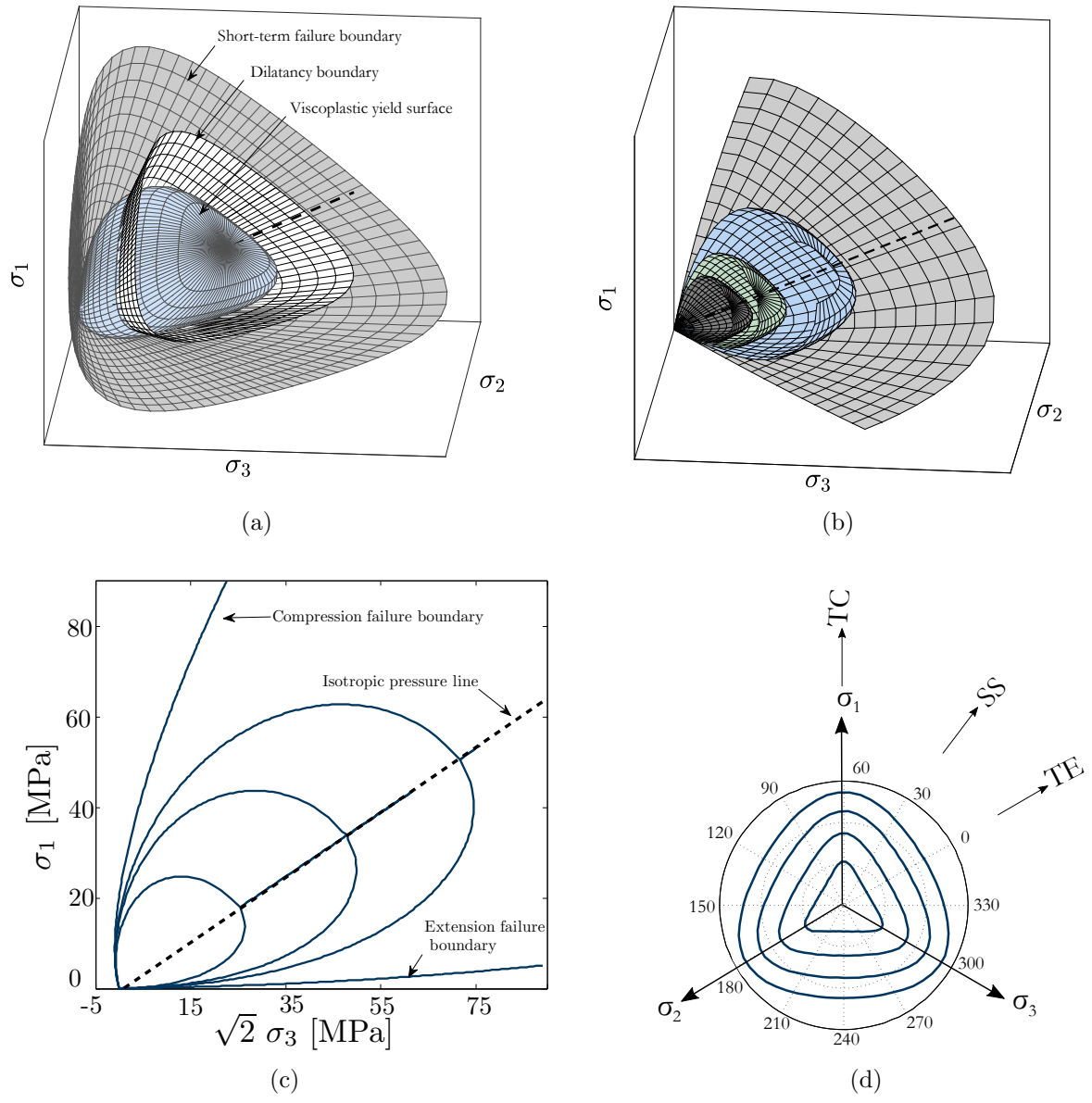

Figure 3.3: Short-term failure, dilatancy and viscoplastic yield surfaces in the stress space; (a) Short-term failure, dilatancy and viscoplastic yield surfaces in the principal stress space; (b) Evolution of viscoplastic yield surface in the principal stress space; (c) Evolution of viscoplastic yield surface in the biaxial stress space; (d) Evolution of viscoplastic yield surface in π-plane.

yield function F^{vp} evolves in $I_1 - \sqrt{J_2}$ plane for $\theta = 60°$ and $\theta = 0°$, respectively. As seen from these figures and also Eq. 3.10, by increasing the viscoplastic deformation, the hardening parameter α reduces. Subsequently, the size of viscoplastic yield surface isotropically grows up. When $\alpha = 0$, the ultimate surface or failure boundary is reached and the material can not carry the load anymore. Fig. 3.2 also shows a boundary passing through the points in which the variation of volumetric viscoplastic strain is zero (i.e. $\frac{\partial Q^{vp}}{\partial I_1} = 0$). This boundary corresponds to the dilatancy boundary which separates the dilatancy domain (i.e. $\frac{\partial Q^{vp}}{\partial I_1} < 0$) from compressibility domain (i.e. $\frac{\partial Q^{vp}}{\partial I_1} > 0$). Fig. 3.3 shows the failure and the dilatancy boundaries in principal stress space. The evolution of viscoplastic yield surface in principal stress space, $\pi-$plane and biaxial stress space has been depicted in this figure as well. The mathematical formulation of dilatancy boundary can be obtained by solving equation $\frac{\partial Q^{vp}}{\partial I_1} = 0$. Equation below represents the mathematical equation for viscoplastic dilatancy boundary in the stress space.

$$J_2 = F^{dil}(I_1, \theta) = (1-\frac{2}{n})\gamma I_1^2 \left(\exp\left(\beta_1 I_1\right) - \beta\cos\left(3\theta\right)\right)^{m_v} \left\{1 + \frac{m_v \beta_1 I_1 \exp(\beta_1 I_1)}{n(\exp(\beta_1 I_1) - \beta\cos(3\theta))}\right\}^{-1}. \tag{3.12}$$

The above-mentioned equation has a complex dependency on stress invariants I_1 and θ. Desai in Desai & Varadarajan (1987) reported that the second term inside the bracket is negligible. Thus, the mathematical equation of dilatancy boundary can be simplified as follows:

$$J_2 = F^{dil}(I_1, \theta) = (1 - \frac{2}{n})\gamma I_1^2 \left(\exp\left(\beta_1 I_1\right) - \beta\cos\left(3\theta\right)\right)^{m_v}. \tag{3.13}$$

Fig. 3.4 is a comparison between the original and the simplified dilatancy boundaries. The simplified dilatancy boundary is used in the next section to define the potential function of creep strain.

3.4.2 Creep deformation

The irreversible time-dependent deformation is obtained using the following equation:

$$\dot{\varepsilon}_{ij}^{cr} = \mu_2 \left\{F^{cr}\right\}^{N_2} \frac{\partial Q^{cr}}{\partial \sigma_{ij}}. \tag{3.14}$$

Eq. 3.14 is the general formulation of the steady-state Norton-Hoff creep law Hunsche & Hampel (1999); Ślizowski & Lankof (2003). The stress exponent N_2 is a material

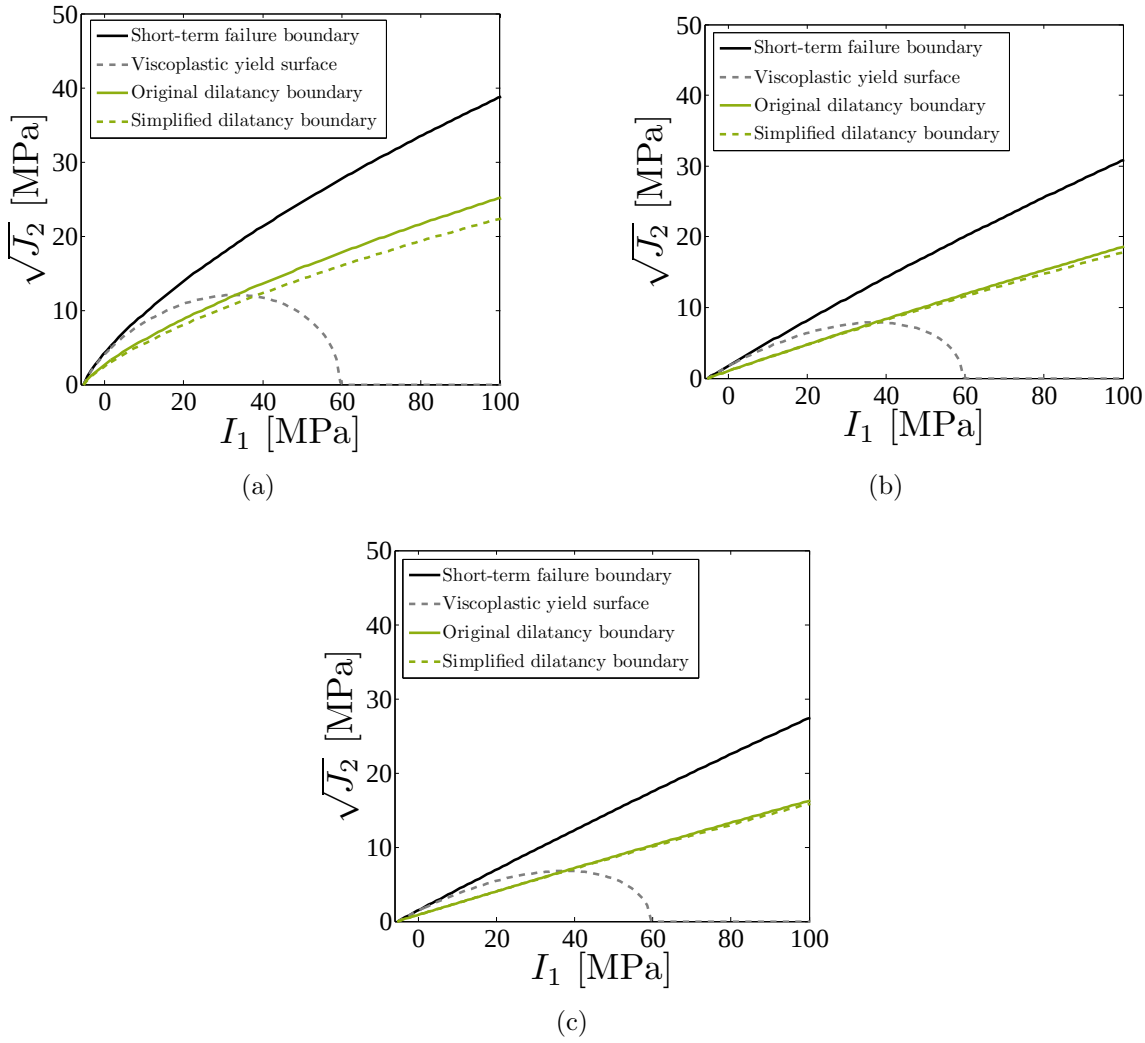

Figure 3.4: The original and simplified dilatancy boundaries; (a) Lode's angle $\theta = 60°$; (b) Lode's angle $\theta = 30°$; (c) Lode's angle $\theta = 0°$

parameter and μ_2 denotes a temperature dependent fluidity parameter. The following function is used to describe the temperature dependency of the creep deformation:

$$\mu_2(T) = \mu_0 \exp\left(\frac{-Q_c}{RT}\right), \tag{3.15}$$

with μ_0 denotes the value of fluidity at a reference temperature; R is the universal constant of perfect gas; Q_c is the activation energy and T is the absolute temperature. The creep yield function of Norton-Hoff model is given by the following equation:

$$F^{cr} = q = \sqrt{3J_2}. \tag{3.16}$$

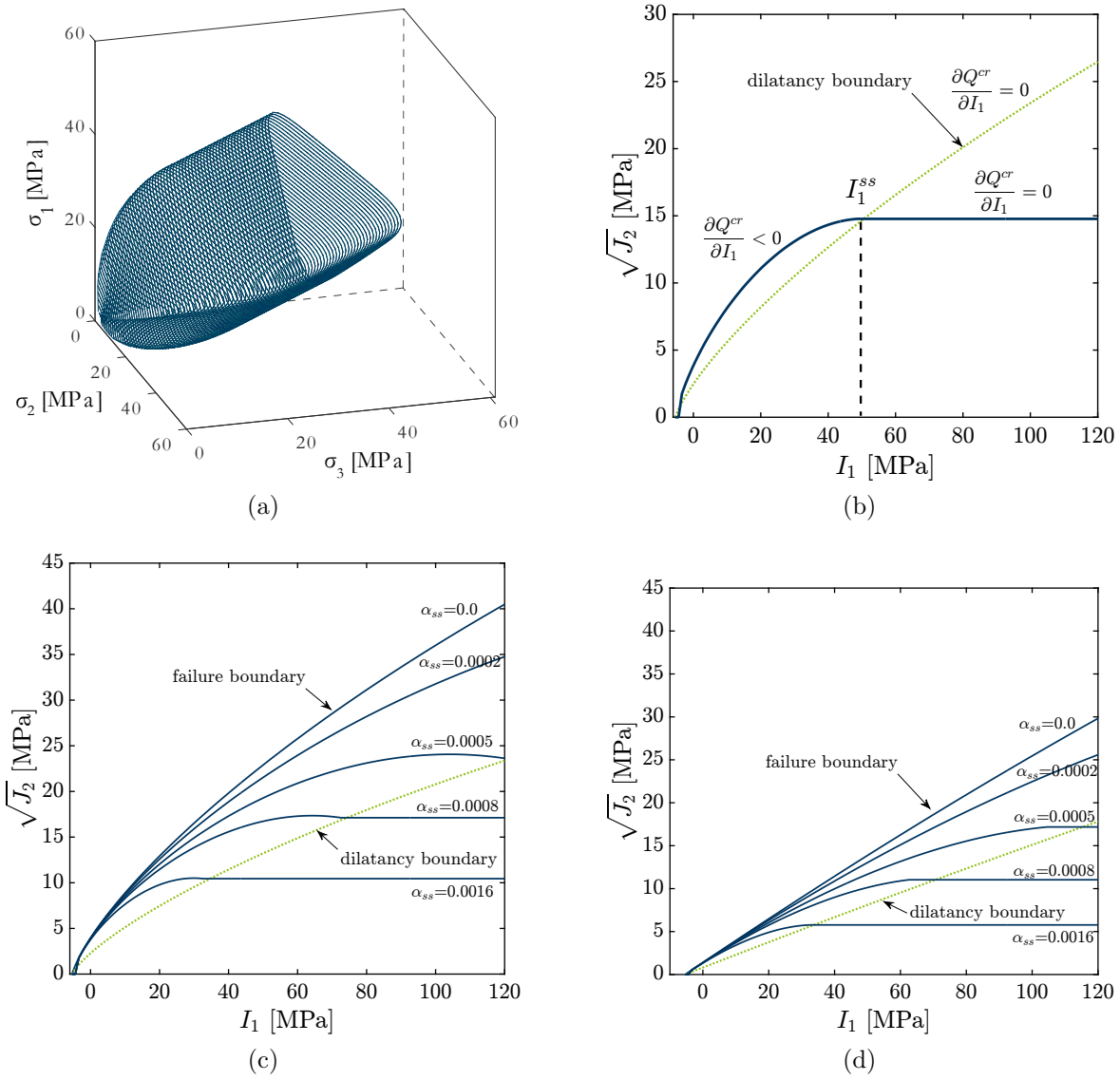

Figure 3.5: Creep potential and yield functions in the stress space; (a) Creep potential function Q^{cr} in the principal stress coordinate; (b) Creep potential function Q^{cr} in $I_1 - \sqrt{J_2}$ plane for $\theta = 60°$, the constant volume and the dilation behaviors are separated by the simplified dilatancy boundary; (c) Creep potential surfaces Q^{cr} in $I_1 - \sqrt{J_2}$ plane for $\theta = 60°$, the size of the surfaces is controlled by the parameter α_{ss}; (d) Creep potential surfaces Q^{cr} in $I_1 - \sqrt{J_2}$ plane for $\theta = 0°$.

As seen, the creep yield function F^{cr} is only dependent on the second invariant of deviatoric stress tensor. Therefore, for any $J_2 > 0$, a steady-state creep deformation occurs according to Eq. 3.14. As mentioned before in Section. 3.2, the creep potential function in Norton-Hoff model (or BGRa model) is independent of the first invariant of stress tensor I_1. For this reason, the time-dependent volumetric deformation cannot be described by this model. To overcome this limitation, the potential surface introduced in Eq. 3.8 is included in Eq. 3.14 with some modifications in order to capture the volumetric creep deformations of rock salt with the same dilatancy boundary as the viscoplastic strain (see Eq. 3.13). Equation below represents the mathematical formulation of the modified creep potential function.

$$Q^{cr} = \begin{cases} J_2 - \left(-\alpha_{ss} I_1^n + \gamma I_1^2\right) \left(\exp\left(\beta_1 I_1\right) - \beta \cos\left(3\theta\right)\right)^{m_v} & J_2 \geq F^{dil}(I_1, \theta) \\ J_2 - \left(1 - \frac{2}{n}\right) \gamma \left(I_1^{ss}\right)^2 \left(\exp\left(\beta_1 I_1^{ss}\right) - \beta \cos\left(3\theta\right)\right)^{m_v} & J_2 \leq F^{dil}(I_1, \theta) \end{cases} \tag{3.17}$$

Fig. 3.5a shows the employed creep potential surface in the principal stress space and Fig. 3.5b illustrates this surface in $I_1 - \sqrt{J_2}$ plane. According to Eq. 3.17, in the compressibility domain(i.e. $J_2 \leq F^{dil}(I_1, \theta)$), the creep strain has only the deviatoric part and the volumetric creep deformation is assumed to be zero. This assumption is made because the volume cannot shrink to zero by the steady-state creep when time goes to infinity Cristescu (1987). Thus, below the dilatancy boundary, the volumetric component of the total strain rate is due to the elastic and viscoplastic components only. However, when the stress state is in the dilatancy domain (i.e. $J_2 \geq F^{dil}(I_1, \theta)$), the irreversible time-dependent dilation occurs and the volumetric creep strain is added to the volumetric elastic and viscoplastic strains. Additionally, with this assumption, the prediction of long-term failure becomes more conservative, because, the healing process which reduces the dilatancy is not taken into account. It should be noted that I_1^{ss} in Eq. 3.17 is the value in which the dilative part of the creep potential surface meets the constant volume part (see Fig. 3.5b), and α_{ss} is a factor which determines the creep potential surface corresponding to the current stress state. Figs. 3.5c and 3.5d show the creep potential surface Q^{vp} in $I_1 - \sqrt{J_2}$ plane for the θ=60° and θ=0°, respectively. The following equations show how I_1^{ss} and α_{ss} are calculated:

$$I_1^{ss} = \sqrt{J_2/(1 - \frac{2}{n})\gamma \left(\exp\left(\beta_1 I_1\right) - \beta \cos\left(3\theta\right)\right)^{m_v}} \tag{3.18}$$

$$\alpha_{ss} = k_{cr}\alpha_{q} \tag{3.19}$$

Where α_{q} is the hardening parameter defined in Eq. 3.11 and k_{cr} is a model parameter which controls the size of the creep potential surface with respect to the viscoplastic potential surface.

3.4.3 Damage parameter

Depending on the experimental observations, different definitions exist in the literature for describing the damage in geomaterials. For example, Hou in Hou (2003) and Ma et al. in Ma, Liu, Fang, Xu, Xia, Li, Yang & Li (2013) used a stress-dependent function to describe the tertiary creep of rock salt. According to this definition, the rate of damage progress during creep test is dependent on the magnitude of stresses applied to the rock sample as well as of the current accumulated damage. Liu et al. in Liu et al. (2014) showed that the released energy during loading–unloading cycles increases exponentially above the dilatancy boundary. They also concluded that, with the onset of volume dilation, the damage development will be accelerated. Therefore, they proposed an exponential function for the damage evolution which increases with the released strain energy. In the same line of thought, Hampel and Schulze in Hampel & Schulze (2007) introduced a damage parameter whose value grows exponentially with the released volumetric strain energy in the dilatancy domain. The exponential evolution of damage have been commonly used to describe the damage process in other types of rock and similar materials. For example, the damage functions suggested by Frantziskonis and Desai Frantziskonis & Desai (1987) for concrete, Wang et al. Wang et al. (2007) for argillaceous quartzite and Unteregger et al. Unteregger et al. (2015) for granite are worth to be mentioned here.
In this thesis, an energetic criterion defined by Cristescu in Cristescu (1993); Cristescu & Hunsche (1998) is used to quantify damage and micro-cracking. Damage of rock salt begins when dilatancy of the rock starts to develop. The amount of energy stored during compression or released during dilatancy is associated to the volumetric inelastic work per unit volume w_{vol} defined as below:

$$w_{vol} = \int_{0}^{t} \left(\frac{I_1}{3}\right) \dot{\varepsilon}_{vol}^{ie} dt. \tag{3.20}$$

The above-mentioned equation quantifies the energy of micro-cracking. In the compressibility domain, the voids and micro-cracks get closed and volume reduces. Therefore,

mechanical energy is stored in the body and a positive value for w_{vol} is obtained. While, during dilatancy, the volume increases and energy is released by micro-cracking, therefore, w_{vol} becomes negative. When the released energy due to micro-cracking reaches to a threshold value w_f the material failure occurs. To describe the damage evolution in the dilatancy domain, the following isotropic damage parameter d has been defined as an exponential function of released energy when dilatancy occurs.

$$d(w_{vol}) = \begin{cases} 0 & w_{vol} \geq 0 \\ 1 - \exp\left(B\left(\frac{w_{vol}}{w_f}\right)^C\right) & w_{vol} \leq 0 \end{cases} \tag{3.21}$$

B and C are model parameters which affect the rate of damage progress and w_f is the maximum released volumetric energy per volume in which the material failure takes place. The effects of each parameter on the damage evolution have been shown in Fig. 3.6. Based on the continuum damage mechanics and definition of an effective area, the damage parameter d is included in the constitutive equations explained in the previous sections by introducing the effective stress tensor as follows Krajcinovic (1996); Voyiadjis et al. (1998):

$$\bar{\boldsymbol{\sigma}} = \frac{\boldsymbol{\sigma}}{(1 - d(w_{vol}))}, \tag{3.22}$$

with $\boldsymbol{\sigma}$ and $\bar{\boldsymbol{\sigma}}$ denoting the nominal and the effective stress tensors, respectively.

3.5 Summary

The structure of three employed constitutive models for modeling of rock salt behavior were introduced in this chapter. The following items summarize the main issues given in this chapter:

- The BGRa model introduced in Section. 3.2 can describe the steady-state creep deformation as a function of deviatoric stress and temperature. The model only describes the ductile behavior of rock salt under constant loading. Therefore, it can be used for the prediction of long-term deformation in nuclear waste disposal galleries or oil storage caverns.
- The LUBBY2 model introduced in Section. 3.3 is a viscoelastic model to describe the transient and the steady-state creep deformation. The model describes the ductile behavior of rock salt under stepwise loading. Therefore, it can be used for the prediction of long-term deformation in seasonal storage caverns.

- The final objective of this study is to describe the behavior of rock salt in renewable energy storage caverns. These caverns are subjected to different types of loading conditions. For example, during excavation time, the applied load to the rock salt medium increases slowly. While, during the cyclic loading operation, the rock salt is subjected to relatively rapid thermo-mechanical load variations. The viscoplastic-creep-damage constitutive model introduced in Section. 3.4 combines three existing models with some modifications to get benefit from their positive features for the specific purpose of the performed investigation.
- The viscoplastic-creep-damage model can be applied in different types of simulations in terms of loading conditions (i.e. constant loading, monotonic loading and cyclic loading) as well as different time scales (i.e. short term or long term).
- The Desai model introduced in Section. 3.4.1 is based on a single-surface plasticity concept which avoids the difficulties regarding numerical implementation. The employed non-associated flow rule in this model yields to better description of the volumetric plastic strain. The dependency of the yield surface on Lode's angle results in different material responses in triaxial compression, shear and extension tests. The model takes into account the material dilatancy and compressibility which enhances the modeling of the volumetric behavior and improves the fit to the experimental data. In addition, the failure boundary allows the model to account for the short-term failure of the rock salt in strength tests. Furthermore, the rate dependency described via the viscoplasticity formulation explains the rate dependent behavior of rock salt.
- To describe the time-dependent behavior of rock salt, the modified creep law in Section. 3.4.2 has been formulated based on the Norton-Hoff creep law (i.e. power law creep) in which the creep strain rate is a function of the applied deviatoric stress and temperature. In this thesis, the model has been modified by introducing a new creep potential surface in order to have a better description for the volumetric creep deformation.
- The damage development in rock salt can be described using the released volumetric strain energy. This idea has been employed in this thesis by including an energy-dependent damage parameter into the constitutive model. A commonly used function for rock materials has been also employed to describe the damage evolution. This formulation allows us to describe the strain softening in triaxial strength test, the tertiary creep in long-term creep tests and the failure in cyclic loading tests.

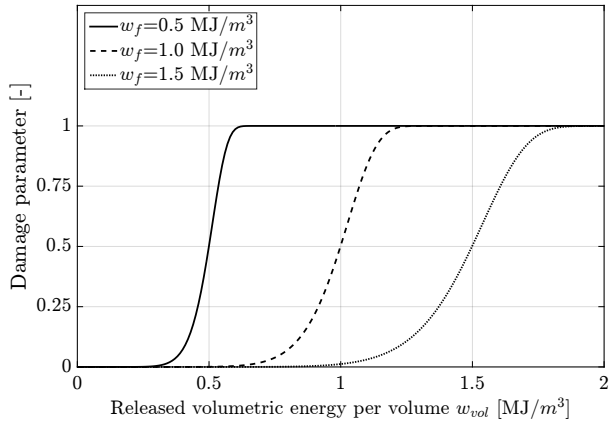

(a)

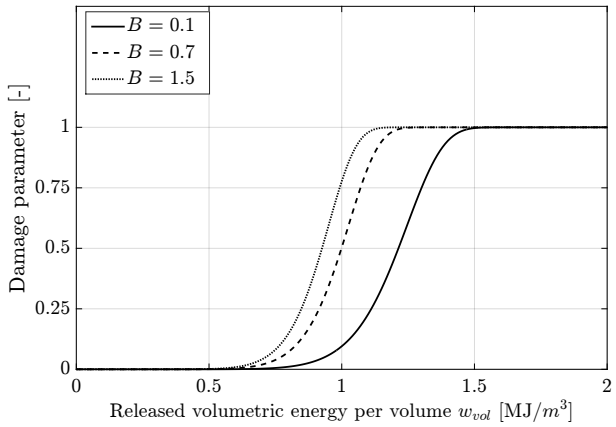

(b)

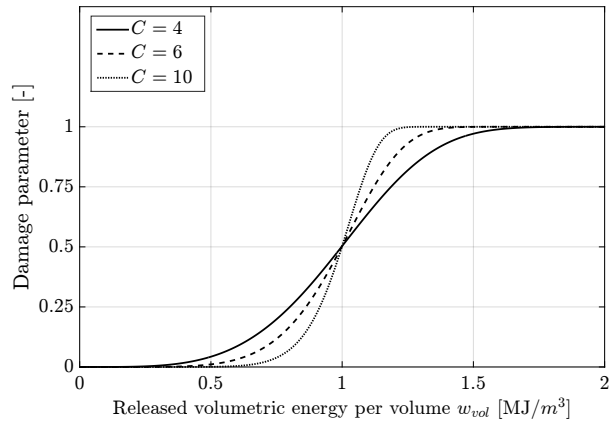

(c)

Figure 3.6: Parametric study of damage evolution; (a) In this figure the effect of parameter w_f has been shown, $B = -0.7$, $C = 10$; (b) In this figure, the effect of parameter B has been shown, $w_f = 1.0$, $C = 10$; (a) In this figure the effect of parameter C has been shown, $w_f = 1.0$, $B = -0.7$

4 Model implementation in FEM

4.1 General procedure

The constitutive equations to model the viscoplastic-creep-damage behavior were described in the previous chapter. In this chapter, these equations are integrated in an implicit scheme and the updated value of stress is obtained accordingly.
All quantities at time t are denoted by subscript t, and those at the next time increment are denoted by $t + \Delta t$. In the Gaussian point level, the total strain increment $\Delta\boldsymbol{\varepsilon}$ and the temperature increment ΔT are known for the current time increment Δt. In a standard finite element code, this quantities are received from the global Newton-Raphson algorithm which iteratively satisfies the balance of momentum and the balance of energy for the continuous medium. Moreover, all the variables such as stress $\boldsymbol{\sigma}_t$, viscoplastic strain $\boldsymbol{\varepsilon}_t^{vp}$, creep strain $\boldsymbol{\varepsilon}_t^{cr}$, damage parameter d_t and other history variables are given at the beginning of a time step. Therefore, the main objective is to find the value of these quantities at time $t + \Delta t$, consistent with the constitutive equations mentioned before. To accomplish this, two subroutines have to be defined in the main finite-element code as follows:

- "Stress update subroutine": this subroutine updates the stress at time $t + \Delta t$ for each Gauss point using a Newton-Raphson algorithm.
- "Constitutive model subroutine": this subroutine contains all the equations related to the constitutive models. The inputs of this subroutine are stress, temperature and history variables, while the outputs are associated with the constitutive equations such as the viscoplastic strain increment $\Delta\boldsymbol{\varepsilon}^{vp}$, the creep strain increment $\Delta\boldsymbol{\varepsilon}^{cr}$, the derivative of viscoplastic strain with respect to stress tensor and temperature i.e. $\dfrac{\partial\dot{\boldsymbol{\varepsilon}}^{vp}}{\partial\boldsymbol{\sigma}}$ and $\dfrac{\partial\dot{\boldsymbol{\varepsilon}}^{vp}}{\partial T}$, the derivative of creep strain with respect to stress tensor and temperature i.e. $\dfrac{\partial\dot{\boldsymbol{\varepsilon}}^{cr}}{\partial\boldsymbol{\sigma}}$ and $\dfrac{\partial\dot{\boldsymbol{\varepsilon}}^{cr}}{\partial T}$ as well as the updated value of damage.

In the following sections, these two subroutines are explained more in detail.

4.2 Stress update subroutine

In this section, an implicit integration scheme is utilized to obtain the updated value of stress at time $t + \Delta t$. Using the generalized Hooke's law, the stress increment at time $t + \Delta t$ can be calculated as follows:

$$\boldsymbol{\sigma}_{t+\Delta t} - \boldsymbol{\sigma}_t = \mathbb{C}\left(\Delta\boldsymbol{\varepsilon} - \Delta\boldsymbol{\varepsilon}^{vp}_{t+\Delta t} - \Delta\boldsymbol{\varepsilon}^{cr}_{t+\Delta t} - \alpha_s(T_{t+\Delta t} - T_t)\mathbb{I}\right) \tag{4.1}$$

where $\mathbb{C}$ is the elastic constitutive tensor and $\mathbb{I}$ is an identity matrix. For each Gauss point in the finite element model, the quantities $\boldsymbol{\sigma}_t$, $\Delta\boldsymbol{\varepsilon}$ and T_t are known. The unknown values in the right side of the equation, are the viscoplastic strain increment $\Delta\boldsymbol{\varepsilon}^{vp}_{t+\Delta t}$, the creep strain increment $\Delta\boldsymbol{\varepsilon}^{vp}_{t+\Delta t}$ and the updated Temperature $T_{t+\Delta t}$. The viscoplastic and creep parts of strain tensor are functions of stress and temperature. Therefore, their increments can be expressed by the following expressions:

$$\Delta\boldsymbol{\varepsilon}^{vp}_{t+\Delta t} = \frac{\partial\dot{\boldsymbol{\varepsilon}}^{vp}}{\partial\boldsymbol{\sigma}}\Delta t\left(\boldsymbol{\sigma}_{t+\Delta t} - \boldsymbol{\sigma}_t\right) + \frac{\partial\dot{\boldsymbol{\varepsilon}}^{vp}}{\partial T}\Delta t\left(T_{t+\Delta t} - T_t\right) \tag{4.2}$$

$$\Delta\boldsymbol{\varepsilon}^{cr}_{t+\Delta t} = \frac{\partial\dot{\boldsymbol{\varepsilon}}^{cr}}{\partial\boldsymbol{\sigma}}\Delta t\left(\boldsymbol{\sigma}_{t+\Delta t} - \boldsymbol{\sigma}_t\right) + \frac{\partial\dot{\boldsymbol{\varepsilon}}^{cr}}{\partial T}\Delta t\left(T_{t+\Delta t} - T_t\right) \tag{4.3}$$

Substituting Eqs. 4.2 and 4.3 in Eq. 4.1 the stress update formula is obtained as:

$$\boldsymbol{\sigma}_{t+\Delta t} - \boldsymbol{\sigma}_t = \mathbb{C}\left(\Delta\boldsymbol{\varepsilon} - \left(\frac{\partial\dot{\boldsymbol{\varepsilon}}^{vp}}{\partial\boldsymbol{\sigma}} + \frac{\partial\dot{\boldsymbol{\varepsilon}}^{cr}}{\partial\boldsymbol{\sigma}}\right)(\boldsymbol{\sigma}_{t+\Delta t} - \boldsymbol{\sigma}_t)\Delta t - \left(\frac{\partial\dot{\boldsymbol{\varepsilon}}^{vp}}{\partial T} + \frac{\partial\dot{\boldsymbol{\varepsilon}}^{cr}}{\partial T}\right)(T_{t+\Delta t} - T_t)\Delta t\right) \tag{4.4}$$

$\boldsymbol{\sigma}_{t+\Delta t}$ and $T_{t+\Delta t}$ are the unknown values in the above equation. Temperature $T_{t+\Delta t}$ should satisfies the energy balance and the heat transfer equations. If we assume that the temperature field is not a function of mechanical variables, then the energy balance and the heat transfer equations can be solved independent of mechanical equations. However, in general, the temperature field can be a function of mechanical variables as well. In this case, the heat equation and Eq. 4.4 have to be solved simultaneously. To accomplish this, iterative methods such as Newton-Raphson algorithm can be applied to solve the nonlinear coupled equations and find $\boldsymbol{\sigma}_{t+\Delta t}$ and $T_{t+\Delta t}$. The above mentioned procedure is performed for all Gauss points in the finite element model in order to satisfy the conservation laws for the whole continuum body. In this section, we assume that the thermal field has no dependency on stresses and strains. Therefore, the temperature $T_{t+\Delta t}$ is known and it has been already obtained by solving the energy balance and the heat transfer equations. In the following, the Newton-Raphson algorithm is formulated to obtain ob-

tain $\boldsymbol{\sigma}_{t+\Delta t}$ by solving Eq. 4.4. To achieve this goal, the following residual function has to be defined. The root of this residual function satisfies the Eq. 4.4.

$$\mathbf{R}(\boldsymbol{\sigma}_{t+\Delta t}) = \boldsymbol{\sigma}_{t+\Delta t} - \boldsymbol{\sigma}_{t} - \mathbb{C}\left(\Delta\boldsymbol{\varepsilon} - \left(\frac{\partial\dot{\boldsymbol{\varepsilon}}^{vp}}{\partial\boldsymbol{\sigma}} + \frac{\partial\dot{\boldsymbol{\varepsilon}}^{cr}}{\partial\boldsymbol{\sigma}}\right)(\boldsymbol{\sigma}_{t+\Delta t} - \boldsymbol{\sigma}_{t})\Delta t - \left(\frac{\partial\dot{\boldsymbol{\varepsilon}}^{vp}}{\partial T} + \frac{\partial\dot{\boldsymbol{\varepsilon}}^{cr}}{\partial T}\right)(T_{t+\Delta t} - T_{t})\Delta t\right) \tag{4.5}$$

According to Newton-Raphson algorithm, the root of residual function $\mathbf{R}$ can be iteratively found as follows:

$$\boldsymbol{\sigma}^{k+1}_{t+\Delta t} = \boldsymbol{\sigma}^{k}_{t+\Delta t} - \left\{\left.\frac{\partial\mathbf{R}}{\partial\boldsymbol{\sigma}}\right|_{\boldsymbol{\sigma}=\boldsymbol{\sigma}^{k}_{t+\Delta t}}\right\}^{-1}\mathbf{R}(\boldsymbol{\sigma}^{k}_{t+\Delta t}) \tag{4.6}$$

Where k is the iteration index here. The term $\dfrac{\partial\mathbf{R}}{\partial\boldsymbol{\sigma}}$ can be obtained by taking derivative of Eq. 4.5 with respect to $\boldsymbol{\sigma}_{t+\Delta t}$ as follows:

$$\frac{\partial\mathbf{R}}{\partial\boldsymbol{\sigma}} = \mathbb{I} + \mathbb{C}\left(\frac{\partial\dot{\boldsymbol{\varepsilon}}^{vp}}{\partial\boldsymbol{\sigma}} + \frac{\partial\dot{\boldsymbol{\varepsilon}}^{cr}}{\partial\boldsymbol{\sigma}}\right)\Delta t \tag{4.7}$$

Substituting Eqs. 4.5 and 4.7 in Eq. 4.6 and using Eqs. 4.2, 4.3 the final stress update formula is obtained as:

$$\begin{cases} \boldsymbol{\sigma}^{k+1}_{t+\Delta t} = \boldsymbol{\sigma}^{k}_{t+\Delta t} - T_1(\boldsymbol{\sigma}^{k}_{t+\Delta t})\; T_2(\boldsymbol{\sigma}^{k}_{t+\Delta t}) \\ T_1(\boldsymbol{\sigma}^{k}_{t+\Delta t}) = \left\{\mathbb{I} + \mathbb{C}\left(\left.\dfrac{\partial\dot{\boldsymbol{\varepsilon}}^{vp}}{\partial\boldsymbol{\sigma}}\right|_{\boldsymbol{\sigma}=\boldsymbol{\sigma}^{k}_{t+\Delta t}} + \left.\dfrac{\partial\dot{\boldsymbol{\varepsilon}}^{cr}}{\partial\boldsymbol{\sigma}}\right|_{\boldsymbol{\sigma}=\boldsymbol{\sigma}^{k}_{t+\Delta t}}\right)\Delta t\right\}^{-1} \\ T_2(\boldsymbol{\sigma}^{k}_{t+\Delta t}) = \boldsymbol{\sigma}^{k}_{t+\Delta t} - \boldsymbol{\sigma}_{t} - \mathbb{C}\left(\Delta\boldsymbol{\varepsilon} - \Delta\boldsymbol{\varepsilon}^{vp}|_{\boldsymbol{\sigma}=\boldsymbol{\sigma}^{k}_{t+\Delta t}} - \Delta\boldsymbol{\varepsilon}^{cr}|_{\boldsymbol{\sigma}=\boldsymbol{\sigma}^{k}_{t+\Delta t}} - \alpha_{s}\Delta T\mathbb{I}\right) \end{cases} \tag{4.8}$$

The value of $\boldsymbol{\sigma}_{t+\Delta t}$ in Eq. 4.8 changes iteratively. The iteration continues until the condition $\|\mathbf{R}\| \leq \epsilon$ is satisfied. Where ϵ is a predefined error. It should be noted, the terms $\dfrac{\partial\dot{\boldsymbol{\varepsilon}}^{vp}}{\partial\boldsymbol{\sigma}}$, $\dfrac{\partial\dot{\boldsymbol{\varepsilon}}^{cr}}{\partial\boldsymbol{\sigma}}$, $\Delta\boldsymbol{\varepsilon}^{vp}$ and $\Delta\boldsymbol{\varepsilon}^{cr}$ in Eq. 4.8 are associated with the constitutive equations. That means, in each iteration, these values are received from the constitutive model subroutine. The flow chart shown in Fig. 4.1 describes the connection between the aforementioned subroutines.

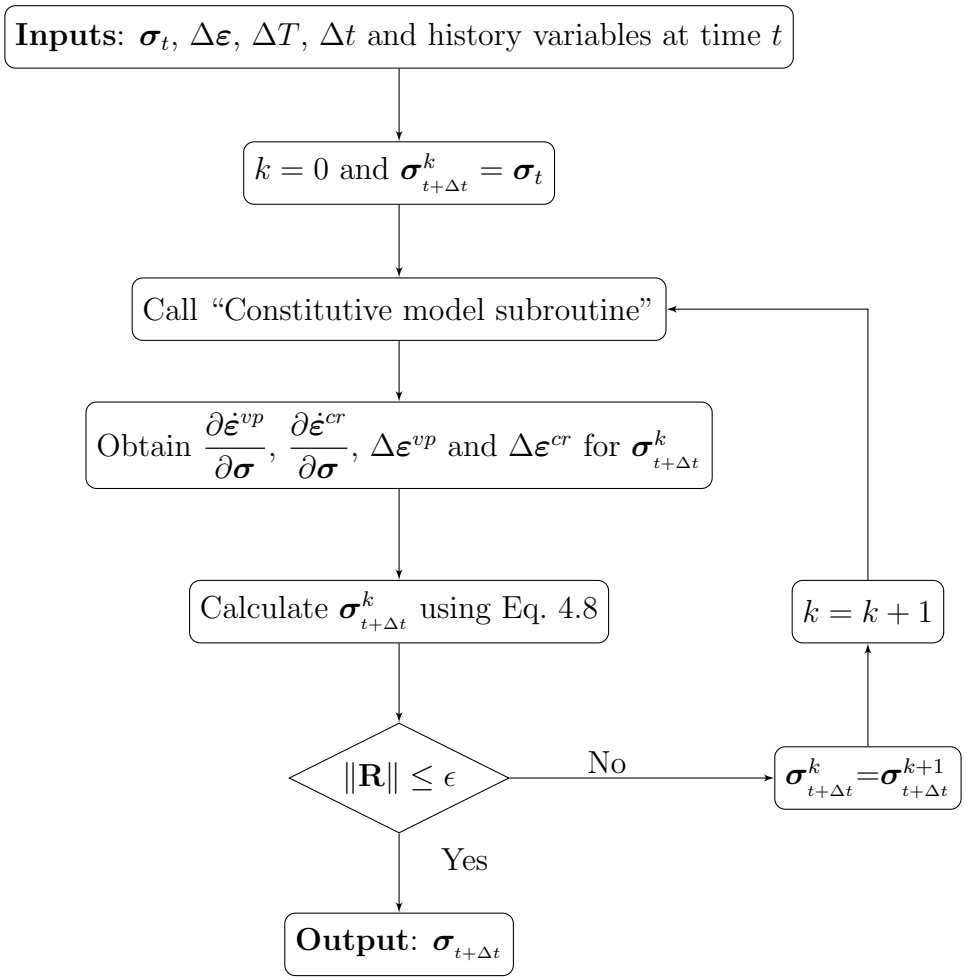

Figure 4.1: The main flowchart of the stress update subroutine

4.3 Constitutive model subroutine

The details regarding the "Constitutive model subroutine" are presented in this section. As explained before, this subroutine is called by the "Stress update subroutine" in each Newton-Raphson iteration. Fig. 4.2 represents the main steps of the constitutive model subroutine. The first item checked within this subroutine is damage parameter d. If damage occurs the nominal stress should be converted to the effective stress through Eq. 3.22. Otherwise, the calculations proceed with the nominal stress. Then, the hardening parameters α, α_q, α_{ss} are calculated using Eqs. 3.10, 3.11 and 3.19, respectively. Having the stress and the hardening parameters, the viscoplastic yield function F^{vp} shown in Eq. 3.7 is checked. If $F^{vp} \leq 0$, then the stress state is inside the viscoplastic yield surface. In this case, no viscoplastic strain is generated and the deformation is due to the creep and elasticity only. In contrast, for $F^{vp} > 0$, the viscoplastic deformation has to be taken into

account. Therefore, the viscoplastic strain increment $\Delta\boldsymbol{\varepsilon}^{vp}$ is obtained using Eq. 3.6 as follows:

$$\Delta\boldsymbol{\varepsilon}^{vp} = \dot{\boldsymbol{\varepsilon}}^{vp}\Delta t = \mu_1 \left\langle \frac{F^{vp}}{F_0} \right\rangle^{N_1} \frac{\partial Q^{vp}}{\partial \boldsymbol{\sigma}} \Delta t \tag{4.9}$$

The derivative of viscoplastic strain rate with respect to stress $\dfrac{\partial \dot{\boldsymbol{\varepsilon}}^{vp}}{\partial \boldsymbol{\sigma}}$ is another quantity which is required for the stress update subroutine. The derivation of viscoplastic strain rate is calculated using following equations:

$$\frac{\partial \dot{\boldsymbol{\varepsilon}}^{vp}}{\partial \boldsymbol{\sigma}} = \frac{\mu_1 N_1}{F_0} \left\langle \frac{F^{vp}}{F_0} \right\rangle^{N_1-1} \frac{\partial F^{vp}}{\partial \boldsymbol{\sigma}} \frac{\partial Q^{vp}}{\partial \boldsymbol{\sigma}} + \mu_1 \left\langle \frac{F^{vp}}{F_0} \right\rangle^{N_1} \frac{\partial^2 Q^{vp}}{\partial \boldsymbol{\sigma}^2} \tag{4.10}$$

$$\frac{\partial F^{vp}}{\partial \boldsymbol{\sigma}} = \frac{\partial F^{vp}}{\partial I_1}\frac{\partial I_1}{\partial \boldsymbol{\sigma}} + \frac{\partial F^{vp}}{\partial J_2}\frac{\partial J_2}{\partial \boldsymbol{\sigma}} + \frac{\partial F^{vp}}{\partial J_3}\frac{\partial J_3}{\partial \boldsymbol{\sigma}} \tag{4.11}$$

$$\frac{\partial Q^{vp}}{\partial \boldsymbol{\sigma}} = \frac{\partial Q^{vp}}{\partial I_1}\frac{\partial I_1}{\partial \boldsymbol{\sigma}} + \frac{\partial Q^{vp}}{\partial J_2}\frac{\partial J_2}{\partial \boldsymbol{\sigma}} + \frac{\partial Q^{vp}}{\partial J_3}\frac{\partial J_3}{\partial \boldsymbol{\sigma}} \tag{4.12}$$

Similar to the viscoplastic strain, the creep strain increment $\Delta\boldsymbol{\varepsilon}^{cr}$ and the derivative of creep strain rate with respect to stress $\dfrac{\partial \dot{\boldsymbol{\varepsilon}}^{cr}}{\partial \boldsymbol{\sigma}}$ are obtained as follows:

$$\Delta\boldsymbol{\varepsilon}^{cr} = \dot{\boldsymbol{\varepsilon}}^{cr}\Delta t = \mu_2 \left\{F^{cr}\right\}^{N_2} \frac{\partial Q^{cr}}{\partial \boldsymbol{\sigma}} \Delta t \tag{4.13}$$

$$\frac{\partial \dot{\boldsymbol{\varepsilon}}^{cr}}{\partial \boldsymbol{\sigma}} = \mu_2 N_2 \left\{F^{cr}\right\}^{N_2-1} \frac{\partial F^{cr}}{\partial \boldsymbol{\sigma}} \frac{\partial Q^{cr}}{\partial \boldsymbol{\sigma}} + \mu_2 \left\{F^{cr}\right\}^{N_2} \frac{\partial^2 Q^{cr}}{\partial \boldsymbol{\sigma}^2} \tag{4.14}$$

$$\frac{\partial F^{cr}}{\partial \boldsymbol{\sigma}} = \frac{\partial F^{cr}}{\partial I_1}\frac{\partial I_1}{\partial \boldsymbol{\sigma}} + \frac{\partial F^{cr}}{\partial J_2}\frac{\partial J_2}{\partial \boldsymbol{\sigma}} + \frac{\partial F^{cr}}{\partial J_3}\frac{\partial J_3}{\partial \boldsymbol{\sigma}} \tag{4.15}$$

$$\frac{\partial Q^{cr}}{\partial \boldsymbol{\sigma}} = \frac{\partial Q^{cr}}{\partial I_1}\frac{\partial I_1}{\partial \boldsymbol{\sigma}} + \frac{\partial Q^{cr}}{\partial J_2}\frac{\partial J_2}{\partial \boldsymbol{\sigma}} + \frac{\partial Q^{cr}}{\partial J_3}\frac{\partial J_3}{\partial \boldsymbol{\sigma}} \tag{4.16}$$

At the end, the released volumetric energy per unit volume w_{vol} shown in Eq. 3.20 is updated and the stress is converted to the nominal stress again.

4.4 Summary

In this chapter, the general procedure to implement the viscoplastic-creep-damage model in a standard finite element code has been presented. The main objective in this chapter is to provide an implicit scheme to update the stress tensor and other constitutive variables. To accomplish this, two subroutines, i.e. (1) stress update subroutine and (2) constitutive model subroutine, have been added to the finite element code "Code-Bright". The stress update subroutine updates the stress at each time step for each Gauss point using a Newton-Raphson algorithm. The constitutive model subroutine contains all the equations related to the constitutive models. The inputs of this subroutine are stress, temperature and history variables, while the outputs are associated with the constitutive equations. The interaction between these two subroutines has been explained in the current chapter.

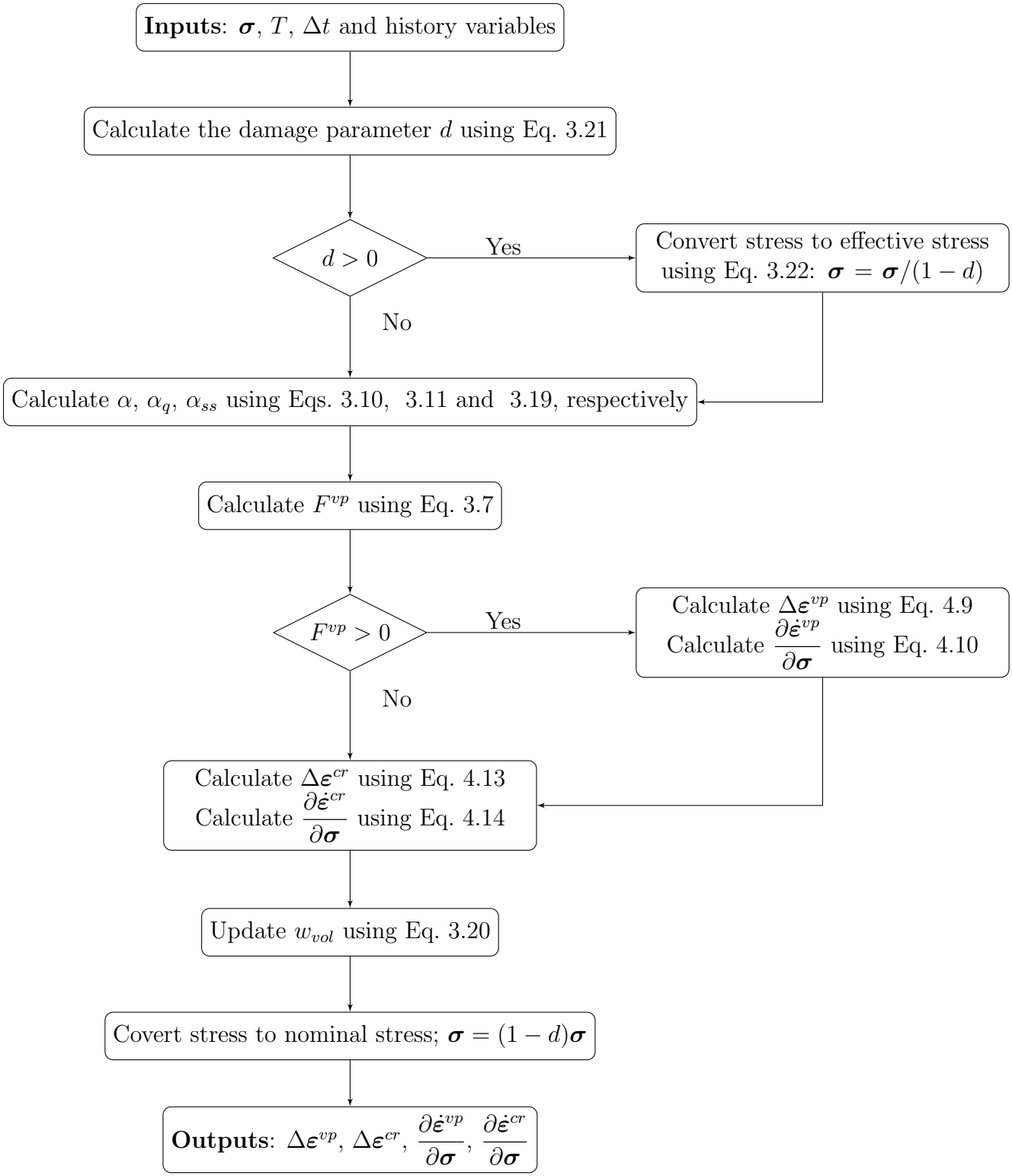

Figure 4.2: The main flowchart of the constitutive model subroutine

5 Determination of material parameters

5.1 Determination of material parameters for BGRa model

As shown in Section. 3.2, the BGRa model has three material parameters which should be determined using long-term creep tests. These parameters are the coefficient A_c, the activation energy Q_c and the stress exponent n_c. Since the model represents the steady-state creep deformation, only those experiments which reach to the steady-state condition have to be utilized for the determination of BGRa parameters. As Hunsche & Hampel (1997) pointed out, different types of rock salt may exhibit different creep behaviors. In fact, the steady-state creep rates observed for different types of the rock salt can show a difference of more than a factor of 100. These differences are associated with the distribution of microscopic impurities within the grains, not with the total amount of the impurity mass Hunsche & Hampel (1997). With this explanation, it is expected that the rock samples obtained from different locations have different creep parameters. In this section, the BGRa creep parameters are back calculated using a series of creep tests performed on samples from Asse mine (northern Germany). Fig. 5.1 shows the experimentally obtained steady-state creep rates versus the applied deviatoric stresses for different temperatures. Each discrete point in this figure corresponds to a single creep experiment. The unknown parameters A_c, Q_c and n_c can be determined for this type of rock salt by minimizing the following function:

$$\min \quad \sum_{i=1}^{N} \left| A_c \exp\left(\frac{Q_c}{RT_i}\right) q_i^{n_c} - \dot{\varepsilon}_i^{\text{experiment}} \right| \tag{5.1}$$

This function shows the misfit between the calculated strain rates by BGRa model and the measured strain rates in experiments. Therefore, the most suitable creep parameters are those which minimize this misfit function. Here, N is the total number of experimental data and the term $|x|$ shows the absolute value of x. The first term inside the absolute

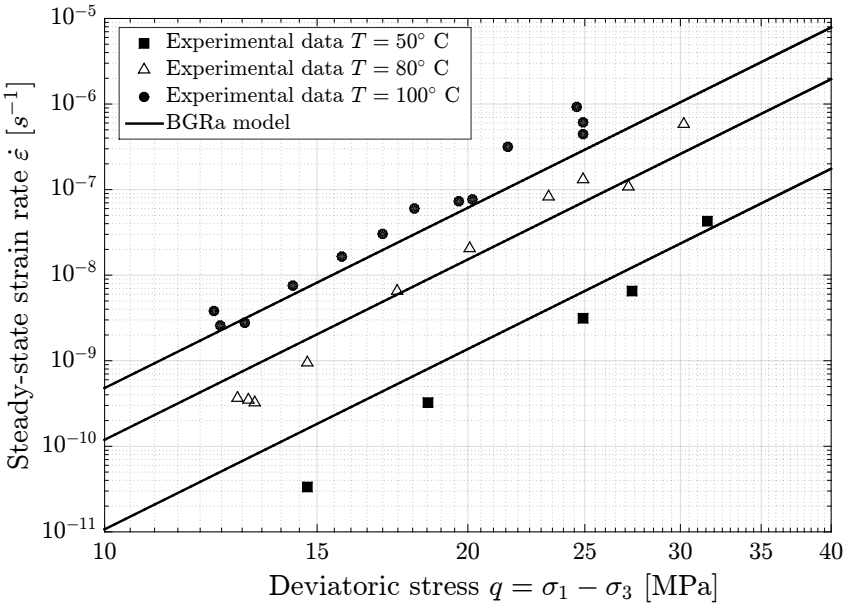

Figure 5.1: Steady-state creep rate versus applied deviatoric stresses for different temperatures; creep tests have been performed on samples from Asse mine (northern Germany); test data from Hunsche & Hampel (1997)

brackets indicates the steady-state creep rate calculated by BGRa model for the i^{th} creep experiment, while the second term is the corresponding experimental data. Fig. 5.1 shows also the steady-state creep rates calculated by BGRa model. The creep parameters have been determined using the above-mentioned procedure. The identified parameters for this type of rock salt are: $A_c = 0.2$ day^{-1}, $Q_c = 76350$ KJ/mol and $n_c = 7$.

5.2 Determination of material parameters for LUBBY2 model

As explained in Section. 3.3, the LUBBY2 model is a viscoelastic model with 7 parameters. The model takes into account both transient and steady-state deformations. Therefore, stepwise creep tests with different stress levels can be used to determine the model parameters. In stepwise creep tests, the stress applied to the sample remains constant for a while. Then, it increases to another constant level. At each stress level, first, a transient creep deformation is observed. At this step, the creep strain rate reduces significantly due to the strain hardening. The strain rate finally reaches to a constant value which is corresponding to the steady-state creep deformation. Fig. 5.2 shows a stepwise uniaxial creep test performed by Heusermann et al. (2003). As it is seen, the stress is applied to

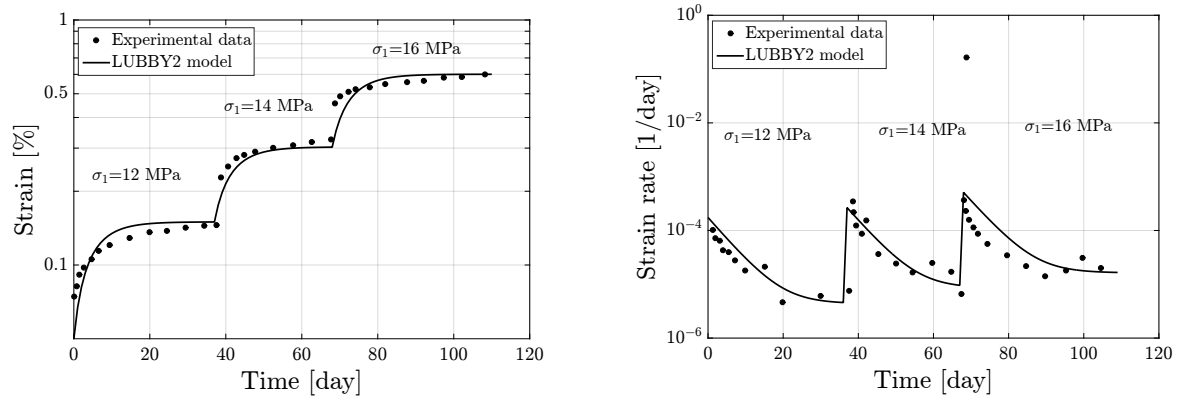

(a) (b)

Figure 5.2: Uniaxial stepwise creep test at constant temperature (experimental data from Heusermann et al. (2003)); (a) Axial strain versus time (b) Strain rate versus time

the sample in three successive steps i.e. 12 MPa, 14 MPa and 16 MPa. Figs. 5.2a and 5.2b show the changes of axial strain and axial strain rate versus time. The LUBBY2 parameters have been determined for this experiment by curve fitting procedure, which minimizes the errors between results of the laboratory tests and the corresponding results predicted by the numerical model. The obtained material parameters for this experiment are shown in Table. 5.1. As shown in this table, the parameter l which is related to the temperature dependency of the steady-state creep has been set to 0 for this experiment. The reason for this assumption is that, the laboratory data given in Heusermann et al. (2003) have been obtained at a constant temperature which is not enough to determine parameter l. To overcome this problem, the steady-state creep tests at different temperatures have to be to used to describe the temperature dependency of the model. For this reason, the steady-state creep data shown in Fig. 5.1 are utilized to calibrate the parameters associated with the Maxwell model i.e. m, η_m and l. The results of this calibration have been shown in Fig. 5.3. Table. 5.1 provides the material parameters obtained for this set of laboratory data.

5.3 Determination of material parameters for the viscoplastic-creep-damage model

The section at hand is mainly taken from Khaledi, Mahmoudi, Datcheva & Schanz (2016*b*). The material parameters related to the viscoplastic-creep-damage model explained in the previous chapter can be identified from laboratory experiments. In partic-

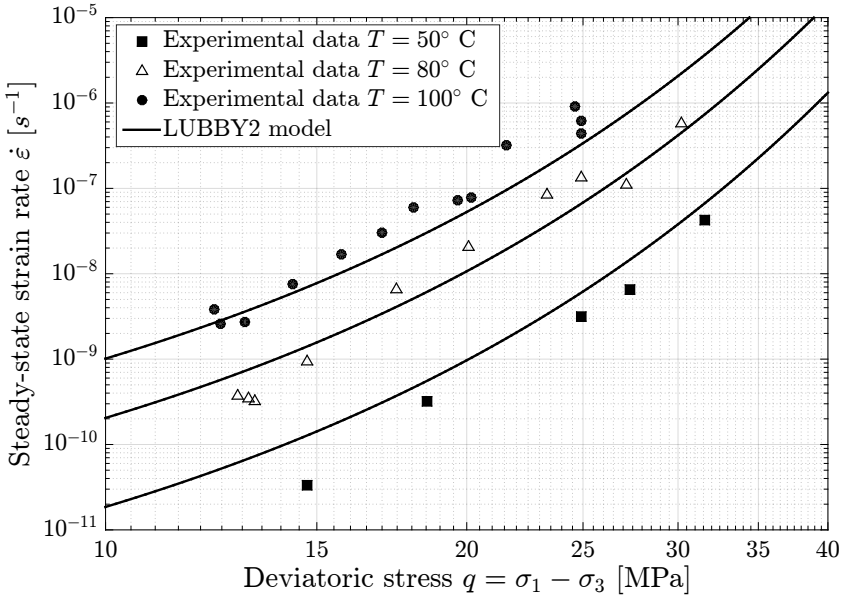

Figure 5.3: Steady-state creep rate versus applied deviatoric stresses for different temperatures; creep tests have been performed on samples from Asse mine (northern Germany); test data from Hunsche & Hampel (1997)

Table 5.1: The identified parameters for LUBBY2 model

	k_1 [1/MPa]	k_2 [1/MPa]	m [1/MPa]	η_k [MPa.d]	η_m [MPa.d]	G_k [MPa]	l [1/K]
Test data from Heusermann et al. (2003)	-0.257	-0.267	-0.275	9.6e5	6.0e7	2.2e5	0
Test data from Hunsche & Hampel (1997)	-0.257	-0.267	-0.3262	9.6e5	2.8e19	2.2e5	0.08

ular, monotonic triaxial compression and extension tests, long-term creep tests as well as cyclic loading tests are required for determining the material parameters of the model. It is obvious that the process of material parameter identification becomes more accurate if these experiments are performed on similar rock samples. Unfortunately, such a data set which comprises all the required experiments for a single type of rock salt is not available. Therefore, in this thesis, a number of laboratory tests have been adopted from references Hunsche & Hampel (1999), Desai & Varadarajan (1987), Minkley & Muehlbauer (2007) and Guo et al. (2012) to examine the capability of the employed constitutive model in describing the stress-strain relation under different loading conditions. Since these tests have been performed on different rock specimens from different locations (i.e Sonderhausen

mine, Salado mine, Jintan mine and Asse mine) and also different testing conditions have been utilized (e.g. different loading rates are used), the material parameters are determined for each type of rock separately. The following steps have been carried out in order to determine the required parameters.

The common values for elasticity parameters of rock salt in the literature are $E = 25000$ MPa and $\nu = 0.27$. Applying these values, the bulk and shear moduli are obtained as $K = 18115$ MPa and $G = 9842$ MPa. Parameter γ is related to the failure boundary of rock salt in the short-term strength tests. Different factors such as the amount of impurities in the rock salt sample as well as the test conditions may affect the strength of rock sample. Depending on the type of rock salt, a value in the range of 0.09 to 0.12 is suggested for this parameter. Fig. 5.4a is a comparison between the applied failure boundary in this study with $\gamma = 0.095$ and four other failure boundaries in the literature. These failure boundaries which have been defined for the triaxial compression tests consist of Cristescu failure boundary, Drucker-Prager criterion, Hoek-Brown criterion and Mohr-Coulomb criterion. As seen, the employed failure boundary in this work has a good agreement with other failure boundaries, in particular, with the empirical non-linear failure boundaries (i.e. Cristescu and Hoek-Brown failure boundaries). Parameters β, β_1 and m_v determine how the failure boundary changes with respect to the Lode's angle θ. The suggested values by Desai in Desai & Varadarajan (1987) have been adopted for these parameters. To examine the validity of selected parameters, the variation of failure boundary with respect to Lode's angle θ has been compared with the rock salt strength data obtained from triaxial compression, shear and extension tests (test data from Cristescu & Gioda (1994)). Fig. 5.4b shows that the model failure boundaries can satisfactorily predict the rock salt strength in different tests. Parameter n defines the location of dilatancy boundary in the stress space. Fig. 5.5 compares the applied dilatancy boundary in this thesis (assuming $n = 3$) with four empirical dilatancy boundaries reported in references Günther & Salzer (2007), Hampel & Schulze (2007), Alkan et al. (2007) and Spiers et al. (1988). As seen, the dilatancy boundary formulated in Eq. 3.13 fits well with the experimentally based dilatancy boundaries.

Parameters μ_1 and N_1 are associated to the rate-dependent behavior of rock salt. The values suggested by Desai in Desai & Varadarajan (1987) have been adopted in this thesis. The hardening behavior of rock salt is described by parameters a_1 and η introduced in Eq. 3.10. Depending on the type of the rock salt and the testing condition, the hardening response of rock salt could be different from one case to another. These parameters are obtained by curve fitting procedures, which minimize the errors between results of

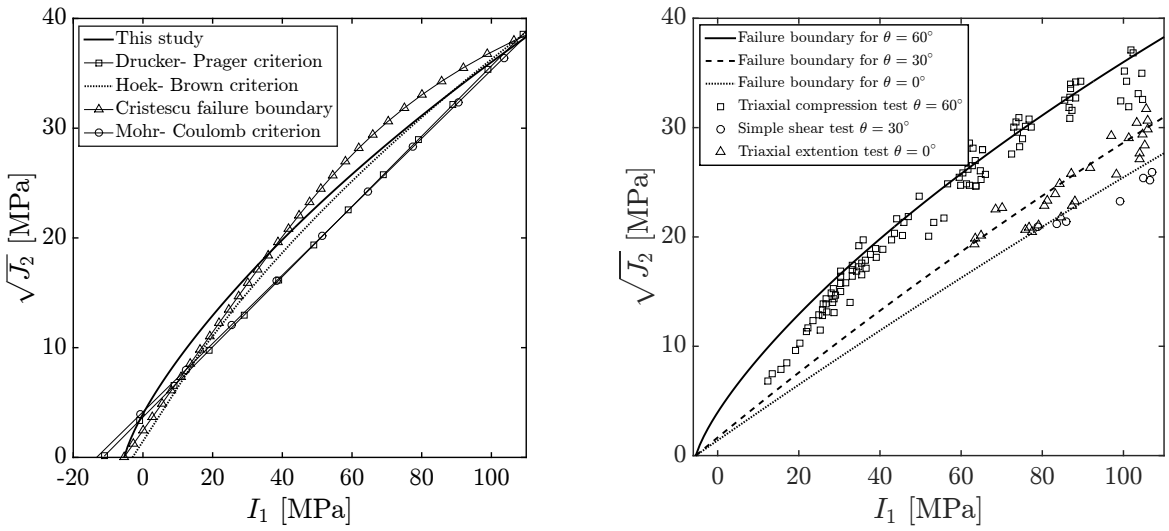

(a) (b)

Figure 5.4: Comparison between (a) different failure boundaries defined for rock salt; Cristescu failure boundary Cristescu (1993), Drucker-Prager criterion Ma, Liu, Fang, Xu, Xia, Li, Yang & Li (2013), Hoek-Brown criterion Ma, Liu, Fang, Xu, Xia, Li, Yang & Li (2013) and Mohr-Coulomb criterion Ma, Liu, Fang, Xu, Xia, Li, Yang & Li (2013) (b) employed failure boundaries in this thesis and the rock salt strength data obtained from experimental investigations (Cristescu & Gioda (1994))

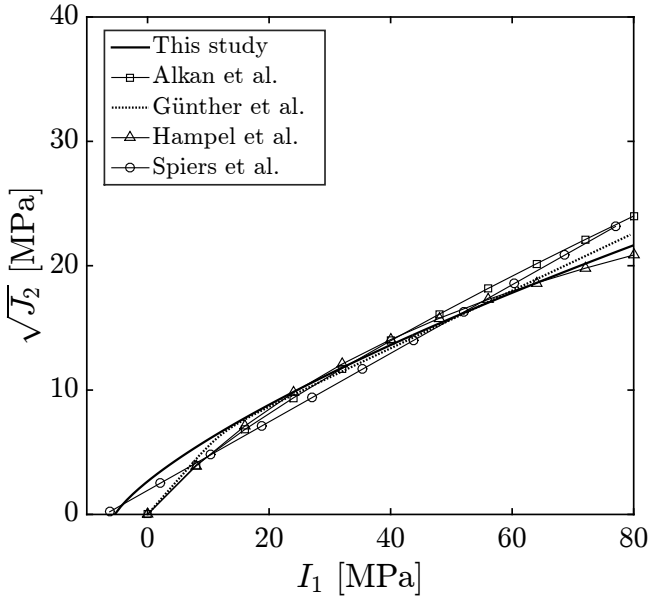

Figure 5.5: Comparison between the applied dilatancy boundary in this thesis and the empirical dilatancy boundaries suggested by Günther et al. in Günther & Salzer (2007), Hampel et al. in Hampel & Schulze (2007), Alkan et al. in Alkan et al. (2007) and Spiers et al. in Spiers et al. (1988).

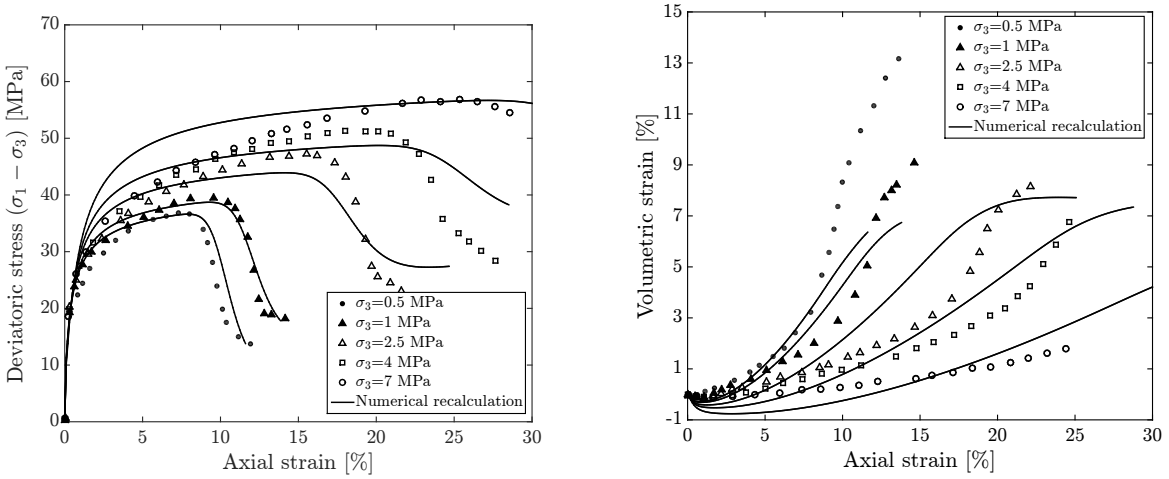

(a) (b)

Figure 5.6: Triaxial compression test of Sonderhausen rock salt under different confining pressures (a) stress-strain relation (b) volumetric strain-axial strain curves (test data from Minkley & Muehlbauer (2007))

laboratory tests and the respective results of numerical recalculation of the laboratory experiments. In this thesis, the non-associative flow rule is used to describe the material behavior. As it is explained later, parameter k_v in Eq. 3.11 which affects the volumetric viscoplastic strain rate has been defined as a function of confining pressure. Parameters μ_0, Q_c and N_2 are associated to the creep behavior of rock salt. These values are obtained by fitting the numerical recalculation curve with the laboratory creep data. The damage parameters, i.e. B, C and w_f, have been identified from the failure and post-failure behavior of rock salt in the triaxial compression tests. The experimental data employed in this study show that the parameter w_f changes with confining pressure. Therefore, a function which is dependent on the minimum principal stress has been defined to describe the variation of w_f with respect to the confining pressure.

In order to model the stress-strain relation in the following tests, a 3D numerical simulation has been performed at integration point level employing an implementation of described model in a finite element subroutine (Code-Bright). The first set of data used in this chapter deals with the triaxial compression test with different confining pressures (i.e. σ_3 =0.5, 1, 2.5, 4 and 7 MPa). These tests have been performed on specimens from Sonderhausen mine in Germany under the constant strain rate $\dot{\varepsilon} = 1 \times 10^{-5}\ s^{-1}$ and the constant temperature $T = 30$ °C Minkley & Muehlbauer (2007). The experimental data as well as the stress-strain curves obtained from numerical recalculation have been shown in Fig. 5.6a. Additionally, the volumetric deformations versus the axial strain have been depicted in Fig. 5.6b. Since the duration of each test is in the range of a few hours, the

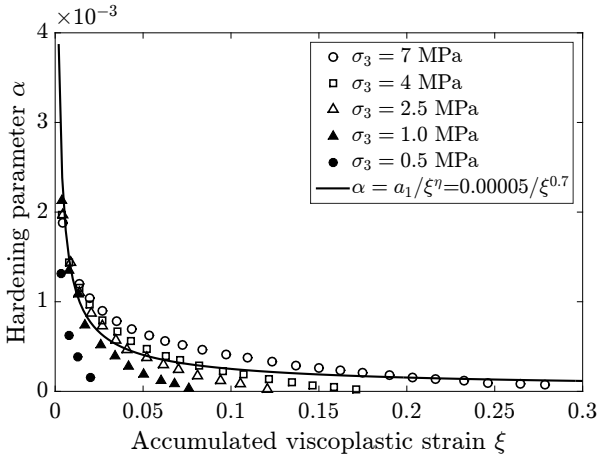

Figure 5.7: Calculation of hardening parameters a_1 and η for the experiment shown in Fig. 5.6

creep deformation is negligible. Thus, this set of data is used to identify the viscoplastic and damage parameters according to the procedure explained before. As seen, the model can adequately predict the evolution of dilatancy and short-term failure as well as the post-failure behavior. Having the experimental data for stress and strain, the hardening parameters a_1 and η have been calculated as shown in Fig. 5.7. In addition, it should be noted that this set of data has been used in this thesis to obtain the dependency of parameters k_v and w_f on the confining pressure σ_3. Figs. 5.8b and 5.8a represent the changes of parameters k_v and w_f with respect to the confining pressure for the above-mentioned experiment.

The second set of experimental data is related to the triaxial extension test which was reported by Desai in Desai & Varadarajan (1987). Fig. 5.9a shows the stress-strain relation of rock salt during the triaxial extension test for confining pressures σ_3 =27.5 and 37.9 MPa. The rock salt specimens used for this testing have been obtained from Salado mine in USA. The tests have been performed under constant loading rate. For this reason, the post-failure behavior is not captured neither in the experiment nor in the numerical simulation. The third data set used in this chapter is related to a long-term creep test conducted by Hunsche et al. Hunsche & Hampel (1999) on a sample from Sonderhausen mine in Germany. The test has been performed at the constant temperature $T = 45$ °C (close to the rock salt temperature at the depth of 1000 m). This set of data is used in this chapter to identify material parameters of the creep model. The obtained results shown in Fig. 5.9b demonstrate that the time-dependent response of the rock salt can be appropriately described by the selected model. Another experimental data set reported in Minkley & Muehlbauer (2007) is selected to verify the time-dependent volumetric stain as

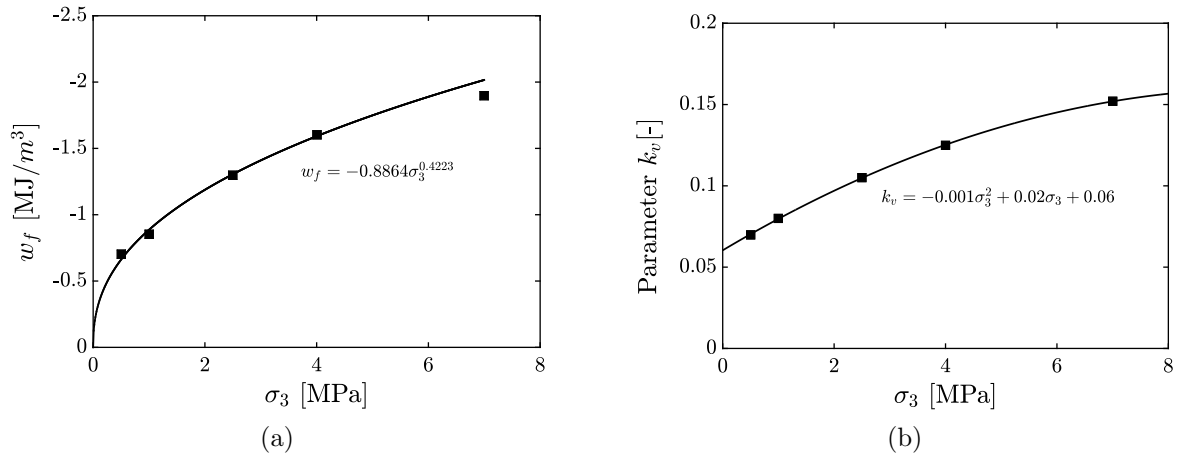

Figure 5.8: The changes of parameters (a) w_f and (b) k_v with respect to the applied confining pressure for the experiment shown in Fig. 5.6

well as the description of transient creep. The experiment is related to a creep test with the axial stress σ_1=41 MPa and the confining pressure σ_3=3 MPa performed on a rock salt sample from Asse mine in Germany. Fortunately, the experimental results for both axial and volumetric deformations have been reported in Minkley & Muehlbauer (2007). The obtained results from numerical modeling are shown in Figs. 5.9c and 5.9d. Because of the time scale of the experiment, the transient part of creep can be clearly observed during the first day of the experiment. The transient creep is modeled using the viscoplastic law described in Section. 3.4.1. When the sample is loaded, because of the viscosity, the stress state lies beyond the viscoplastic yield surface. If the load remains constant, the viscoplastic deformation continues with time and the strain hardening takes place until the viscoplastic yield surface reaches the stress point. After that, the viscoplastic strain rate is zero (end of the transient creep) and the deformation continues steadily by the modified form of Norton-Hoff creep law explained in Section. 3.4.2. As seen, during the steady-state phase, the volumetric strain increases as well. Since the stress state is inside the dilatancy zone, the released inelastic volumetric energy due to microcracking increases with time. Finally, when the damage reaches the threshold value, the tertiary creep is experienced.

The viscoplastic-creep-damage model in this study is also used to model the cyclic response of rock salt around the caverns. Therefore, it should be able to describe the mechanical behavior of rock salt under cyclic loading condition. The fifth laboratory test used in this chapter describes the cyclic loading response of rock salt. Fig. 5.10a shows the experimental stress-strain curve of Jintan rock salt under uniaxial cyclic loading reported by Guo et al. in Guo et al. (2012). As shown in this figure, the axial stress monotonically

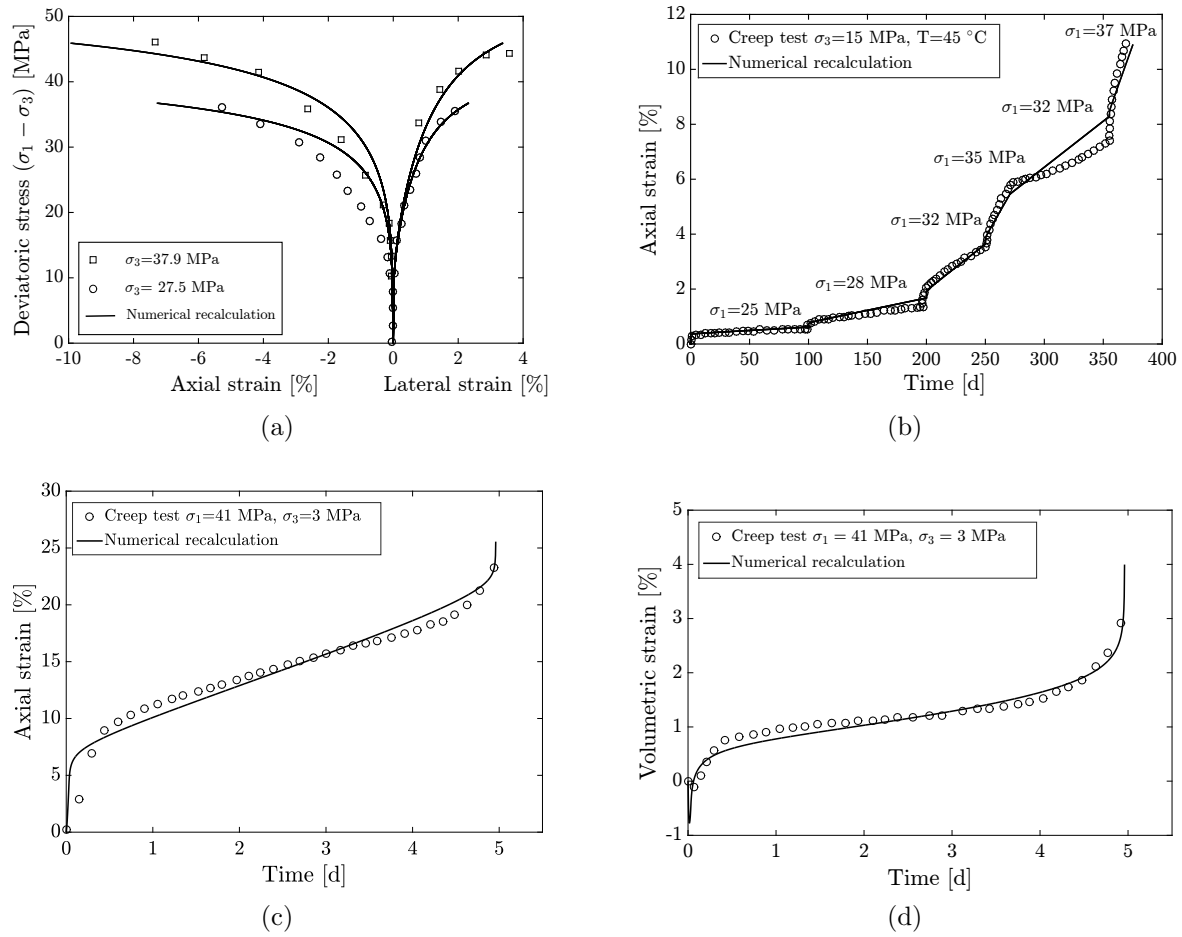

Figure 5.9: (a) Triaxial extension test of Salado rock salt under confining pressures $\sigma_3 = 27.5, 37.9$ MPa (test data from Desai & Varadarajan (1987)), (b) Long-term creep test of Sonderhausen rock salt under different axial loads (test data from Hunsche & Hampel (1999)), (c) variation of axial strain in creep test for Asse mine rock salt (test data from Minkley & Muehlbauer (2007)), (d) variation of volumetric strain in creep test for Asse mine rock salt (test data from Minkley & Muehlbauer (2007))

increases from 0 to 22.5 MPa (90% of compressive strength), then, it varies between 11.25 and 22.5 MPa. Figs. 5.10b and 5.10c represent the results obtained from numerical simulation of the laboratory tests. As seen, the employed constitutive model adequately reproduces the stress-strain relation under cyclic loading condition. On the other hand, the plotted axial strain versus time in Fig. 5.10c shows that the whole cyclic loading process can be divided into three stages. In the first stage, the axial strain increases rapidly and there is a large accumulation of strain. Then, in the second stage, the axial strain accumulates slowly with a relatively constant rate and finally, after a number of cycles, the axial strain increases considerably and the specimen reaches the fatigue failure. Fatigue failure occurs when the strain energy exceeds a critical energy level equivalent to

failure under non-cyclic load Ma, Liu, Wang, Xu, Hua, Fan, Jiang, Wang & Yi (2013); Attewell & Farmer (1973). As shown, the model can adequately describe the three stages of the strain accumulation process resulted from cyclic loading. The parameters required to fit the simulation curves with experimental data are given in Table 5.2.

Table 5.2: The viscoplastic-creep-damage model parameters for different rock salts
Identified parameters for the viscoplastic-creep-damage model using different types of rock salt

		Sonderhausen	Salado	Jintan	Asse mine
Elastic parameters	K [MPa]	18115	18115	18115	18115
	G [MPa]	9842	9842	9842	9842
Viscoplastic parameters	μ_1 [day^{-1}]	5.06e-7	5.06e-7	5.06e-7	5.06e-7
	N_1	3	3	3	3
	n	3	3	3	3
	a_1 [MPa^{2-n}]	0.00005	0.00005	0.00009	0.00004
	η	0.7	0.7	0.7	0.6
	β_1 [MPa^{-1}]	4.8e-3	4.8e-3	4.8e-3	4.8e-3
	β	0.995	0.995	0.995	0.995
	m_v	-0.5	-0.5	-0.5	-0.5
	γ	0.11	0.095	0.095	0.11
	F_0 [MPa^2]	1	1	1	1
	k_{cr}	1	1	1	1.43
	σ_{tensile} [MPa]	1.8	1.8	1.8	1.8
Creep parameters	μ_0 [day^{-1}]	0.27	0.27	0.27	0.27
	Q_c [kJ/mol]	-54000	-54000	-54000	-54000
	N_2	4.0	4.0	4.0	4.15
Damage parameters	B	-0.7	-0.7	-0.7	-0.8
	C	10	10	10	9

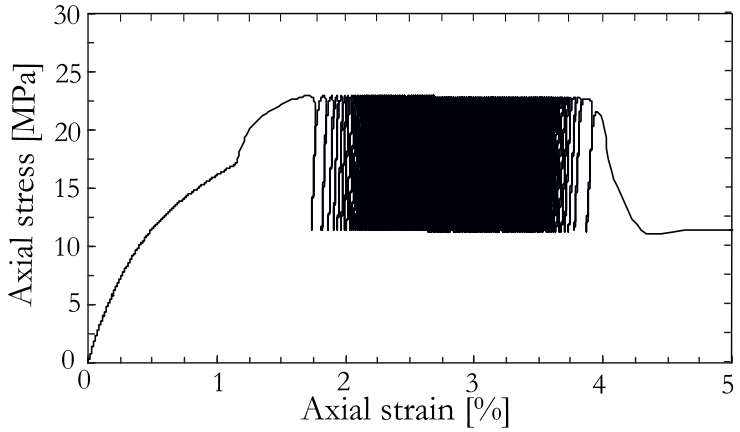

(a)

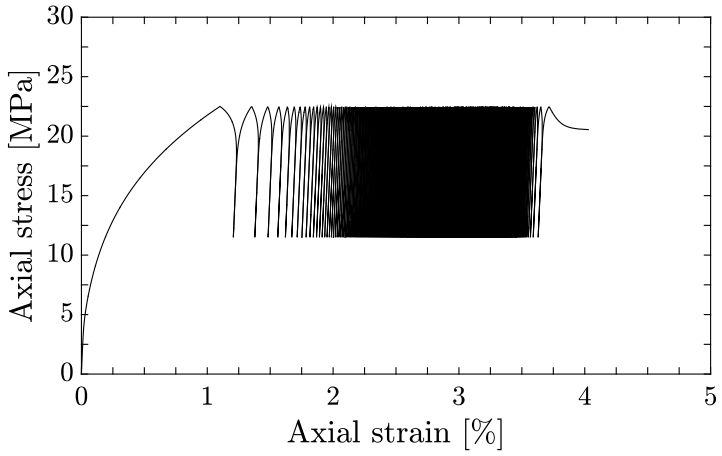

(b)

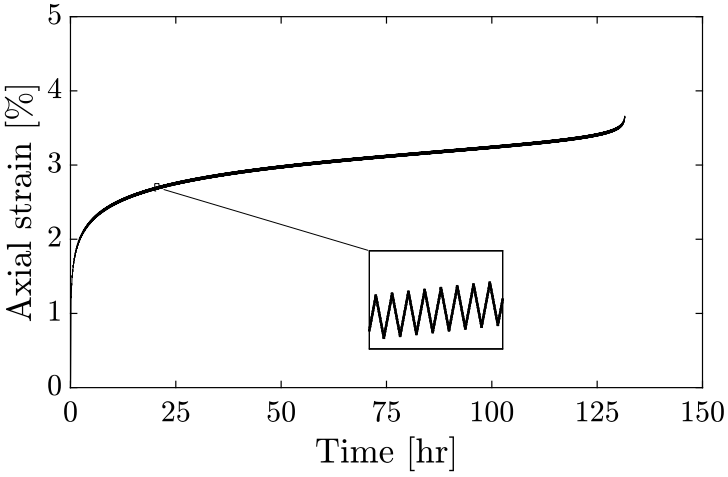

(c)

Figure 5.10: (a) Uniaxial cyclic loading test of Jintan rock salt (test data from Guo et al. (2012)) (b) uniaxial cyclic loading stress-strain curve obtained from numerical simulation (c) evolution of axial strain with time obtained from numerical simulation

5.4 Parametric study of the viscoplastic-creep-damage model

In this section, a parametric study is carried out to assess the performance of the viscoplastic-creep-damage model in different loading conditions. In addition to this, some of the key factors influencing the model responses are introduced and their effects are qualitatively represented. To achieve this goal, the performance of the viscoplastic-creep-damage model in triaxial quasi-static tests, long-term creep tests and cyclic loading tests is numerically investigated. That means, a number of numerical simulations are performed in the integration point level in order to reproduce the laboratory conditions. The parametric study begins with the numerical simulation of triaxial quasi-static tests. Then, it continues with the modeling of creep tests and cyclic loading tests. In each simulation, only one of the influencing factors is changed and the rest remain constant. The influencing factors can be either the material parameters or the boundary conditions. In all simulations, the material parameters shown in Table. 5.3 are considered as the predefined values. The boundary conditions applied to the rock samples in these simulations are as follows:

- The confining pressure applied to the rock sample in all simulations is assumed to be 4 MPa.
- The triaxial quasi-static tests are performed under constant strain rate. The applied strain rate to the rock salt sample in all simulations is $1 \times 10^{-5} s^{-1}$ (except those in which the effect of strain rate on the model response is investigated).
- All simulations are performed under constant temperature of 40 °C (except those in which the effect of temperature on the model response is investigated).
- The cyclic loading tests are performed under load-controlled conditions. The frequency of cyclic loads in all simulations is assumed to be 1×10^{-3} Hz (except those in which the effect of cyclic frequency on the model response is investigated).

Among the material parameters which were introduced in Section. 3.4, the parameters γ, n, k_v, μ_1, w_f have been selected for this parametric study. Parameter γ is associated with the locus of short-term failure boundary in the stress space. Its effect on the model response in triaxial quasi-static tests has been shown in Fig. 5.11. Parameter n is related to the locus of dilatancy boundary in the stress space. Fig. 5.12 describes the effect of parameter n on the model response in triaxial strength tests. In a similar manner, the influences of parameters k_v, μ_1, w_f have been demonstrated in Figs. 5.13 to 5.16. On the other hand, the strain rate and the temperature applying to the rock salt sample in the

triaxial quasi-static tests can be considered as two key factors that may affect the response of the model. The effect of these two factors on the model behavior have been shown in Figs. 5.17 and 5.18. Regarding the creep behavior, the model responses with respect to the applied deviatoric stress and the temperature have been investigated. The results of these studies are shown in Figs. 5.19 and 5.20. Finally, the performance of the model in cyclic loading tests has been investigated. To accomplish this, several key factors such as maximum and minimum applied stresses during cyclic loading, frequency of cycles and temperature are considered. Figs. 5.21 to 5.28 represent the results of parametric study for the cyclic loading.

Table 5.3: Predefined material parameters of rock salt for the parametric study

Elastic parameters	K [MPa]	18115
	G [MPa]	9842
Viscoplastic parameters	μ_1 [day^{-1}]	5.0e-7
	N_1	3
	n	3
	a_1 [MPa^{2-n}]	0.00005
	η	0.7
	β_1 [MPa^{-1}]	4.8e-3
	β	0.995
	m_v	-0.5
	γ	0.11
	F_0 [MPa^2]	1
	k_{cr}	1
	σ_{tensile} [MPa]	1.8
Creep parameters	μ_0 [day^{-1}]	0.2
	Q_c [kJ/mol]	-76350
	N_2	6.0
Damage parameters	B	-0.7
	C	10
	w_f [MJ/m^3]	1.59

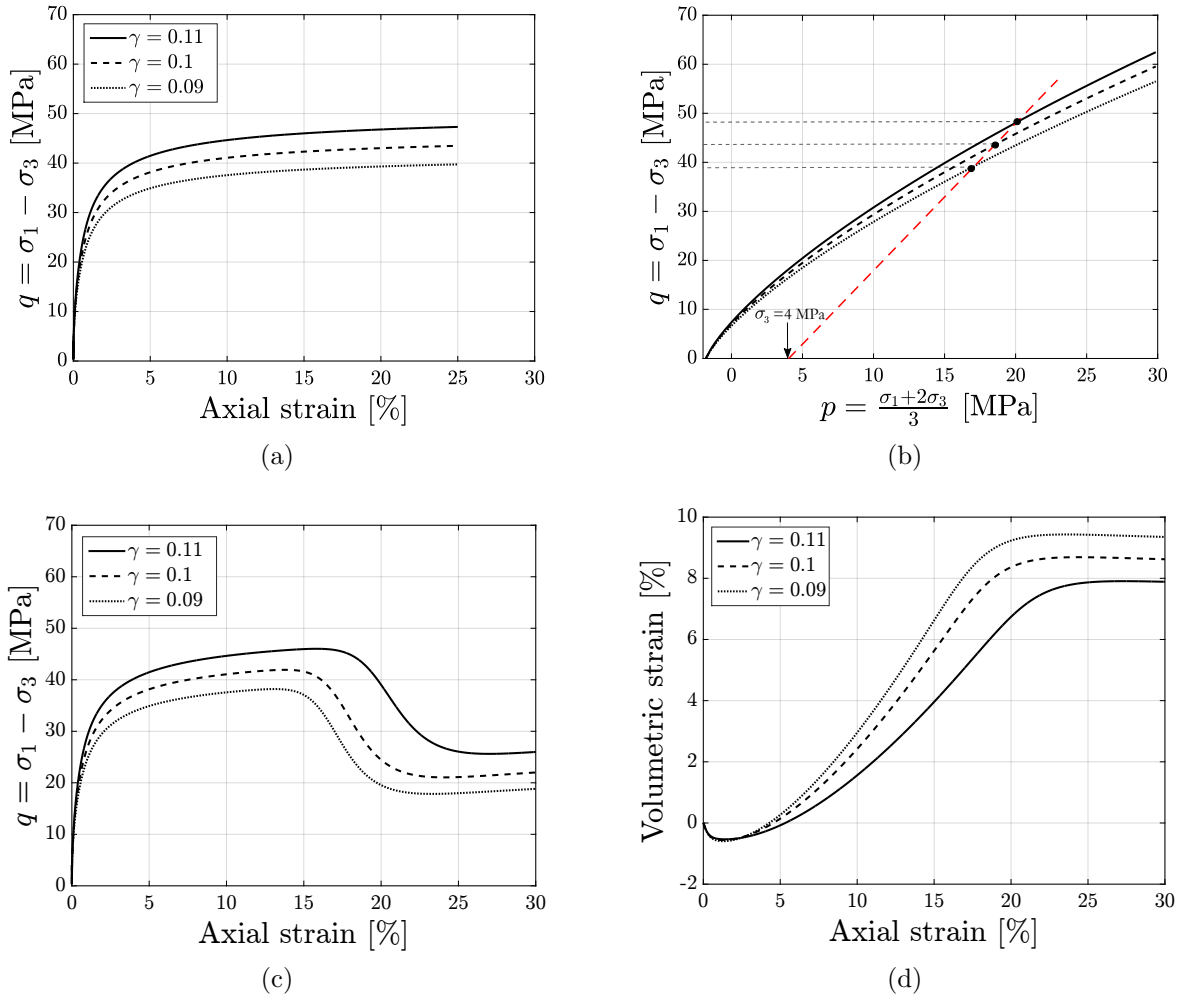

Figure 5.11: The effects of parameter γ on the model response in triaxial strength tests have been shown in these figures. In general, this parameter is related to the short-term failure boundary of rock salt in quasi-static tests; (a) This figure shows the stress-strain relations in a triaxial compression test for three different values of γ. The confining pressure and the strain rate in these simulations are 4 MPa and $1 \times 10^{-5} s^{-1}$, respectively. As seen, the peak strength value reduces by decreasing the γ value. It should be noted that the damage evolution has not been taken into account in these simulations. Therefore, no softening is seen in the model responses; (b) This figure shows the corresponding stress path for the same simulation in $p-q$ stress space. As seen, the locus of short-term failure boundary in stress space can be adjusted by parameter γ; (c) This figure shows the stress-strain relations with damage evolution. The parameters related to the damage evolution are similar for all three curves. The peak strength is reached faster as the γ value reduces; (d) This figure represents the changes of the volumetric strain with respect to the axial strain for different γ values. As seen, for a certain value of axial strain, more dilatancy is observed as the parameter γ reduces. Since the evolution of damage is related to the dilatancy, the smaller values of γ result in the higher damage values.

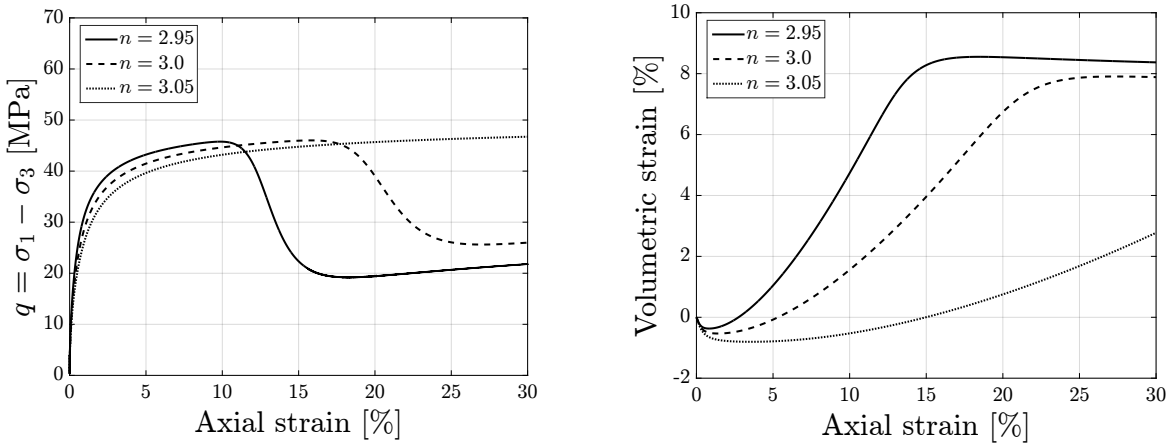

(a) (b)

Figure 5.12: The effects of parameter n on the model response in triaxial strength tests have been shown in these figures. In general, this parameter is related to the onset of dilatancy in quasi-static tests; (a) This figure shows the stress-strain relations in a triaxial compression test for three different values of n. As seen, the peak strength value remains relatively constant as the parameter n changes. However, the axial stain at failure reduces by decreasing the n value (b) This figure represents the volumetric strain versus the axial strain for different n values. As the parameter n reduces, the onset of dilatancy is reached faster, and subsequently, the dilatancy and damage progress become more significant.

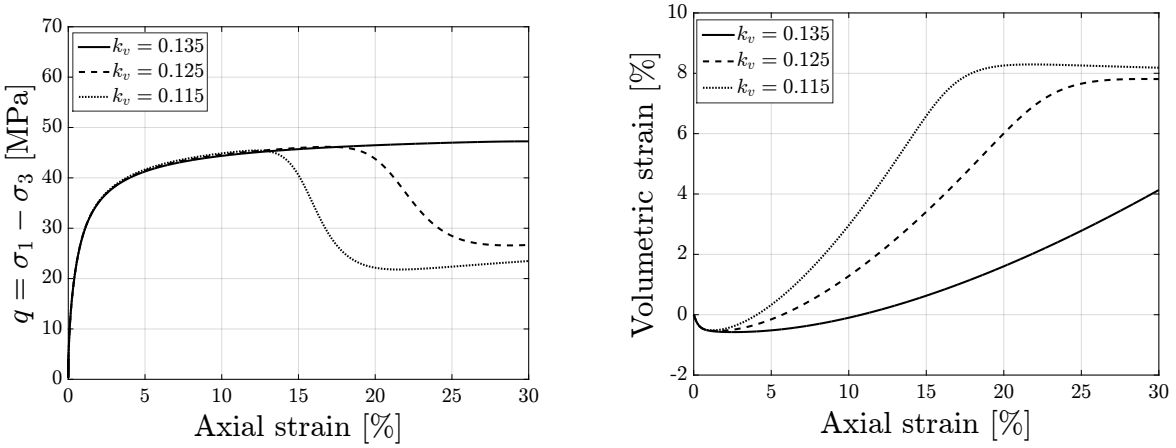

(a) (b)

Figure 5.13: The effects of parameter k_v on the model response in triaxial strength tests have been investigated in this numerical example. In general, this parameter controls the size of the viscoplastic potential surface; (a) This figure shows the stress-strain relations in a triaxial compression test for three different values of k_v. As seen, as parameter k_v reduces the softening is observed at smaller values of axial strain; (b) This figure shows how the evolution of the volumetric strain can be adjusted by changes of k_v value. In other words, the size of viscoplastic potential surface can be controlled by this parameter.

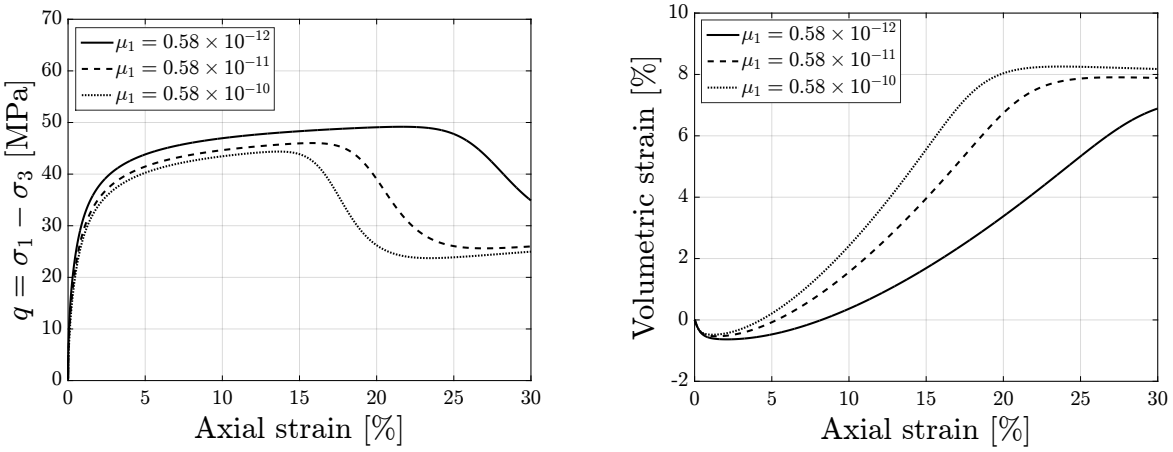

(a) (b)

Figure 5.14: The effects of fluidity parameter μ_1 on the model response in triaxial strength tests have been investigated. In general, this parameter is the inverse of viscosity; (a) This figure shows the stress-strain relations in a triaxial compression test for three different values of μ_1. Smaller values of fluidity results in higher viscosity, and subsequently, more ductile deformation is observed. That means, the material softening occurs at higher axial strains; (b) This figure shows that, by decreasing the fluidity parameter μ_1 (or increasing the viscosity), the dilatancy decreases. This reduction is due to the increase of ductility.

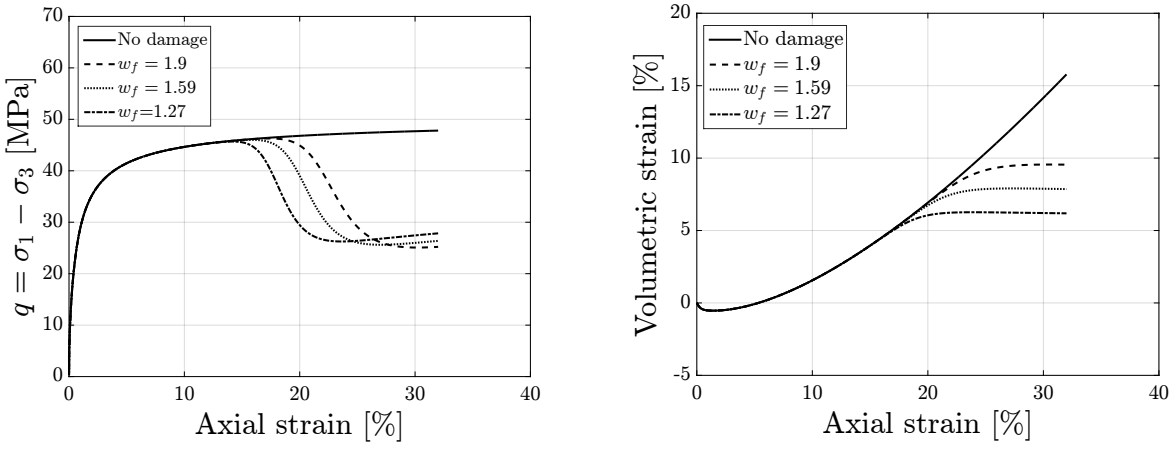

(a) (b)

Figure 5.15: The effects of parameter w_f on the model response in triaxial strength tests have been investigated in this numerical example. This parameter is equal to the released volumetric energy per volume at peak strength and it affects the damage evolution. Therefore, the onset of softening can be adjusted by this parameter; (a) This figure shows the stress-strain relations in a triaxial compression test for different values of w_f. As it can be seen, no damage is observed for large values of w_f. As the parameter w_f reduces the material becomes more brittle and softening occurs faster; (b) This figure represents the changes of the volumetric strain with respect to the axial strain for different w_f values.

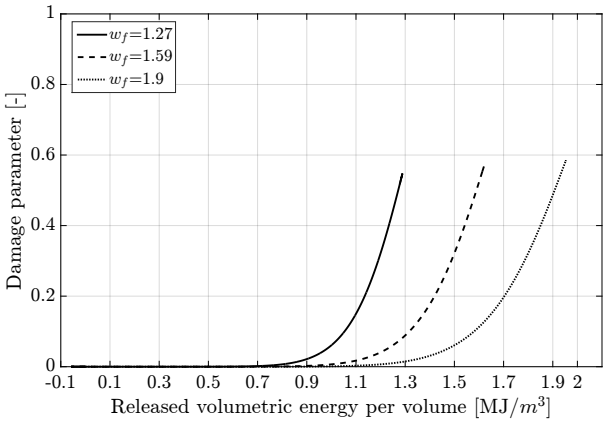

Figure 5.16: Damage evolution versus released volumetric energy per volume for the numerical example shown in Figure. 5.15

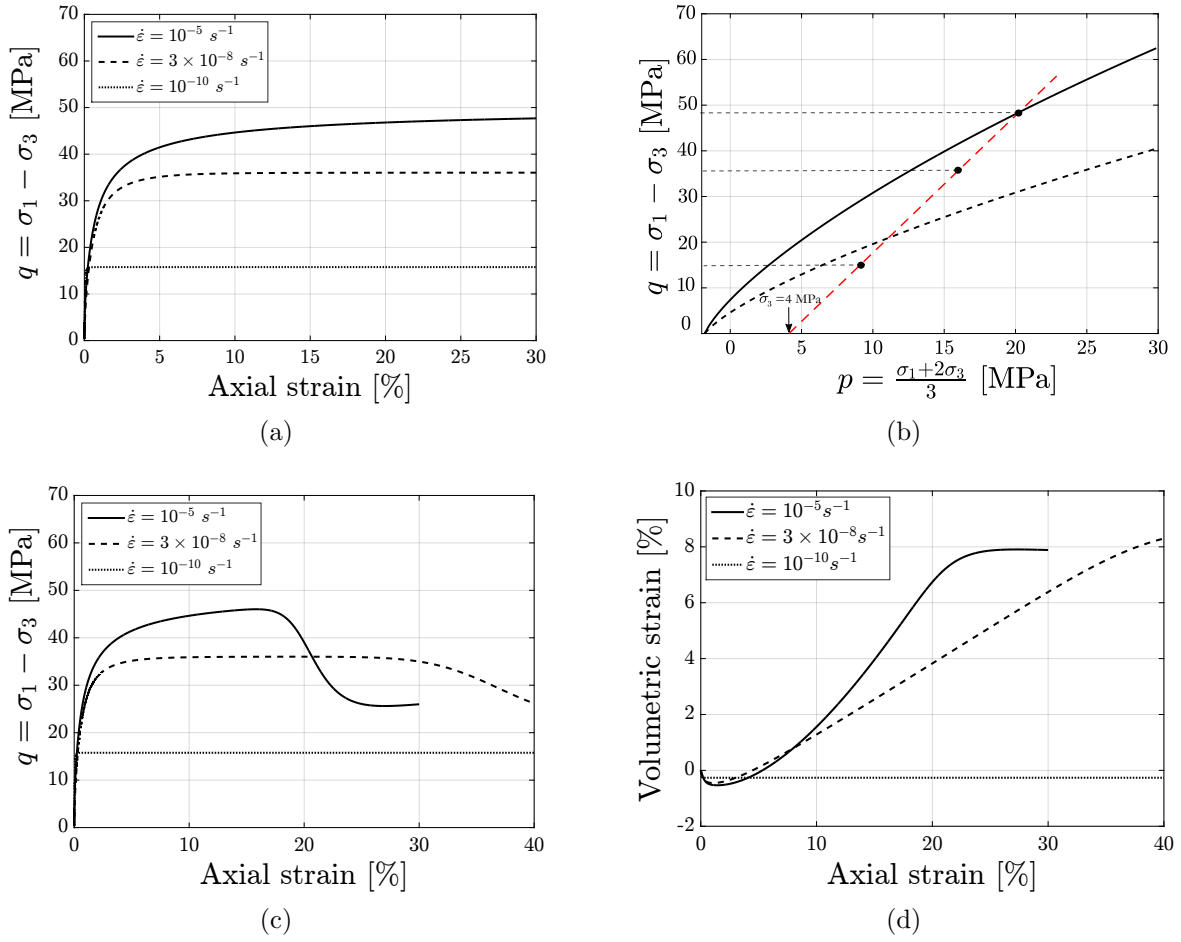

Figure 5.17: In general, as the strain rate decreases the material ductility increases. Therefore, for very small stain rates no softening takes place; (a) Stress-strain relations for different strain rates without damage (b) The corresponding stress path in $p - q$ stress space; (c) Stress-strain relations with damage; (d) Volumetric strain versus axial strain.

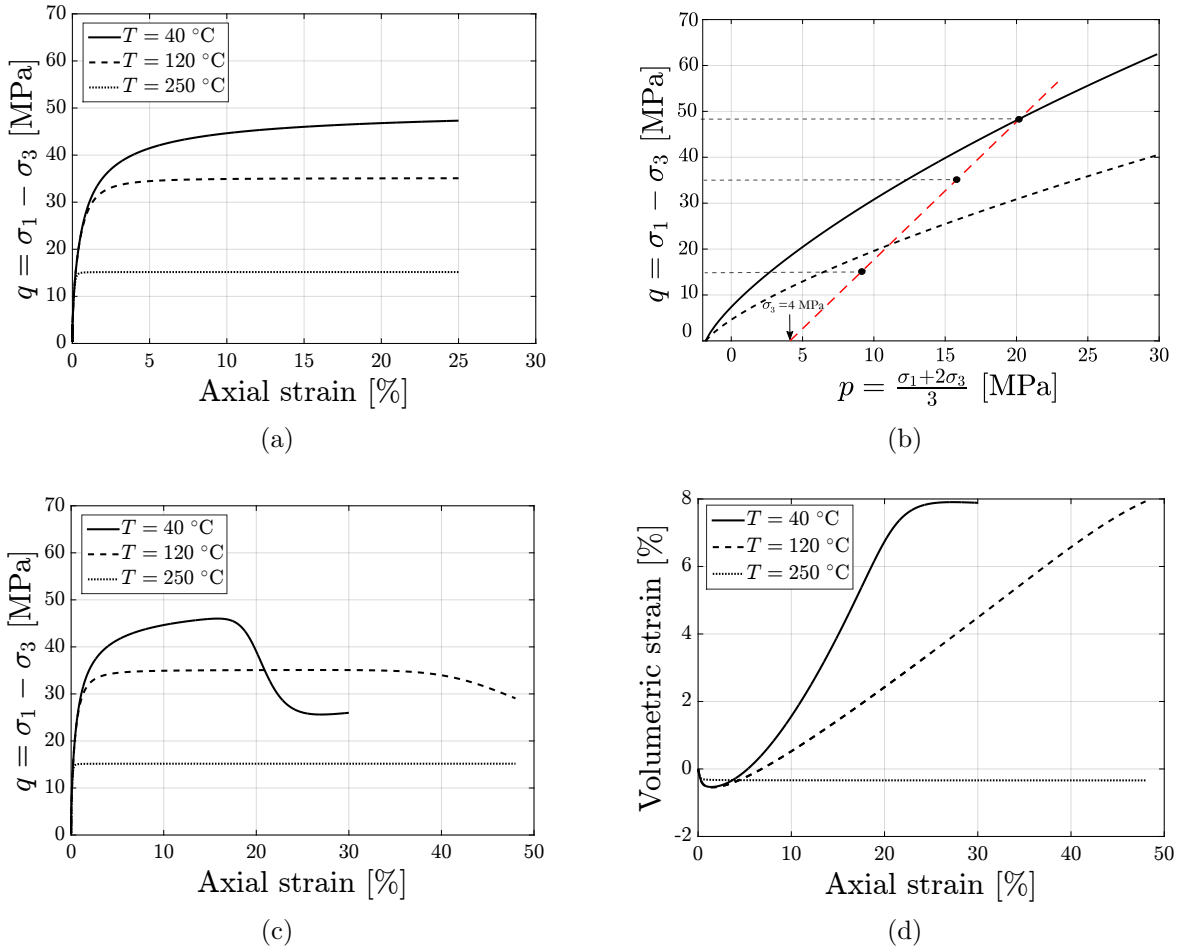

Figure 5.18: The effects of temperature on the model response in triaxial strength tests are shown in these figures. In general, as the temperature increases the rock salt behavior becomes more ductile. That means, at higher temperatures, the inter-granular mechanisms that control the creep deformation take the dominating role. Under such condition, the damage evolution resulted from the opening of microcracks becomes slower. At high temperatures, the deformation is more carried by the creep term which is highly temperature dependent; (a) This figure shows the stress-strain relations for different temperatures without damage. As seen, by increasing temperature, the peak stress reduces; (b) The corresponding stress path in $p - q$ stress space; (c) This figure shows the stress-strain relation considering damage. As it is seen, softening occurs at higher axial strains and lower peak strength. At very high temperature (i.e. $T = 250$ °C), the rock salt sample becomes a perfectly ductile material and no softening is observed; (d) This figure shows the volumetric strain versus axial strain for different temperatures.

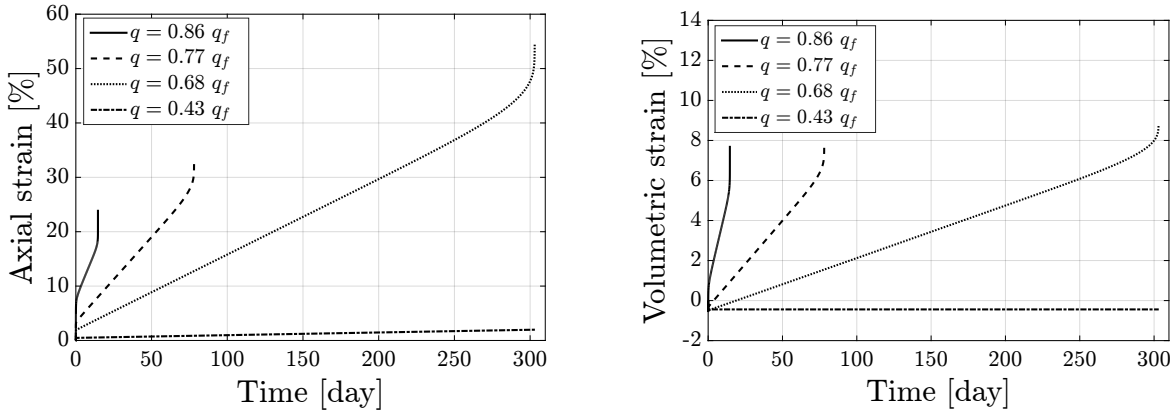

(a) (b)

Figure 5.19: The effects of deviatoric stress on creep behavior have been shown in these figures; (a) The axial strain versus time is depicted in this figure. As seen, when the equivalent deviatoric stress q is equal to 86% of its peak value (i.e. q_f), the tertiary creep occurs after almost 15 days. As the applied deviatoric stress reduces, the failure is observed after a longer time. Finally, when the stress state lies below the dilatancy boundary (e.g. $q = 0.43\ q_f$), the rock salt exhibits only a steady-state deformation without any failure; (b) This figure represents the development of volumetric strains. As seen, the dilatancy develops significantly faster when the magnitude of the applied deviatoric stress increases.

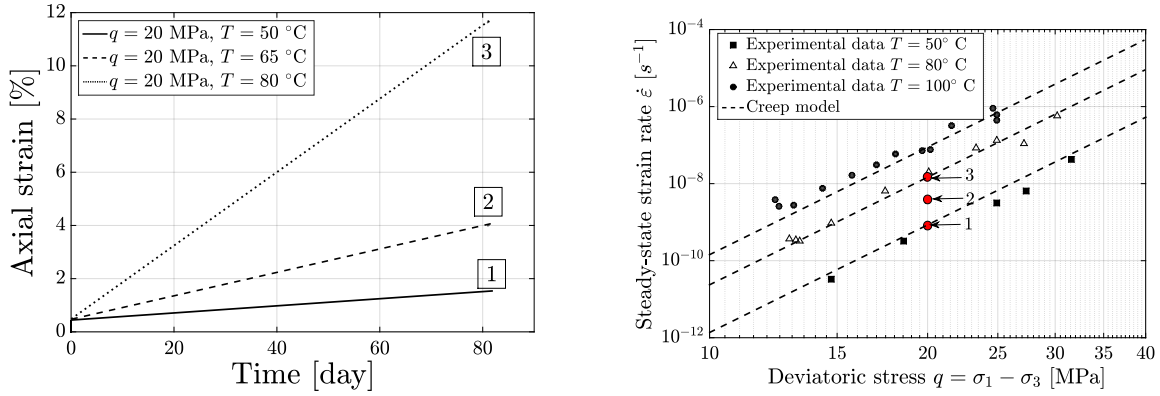

(a) (b)

Figure 5.20: The effects of temperature on creep behavior have been shown in these figures; (a) The axial strain versus time is depicted in this figure. The equivalent deviatoric stress q is equal to 43% of its peak value (i.e. q_f) for the three cases.That means, the stress state lies below the dilatancy boundary. Therefore, the rock salt exhibits steady-state deformations without any failure but with different rates. It is obvious that at elevated temperatures the steady-state creep rate increases significantly ; (b) In order to emphasis the effect of temperature on creep behavior, the boundary conditions related to the three numerical examples in Fig. 5.20a are marked in Fig. 5.1.

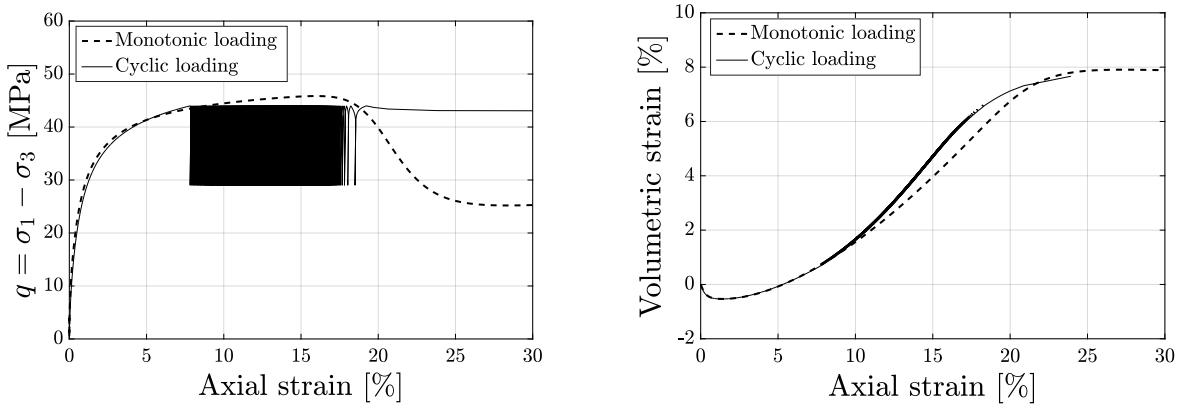

(a) (b)

Figure 5.21: The effect of maximum applied stress in cyclic loading test is shown in these figures. In this example, first, the applied stress to the sample increases monotonically up to ca. 95 % of its peak value in quasi-static test (i.e. $q_{max} = 95\%\ q_f$). This step has been performed with constant strain rate of $1 \times 10^{-5} s^{-1}$ and the temperature is 40 °C. Then, the cyclic loading has been modeled with the frequency of 1×10^{-3} Hz. The amplitude of each cycle is equal to 15 MPa; (a) The stress-strain curve for the cyclic loading is shown in this figure. The failure occurs after ca. 930 cycles; (b) The development of volumetric strain is shown in this figure.

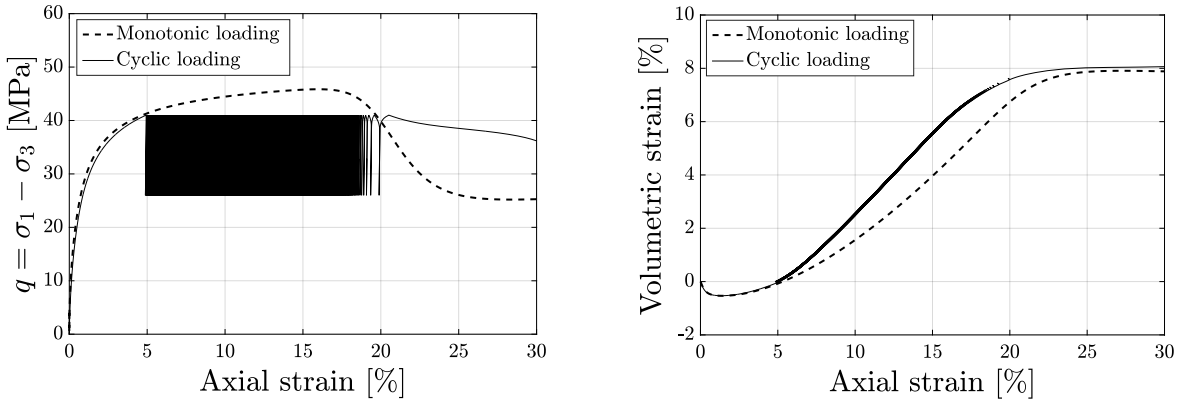

(a) (b)

Figure 5.22: The effect of maximum applied stress in cyclic loading test is shown in these figures. In this example, first, the applied stress to the sample increases monotonically up to ca. 89 % of its peak value in quasi-static test (i.e. $q_{max} = 89\%\ q_f$). This step has been performed with constant strain rate of $1 \times 10^{-5} s^{-1}$ and the temperature is 40 °C. Then, the cyclic loading has been modeled with the frequency of 1×10^{-3} Hz. The amplitude of each cycle is equal to 15 MPa; (a) The stress-strain curve for the cyclic loading is shown in this figure. The failure occurs after ca. 4300 cycles; (b) The development of volumetric strain is shown in this figure.

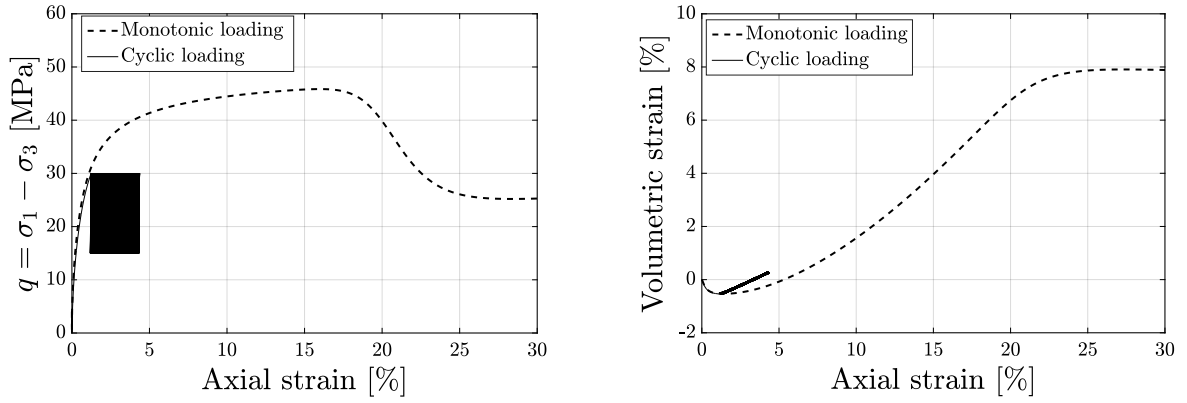

(a) (b)

Figure 5.23: In this example, first, the applied stress to the sample increases monotonically up to ca. 65% of its peak value in quasi-static test (i.e. $q_{max} = 65\ \%q_f$). This step has been performed with constant strain rate of $1 \times 10^{-5}s^{-1}$ and the temperature is 40 °C. Then, the cyclic loading has been modeled with the frequency of 1×10^{-3} Hz. The amplitude of each cycle is equal to 15 MPa; (a) The stress-strain curve for the cyclic loading is shown in this figure. No cyclic failure is observed after 14000 cycles; (b) The development of volumetric strain is shown in this figure. The volumetric strain has still an upward trend, but it has not reached to its critical value. This shows that the maximum stress in cyclic loading lies in the dilatancy zone. Therefore, it is expected to meet the cyclic failure after a larger number of cycles. As explained before, the constitutive model shows no cyclic failure if the maximum stress in cyclic loading is below the dilatancy boundary.

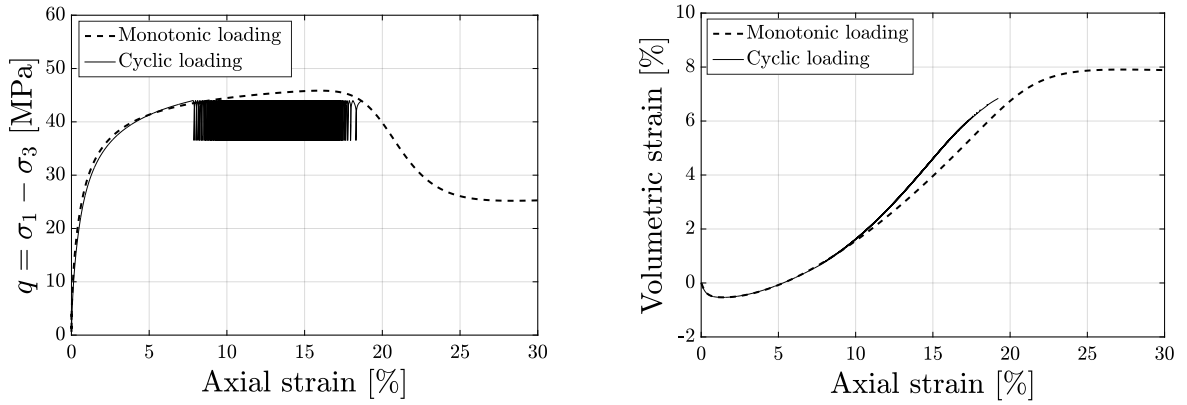

(a) (b)

Figure 5.24: In this example, the minimum applied stress shown in Fig.5.21 is increased. To accomplish this, the amplitude of each cycle reduces to 7.5 MPa with the frequency of 1×10^{-3} Hz. Therefore, in comparison to Fig.5.21, the minimum applied deviatoric stress increases to 36.5 MPa ; (a) The stress-strain curve for the cyclic loading is shown in this figure. The failure occurs after ca. 570 cycles. As the minimum applied stress increases the average stress applied to the sample increases as well. Therefore, the cyclic failure is experienced faster; (b) The development of volumetric strain is shown in this figure.

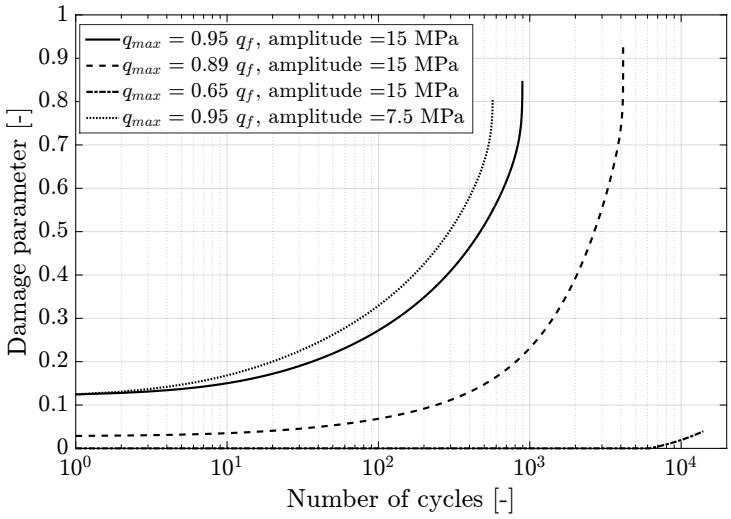

Figure 5.25: Damage evolution with respect to the number of cycles for the examples shown in Figs. 5.21 to 5.24. It is clear from this figure that as the maximum applied stress in cyclic loading decreases the damage evolution slows down significantly.

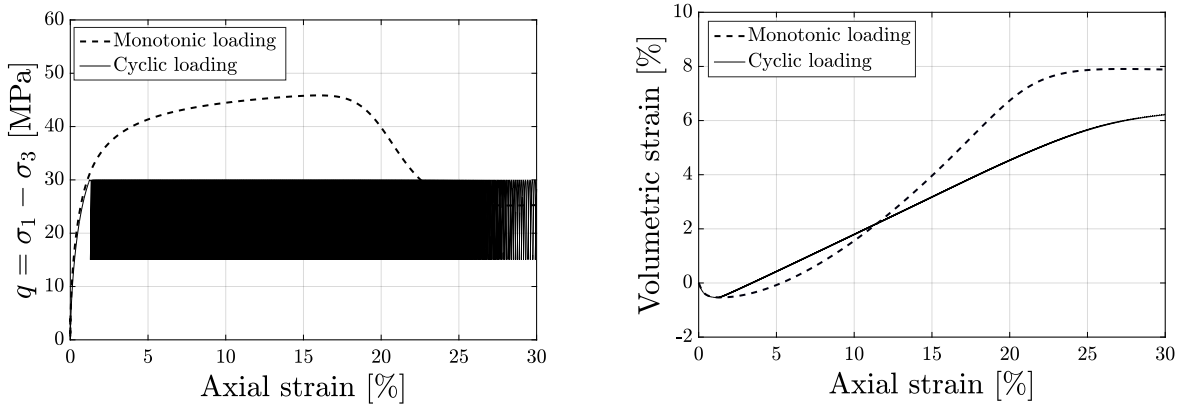

(a) (b)

Figure 5.26: In this example, the frequency of cycles for the example shown in Fig. 5.23 has been reduced to 1.38×10^{-5} Hz; (a) The stress-strain curve for the cyclic loading is shown in this figure. The cyclic failure occurs after ca. 1400 cycles. As the frequency of cycles reduces, the stress can remain for a longer time in the dilatancy zone. Therefore, more damage and dilatancy occur during each cycle. However, the axial strain at failure increases in this case, which is due to the increase of creep deformation; (b) The development of volumetric strain is shown in this figure. As seen, unlike the example shown in Fig. 5.23, the volumetric strain reaches to a critical value after ca. 1400 cycles.

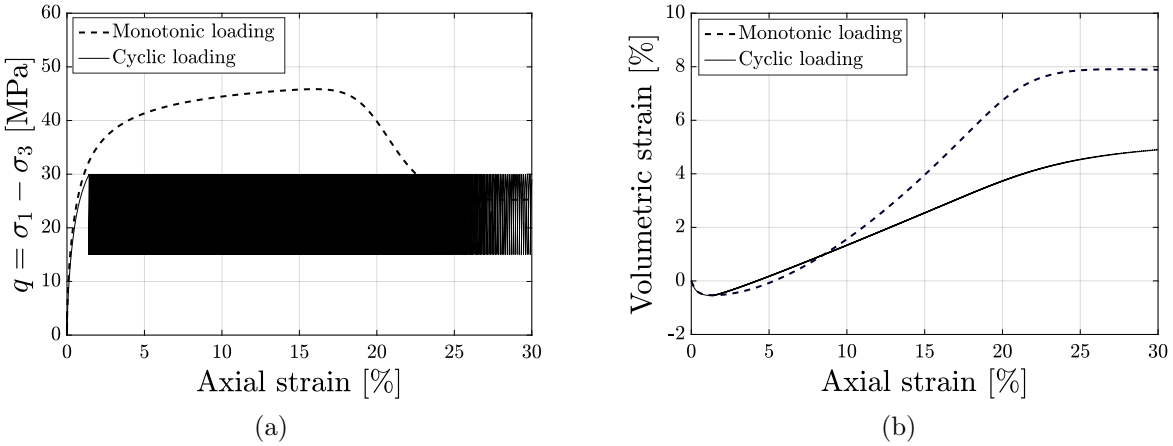

Figure 5.27: In this example, the applied temperature to the rock salt sample shown in Fig. 5.23 increases to 100 °C; (a) The stress-strain curve for the cyclic loading is shown in this figure. The cyclic failure occurs after ca. 950 cycles. As the temperature increases, the damage progress in the dilatancy zone becomes faster. Therefore, in comparison to Fig. 5.23, the cyclic failure is reached after a lower number of cycles. However, the axial strain at failure increases in this case, which is due to the increase of creep deformation; (b) The development of volumetric strain is shown in this figure. As seen, unlike the example shown in Fig. 5.23, the volumetric strain reaches to a critical value after ca. 950 cycles.

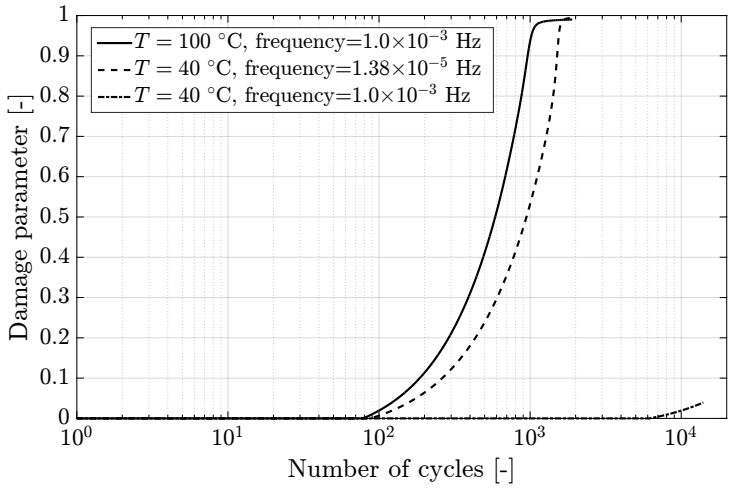

Figure 5.28: Damage evolution with respect to the number of cycles for the examples shown in Figs. 5.26 and 5.27. It is clear from this figure that by increasing temperature or decreasing the frequency of cycles the damage evolution accelerates.

5.5 Summary

The following items summarize the main issues given in this chapter:

- The BGRa model has three material parameters which should be determined using long-term creep tests. To accomplish this, the BGRa creep parameters were back calculated using a series of steady-state creep tests existing in literature performed on samples from Asse mine. The employed experimental data were obtained using different deviatoric stresses and different temperatures.

- The LUBBY2 model has seven parameters. The model takes into account both transient and steady-state deformations. Therefore, stepwise creep tests with different stress levels have been used to determine the model parameters.

- The material parameters related to the viscoplastic-creep-damage model explained in the previous chapter have to be determined from different types of laboratory experiments. In particular, monotonic triaxial compression and extension tests, long-term creep tests as well as cyclic loading tests are required for determining the material parameters of the model. The procedure to determine the required parameters was explained in this chapter. The obtained results show that the model can adequately describe many material responses observed in the experimental investigations. For example, the model can describe the volume dilatation, failure and post-failure in quasi-static strength tests for both compression and extension paths. The model can be also applied to model the transient, steady-state and tertiary creep under constant loading condition. The effect of temperature on the creep behavior can be also described by the model. In addition to this, the model can represent the material response of rock salt under cyclic loading. The strain accumulation during cyclic loading and the fatigue failure in dilatancy domain are the main features of the model in cyclic loading tests.

- A parametric study was carried out in this chapter to assess the performance of the viscoplastic-creep-damage model in different loading conditions. In addition to this, some of the key factors were introduced and their effects on the model response were qualitatively represented.

- As the confining pressure increases, the rock salt ductility increases as well. Under low confining pressures and high deviatoric stresses, rock salt behaves as a brittle material.

- The peak strength in quasi-static tests reduces by reducing the applied strain rate. In general, as the strain rate decreases the rock salt ductility increases. Therefore, for very small stain rates, the test becomes like a creep test with constant stress and no softening takes place.
- The effect of temperature on the model response in triaxial strength tests is similar to the strain rate. In general, as the temperature increases, the rock salt behavior becomes more ductile. That means, at higher temperatures, the inter-granular mechanisms that control the creep deformation take the dominating role. Under such condition, the damage evolution resulted from the opening of microcracks becomes slower. At higher temperatures, the deformation is more carried by the movement of disloations which is highly temperature dependent.
- As the applied deviatoric stress to the rock salt in creep tests reduces, the time to reach to the long-term failure increases. Finally, when the stress state lies below the dilatancy boundary, the rock salt exhibits only a steady-state deformation without any failure. That means, no tertiary creep occurs below the dilatancy boundary.
- Several factors may affect the rock salt behavior in cyclic loading tests. Maximum and minimum stresses, frequency of cycles and temperature are the most important factors.
- It is expected to experience the fatigue failure, when the maximum stress in cyclic loading lies in the dilatancy zone. As explained before, the constitutive model shows no cyclic failure if the maximum stress in cyclic loading is below the dilatancy boundary. Fatigue failure occurs when the strain energy exceeds a critical energy level equivalent to failure under non-cyclic load.
- The effect of temperature on cyclic behavior is similar to the creep behavior. By increasing the temperature, the material ductility increases. Therefore, more strain accumulation is observed within the cyclic loading.
- As the frequency of cycles reduces, more strain accumulates during the cyclic loading. Under such condition, the rock salt sample may experience failure at less number of cycles.

6 Introduction to the employed modeling techniques

6.1 Staggered thermo-mechanical modeling

During a CAES plant operation, the air injection and withdrawal produce temperature and pressure fluctuations within the storage cavern. The main objective in this section is to provide a solution for prediction of these fluctuations. This solution can be used in the numerical calculations as a tool to generate reasonable thermo-mechanical boundary conditions for the finite element model of salt cavern. Fig. 6.1 represents a staggered procedure to model the thermo-mechanical behavior of compressed air storage cavern. Based on this procedure, first, the air temperature and the air pressure inside the cavern are calculated by an analytical solution. The mathematical equations related to the applied analytical solution is explained in this section. Then, the calculated values are used as boundary conditions for the finite element model. The numerical example given in Section. 7.3 employs the staggered procedure to model the thermo-mechanical response of rock salt caverns.

6.1.1 Thermodynamics of the gas inside the cavern

The mass and energy transfer in a compressed air storage cavern are essentially complex processes. However, by applying simplification rules and with the aid of thermodynamic laws, the temperature and pressure variations inside the storage place can be predicted with an acceptable level of accuracy. In this section, an analytical solution suggested in Raju & Khaitan (2012); Kushnir et al. (2012); Xia et al. (2015) is used to obtain the temperature and pressure variations during the charge and discharge periods. To formulate the mathematical problem governing the temperature and pressure variations, the following assumptions have been made:

- As shown in Fig. 6.2, the cavern itself is considered as a control volume for the thermodynamic problem.

- The rock salt compressibility is quite small when it is compared to the gas compressibility, therefore cavern volume is assumed to remain constant in the analytical model Bérest et al. (2012). In other words, since the volume change of cavern is much smaller than the total volume, its effect on the air temperature and pressure variations are neglected. Therefore, to formulate the mass and energy balance equations, a constant volume V is assumed for the cavern. However, to enhance the quality of estimation in long-term evaluations and to improve the link between the analytical solution and the numerical model, the value of cavern volume V has to be updated at regular time intervals (e.g. monthly or yearly). Then, the updated value of cavern volume obtained from FEM simulation is substituted in the analytical solution to calculate the air temperature and pressure variations (see Fig. 6.1).

- The air flow during injection and withdrawal processes is turbulent. As a result, the air temperature and pressure gradients are quite small Bérest et al. (2011, 2013). For this reason, the air temperature T_a, pressure p_a and density ρ_a are assumed to be uniform throughout the storage space.

- The air properties of inflow and outflow such as temperatures (T_{in} and T_{out}), specific enthalpies (h_{in} and h_{out}) and mass flow rates ($\dot{m}_{in}$ and $\dot{m}_{out}$) are controlled by the CAES operator. Practically, depending on the electricity demand from power grid and the generated electricity by renewable energy sources as well as some technical considerations such as the capacity of compressor and gas turbine, the operating condition of cavern can be scheduled by the plant operators. Therefore, it is assumed that the air properties at the inlet and outlet of the cavern are known during the charge and discharge processes.

- The air is considered as an ideal gas. In the operating range of pressures and temperatures within the cavern, ideal gas assumption for air is nearly valid Raju & Khaitan (2012).

Taking the above-mentioned assumptions into account and employing the mass and energy conservation laws, the mathematical formulation of the air injection/withdrawal problem is obtained according to the following section. This section is mainly taken from Khaledi, Mahmoudi, Datcheva & Schanz (2016*a*).

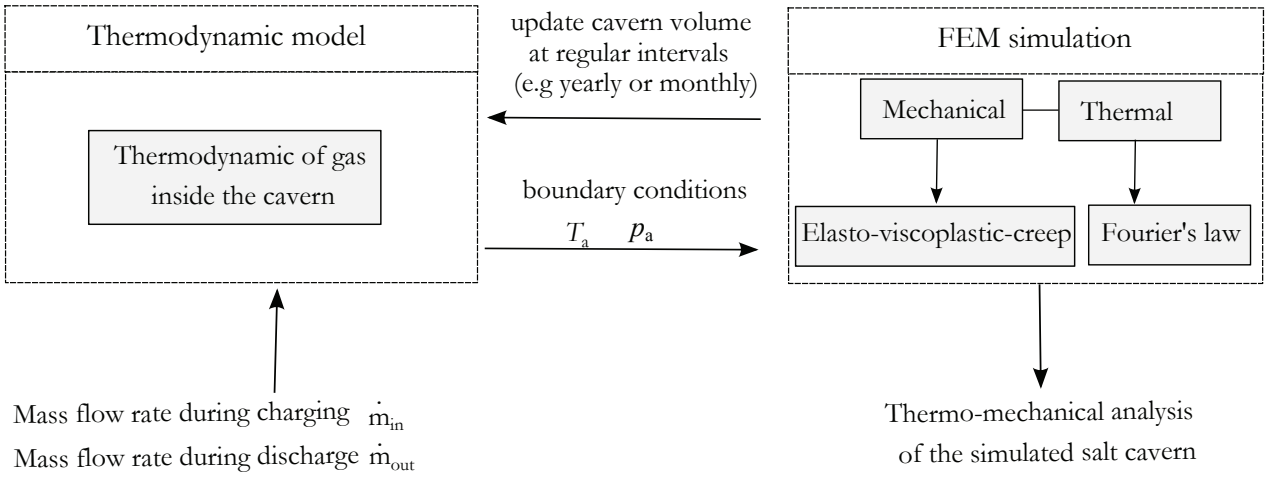

Figure 6.1: Schematic representation of the applied procedure to model the thermo-mechanical behavior of compressed air storage cavern

6.1.2 Mass and energy balance equations

Assuming a constant volume V for the cavern, the mass balance equation during the charge and discharge processes is written as :

$$V\dot{\rho}_a = \dot{m}_{in} - \dot{m}_{out}. \tag{6.1}$$

Here, $\dot{\rho}_a$ is the rate of density change for the air inside the cavern. In addition, $\dot{m}_{in}$ and $\dot{m}_{out}$ denote the mass flow rate over the charge and discharge time, respectively. These two quantities are dependent on the technical requirements of the plant (for example, maximum capacity of the compressor or the allowable inflow rate of the turbine) as well as the energy demand from the power grid. The cavern operators can adjust the properties of air inside the cavern within the desired range by controlling these two factors. Therefore, $\dot{m}_{in}$ and $\dot{m}_{out}$ are considered as known values in the heat and mass transfer simulation. On the other hand, the energy balance equation for the cavern is written as follows:

$$V\left(\dot{\rho}_a u_a + \rho_a \dot{u}_a\right) = \dot{m}_{in}h_{in} - \dot{m}_{out}h_{out} - h_c A_c(T_a - T_s). \tag{6.2}$$

Where subscripts *in* and *out* denote the properties of air at the inlet and outlet of the cavern during charge and discharge processes, receptively. u_a is the specific internal energy and h is the specific enthalpy of the air. The last term on the right hand side of the Eq. 6.2 represents the heat transfer between air and rock salt medium. h_c is the heat transfer coefficient between the cavern wall and the air and A_c is the heat transferring

area. Moreover, T_a and T_s represent the temperature of air inside the cavern and the temperature of surrounding rock, respectively. Assuming air as an ideal gas, the following equations can be used to calculate the pressure p_a, specific internal energy u and specific enthalpy of the air h.

$$p_a = \rho_a R T_a, \quad u_a = h - \frac{p_a}{\rho_a}, \quad \dot{h} = c_a \dot{T}_a. \tag{6.3}$$

R and c_a are the specific gas constant and the specific heat capacity of the air, respectively. Substituting the above-mentioned equations in Eq. 6.2 and using the mass balance equation shown in Eq. 6.1, the following ordinary differential equation is obtained to describe the air temperature variation. Having air properties at the inlet and outlet of the cavern, the equation below is solved for any time t. In this thesis, an implicit scheme is used to solve the following equation.

$$\begin{aligned} \rho_a (c_a - R)\dot{T}_a + \frac{\dot{m}_{in} c_a}{V}(T_a - T_{in}) \\ + \frac{R T_a}{V}(\dot{m}_{out} - \dot{m}_{in}) + \frac{h_c A_c}{V}(T_a - T_s) = 0. \end{aligned} \tag{6.4}$$

The heat transfer coefficient h_c and the heat transferring area A_c are the factors which can not be determined easily Raju & Khaitan (2012); Kushnir et al. (2012). As suggested in Raju & Khaitan (2012), the term $\frac{h_c A_c}{V}$ can be replaced by an effective heat transfer coefficient h_{eff} which is a function of air mass flow rate at the cavern inlet and outlet. The equation below is used to correlate the charge and discharge mass flow rates with the effective heat transfer coefficient.

$$h_{\text{eff}} = a_1 + a_2 \left| \dot{m}_{in} - \dot{m}_{out} \right|^{a_3}. \tag{6.5}$$

The parameters a_1, a_2 and a_3 are obtained by calibration with the in-situ measured test data.

6.1.3 Validation via two case studies

As represented in Fig. 6.1, the analytical thermodynamic model in this thesis is used as a tool to generate admissible thermo-mechanical boundary conditions for the finite element model of salt cavern. Here, the validity of the analytical model is examined by recalculating two examples given in Raju & Khaitan (2012) and Kushnir et al. (2012). In these examples, the measured in-situ data of Huntorf plant within 24 hours have been

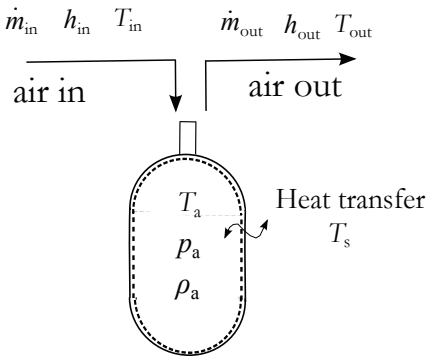

Figure 6.2: The control volume and the air properties at inlet and outlet during the charge and discharge processes

Table 6.1: Required data for the analytical simulation (Raju & Khaitan, 2012)

Temperature of rock salt medium T_s	323 K
Air temperature at the inlet T_{in}	323 K
Specific gas constant R	287 J/(kgK)
Specific heat, c_a	1006 J/(kgK)
Constant a_1 in Eq. 6.5	0.2356 W/(m^{3}K)
Constant a_2 in Eq. 6.5	0.0149 J/(s$^{(1-a_3)}$kg^{a_3}m^{3}K)
Constant a_3 in Eq. 6.5	0.8
Total storage volume V (for Huntorf)	300000 m^3

back calculated using the aforementioned equations. The Huntorf plant has been located in the north of Germany and recognized as the world's first CAES plant (Cortogino et al., 2001). Figs. 6.3a and 6.3b compare the calculated air temperature and pressure with the in-situ data given in Raju & Khaitan (2012). Table 6.1 provides the model parameters used in these simulations. Similarly, Figs. 6.3c and 6.3d show the air temperature and pressure obtained from analytical model in comparison to the in-situ data given in Kushnir et al. (2012). The air mass flow rate over the experiment time which is the input for the heat and mass transfer simulation is also shown in the figures. In general, during the charge period (i.e. positive mass flow rates), the air pressure inside the cavern rises up and the same time, the air temperature increases. While, over the discharge time (i.e. negative mass flow rates), the trend of pressure and temperature changes are reversed. However, as represented in Eq. 6.4, the rate and the magnitude of temperature and pressure changes are dependent on several factors such as the volume of the cavern, the inflow/outflow properties and the heat transfer between air and the rock mass. Applying the aforementioned assumptions, the model can adequately estimate the variation of air temperature and pressure inside the storage space. Therefore, in Section. 7.3, this model

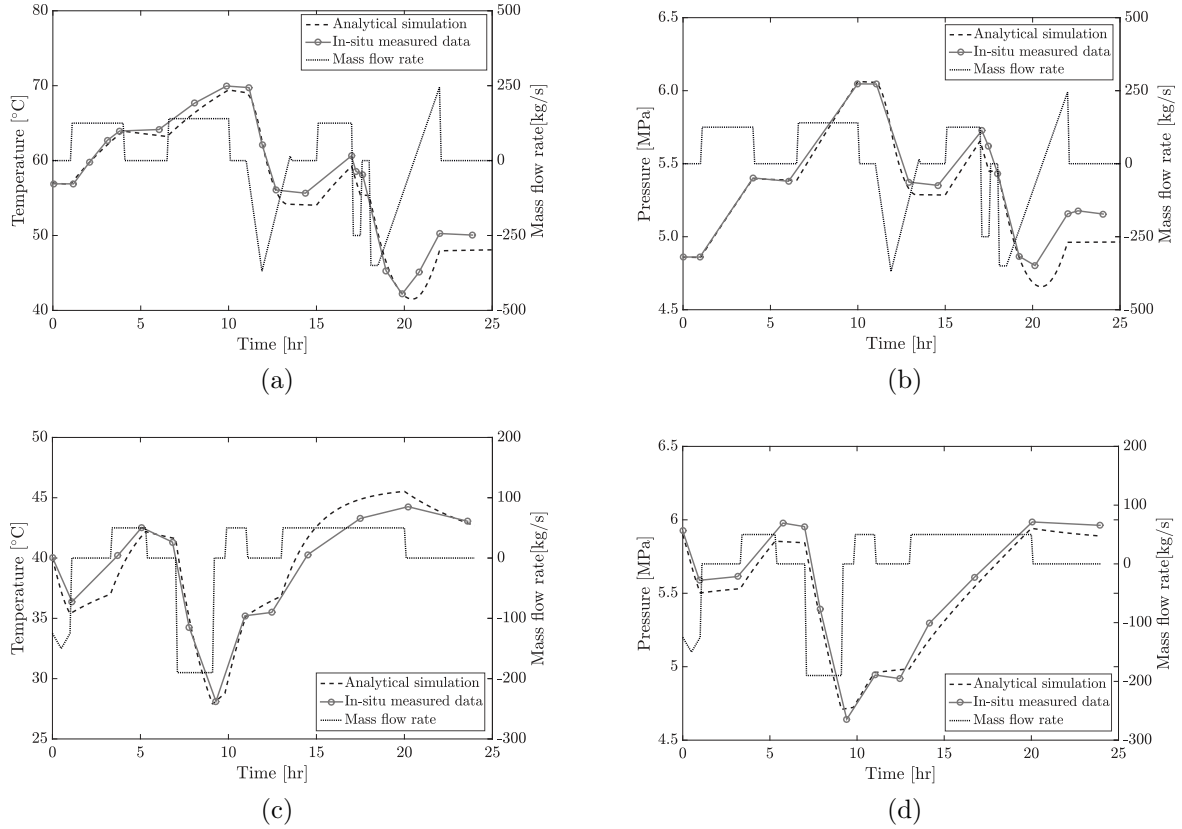

Figure 6.3: Comparison between in-situ measured data and the analytical simulation (a) temperature data from Raju & Khaitan (2012) (b) pressure data from Raju & Khaitan (2012) (c) temperature data from Kushnir et al. (2012) (d) pressure data from Kushnir et al. (2012)

is employed as a tool to generate the thermo-mechanical loads which should be applied as the boundary condition for the finite element model of salt cavern.

6.2 Model approximation using metamodeling technique

In design optimization, parameter identification or global sensitivity analysis, it is required to carry out repeated computations, where only a few number of model parameters are changed among those defining the problem of interest. These computations are normally performed by finite element method, which require in most cases considerable amount of time. This makes the repeated calculations computationally very expensive. In such cases, approximation models known as metamodels (or surrogate models) are used to reproduce the system behavior in a tremendously less time than that used by the numerical simulation methods. Fig. 6.4 is a schematic representation of the metamodeling process.

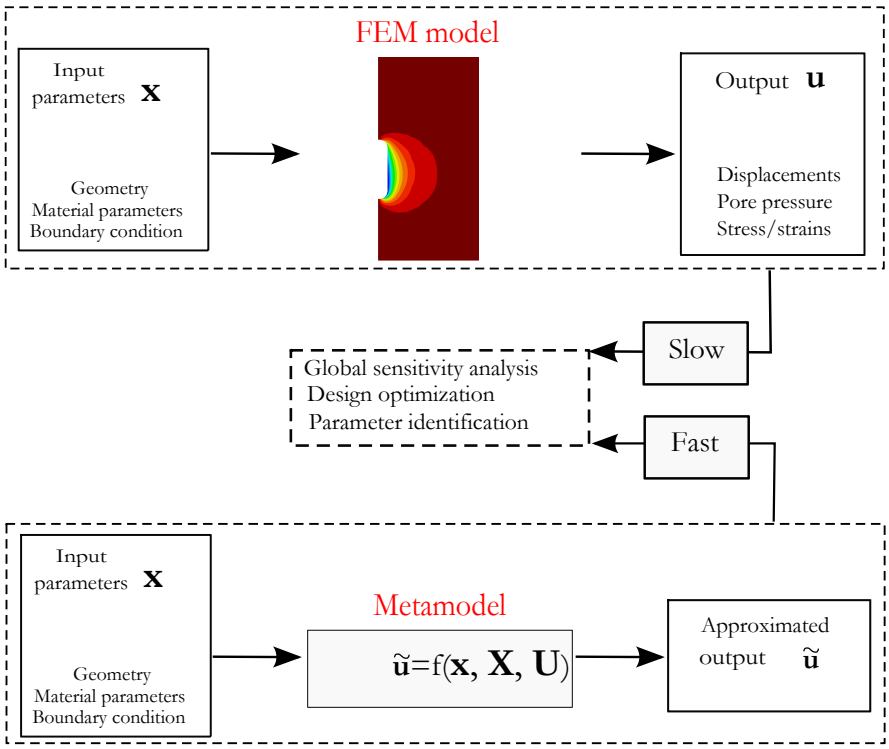

Figure 6.4: Schematic representation of the metamodeling process

From mathematical point of view, the main goal of metamodeling is to approximate the governing function which describes the behavior of an engineering problem Khaledi, Schanz & Miro (2014). The only available information is the input and output data in the form of some scattered samples like (**X**,**U**) obtained from physical or computational experiments. In order to construct a metamodel, two main components are required: (1) the input parameter matrix (**X**) which includes the s parameters of n_p sample points (2) the matrix of system responses or snapshot matrix (**U**) in which the n_p function values of m observation points are recorded. Therefore, **X** and **U** matrices are of size $s \times n_p$ and $m \times n_p$ respectively. Depending on the structure of **X** and **U**, several approximation techniques may be applicable. In this thesis, Proper Orthogonal Decomposition (POD) combined with Radial Basis Functions (RBF) proposed by Buljak (2010) is used to construct a reliable metamodel. Fig. 6.5 shows the flowchart of POD-RBF metamodel. The algorithm consists of two main parts: (1) proper orthogonal decomposition of the snapshot matrix; and (2) interpolation using radial basis functions. The basic idea of POD method is to

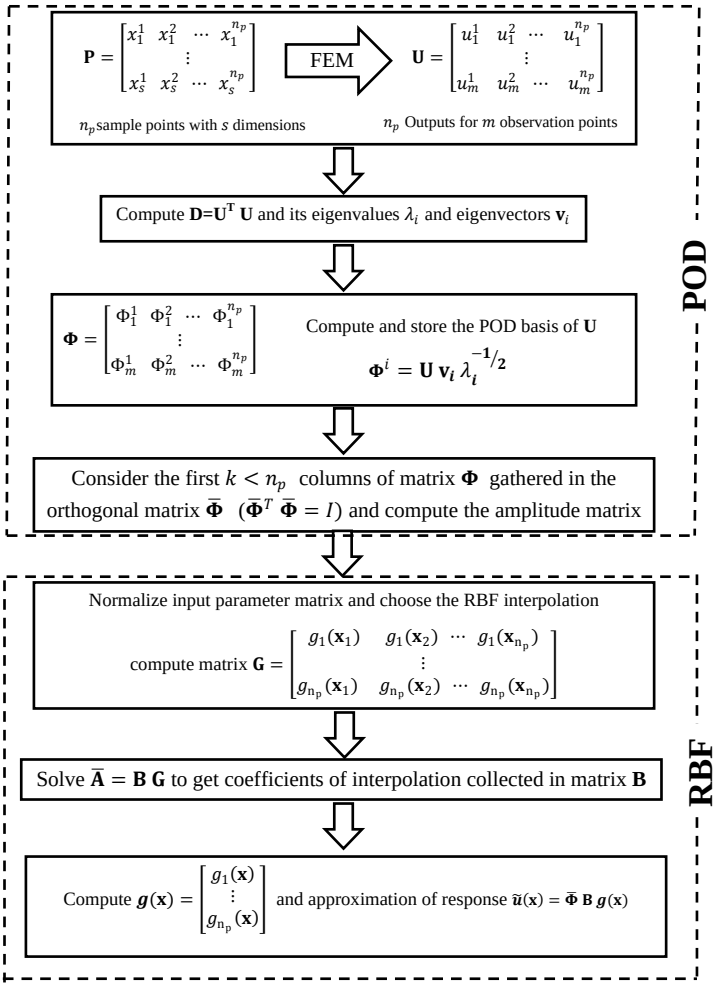

Figure 6.5: Flowchart of POD-RBF metamodeling process

present the snapshot matrix $\mathbf{U}$ as:

$$[\mathbf{U}]_{m\times n_p} = [\boldsymbol{\Phi}]_{m\times n_p}\,[\mathbf{A}]_{n_p\times n_p}\,, \tag{6.6}$$

here, $\mathbf{A}$ is the amplitude matrix and $\boldsymbol{\Phi}$ includes the proper orthogonal basis vectors. The POD basis vectors $\boldsymbol{\Phi}$ can be obtained by finding the normalized eigenvectors and eigenvalues of the symmetrical matrix $\mathbf{D} = \mathbf{U}^T\mathbf{U}$ (see Buljak (2010); Bolzon & Buljak (2011)). Since the matrix $\boldsymbol{\Phi}$ fulfills the orthogonality condition i.e. $\boldsymbol{\Phi}^T = \boldsymbol{\Phi}^{-1}$, the amplitude matrix is calculated as follows:

$$[\mathbf{A}]_{n_p\times n_p} = \left[\boldsymbol{\Phi}^T\right]_{n_p\times m}[\mathbf{U}]_{m\times n_p}\,. \tag{6.7}$$

The size of matrix $\mathbf{\Phi}$ can be reduced if the basis vectors corresponding to small eigenvalues are omitted. To accomplish this, first the basis vectors are sorted in a descending order according to the magnitude of their eigenvalues. Then, the first k columns of matrix $\mathbf{\Phi}$ are taken and the rest are removed ($k \leq n_p$). In this way, the reduced basis vectors $\overline{\mathbf{\Phi}}^T$ can be obtained. Subsequently, the reduced amplitude matrix $\overline{\mathbf{A}}$ is calculated as follows:

$$\left[\overline{\mathbf{A}}\right]_{k\times n_p} = \left[\overline{\mathbf{\Phi}}^T\right]_{k\times m} \left[\mathbf{U}\right]_{m\times n_p}. \tag{6.8}$$

The second step is to use a linear combination of radially symmetric functions in order to approximate the reduced amplitude matrix $\overline{\mathbf{A}}$. Having n_p sample points in the s dimensional space, each component of reduced amplitude matrix $\overline{\mathbf{A}}$ is computed by radial functions as follows:

$$\overline{a}_l^j = \sum_{i=1}^{n_p} b_l^i g_i(\mathbf{x}^j) \quad j = 1, \cdots, n_p \quad l = 1, \cdots, k, \tag{6.9}$$

where b_l^i are unknown coefficients and $g_i(\mathbf{x}^j)$ gives the value of the radial function g with the center point $\mathbf{x}^i$ at the sample point $\mathbf{x}^j$. In this study, inverse multiquadratic function is applied which has the form:

$$g_i(\mathbf{x}) = \left(\left\|\mathbf{x} - \mathbf{x}^i\right\|^2 + c^2\right)^{-0.5}, \tag{6.10}$$

where parameter c is a predefined constant which controls the smoothness of the radial basis function Khaledi, Miro, König & Schanz (2014). It is computationally of advantage to select this value within the $[0-1]$ range. Equation 6.9 provides $k \times n_p$ linear equations with $k \times n_p$ unknowns. This system of equations is solved to find the unknown coefficients.

$$\left[\overline{\mathbf{A}}\right]_{k\times n_p} = \left[\mathbf{B}\right]_{k\times n_p} \left[\mathbf{G}\right]_{n_p\times n_p} \quad \Longrightarrow \left[\mathbf{B}\right]_{k\times n_p} = \left[\overline{\mathbf{A}}\right]_{k\times n_p} \left[\mathbf{G}\right]^{-1}_{n_p\times n_p}, \tag{6.11}$$

here, matrix $\mathbf{G}$ gathers the values of radial functions at the sample points and matrix $\mathbf{B}$ includes the unknown coefficients. Finally, the equation below is used to find the function value at the observation point m for an arbitrary input point $\mathbf{x}$:

$$\left[\tilde{\boldsymbol{u}}\left(\mathbf{x}\right)\right]_{m\times 1} = \left[\overline{\mathbf{\Phi}}\right]_{m\times k} \left[\mathbf{B}\right]_{k\times n_p} \begin{bmatrix} \boldsymbol{g}_1\left(\mathbf{x}\right) \\ \vdots \\ \boldsymbol{g}_{n_p}\left(\mathbf{x}\right) \end{bmatrix}_{n_p\times 1} \tag{6.12}$$

6.3 Parameter identification technique

In general, the material parameters of the rock salt around the cavern are determined through the inverse analysis of experimental measurements. To accomplish this, the values of the constitutive parameters should be adjusted in the finite element model until the difference between the calculated results and the recorded measurements is minimized. The main goal of inverse analysis is to identify an optimum set of parameters for which the predicted responses at observation points are closest to the measurements. Mathematically, the identified parameters should minimize the following objective function:

$$f(\mathbf{x}) = \frac{\|\mathbf{u}^c(\mathbf{x}) - \mathbf{u}^m\|}{\|\mathbf{u}^m\|}, \tag{6.13}$$

where $\mathbf{u}^m$ is the vector of measurements and $\mathbf{u}^c$ is the vector of corresponding computed value obtained from the numerical simulation. The minimum of the objective function 6.13 can be found effectively through evolutionary algorithms like Genetic Algorithms(GA) or Particle Swarm Optimization(PSO) (see Khaledi, Miro, König & Schanz (2014); Meier et al. (2009, 2013); Knabe et al. (2012); Levasseur et al. (2008)). In this study, the genetic algorithm is chosen for solving the optimization problem. Genetic algorithms are inspired by Darwin's evolution theory. The algorithm is started with the initial set of parameter vectors called initial population which is randomly generated. Some of the population members (individuals) are selected and used to form a new population by applying crossover and mutation functions. The whole process is done with the scope that the new population will be better than the old one. Selection of parameter vectors is done according to their objective function (called fitness function). The more suitable the individuals are, the more chances they have to be selected and reproduced. This procedure is repeated until some criteria (for example number of generations or improvement of the best solution) are satisfied.

If the objective function is highly non-linear with a large number of input variables, a large number of evaluations of the objective function may be needed before the best set of parameters is identified. This high computation cost makes the algorithm of inverse analysis inefficient. Therefore, a practical solution is to replace the original finite element model by a metamodel explained in previous section. Therefore, computing the value of $\mathbf{u}^c$ directly from the metamodel reduces the computation time for solving the optimization problem. The flow chart shown in Fig. 6.6 describes the parameter identification procedure using the genetic algorithm combined with the metamodel Khaledi, Miro, König & Schanz

(2014). The numerical example given in Section. 7.1 illustrates both metamodeling and parameter identification techniques.

6.4 Global sensitivity analysis

The basic definition of sensitivity analysis is the study of how uncertainty in the output of a model can be apportioned to different sources of uncertainty in the model input Saltelli et al. (2008). Global sensitivity analysis explores the whole input parameter space, and therefore the information is independent of the model nature and is more reliable and comprehensive as a result Mahmoudi et al. (2016). In the following subsections, the applied global sensitivity methods in this study are presented.

6.4.1 Variance based method

The main idea of variance based method (VB) is to evaluate how the variance of inputs contributes into the variance of the model output. The S_i is the first order sensitivity measure which evaluates the sensitivity of model to input parameter x_i without considering the interaction between input parameters. The total effect sensitivity index S_{Ti} is a more comprehensive index which takes the interaction between parameters into account Saltelli et al. (2008).
The calculation procedure of the first order and total effect sensitivity indices has been presented by Saltelli et al. (2008). Firstly, two (n_p, s) matrices $\mathbf{A}$ and $\mathbf{B}$ which include random sets of parameters are generated. n_p is the number of samples and s is the number of input parameters. In this thesis, Latin Hypercube sampling method is used to generate uniformly distributed sample points. The sample points generated by this method appear to be random overall, but they are uniformly distributed if each dimension is viewed separately. Concerning the distribution type, three types of parameter distribution are possible, i.e. uniform, normal and log-normal. In general, there are differences between the uniform and the other two distributions. However, the difference between normal and log-normal is apparent only in case of input parameters with large coefficients of variations. For input parameters with coefficients of variation COV $< 20\%$, there is almost no difference. However, in this study the uniform distribution has been used and with the aid of metamodel, we are able to generate high number of samples inside the input parameter space. Therefore, almost the whole input parameter space is covered. Subsequently, another matrix $\mathbf{C}_i$ is produced with same arrays as $\mathbf{B}$, but its i^{th} column is

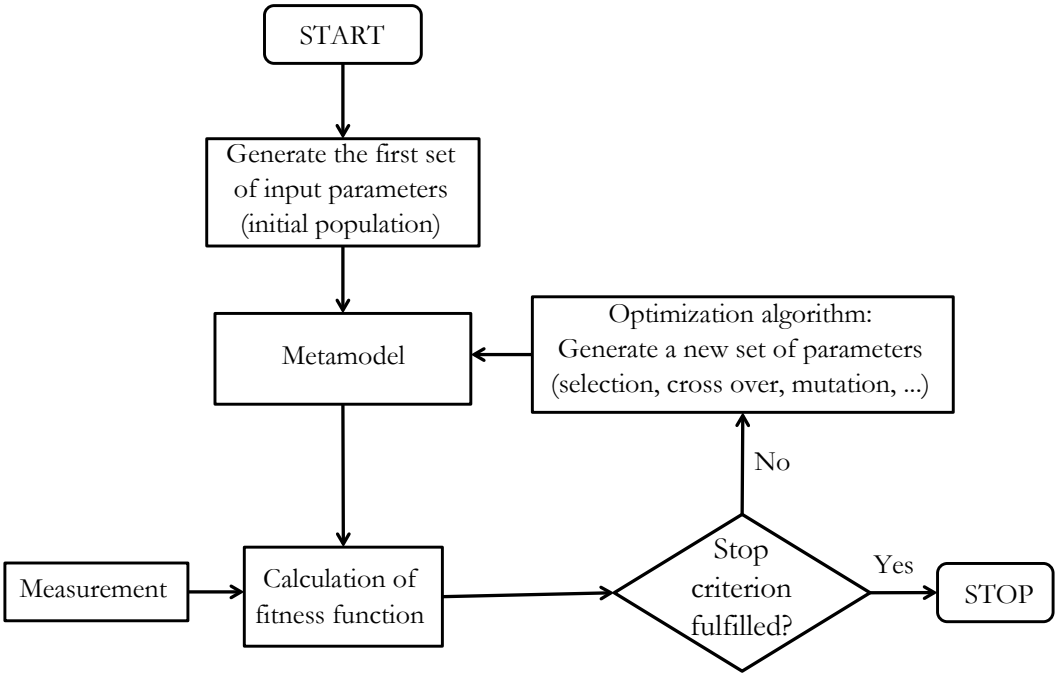

Figure 6.6: Flow chart of inverse analysis algorithm using metamodel

replaced by the i^{th} column of matrix $\mathbf{A}$. In the next step, the model outputs for all input values in the sample matrices $\mathbf{A}$, $\mathbf{B}$ and $\mathbf{C}_i$ are to be calculated. Finally, with equations (6.14) and (6.15) VB indices for each parameter are obtained.

$$S_i = \frac{(\mathbf{u}_\mathbf{A}^T \mathbf{u}_{\mathbf{C}_i}) - n_p(\overline{\mathbf{u}}_\mathbf{A})^2}{\mathbf{u}_\mathbf{A}^T \mathbf{u}_\mathbf{A} - n_p(\overline{\mathbf{u}}_\mathbf{A})^2}, \tag{6.14}$$

$$S_{Ti} = \frac{(\mathbf{u}_\mathbf{B} - \mathbf{u}_{\mathbf{C}_i})^T (\mathbf{u}_\mathbf{B} - \mathbf{u}_{\mathbf{C}_i})}{2\mathbf{u}_\mathbf{B}^T \mathbf{u}_\mathbf{B} - 2n_p(\overline{\mathbf{u}}_\mathbf{A})^2}, \tag{6.15}$$

here $\mathbf{u}_\mathbf{A}$, $\mathbf{u}_\mathbf{B}$ and $\mathbf{u}_{\mathbf{C}_i}$ are vectors containing model evaluations for matrices $\mathbf{A}$, $\mathbf{B}$ and $\mathbf{C}_i$ respectively. $\overline{\mathbf{u}}_\mathbf{A}$ and $\overline{\mathbf{u}}_\mathbf{B}$ are the mean value estimates for the components of $\mathbf{u}_\mathbf{A}$ and $\mathbf{u}_\mathbf{B}$.

6.4.2 Elementary effect method

The elementary effect method (EE) is an effective method to observe some important inputs among all input parameters of a model. For a model with $\mathbf{x} = (x_1, x_2, x_3, ..., x_s)$ normalized input parameters, the input space constructs a s-dimensional unit cube. This

unit cube, is discretized into a p-level grid, where p is an integer number. The elementary effect of the i^{th} input parameter in a certain point $\mathbf{x}$ is calculated using equation 6.16.

$$\text{EE}_i = \frac{\mathbf{u}(\mathbf{x} + \Delta e_i) - \mathbf{u}(\mathbf{x})}{\Delta}, \tag{6.16}$$

where, Δ is a value in $\{1/(p-1), ..., 1 - 1/(p-1)\}$ and e_i is a vector of 0 components but with 1 as i^{th} direction where $i = (1, 2, ..., s)$ and each e_i produces a different value for EE_i. In order to determine the overall influence of the i^{th} input parameter to the model output, the elementary effect of each parameter needs to be obtained for a number of sample points which are well distributed inside the input parameter space. In this thesis, Latin Hypercubic sampling method is used to generated n_p sample points within the s-dimensional input parameter space Miro et al. (2014). For each input parameter, n_p elementary effects are calculated using equation 6.16. Therefore, in total, $n_p(s+1)$ model evaluations are needed to be performed. The mean value of EE_i, μ_i^* estimates the overall influence of the i^{th} input parameter to the model output.

$$\mu_i^* = \frac{1}{n_p} \sum_{j=1}^{n_p} |\text{EE}_i^j|. \tag{6.17}$$

6.5 Summary

The following items summarize the main issues given in this chapter:

- The current chapter presents a staggered procedure to model the thermo-mechanical behavior of compressed air storage cavern. Based on this procedure, first, the air temperature and the air pressure inside the cavern are calculated by an analytical solution. The mathematical equations related to the applied analytical solution has been explained in this chapter. Then, the calculated values are used as boundary conditions for the finite element model. During a CAES plant operation, the air injection and withdrawal produce temperature and pressure fluctuations within the storage cavern. Therefore, it is needed to predict these fluctuations. The analytical solution employed in this study can be used in the numerical calculations as a tool to generate reasonable thermo-mechanical boundary conditions for the finite element model of salt cavern.

- In general, during the charging period of caverns (i.e. positive mass flow rates), the pressure inside the cavern rises up and the same time, the air temperature increases. While, over the discharge time (i.e. negative mass flow rates), the trend of pressure and temperature changes are reversed. However, the rate and the magnitude of temperature and pressure changes are dependent on several factors such as the volume of the cavern, the inflow/outflow properties and the heat transfer between air and the rock mass. For example, rapid discharge rates may result in very low temperature condition in caverns.
- Metamodeling technique has been used in this thesis as a tool to reduce the computation time in global sensitivity analysis and parameter identification. To accomplish this, approximation models obtained by POD-RBF technique are used to reproduce the system behavior in a tremendously less time than that used by the numerical forward models.
- In general, the material parameters of the rock salt around the cavern are determined through the inverse analysis of experimental measurements. To accomplish this, the values of the constitutive parameters should be adjusted in the finite element model until the difference between the calculated results and the recorded measurements is minimized. In this chapter, a parameter identification algorithm using the genetic algorithm combined with the metamodeling technique was presented.
- Global sensitivity analysis can be applied as a tool to explore the whole input parameter space and to identify the key parameters. It is also useful to assess the quality of numerical models.

7 Numerical simulation of gas storage caverns in rock salt formations

7.1 Example I: constant mechanical loading

This example has been presented in Khaledi, Mahmoudi, Datcheva, König & Schanz (2016). A typical salt cavern with a simplified geometry has been modeled using GID software Code-Bright (2010). GID is used as the pre-processor and post-processor of the Code–Bright finite element solver. Since the cavern has a cylindrical shape, only half of the geometry has been simulated. The axisymmetrical model with a height of 800 m and a width of 300 m is shown in Fig. 7.1. The cavern itself has a radius of 37.5 m and a height of 233 m and its top and bottom have the spherical form. The boundary and initial conditions are defined as follows:

$$\text{Boundary condition: } \begin{cases} \sigma_{yy} = \sigma_v \quad \text{at} \;\; y = H,\; 0 < x < L \\ \sigma_{xx} = \sigma_v + \rho g(H-y)/10^6 \quad \text{at} \;\; 0 < y < H,\; x = L \\ u_x = 0 \quad \text{at} \;\; 0 < y < H,\; x = 0 \\ u_y = 0 \quad \text{at} \;\; y = 0,\; 0 < x < L, \end{cases} \tag{7.1}$$

$$\text{Initial condition: } \begin{cases} \sigma_{xx} = \sigma_{yy} = \sigma_{zz} = \sigma_v + \rho g(H-y)/10^6 \quad \text{at} \;\; 0 < y < H, 0 < x < L \\ u_x = u_y = u_z = 0 \quad \text{at} \;\; 0 < y < H,\; 0 < x < L, \end{cases} \tag{7.2}$$

with $L = 300\ m$; $H = 800\ m$; $\sigma_v = 10$ MPa; $g = 10\ m/s^2$; $\rho = 2000\ kg/m^3$. It is assumed that the salt cavern is filled with pressurized gas with no leakage or discharge. Therefore,

the internal pressure of the cavern remains at a constant level of 7 MPa. The material parameters of rock salt and the bounds of unknown parameters are shown in Table 7.1.

7.1.1 Metamodel construction for the cavern

The output data at the observation points (snapshots) can be any physical quantity such as pressure, strain, temperature, displacement etc. In this numerical example, the horizontal displacement at the cavern's wall is the quantity that is read and recorded as the output (see point A in Fig. 7.1). This quantity is an important factor for designing caverns and it can be considered as a stability criterion. The following steps have been conducted to establish the POD-RBF metamodel for this example:

1. η_k, η_m and G_k are the essential material parameters of LUBBY2 model which have been selected as the input parameters of metamodel to describe the visco-elastic behavior of the rock salt. In the first step of metamodel construction, n_p different parameter sets have to be created inside the input parameter space. The lower and upper bounds of each parameter have been shown in Table 7.1. In this example, $n_p = 90$ has been selected to construct the metamodel. Thus, the size of input parameter matrix ($\mathbf{X}$) for this example is 3×90. The sample generation has been performed using Latin Hypercube method.

2. The finite element model is run for each parameter set within a predefined time scale. In each solver run, m output values (i.e. horizontal displacement of point A) corresponding to the predefined observation times are stored in the snapshot matrix ($\mathbf{U}$). Then The POD-RBF metamodeling technique is used to reduce the computation time for two applications; i.e. (1) sensitivity analysis and (2) parameter identification. Regarding sensitivity analysis, both short and long term behaviors of the cavern are important. The constructed metamodel for this case has 12 output values ($m = 12$) including 3 hourly observations (i.e. 4, 9 and 12 hours) and 9 daily observations (1, 3, 10, 15, 20, 30, 40, 50 and 60 days). While, for the parameter

Table 7.1: Material parameters for rock salt

Elasticity		LUBBY2 Model					
E (MPa)	ν	k_1(1/MPa)	k_2(1/MPa)	m(1/MPa)	η_k(MPa.d)	η_m(MPa.d)	G_k(MPa)
25000	0.3	-0.191	-0.168	-0.247	[4.6e4 - 1.1e5]	[5.8e6 - 2.9e7]	[3e5 - 6e5]

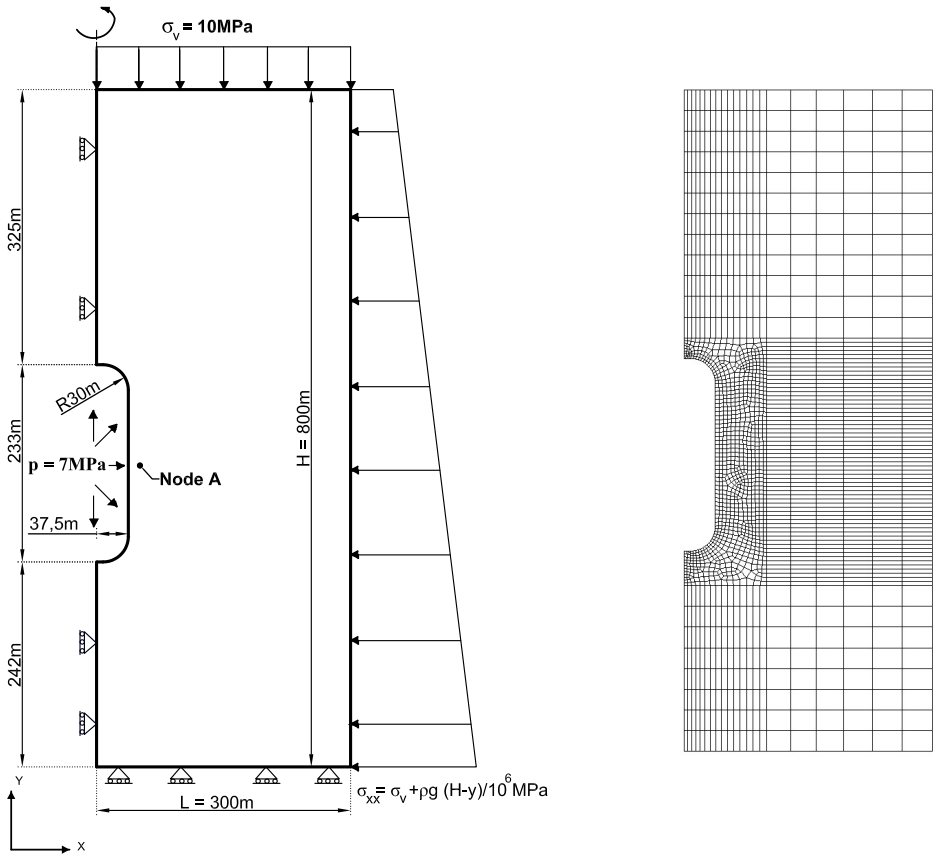

(a) (b)

Figure 7.1: Salt cavern model a) Geometry and boundary condition b)Finite element mesh of the model

identification, only the long term behavior of rock salt has been taken into account. In this case, the snapshot matrix ($\mathbf{U}$) has 100 columns ($m = 100$) and each column corresponds to the horizontal displacement of point A at the end of each day.

3. The input parameter matrix ($\mathbf{X}$) is normalized between 0 and 1 in order to avoid the potential scaling errors due to the disparate magnitudes of input parameters.

4. Having the input parameter and snapshot matrices the POD-RBF metamodel is constructed according to section 6.2.

Before proceeding to the next step, the accuracy of the constructed metamodel is to be evaluated. Therefore, 20 test points have been generated randomly inside the design domain. Then, the exact output value $\mathbf{u}$ (obtained from Code–Bright model) and the approximate value $\tilde{\mathbf{u}}$ (generated by metamodel) are computed for the test points and compared by the following standard accuracy measure NRMSE.

$$\text{NRMSE} = \left\{ \left(\sum_{i=1}^{20} \sum_{j=1}^{m} (u_j^i - \tilde{u}_j^i)^2 \right) / \left(\sum_{i=1}^{20} \sum_{j=1}^{m} (u_j^i)^2 \right) \right\}^{(1/2)} . \tag{7.3}$$

The obtained NRMSE for this case is equal to 0.0043 which demonstrates the accuracy of the constructed metamodel inside the selected design domain. The required time for one single evaluation of the FE cavern example by Code–Bright is 40 minutes. Thus, it takes about 60 hours to create 90 sample points and their corresponding snapshots. However, once the metamodel is created, the computation time decreases drastically. The time needed to obtain results from the metamodel is about one second which is much less than the computation time of the original model.

7.1.2 Sensitivity analysis of the numerical salt cavern

The main goal of this section is to investigate the effect of three selected material parameters on the horizontal displacement of cavern's wall during its operation. To achieve this goal, the constructed metamodel in section 7.1.1 is used and the sensitivity of numerical outputs to the input data are analyzed by EE and VB methods. Two variance based indices i.e. S_i, S_{Ti} and one elementary effect index μ^* calculated versus time of loading have been shown in Figs. 7.2, 7.3 and 7.4 respectively. As it can be seen, the sensitivity measures of mechanical behavior of salt cavern to various material parameters changes versus time. According to the results, the sensitivity indeces for the dashpot coefficients show monotonic behavior over time of the system operation. The Kelvin dashpot coefficient is most influential at the early time of the cavern creep. Its importance decreases monotonically and vanishes within the first day of the observation time period. Contrary, the the effect of the η_m increases monotonically and it becomes dominant very fast just only after 30% of the whole observation time period. The sensitivity of the model to the Kelvin spring coefficient G_k shows non monotonic pattern over time. G_k becomes dominant at the end of the first day of the cavern operation and its influence monotonically decreases after that. This implies that the transient creep is govern firstly but for a short time by the Kelvin dashpot, whereas the Kelvin spring term keeps important over longer time. Therefore, this parameter plays a significant role in long–term analysis of the cavern. In other words, more accurate value than other parameters is needed for this parameter.

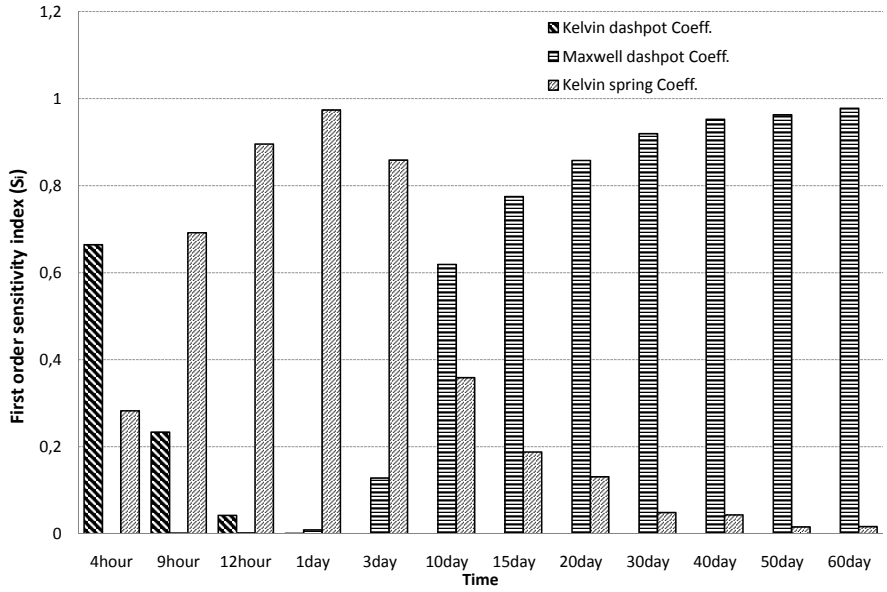

Figure 7.2: First order sensitivity index S_i versus time

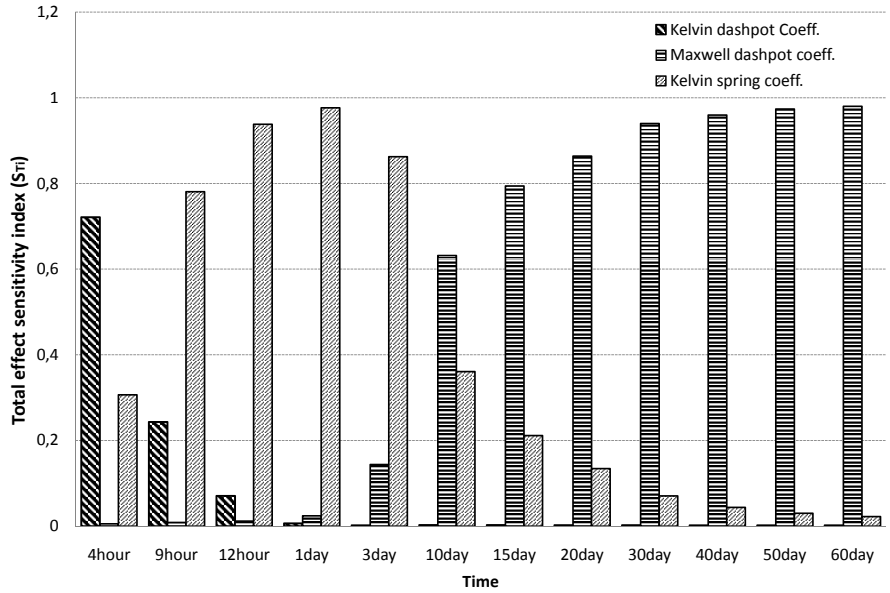

Figure 7.3: Total effect index S_{Ti} versus time

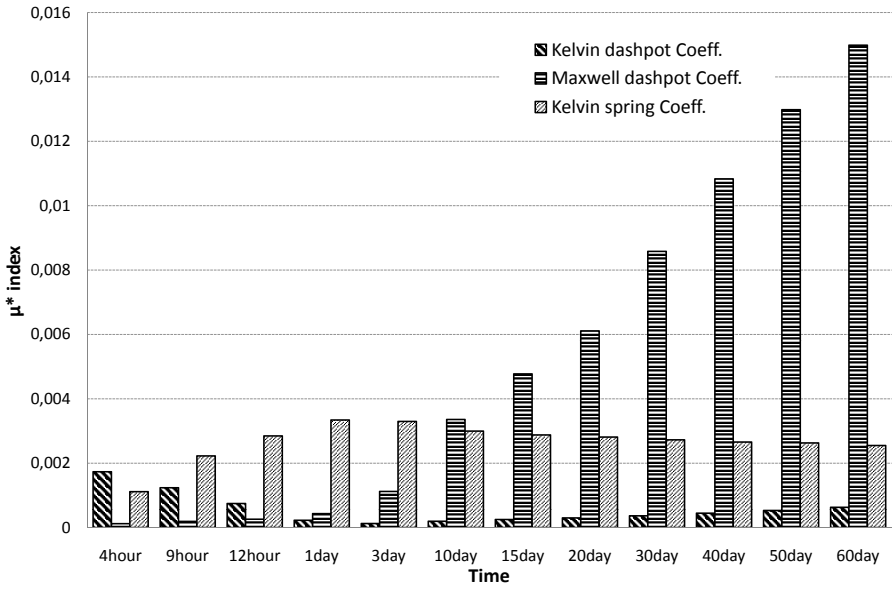

Figure 7.4: μ^* index versus time, $\mu*$ versus time (p=10)

7.1.3 Parameter identification for the salt cavern model

The main objective of this part is to obtain material parameters of LUBBY2 model by inverse analysis of synthetic data for the simulated salt cavern. The word "synthetic" is used here because the observation data are obtained from numerical simulations and not from field measurements. For this purpose, the horizontal displacement at the observation point A is calculated within 100 days by the FE solver using a set of predefined parameter values of LUBBY2 model. It is assumed that these calculated outputs correspond to the in-situ measurement data which can be used in the parameter identification algorithm shown in Fig. 6.6. However, the real measurement data which are obtained from the

Table 7.2: Pre-defined parameter set and the identified values by inverse analysis

Pre-defined parameters			Identified parameters		
η_k [MPa.d]	η_m [MPa.d]	G_k [MPa]	η_k [MPa.d]	η_m [MPa.d]	G_k [MPa]
8.9e4	7.89e6	5.97e5	7.3e4	8.3e6	5.3e5

field are always accompanied by some errors and uncertainties. Therefore, in order to consider the effects of the probable errors, the synthetic measurements are randomly varied within a certain range. The measurement errors are assumed to be ±2 mm in this example. Fig. 7.5 represents the generated synthetic data for the predefined parameter set shown in Table 7.2. After obtaining the synthetic measurements, the original model is replaced by the POD-RBF metamodel constructed in the previous section and parameter back calculation is performed according to the flowchart shown in Fig. 6.6. The global optimization toolbox available in MATLAB version 2012b, is used to perform the optimization process. For the 2D cavern model studied here, an average of 40 min is required on a standard PC for a single evaluation of the objective function. As shown in Table 7.3, the optimal values of LUBBY2 parameters have been found after 3000 evaluations of the objective function. These results could have been obtained after 84 days if the original FE model was employed, while with the aid of the metamodeling, the total time needed for parameter identification reduced to 60 hours. The identified parameter values are shown in Table 7.2. The main information from the performed sensitivity analysis that has to be accounted in the model parameter identification procedure is that η_k may not be reliably identified if the observation data do not include short time measurements (e.g. within the first day of the cavern operation). Sparse data before the first 10 days may yield poor prediction to G_k. Moreover, η_m is expected to be most reliably identified as its importance to the model response rapidly increases after the first few days of the considered time period. However, it is important to realize that including η_k as a parameter to be back-analyzed may also lead to non-unique solution of the posed optimization problem. The results presented in Table 2 confirm these conclusions as the difference between η_k to get the exact model data and η_k obtained via back analysis to noisy data is the highest (approx. 17%), whereas for G_k it is about 11% and for η_m only 5%. To visualize the accuracy of the identified parameters, they have been inserted into the FE model and the responses at the observation points have been compared with the original responses. Fig. 7.5 demonstrates the accuracy of the identified parameter values.

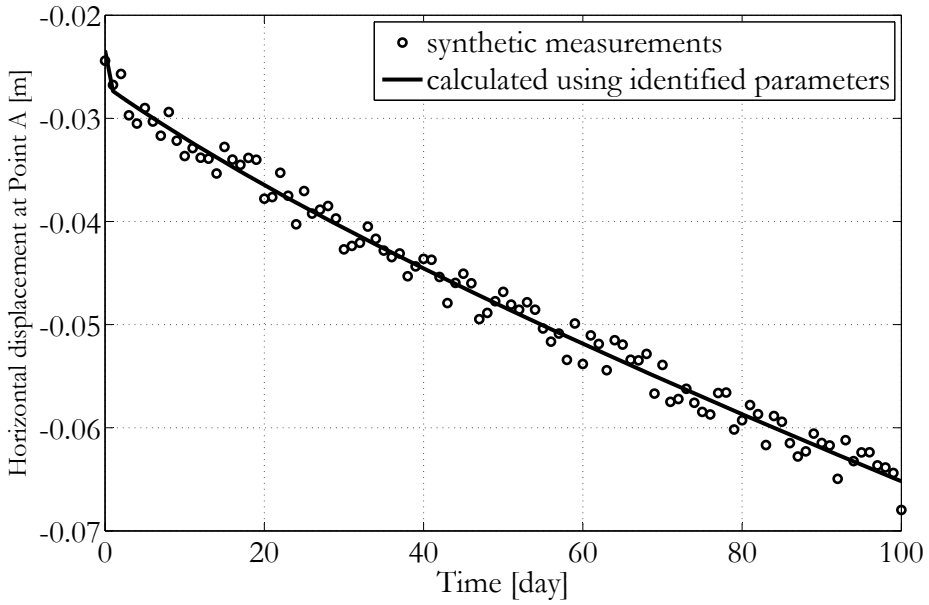

Figure 7.5: Obtained results by the constructed metamodel using the identified parameters in comparison with the synthetic measurements

Table 7.3: GA parameters and computation time for the test case

Cross over function	Two points
Population type	Double vector
Total evaluations	3000
Best fitness value	0.0263
Computation time	FEM solver: 84 days, Metamodel: 60 hours

Obtained sensitivity indices clearly demonstrate the importance level of each parameter in short/long term analysis. Inverse analysis of measurements has been carried out for a typical rock salt cavern to identify the material parameters of a visco-elastic model. To accomplish this, the error between the synthetic measurements and the calculated data has been minimized by a genetic algorithm combined with the metamodeling technique. The obtained results show that with the aid of accurate and efficient metamodeling method such as the combination POD-RBF, it is possible to obtain the solution of the optimization problem with a very small error in a significantly shorter time. In this way, solving computationally expensive problems such as parameter identification and sensitivity analysis becomes possible to tackle if the original model is replaced by a reliable and robust metamodel.

7.2 Example II: cyclic mechanical loading

This numerical example has been taken from Khaledi, Mahmoudi, Datcheva & Schanz (2016*b*). A typical salt cavern with a simplified geometry has been modeled using GID software. The axisymmetrical model with a height of 800 m and a width of 500 m is shown in Fig. 7.6a. The cavern itself has a diameter of 37.5 m and a height of 233 m and its top and bottom have the spherical form. On the upper model boundary a load of 10 MPa is applied which represents the overburden load at the top of the model. The vertical displacement at the model bottom is restrained. The density of compact rock salt is assumed to be $\rho_{salt} = 2000$ kg/m^3 and the numerical simulation is done at constant temperature $T = 318$ K. The initial stress at field is assumed to be isotropic (i.e. $\sigma_{xx} = \sigma_{yy} = \sigma_{zz}$). The boundary condition and finite element discretization of the model have been shown in Fig. 7.6a. The material parameters for Sonderhausen rock salt which have been shown in Table 7.4 are used in this section to describe the mechanical behavior of salt.
The following steps are performed to simulate the construction process and cyclic loading operation:

Initial phase: it is assumed, at time $t = 0$, no excavation has been performed. For this reason, a uniformly increasing load equal to the geostatic pressure is applied to the boundary of cavern. Since the initial stress state is isotropic, the principal stresses around the cavern before excavation are identical (see Fig. 7.7a).

Leaching phase: in order to model the leaching process, the applied load inside the cavern which is equal to the geostatic pressure is gradually reduced to the brine pressure (with $\rho_{brine} = 1100$ kg/m^3). This process has been performed in 9 excavation steps from bottom to the top of the cavern. The duration of each step is assumed to be 160 days. That means the whole cavern is excavated after 4 years (see Fig. 7.7b).

Debrining phase: in this example, the debrining phase has been modeled in 9 steps from top to the bottom of the cavern. In each step, the brine pressure is replaced by the gas pressure which is equal to the weight of brine column from ground surface to the current brine level (see Fig. 7.7c). Thus, when the pressure of injected gas is equal to the brine pressure at the bottom of cavern, the whole brine is ejected. In this numerical example, each debrining step takes 20 days and the whole process is carried out within 6 months.

First filling phase: in this phase, the pressure inside the cavern reduces to the minimum pressure of the cavern. It is assumed that the pressure reduction is carried out within 5 days.

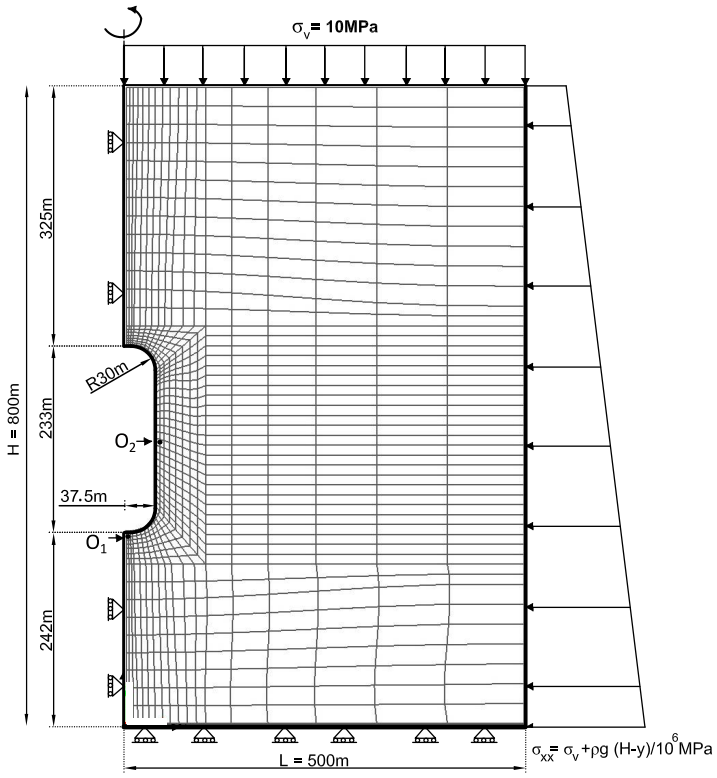

(a)

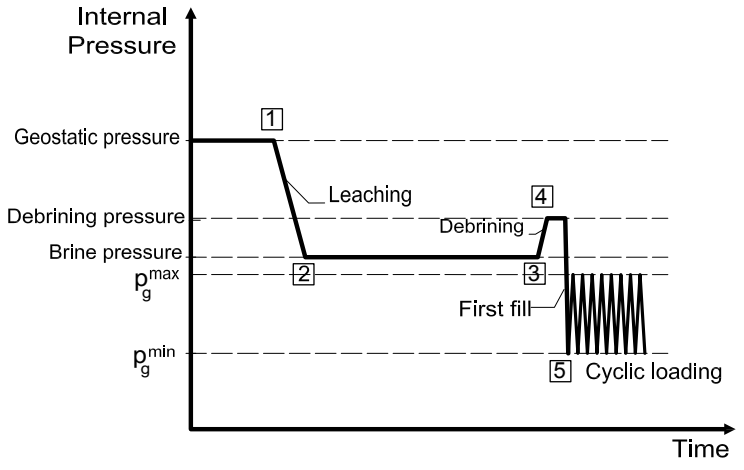

(b)

Figure 7.6: (a) Geometry, boundary conditions, finite element discretization of the salt cavern model as well as the location of observation points O_1 and O_2 (b) changing of internal pressure of the cavern during leaching phase, debrining process, first filling and cyclic operation

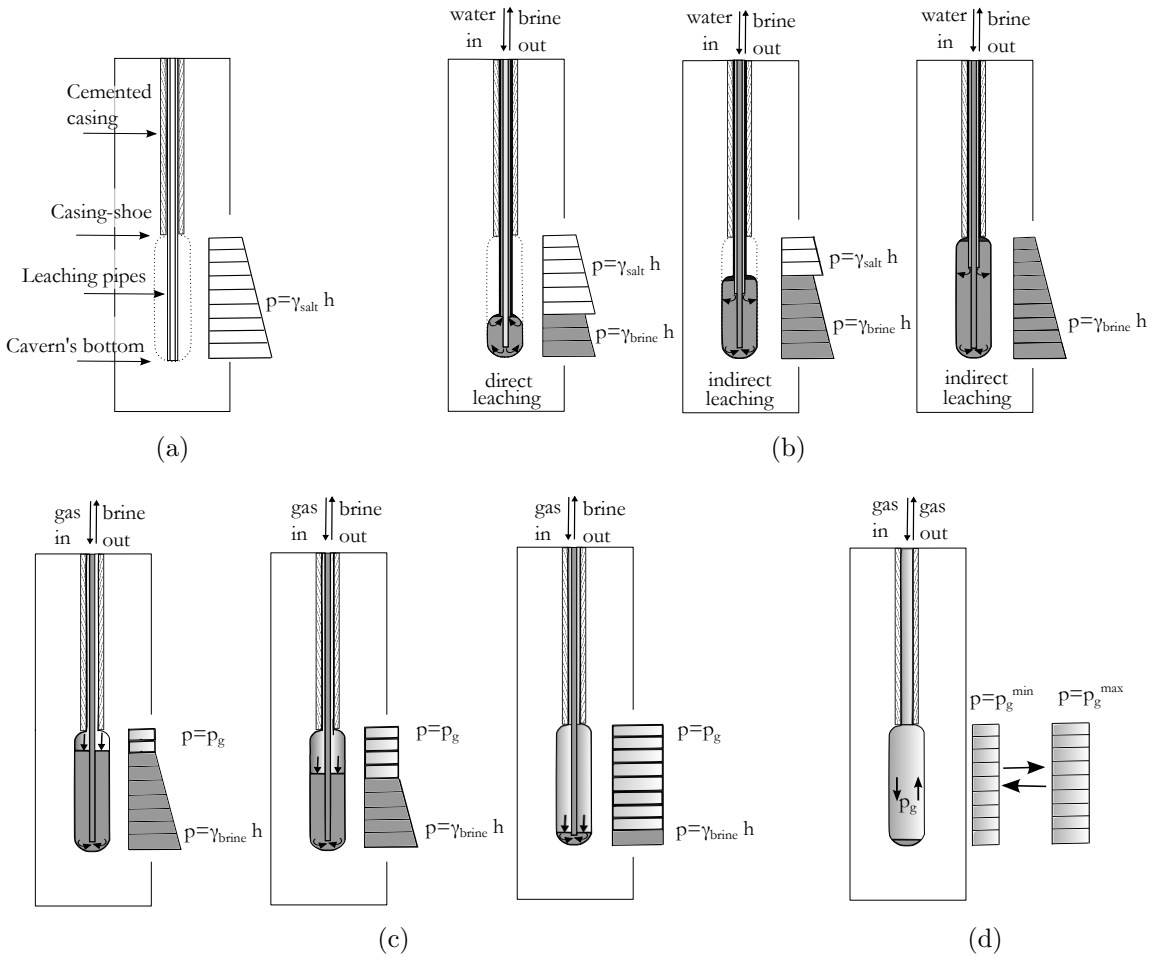

Figure 7.7: Schematic representation of salt cavern excavation process (a) initial phase, no cavern exists, geostatic condition (b) leaching phase, rock salt is excavated using solution mining technique (c) debrinning phase, brine is extracted by injecting the storage product i.e. compressed air or hydrogen (d) first filling and cyclic loading operation, the internal pressure of the cavern fluctuates within a predefined range

Cyclic loading phase: to model the cyclic operating condition, the internal pressure of the cavern fluctuates within a predefined range (see Fig. 7.7d). Furthermore, it is assumed that the pressure variations during the charge and discharge of the cavern are linear.
In this numerical example, two loading scenarios have been defined for the cyclic loading operation. In the first loading scenario, the internal pressure fluctuates between 7 to 12 MPa, while, in the second scenario the pressure varies between 3 and 8 MPa. The duration of each cycle is assumed to be 1 day and 100 loading cycles are simulated. Fig. 7.6a shows two observation points located at the bottom of the cavern (O_1) and the cavern wall (O_2). These points are used in the next section in order to evaluate the mechanical behavior of rock salt at the boundary of the cavern. Fig. 7.6b describes schematically the loading pattern which has been defined to simulate the cavern excavation process as well as its cyclic loading operation.

7.2.1 Results and discussion

The main objective in this section is to investigate how the mechanical behavior of salt cavern changes with respect to the internal gas pressure. In the following, the stress paths at the observation points O_1 and O_2 are investigated over the performance life of the cavern. In addition, the stability and serviceability of the simulated cavern with respect to the internal pressure will be discussed.

7.2.2 Stress paths around the cavern

As discussed in Section. 6.1.1, the dilatancy and failure boundaries are functions of the Lode's angle θ. In order to compare the stress paths of different points around the cavern independent of Lode's angle, all stress points are mapped to the $\theta = 60°$ plane. To accomplish this, the second invariant of deviatoric stress (J_2) is scaled using the equation below:

$$\text{scaled } J_2 = J_2 \frac{F^{dil}(I_1, 60°)}{F^{dil}(I_1, \theta)}. \tag{7.4}$$

Where $F^{dil}(I_1, 60°)$ and $F^{dil}(I_1, \theta)$ indicate the distance of dilatancy boundary from hydrostatic axis in π-plane for $\theta = 60°$ and the current Lode's angle θ, respectively. Figs. 7.8a–7.8d show the stress path of observation points O_1 and O_2 in the ($I_1 -$ scaled $\sqrt{J_2}$) plane. Also depicted in these figures are the dilatancy and failure boundaries as well as the initial

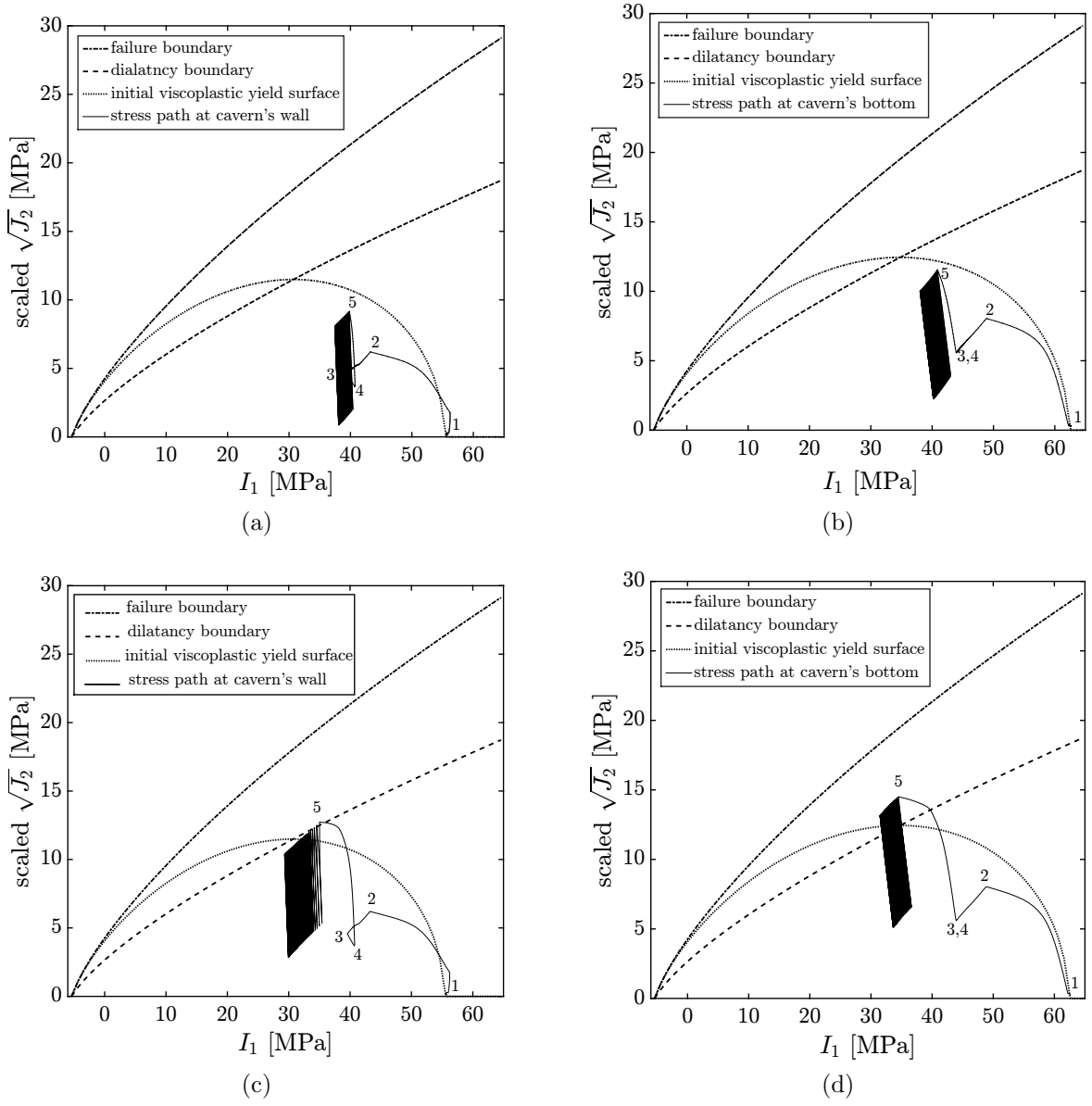

Figure 7.8: Stress path in $I_1 - \text{scaled}\sqrt{J_2}$ plane (a) at the cavern wall (O_2) for $p_g^{min} = 7$, $p_g^{max} = 12$ (b) at the bottom of the cavern (O_1) for $p_g^{min} = 7$, $p_g^{max} = 12$ (c) at the cavern wall (O_2) for $p_g^{min} = 3$, $p_g^{max} = 8$ (d) at the bottom of the cavern (O_1) for $p_g^{min} = 3$, $p_g^{max} = 8$

1→ isotropic stress state and beginning of leaching
1→2 leaching process reaches to the observation point
2→3 leaching process continues until the end of solution mining
3→4 debrining phase
4→5 first filling phase
5→ beginning of cyclic loading

viscoplastic yield surface obtained from initial stress conditions. In addition, the stress states at the beginning of each phase have been marked in these figures with numbers 1 to 5. As explained before, during the leaching process, the geostatic pressure applied to the boundary of cavern is replaced by the brine pressure. Due to this pressure reduction, the value of I_1 reduces, while J_2 increases. Subsequently, the stress at the point which is leached out moves from state (1) located on the hydrostatic axis to the state (2) located inside the initial viscoplastic yield surface. Then, the solution mining process continues until the whole cavern is excavated. The state (3) shows the stress condition at the end of solution-mining process. As it is observed, due to the stress relaxation occurring in the course of cavern excavation, the stress state (3) is lower than the stress state (2). Since the stress paths throughout the leaching phase are inside the initial viscoplastic yield surface, the viscoplastic component of the total strain becomes zero and only an elastic deformation combined with a steady-state creep deformation take place. In the next step, by replacing the brine pressure with the gas pressure during the debrining phase, the stress state slightly changes from (3) to (4). From stress state (4) to (5), the internal pressure of cavern reduces rapidly to the minimum defined pressure. This process is performed within a few days, therefore the creep strain is negligible and depending on the pressure reduction level the following cases may encountered:

When the internal pressure reduces to 7 MPa, the stress states at the observation points remain inside the initial viscoplastic yield surface (see Figs 7.8a and 7.8b). Therefore, only elastic deformation takes place during the first filling phase. On the other hand, the stress states of both observation points are still below the dilatancy line. Therefore, no damage progress is experienced. During the cyclic loading phase, a steady-state creep deformation without any volumetric strain is added to the elastic part of strain.

In the second scenario with minimum internal pressure of 3 MPa, the observation points exhibit different stress conditions. For the cavern wall, the stress point goes beyond the initial viscoplastic yield surface and an elasto-viscoplastic deformation happens. However, because the cyclic loading is still performed inside the compressibility domain, damage parameter does not grow up. Regarding the observation point O_1 located at the bottom of the cavern, the stress state is beyond both the dilatancy boundary and the initial viscoplastic yield surface. In this case, an elaso-viscoplastic-creep deformation combined with damage is observed.

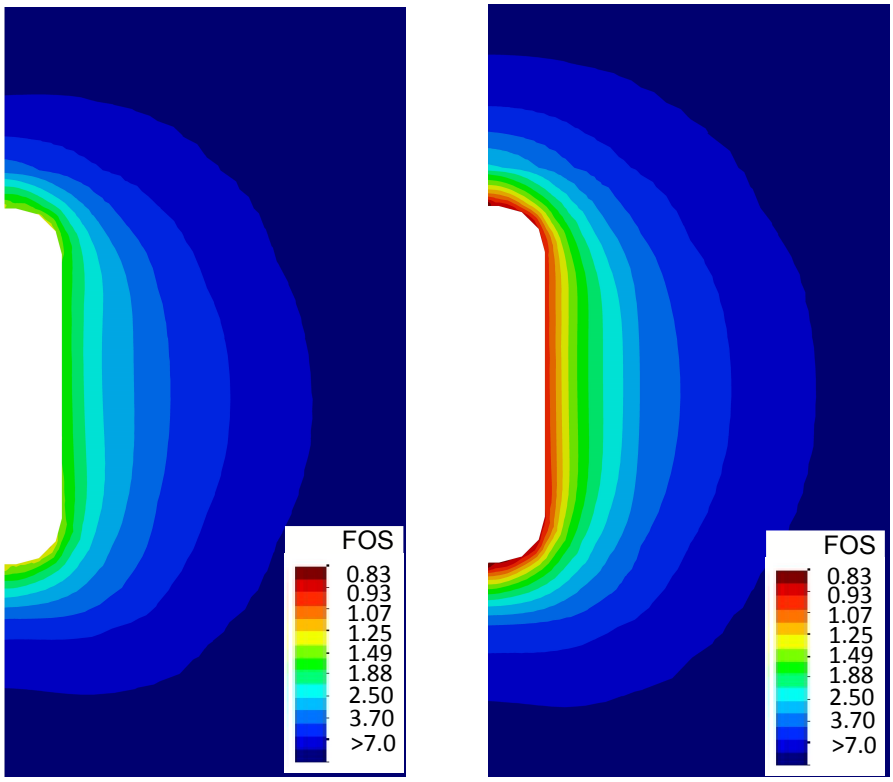

(a) (b)

Figure 7.9: Contour plot of factor of safety (FOS) at the end of first filling phase for (a) $p_g^{min} = 7$, $p_g^{max} = 12$ (b) $p_g^{min} = 3$, $p_g^{max} = 8$

7.2.3 Factor of safety of the cavern

As explained in the previous section, the mechanical behavior of rock salt shows significant changes when dilatancy occurs. Therefore, all design factors of cavern including geometry and boundary conditions should be defined in a way that stresses remain below the dilatancy boundary. For this reason, the quantity below is defined which determines the factor of safety of the cavern.

$$\mathrm{FOS} = \frac{\sqrt{F^{dil}(I_1, \theta)}}{\sqrt{J_2}}. \tag{7.5}$$

When FOS > 1, the stresses are inside the compressibility domain and cavern works under safe operating conditions. Opening of micro-cracks does not occur in this domain and subsequently, damage does not progress. In contrary, when FOS ≤ 1, the operating condition of the cavern is not safe and cavern may experience long-time failure due to the damage progress. The FOS criterion is identical to the Utilization Criterion (UC) which

was introduced in Section. 2.4.3.1. In the numerical example presented in this section, the maximum pressure reduction is experienced at the end of first filling phase. Therefore, the FOS value at this time step is used to quantify the allowable minimum pressure of the cavern. Fig. 7.9 compares the FOS values around the cavern for the defined loading scenarios. The contour plot of FOS clearly shows that all the points around the cavern remain in the safe range for the first loading scenario ($p_g^{min} = 7$ MPa). While, in the second loading scenario, the internal pressure reduces to 3 MPa and all the points located at the boundary of the cavern experience the FOS value of one or less than one. In this case, the smallest value of FOS is observed at the bottom of the cavern where the highest deviatoric stress J_2 and the lowest dilatancy boundary $F^{dil}(I_1, \theta)$ exist. As a result, by decreasing the internal pressure of the cavern, the FOS value reduces. The minimum allowable pressure identified for this numerical example is slightly more that 5 MPa. Applying pressures higher than this value, keeps the stress state of all the points around the cavern below the dilatancy boundary and ensures the safe operating condition for the cavern.

7.2.4 Long-term failure due to the damage progress

In this section, the long-term failure ratio (LFR) introduced by Cristescu in Cristescu & Gioda (1994) is used to evaluate the micro-cracking and damage propagation around the cavern. The LFR is defined as the ratio of released volumetric inelastic work per unit volume (w_{vol}) due to dilatancy of rock salt, to the failure strain energy (w_f), such that:

$$\text{LFR} = \frac{w_{vol}}{w_f} \tag{7.6}$$

Both w_{vol} and w_f have been already defined in Section. 3.4.3. When the LFR value becomes greater than zero, damage and micro-cracking start to grow up in the material body. If during the cyclic loading, the stress state goes beyond the dilatancy boundary, the energy is released and damage propagation becomes more significant. In case the value of released volumetric strain work per unit volume (w_{vol}) due to micro-cracking reaches to the threshold value w_f, fatigue failure is encountered. Therefore, the underground cavern is stable as long as the parameter LFR is smaller than one. As shown in the previous section, the stress state at the bottom of cavern goes beyond the dilatancy boundary for the case with minimum internal pressure of 3 MPa. Therefore, for this loading scenario, only the bottom of the cavern is affected by the damage. Fig. 7.10 shows the LFR

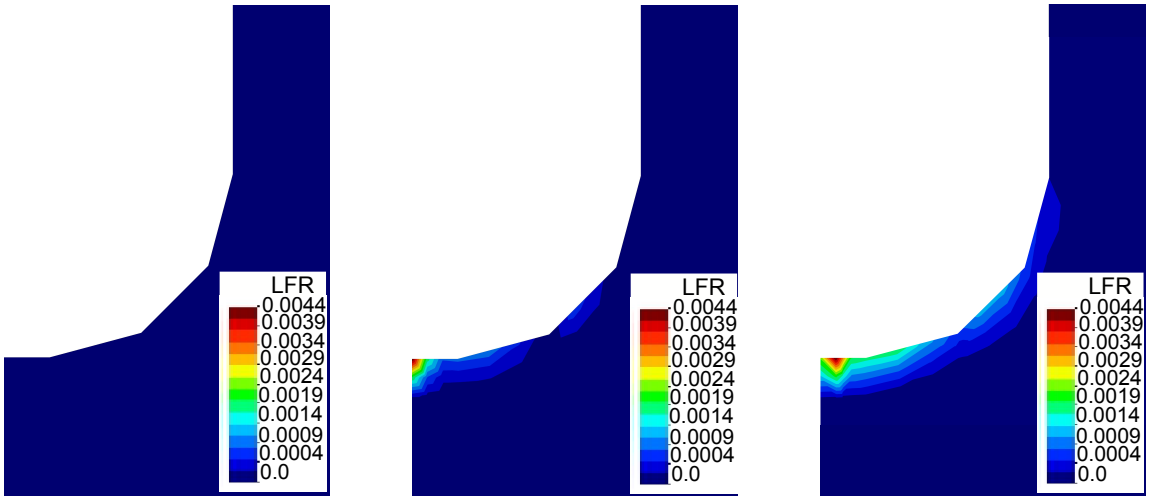

(a) (b) (c)

Figure 7.10: Contour plot of long-term failure ratio (LFR) for (a) $p_g^{min} = 7$, $p_g^{max} = 12$, after 100 cycles (b) $p_g^{min} = 3$, $p_g^{max} = 8$, at the end of first filling phase (c) $p_g^{min} = 3$, $p_g^{max} = 8$, after 100 cycles

value at the bottom of the cavern for the defined loading scenarios. As it is seen, in the first loading scenario, all the points at the bottom of the cavern remain undamaged. In contrary, in the second loading case, damage appears first in the lowest point of the cavern then it propagates to other neighbor points during cyclic loading phase. As a result, it is expected to encounter the fatigue failure at the bottom of the cavern due to the damage propagation when the number of cycles increases.

7.2.5 Serviceability of the cavern

The objective here is to investigate the serviceability of the simulated cavern with respect to the applied internal pressure. For this reason, the volume loss of the cavern (VL) during the cyclic loading phase is calculated using the following equation:

$$\mathrm{VL} = \frac{V_0 - V_n}{V_0} \times 100, \tag{7.7}$$

here, V_0 and V_n are the initial defined volume and the volume after n loading cycles, respectively. Fig. 7.11a compares the VL values obtained for the defined loading scenarios in this section. It is seen that the rate of volume convergence increases significantly when the minimum internal pressure reduces. As the volume decreases, the storage capacity of the cavern reduces, and this may affect the serviceability of the whole storage system.

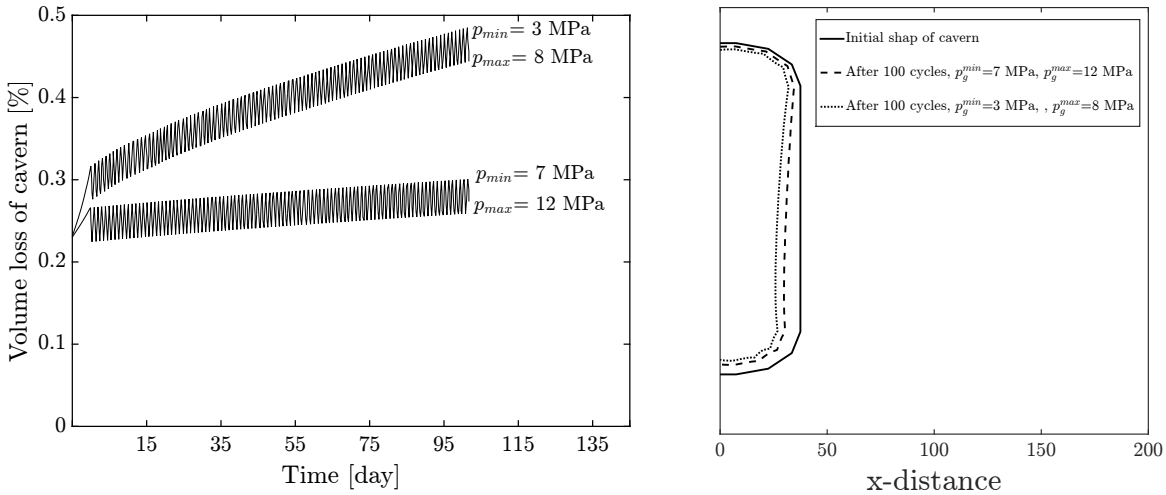

(a) (b)

Figure 7.11: (a) Volume loss of the cavern (VL) for the two loading scenarios (b) the effect of internal pressure on the shape of the cavern after 100 cycles (displacements have been scaled with a factor of 100)

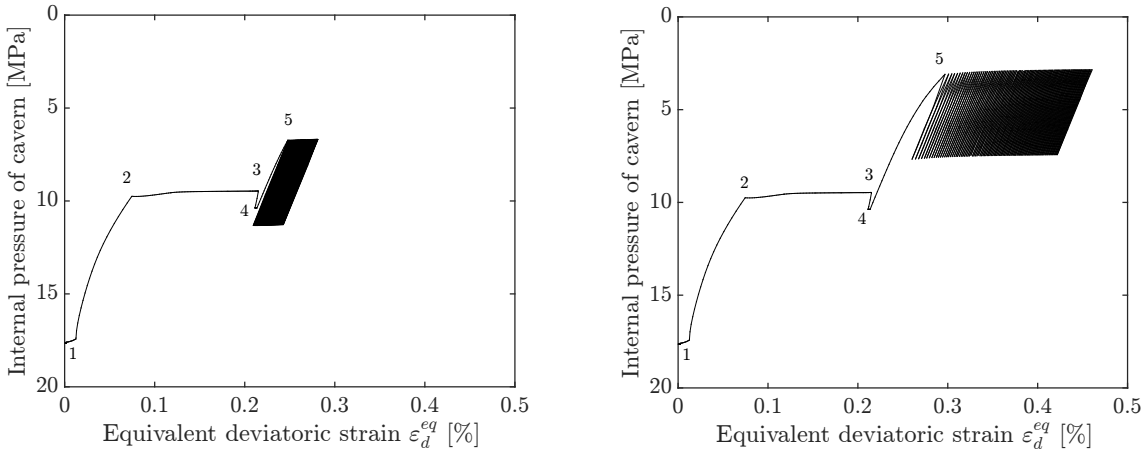

(a) (b)

Figure 7.12: The equivalent deviatoric strain, i.e. $\varepsilon_d^{\mathrm{eq}} = \sqrt{\frac{2}{3}\boldsymbol{\varepsilon}^{\mathrm{dev}} : \boldsymbol{\varepsilon}^{\mathrm{dev}}}$, at the cavern wall ($O_2$) versus the internal pressure of the cavern for (a) $p_g^{min} = 7$, $p_g^{max} = 12$ (b) $p_g^{min} = 3$, $p_g^{max} = 8$
1→ isotropic stress state and beginning of leaching
1→2 leaching process reaches to the observation point
2→3 leaching process continues until the end of solution mining
3→4 debrining phase
4→5 first filling phase
5→ beginning of cyclic loading

The closure of the cavern for the two cases is shown in Fig. 7.11b. The effect of internal pressure on the cavern's performance can be also explained by checking the strains at the boundary of cavern. Fig. 7.12 shows how the mechanical behavior of rock salt during the cyclic loading phase changes when the internal pressure of the cavern reduces. As it can be seen from Fig. 7.12a, for the first loading scenario, the equivalent deviatoric strain at the cavern wall (defined as $\varepsilon_d^{\mathrm{eq}} = \sqrt{\frac{2}{3}\boldsymbol{\varepsilon}^{\mathrm{dev}} : \boldsymbol{\varepsilon}^{\mathrm{dev}}}$) accumulates slowly in a small range. while, for the second loading scenario, the strain accumulation is more significant.

7.2.6 Permeability changes around the cavern

The low permeability of rock salt is an important factor to guarantee the safety and tightness of the caverns. Generally, rock salt in undisturbed state has extremely low permeability, usually less than $10^{-20}\ m^2$ based on laboratory measurements Peach (1991). Volume increase of rock salt in dilatancy domain is expected to increase the permeability because of the new porosity created during the micro-cracking process. Therefore, for caverns which are working under cyclic loading conditions, implementing safe operating pressures is one of the requirements to avoid rock salt dilation and subsequently, to satisfy the stability and tightness of the cavern. Numerous experimental investigations have been conducted during the past decades in order to describe the permeability changes of rock salt (e.g. see Schulze et al. (2001); Peach (1991); Pfeifle et al. (1998); Popp et al. (2001); Alkan (2009)). In this example, the model proposed by Peach in Peach (1991) is used to characterize the permeability changes around the cavern. According to this model, the permeability is related to the dilatant volumetric strain through a power function as follows:

$$k = a\varepsilon_{vol}^{b}, \tag{7.8}$$

where a and b are model parameters. The suggested values for a and b by Peach are 2.13×10^{-8} and 3, respectively. Fig. 7.13 demonstrates the gas permeability changes around the cavern for the defined loading scenarios. As it is seen, for the first loading scenario, the rock medium remains almost impermeable. Regarding the second loading scenario, it can be observed that the highest values of permeability are located at the top and bottom of the cavern where the stress state is fairly inside the dilatancy domain. It should be noted that the permeability increase around the cavern roof may endanger the tightness of the cavern near the casing-shoe and lead to the unfavorable leakage of gas.

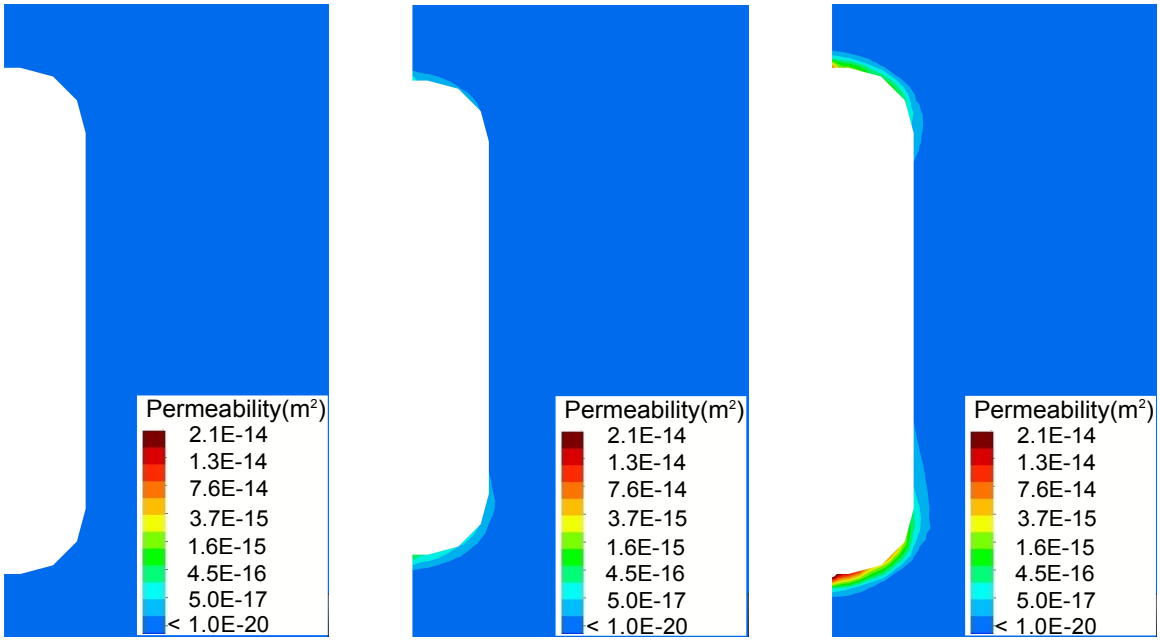

(a) (b) (c)

Figure 7.13: Contour plot of permeability around the cavern for (a) $p_g^{min} = 7$, $p_g^{max} = 12$, after 100 cycles (b) $p_g^{min} = 3$, $p_g^{max} = 8$, at the end of first filling phase (c) $p_g^{min} = 3$, $p_g^{max} = 8$, after 100 cycles

7.3 Example III: cyclic thermo-mechanical loading

This numerical example has been taken from Khaledi, Mahmoudi, Datcheva & Schanz (2016*a*). To investigate the effect of thermo-mechanical cyclic loading on the behavior of salt cavern, a finite element model has been built using GID software. In this section, the real data of Huntorf CAES plant is adopted to define the dimensions and working conditions of the model. In Huntorf plant, the compressed air is stored in two relatively identical storage caverns (i.e. in terms of dimension, depth and storage capacity). The total storage capacity of the plant is about 300000 m^3. However, to efficiently model the geometry of the cavern, some simplifications are required. In this study, only one of the caverns is selected for the simulation. The real geometry of the selected cavern as well as the simplified model are shown in Fig. 7.14a. As seen, the cavern has been idealized as a half cylinder with a radius of 18 m and a height of 150 m. The top and bottom of the cavern have the semi-spherical form. The axisymmetrical model with the height and width of 500 m is shown in Fig. 7.14a as well. With this assumptions, the storage volume of the simulated cavern is about 150000 m^3. On the upper boundary of the model, a load of 10 MPa is applied which represents the overburden load at the top

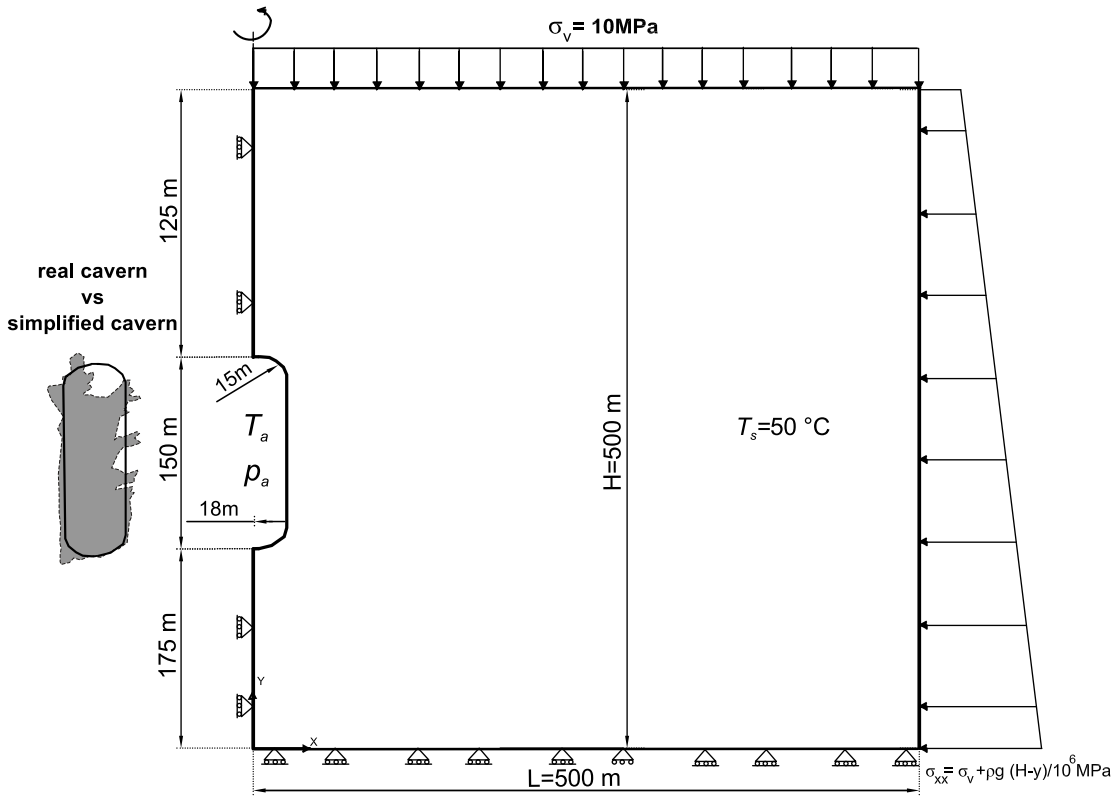

(a)

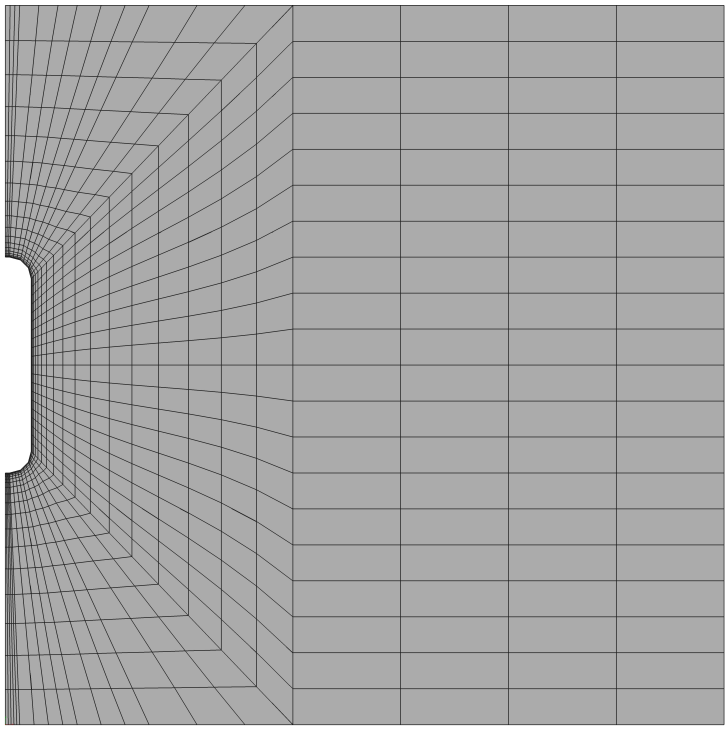

(b)

Figure 7.14: (a) Geometry and boundary conditions of the model b) finite element discretization of the salt cavern model

Table 7.4: Material parameters of rock salt for numerical example III

Elastic parameters	K [MPa]	18115
	G [MPa]	9842
Viscoplastic parameters	μ_1 $[day^{-1}]$	5.06e-7
	N_1	3
	n	3
	a_1 [MPa^{2-n}]	0.00005
	η	0.7
	β_1 [MPa^{-1}]	4.8e-3
	β	0.995
	m	-0.5
	γ	0.11
	F_0 [MPa^2]	1
	R_s [MPa]	5.4
Creep parameters	μ_0 (day^{-1})	0.27
	Q_c [kJ/mol]	-54000
	N_2	4.0
Thermal properties	k_s [W/mK]	5.3
	α_s [1/°C]	1e-5
	c_s [J/kgK]	985
	ρ_s [kg/m^3]	2000

of the model. The vertical displacement at the model bottom is restrained. The finite element discretization of the model is shown in Fig. 7.14b. The material parameters for rock salt have been shown in Table 7.4. The following steps are performed to simulate the construction process and cyclic loading operation of the salt cavern:

- The initial stress state is considered to be isotropic (i.e. $\sigma_{xx} = \sigma_{yy} = \sigma_{zz}$). Therefore, at the beginning of the simulation, a load which is represents the geostatic pressure is applied to the boundary of the cavern. According to Serbin et al. (2015), the initial rock mass temperature changes linearly with depth with a temperature gradient of 0.03 °C/m. Since the height of the modeled cavern is 150 m, this temperature gradient leads to a temperature difference of 4.5 °C at the top and bottom of the cavern. For the sake of simplicity, this temperature difference is neglected and the temperature at the lowest point of the cavern has been selected as the initial temperature for the entire rock mass. The lowest point of the Huntorf cavern is located around 820 m below ground level Cortogino et al. (2001). Taking into account a ground surface temperature equal to 25 °C, the initial temperature of the rock salt is obtained as 50 °C.

- In order to model the excavation process, the applied mechanical loads to the inner boundary of cavern are gradually reduced to the minimum air pressure (in this example: 4.7 MPa). Assuming a leaching rate of 35 m^3/h and considering the time needed for debrining phase Tryller & Musso (2006), the whole construction period takes approximately 230 days. Additionally, the temperature of the inner boundary is reduced to 35 °C in this phase. This temperature reduction is due to the heat transfer between brine and the rock medium during the leaching process.

- In the next step, the thermo-mechanical cyclic loads resulted from the charge and discharge processes are simulated. It is assumed that, during the first 100 cycles, the cavern works under the normal operating conditions reported in (Cortogino et al., 2001). The mass flow rate during the charging period is 108 kg/s (air flow rate of the compressor), while the discharge rate is equal to 417 kg/s (air consumption of the turbine). According to (Cortogino et al., 2001), the charge and discharge time of the cavern are 8 and 2 hours, respectively. Therefore, this simulation phase takes about 41 days (i.e. days: 230–271). Having the mass flow rates and the charge and discharge durations, the pressure and temperature variations are obtained using the analytical solution given in Section. 6.1.1. The obtained results from the heat and mass transfer simulation show that the air pressure fluctuates between 4.7 MPa and 7.2 MPa, while, the temperature ranges between 30-70 °C.

- After the first 100 cycle, two extreme loading conditions are defined and applied to the boundary of the cavern for another 100 cycles. The time duration of this simulation step is about 41 days (i.e. days: 271–312). The extreme loading scenarios are as follows:

  Scenario 1, low pressure working condition: The range of cyclic pressure drops down to 2.2-4.7 MPa. With this pressure reduction, the temperature cycles are obtained in the range 10-80 °C. (see Fig. 7.15)

  Scenario 2, high temperature working condition: According to the Huntorf plant data, the temperature of injected air to the cavern (T_{in}) is equal to approximately 50 °C during the normal operating condition. The inflow temperature T_{in} is controlled by the CAES operators via an after-cooler (as explained in Section. 1.1). In this scenario, the inflow temperature is set to 150 °C to investigate the consequences of having high temperature air inside the cavern. This scenario may occur if an after-cooler with lower heat transfer capacity is used. By increasing the in-

flow temperature, the temperature inside the cavern rises up and varies between 55-110 °C. While the cyclic pressure slightly increases to 5-8 MPa.(see Fig. 7.15).

It should be noted that the considered time span for this numerical example is relatively a short period in comparison to the cavern's operating life (for example, 30 years). However, the main aim of the numerical example is to demonstrate the unfavorable consequences of extreme loading conditions such as dilatancy, damage progress, tensile stress or cavern closure. In other words, even for the considered relatively short operation time, the obtained results up to 312 days can clearly show the changing trend of stability and serviceability factors.

7.3.1 Results and discussion

The main objective in this section is to assess the performance of the simulated salt cavern under the influence of defined extreme loading conditions. In the following, the temperature distribution around the cavern as well as the changes in mechanical stability and serviceability of the cavern are discussed.

7.3.2 Temperature around the cavern

Because of the temperature difference between the cavern's inner boundary and the surroundings, the thermal energy is transferred through the rock salt medium by conduction. Because of this reason, the temperature distribution changes in the vicinity of the cavern. During the injection process the temperature of air inside the cavern increases. When the air temperature is higher than the surrounding rock, heat is transferred from the air to the rock. Therefore, the temperature of the surrounding rock salt rises up. Over the discharge time, because of the reverse heat transfer from the rock to the air, the rock salt temperature reduces. Figs. 7.16a and 7.16b show the variation of rock salt temperature at four selected distances from the cavern boundary during cyclic loading phases. As depicted in these figures, during the normal operation, the average temperature of each cycle remains approximately 50 °C (i.e. equal to the inflow temperature and initial ground temperature). In addition, the temperature fluctuation in the rock only takes place in a narrow zone less than one meter thick. Inside this zone, the amplitude of temperature cycles reduces as the distance from the cavern's boundary increases and finally, it approaches the ground temperature. In the second loading scenario, in which the average temperature of cycles is increased considerably, the thermal affected zone becomes larger.

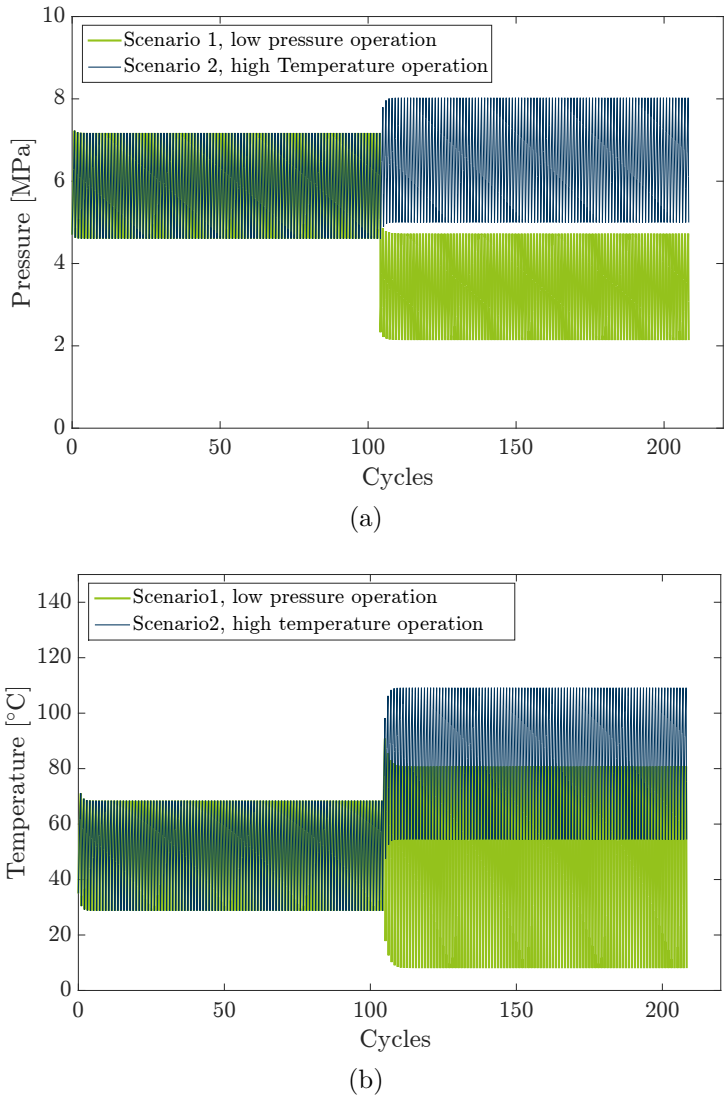

Figure 7.15: Variation of air temperature and pressure during the normal operating condition (cycles: 1-100) and extreme working conditions (cycles: 100-200)

This can be seen from Fig. 7.17 which shows the temperature distribution on a horizontal line at half cavern height during extreme cyclic loading.

7.3.3 Stability of the cavern

In this section, the mechanical stability of the simulated cavern is investigated considering three criteria:

1. "No-dilatancy" criterion: this criterion indicates whether the stress state around the cavern is in the dilatancy zone or not.

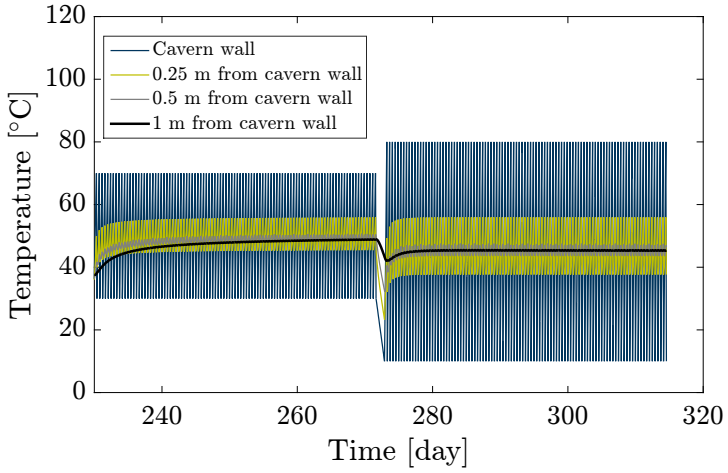

(a)

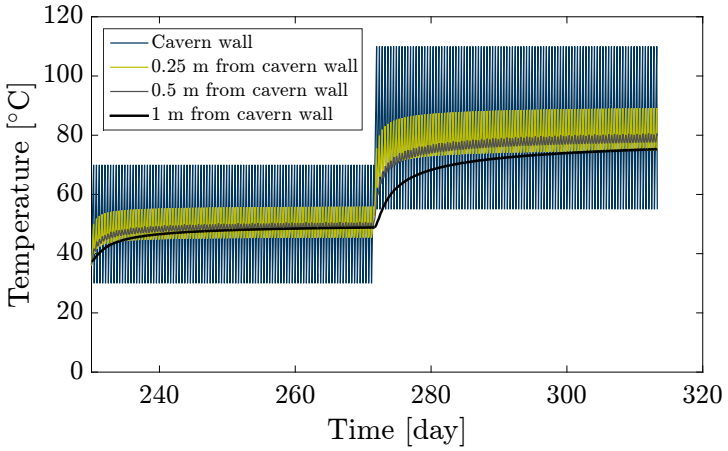

(b)

Figure 7.16: Variation of rock salt temperature at selected distances from the cavern boundary during cyclic loading phase (a) Scenario 1: low pressure operation (b) Scenario 2: high temperature operation

2. "No-damage" criterion: if the stress state goes beyond the dilatancy boundary, the damage and micro-cracking start to develop. In order to avoid such a condition, this criterion has to be fulfilled..

3. "No-tensile stress" criterion: rock salt exhibits poor tensile strength. Therefore, no tensile stress should be experienced around the cavern.

In the following, the above-mentioned stability criteria are evaluated for the numerical example explained in the previous section.

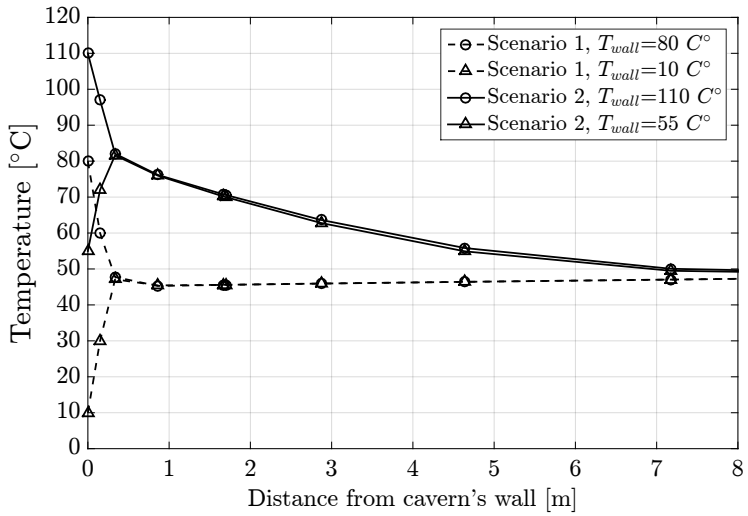

Figure 7.17: Calculated temperature distribution on a horizontal line at half cavern height during extreme cyclic loading; rock mass temperature at far distance : 50 °C

7.3.3.1 "No-dilatancy" criterion

The loading conditions of cavern have to be defined in a way that the stresses around the cavity remain in the compressibility zone. To determine the state of stress with respect to dilatancy boundary, the following utilization criterion is defined (Jafari et al., 2011; Brouard et al., 2011; Wang et al., 2013; Yang et al., 2015):

$$\mathrm{UC} = \frac{\sqrt{F^{dil}(I_1, \theta)}}{\sqrt{J_2}} \tag{7.9}$$

Where $\sqrt{F^{dil}(I_1, \theta)}$ is the equation of dilatancy boundary in the $I_1 - \sqrt{J_2}$ plane defined in Eq. 3.13. Fig. 7.18a shows the schematic representation of "No-dilatancy" criterion. When UC > 1, the current stress state is below the dilatancy boundary. In this case, the opening of micro-cracks does not occur and subsequently, damage does not progress. In contrary, when UC < 1, the stress state locates beyond the dilatancy bounday. Thus, the operating condition of the cavern is not safe and cavern may experience long-time failure due to the damage progress. Fig. 7.19 compares the minimum value of UC around the cavern obtained for the normal operating condition, scenario 1 and scenario 2, respectively. As it is observed, during the normal and the high temperature operation, the UC value is more than 1.2 . That means, the internal pressure of the cavern in these loading scenarios is high enough to keep the stresses below the dilatancy boundary. While, during the first loading scenario, where the internal pressure reduces drastically, the UC value becomes

less than one for the points located around the cavern. Thus, for this loading scenario, the stresses are in the dilatancy zone and the "No-dilatancy" criterion is not fulfilled.

7.3.3.2 "No-damage" criterion

An energy-based quantity defined in Section. 3.4.3 is used to describe damage and micro-cracking. The amount of energy stored during compression or released during dilatancy is associated with the volumetric inelastic work per unit volume w_{vol} defined as:

$$w_{vol} = \int_0^t \left(\frac{I_1}{3}\right) \dot{\varepsilon}_{vol}^{ie} \, dt. \tag{7.10}$$

Where ε_{vol}^{ie} denotes the inelastic volumetric strain and I_1 has been already defined in Eq. 3.9. The above-mentioned equation quantifies the energy of micro-cracking. In the compressibility domain, the volume of material reduces due to the closing of voids and micro-cracks. Therefore, mechanical energy is stored in the body and a positive value for w_{vol} is obtained. While, during dilatancy, the volume increases and energy is released by micro-cracking, therefore, w_{vol} becomes negative. When the released energy due to micro-cracking reaches a threshold value w_f the material failure occurs. To describe the damage evolution in the dilatancy domain, the following quantity has been defined as a ratio between the released inelastic volumetric energy w_{vol} and the maximum released energy w_f in which the material failure takes place.

$$\text{LFR} = \begin{cases} 0 & w_{vol} \geq 0 \\ \frac{w_{vol}}{w_f} & w_{vol} \leq 0 \end{cases} \tag{7.11}$$

Fig. 7.18b is the schematic definition of the LFR factor. In general, the maximum released energy at failure w_f may depend on the stress path. In this thesis, a series of trixial compression tests with different confining pressures were utilized to quantify the threshold value w_f as a function of minimum principal stress (i.e. $w_f = f(\sigma_3)$). As shown in the previous section, during the low pressure operation, dilatancy occurs around the cavern. Therefore, the LFR factor becomes greater than zero, damage and micro-cracking start to grow up in the material body. Fig. 7.20 shows the contour plot of LFR after 100 cycles for low pressure operating condition. As it is observed, the bottom and the roof of the cavern are affected by micro-cracking. The evolution of LFR factors for three points located at the bottom, roof and wall of the cavern have been depicted in Fig. 7.21. The

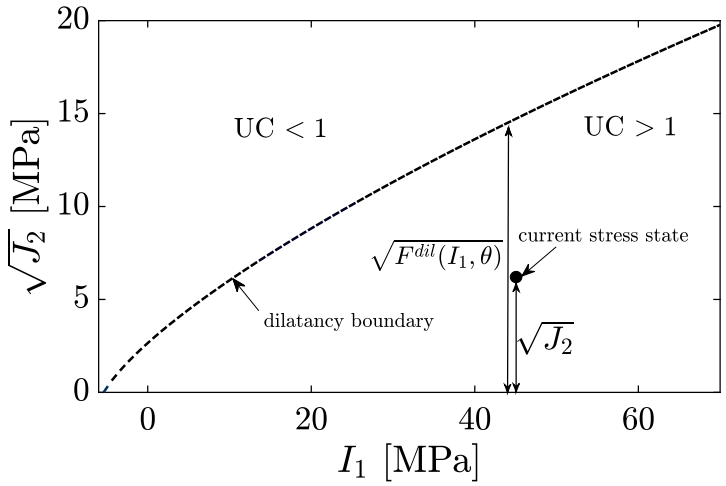

(a)

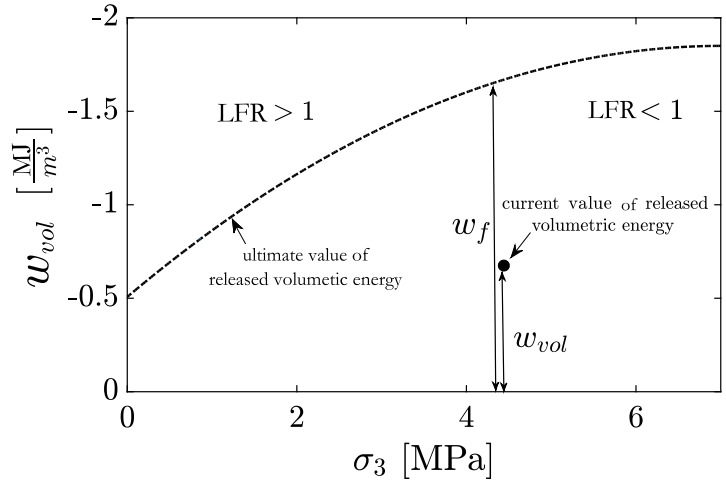

(b)

Figure 7.18: Schematic definition of stability criteria (a) UC $= \dfrac{\sqrt{F^{dil}(I_1,\theta)}}{\sqrt{J_2}}$ (b) LFR $= \dfrac{w_{vol}}{w_f}$

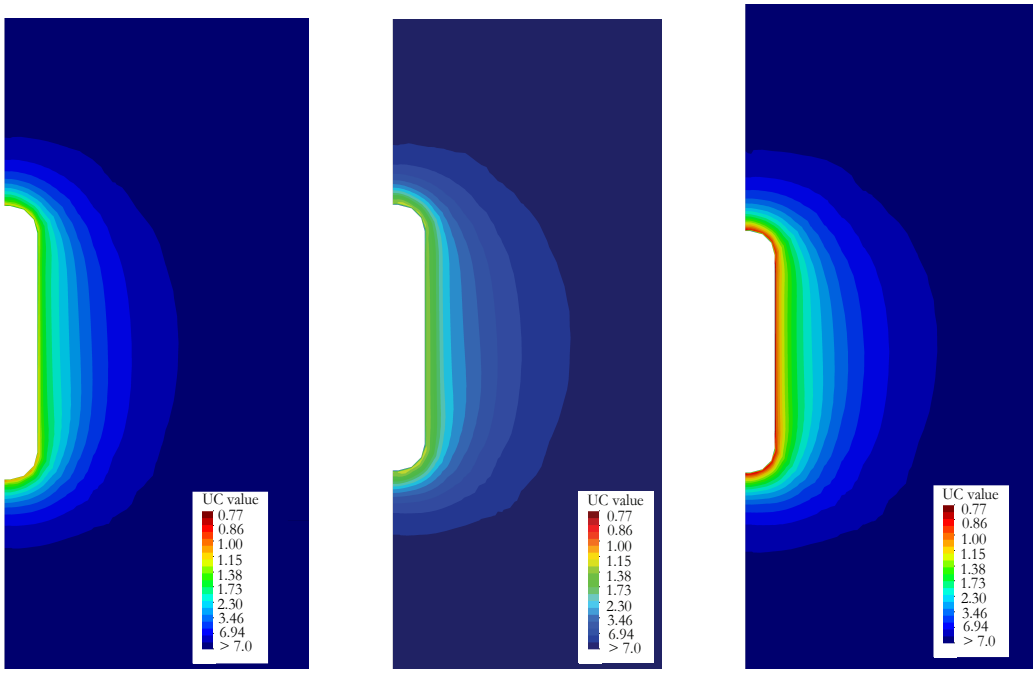

Figure 7.19: Contour plot of utilization criterion UC for (a) normal operation after 100 cycles (b) high temperature operation after 100 cycles (c) low pressure operation after 100 cycles

damage progress shows an upward trend at all observation points but with different rates. Increasing permeability due to the dilatancy and subsequently the long-term failure due to the micro-cracking are the unfavorable consequences of this loading condition.

7.3.3.3 "No-tensile stress" criterion

Rock salt has a poor tensile strength. The thermo–mechanical loading conditions have to be defined in a way that no tensile stress is experienced around the cavern. As explained before, the air temperature during the low pressure working condition reduces to 10 °C over the cyclic loading. This temperature reduction induces high thermal stresses in an area less than one meter thick around the cavern. Thus, due to the fast cooling and extra thermal contraction, the tangential component of stress becomes positive at the points which are very close to the boundary (in particular at the cavern roof). Fig. 7.22 shows the variation of principal stresses at cavern roof during excavation (days: 0–230), normal cyclic loading (days: 230–271) and extreme working condition (days: 271–312). As it is seen from this figure, the minimum principal (i.e. in this case the tangential stress)

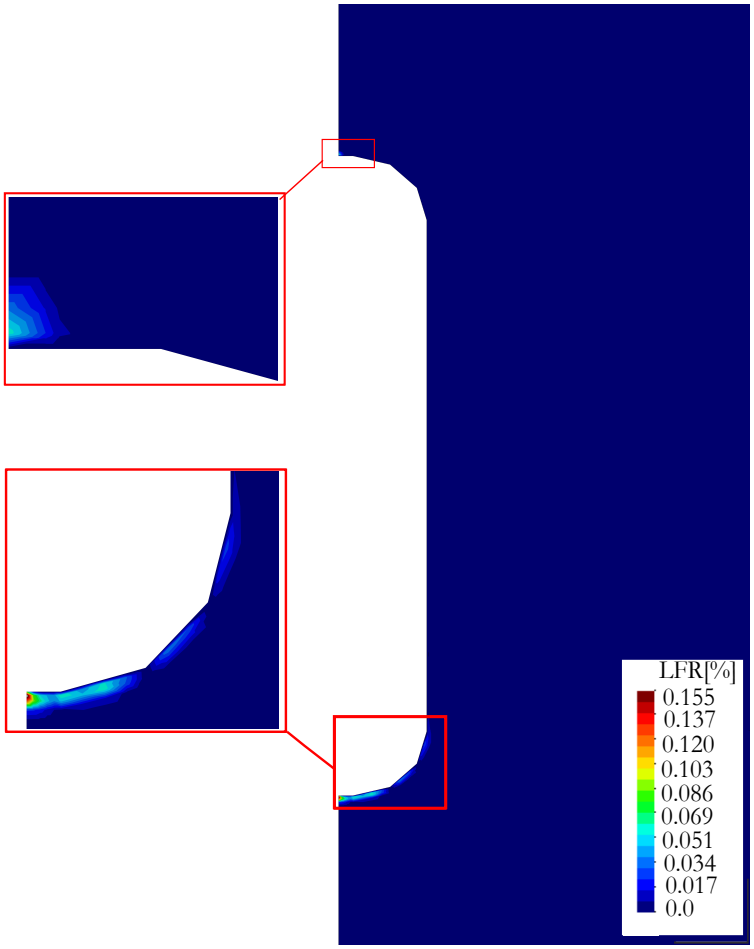

Figure 7.20: Contour plot of LFR for low pressure operation after 100 cycles

becomes positive for loading scenario 1. Therefore, "No-tensile stress" criterion is not satisfied for this loading condition.

7.3.4 Serviceability of the cavern

The serviceability of the system is affected if a significant reduction in the storage capacity of the cavern occurs. For this reason, it is important to control the factors which may increase the rate of cavern closure. In this section, the volume loss of the cavern (VL) during the cyclic loading phase is evaluated for the defined loading scenarios. The volume loss of the cavern is calculated as:

$$\mathrm{VL} = \frac{V_0 - V_t}{V_0}. \tag{7.12}$$

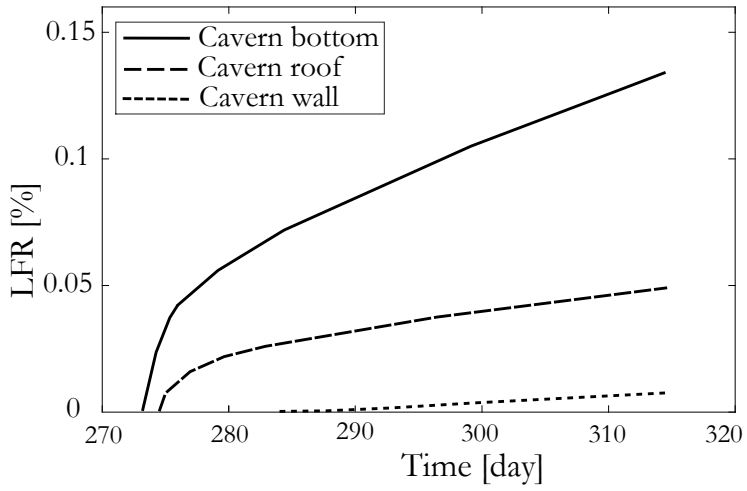

Figure 7.21: LFR versus time for the bottom, roof and wall of the cavern for loading scenario 1

here, V_0 and V_t are the initial defined volume and the volume after time t, respectively. Fig. 7.23 shows the changing of VL values for the defined loading scenarios. As it is observed, the rate of volume loss increases in both loading scenarios. In scenario 1, when the internal pressure drops down , the rate of volume convergence increases significantly in comparison to the normal working condition. In this case, the increased creep strain rate resulted from the higher deviatoric stresses accelerates the cavern closure. Regarding the second loading scenario, although, the internal pressure of the cavern slightly increases, the rate of volume loss has still an upward trend. In this case, the creep strain rate increases under the influence of temperature. Thus, the rate of volume loss increases in both cases.

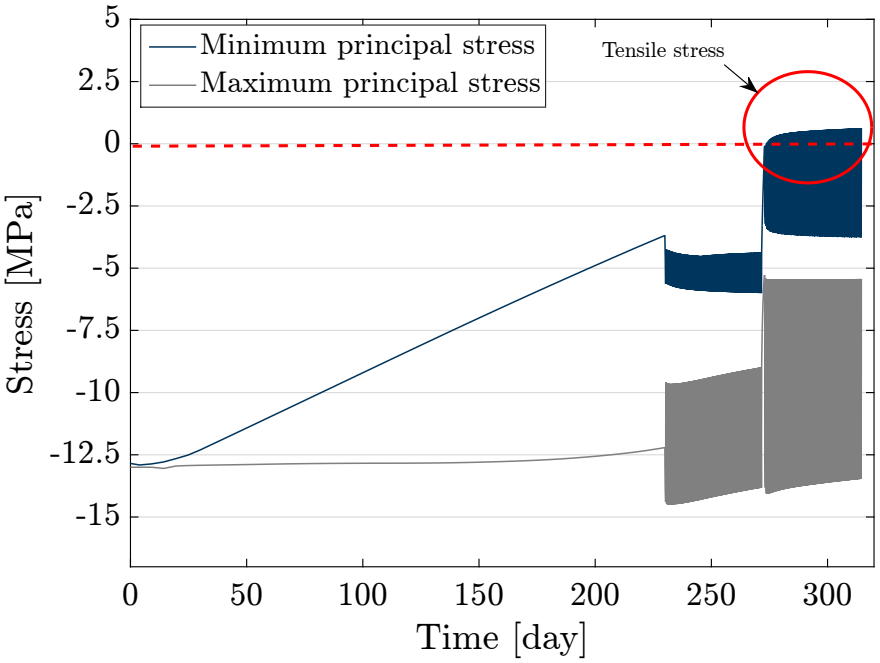

(a)

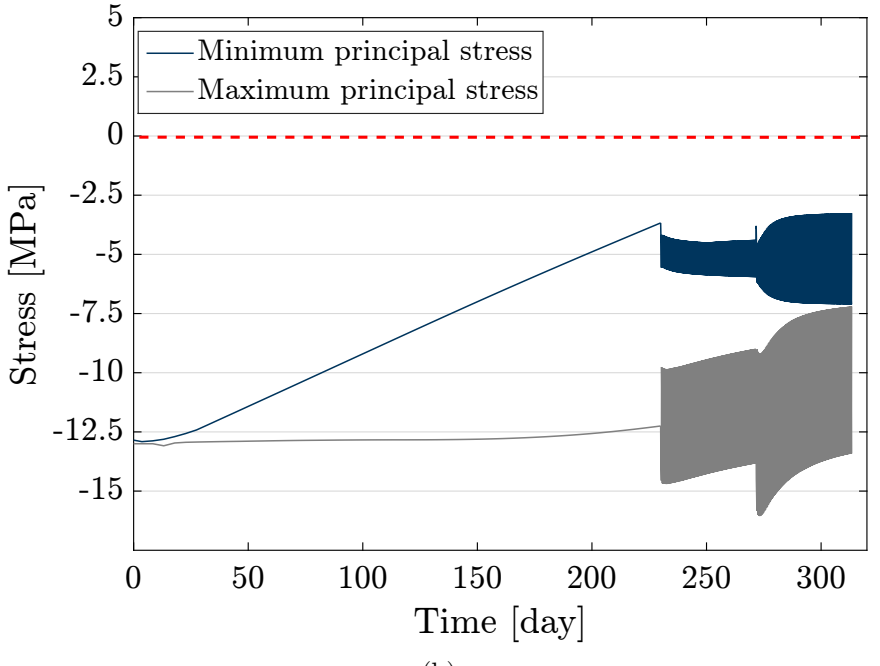

(b)

Figure 7.22: The principal stresses at cavern roof during excavation (days: 0-230), normal cyclic loading (days: 230-271) and extreme working condition (days: 271-312) (a) low pressure operation (b) high temperature operation

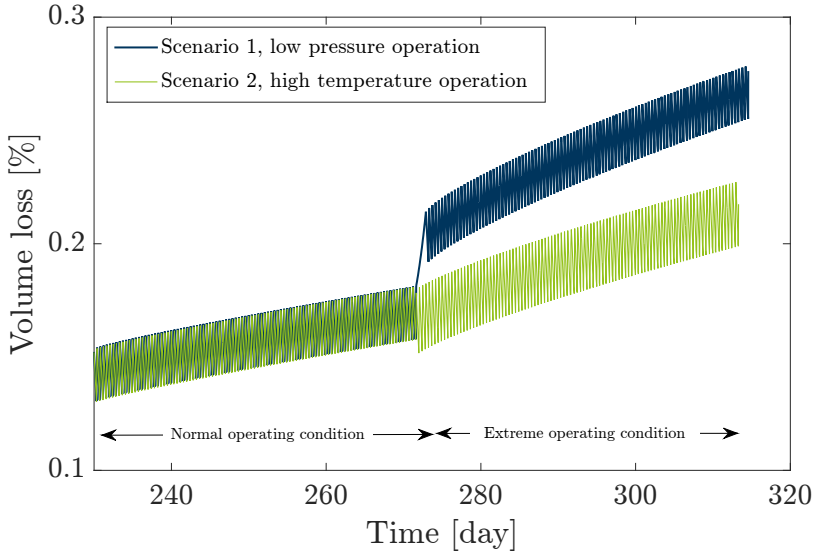

Figure 7.23: Volume loss of cavern during normal operation (days: 230-271) in comparison to extreme cyclic loading (days: 271-312)

8 Conclusions and recommendations

8.1 Summary and conclusions

In the present work, the effects of stress, temperature and time on the mechanical behavior of rock salt have been investigated. The main objective of the study is to develop an adequate numerical model which takes into account the most important processes affecting the development of stresses and strains around salt caverns. To achieve this goal, proper constitutive models are required to describe the material behavior of rock salt under different loading conditions at different time scales. The employed constitutive model in this thesis combines three existing models with some modifications to get benefit from their positive features for the specific purpose of the performed investigation. This allows applying the model in different types of simulations in terms of loading conditions (i.e. constant loading, monotonic loading and cyclic loading) as well as different time scales (i.e. short term or long term). The Desai model introduced in Section. 3.4.1 is based on a single-surface plasticity concept which avoids the difficulties regarding numerical implementation. The employed non-associated flow rule in this model yields to better description of the volumetric plastic strain. The dependency of the yield surface on Lode's angle results in different material responses in triaxial compression, shear and extension tests. The model takes into account the material dilatancy and compressibility which enhances the modeling of the volumetric behavior and improves the fit to the experimental data. In addition, the failure boundary allows the model to account for the short-term failure of the rock salt in strength tests. Furthermore, the rate dependency described via the viscoplasticity formulation explains the rate dependent behavior of rock salt. To describe the time–dependent behavior of rock salt, the modified creep law in Section. 3.4.2 has been formulated based on the Norton-Hoff creep model in which the creep strain rate is a function of the applied deviatoric stress and temperature. In this study, the Norton-Hoff model has been modified by introducing a new creep potential surface in order to have a better description for the volumetric creep deformation. According to Cristescu (1993), the damage development in rock salt can be described using the released volumetric strain

energy. This idea has been employed by including an energy-dependent damage parameter into the constitutive model. A commonly used function for rock materials has been also employed to describe the damage evolution. This formulation allows us to describe the strain softening in triaxial strength test, the tertiary creep in long-term creep tests and the failure in cyclic loading tests. The constitutive model has been implemented in the finite element code Code-Bright and the material parameters have been identified using relevant experimental data. After that, in order to investigate the influence of internal pressure and temperature on the stability and serviceability of cavern, it's operation has been analyzed numerically. In Chapters. 6.1 and 7.3, a staggered approach has been presented to model the coupled thermo-mechanical cyclic behavior in a typical compressed air storage cavern excavated in rock salt. The proposed approach includes the estimation of the air pressure and temperature variations inside the cavern as well as the safety and serviceability assessment of the storage cavern. This approach may be considered as a useful tool for engineering design and operation of such facilities. To accomplish this, first, the internal pressure and temperature of the cavern are estimated using an analytical thermodynamic model for the air injection/withdrawal processes. Then, in the second step, the obtained results from the first step are defined as the boundary condition for the finite element model of the cavern. The introduced constitutive model has been employed to describe the stress-strain relation of rock salt under the influence thermo-mechanical loading conditions. After that, in order to investigate the effect of internal temperature and pressure on the stability and serviceability of cavern, its operation under extreme loading conditions have been analyzed numerically. The obtained results show that during the normal operating condition, the applied loads to the rock salt medium generate only thermoelastic and steady-state creep deformations without any dilation or micro-cracking. However, when the loading pattern of the cavern is changed to the extreme condition, the stability and serviceability of the system are clearly affected by the internal pressure and temperature. The numerical results demonstrated that the stability factors of the system are strongly governed by the internal pressure of the cavern. For this reason, the internal pressure during the cyclic loading operation should be set in a way that the stresses around the cavern satisfy the "No-dilatancy", "No-damage" and "No-tensile stress" criteria. Otherwise, the micro-cracking and damage propagation may result in unfavorable consequences such as gas leakage and rock spalling around the cavern. On the other hand, the high temperature working condition mostly affected the long-term serviceability of the cavern. In this case, the increased creep strain rate at elevated temperature reduces the storage capacity of the cavern in long time periods

and endangers the serviceability of the system. Finally, the following conclusions may be drawn based on the results obtained in this study:

- Obviously, the safety assessment of rock salt caverns requires careful consideration of thermo-hydro-mechanical (and chemical) processes. These processes interact and influence each other in a complex manner. Additionally, they do not necessarily have the same spatial and temporal scales. For example, the flow pathways created by the damage increase the permeability of rock and represent the potential risk for gas leakage around the cavern. Subsequently, if the pore pressure locally exceeds the minimum principal stress, the fluid infiltration in rock salt takes place and the local widening of grain boundaries occurs. Under such conditions, the mechanical behavior of the rock salt is affected by the gas and liquid phases. On the other hand, the temperature of rock salt around the cavern may change due to the gas injection and withdrawal processes. This temperature change introduces additional stresses in a narrow zone around the cavern due to the thermal expansion and contraction. Moreover, the temperature variation affects the rate of creep deformation and changes the cavern closure rate.

- The minimum pressure in a compressed air storage cavern has to be set in a way that all the stresses around the cavern remain below the dilatancy threshold. This minimum pressure value depends on the cavern depth, in-situ stresses as well as the mechanical properties of rock salt medium. The "No-dilatancy" criterion explained in Section 7.3.3.1 is a utilization criterion that can be used in simulation-based predictions to make sure that the stresses are below the dilatancy boundary.

- The "No-damage" criterion explained in Section. 7.3.3.2 is a measure to identify the areas which are more prone to micro-cracking. Obtained results from the presented numerical example show that, the bottom and the roof of the cavern are more likely to experience damage and micro-cracking if the internal pressure of the cavern is relatively low. Increasing the rock permeability due to dilatancy and subsequently the gas leakage are some of the unfavorable consequences of this loading condition.

- The low pressure working condition results in high deviatoric stresses around the cavern. Due to this fact, the creep strain rate which is a function of deviatoric stress increases as well. It has been shown in Section. 7.3.4 that the volume loss of the cavern is another criterion which should be checked to identify the minimum allowable pressure.

- As shown in Section. 7.3.2, the temperature fluctuation in the rock around the cavern only takes place in a narrow zone less than one meter thick. However, due to its effect on the stress distribution (i.e. tensile stress at the boundary due to the low temperature), the thermal induced deformation in this zone should not be neglected for reliable predictions.
- Very low pressure working condition leads to the low temperature condition inside the cavern. As shown in Section. 7.3.3.3, the low temperature condition results in thermal contraction at the points which are located close to the boundary and may create tensile stresses at the wall. Since the tensile strength of the rock salt is very small (i.e. around 1.8 MPa), such operating conditions should be avoided. The "No-tensile stress" criterion explained in Section 7.3.3.3 can be used to find the allowable minimum temperature in the cavern. The suggested minimum temperature for the numerical example in this study is around 25 °C.
- The maximum allowable temperature of air is also a key factor within the design and operating process of the storage cavern. As shown in Section. 7.3.4, the creep deformation is an exponential function of temperature. Therefore, high temperature condition in a cavern increases the creep deformation of rock salt and subsequently, accelerates the cavern convergence. Another drawback of high temperature working condition could be the material weakening due to the high temperature. The volume loss of the cavern (as shown in Section. 7.3.4) can be considered as a criterion to identify the maximum allowable temperature. The suggested maximum temperature for the numerical example in this study is around 90 °C.

8.2 Suggestions for further investigations

In conclusion, the following items are suggested for further investigations in this field of study.

- Verification of constitutive models using in-situ measurement data; The presented approach needs to be verified against real data or/and representative laboratory tests that may be considered as a challenging task for future. Since the solution-mined caverns are very deep structures, conducting the field measurements which might help us to understand the real response of the host rock are practically very difficult. Therefore, it is needed to development new in-situ investigatory methods for determining rheological material parameters.

- The numerical simulations can be extended to three dimensions. The 3D simulations are useful to model a group of caverns and investigate their effect on each other.
- It is suggested to investigate the influence of healing, in particular, in cyclic loading conditions.
- The effects of temperature, loading rate and cyclic loading on the locus of dilatancy boundary in the stress space are still open questions.
- The stress field changes in the presence of pore fluid pressure. More investigations regarding the development of effective stress in the presence of pore fluid pressure are suggested.
- More accurate prediction regarding the thermodynamics of gas/air in caverns is an interesting research topic. This can be achieved through CFD modeling (computational fluid dynamics) of gas inside the cavern.
- The deformation mechanism under low stress and temperature has not been fully understood and it may affect the long-term predictions. This mechanism can be included in calculations.

Bibliography

Bräuer, V., Eisenburger, R. E. D. & Grissemann, C. (2011), Description of the Gorleben site part4: Geotechnical exploration of the Gorleben salt dome, Technical report, Die Bundesanstalt für Geowissenschaften und Rohstoffe.

Alkan, H. (2009), 'Percolation model for dilatancy-induced permeability of the excavation damaged zone in rock salt', *Int. J. Rock. Mech. Min. Sci.* **46**, 716–724.

Alkan, H., Cin, Y. & Pusch, G. (2007), 'Rock salt dilatancy boundary from combined acoustic emission and triaxial compression tests', *Int. J. Rock. Mech. Min. Sci.* **44**, 108–119.

Asgari, A., Ramezanzadeh, A., Jalali, S. M. E. & Brouard, B. (2012), Stability analysis of natural gas storage caverns in salt formations, *in* 'SMRI conference, Bremen, Germany, 1-2 October'.

Attewell, P. B. & Farmer, I. W. (1973), 'Fatigue behavior of rock', *Int. J. Rock. Mech. Min. Sci* **10**, 1–9.

Aubertin, M., Gill, D. & Ladanyi, B. (1991), 'An internal variable model for the creep of rocksalt', *Rock. Mech. Rock. Eng.* **24**(2), 81–97.

Aubertin, M., Gill, D. & Ladanyi, B. (1993), Modeling the transient inelastic flow of rocksalt, *in* '7th Symposium on Salt', Vol. 1, pp. 93–104.

Aubertin, M., Julien, M. R., Servant, S. & Gill, D. E. (1999), 'A rate-dependent model for the ductile behavior of salt rocks', *Can. Geotech. J.* **36**(4), 660–674.

Bai, M., Song, K., Sun, Y., He, M., Li, Y. & Sun, J. (2014), 'An overview of Hydrogen underground storage technology and prospects in China', *J. Petrol. Sci. Eng.* **124**, 132–136.

Bauer, S., Broome, S., Bronowski, D., Rinehart, A. & Ingraham, M. D. (2011), Experimental deformation of salt in cyclic loading, insights from acoustic emission measurements, *in* 'SMRI conference, Galveston, Texas, USA'.

Bérest, P. & Brouard, B. (2003), 'Safety of salt caverns used for underground storage: Blow out, mechanical instability, seepage, cavern abandonment', *Oil. Gas. Sci. Techno.* **58**, 361–384.

Bérest, P., Brouard, B., Djakeun-Djizanne, H. & Hévin, G. (2013), 'Thermomechanical effects of a rapid depressurization in a gas cavern', *Acta. Geot.* **9**(1), 181–186.

Bérest, P., Brouard, B., Favret, F., Hévin, G. & Jafari, M. K. (2015), Maximum pressure in gas storage caverns, *in* 'SMRI conference, Rochester, New York, USA, 27-28 April'.

Bérest, P., Brouard, B., Jafari, M. K. & Sambeek, L. V. (2007), 'Transient behavior of salt caverns-interpretation of mechanical integrity tests', *Int. J. Rock. Mech. Min. Sci* **44**, 767–786.

Bérest, P., Brouard, B., Jafari, M. K. & Sambeek, L. V. (2011), Thermomechanical aspects of high frequency cyclic in salt storage caverns, *in* 'International Gas Union Research Conference, Seoul, Korea, 19-21 October'.

Bérest, P., Djizanne, H., Brouard, B. & Hévin, G. (2012), Rapid depressurization: can they lead to irreversible damage?, *in* 'SMRI conference, Regina, Canada, 23-24 April'.

Bolzon, G. & Buljak, V. (2011), 'An effective computational tool for parametric studies and identification problems in materials mechanics', *Comput Mech* **48**, 657–687.

Brouard, B., Bérest, P., de Greef, V., Béraud, J., Lheur, C. & Hertz, E. (2013), 'Creep closure rate of a shallow salt cavern at Gellenoncourt, France', *Int. J. Rock. Mech. Min. Sci.* **62**, 42 – 50.

Brouard, B., Frangi, A. & Bérest, P. (2011), Mechanical stability of a cavern submitted to high-frequency cycles, *in* 'SMRI conference, Texas, USA, 18-19 April'.

Buljak, V. (2010), 'Proper orthogonal decomposition and radial basis functions algorithm for diagnostic procedure based on inverse analysis', *FME Transactions* **38**, 129–136.

Carter, N., Horseman, S., Russell, J. & Handin, J. (1993), 'Rheology of rocksalt', *J. Struct. Geol.* **15**(9), 1257–1271.

Carter, N. L. & Hansen, F. D. (1983), 'Creep of rocksalt', *Tectonophysics* **92**(4), 275 – 333.

Chan, K., Bodner, S., Fossum, A. & Munson, D. (1997), 'A damage mechanics treatment of creep failure in rock salt', *Int. J. Damage Mech.* **6**(2), 121–152.

Chan, K., Brodsky, N., Fossum, A., Bodner, S. & Munson, D. (1994), 'Damage-induced nonassociated inelastic flow in rock salt', *Int. J. Plasticity.* **10**(6), 623–642.

Code-Bright (2010), *A 3D program for Thermo-Hydro-Mechanical analysis in geological media, user's guide*, Universitat Politècnica de Catalunya.

Cortogino, F., Mohmeyer, K.-U. & Scharf, R. (2001), Huntorf CAES: More than 20 years of successful operation, *in* 'SMRI Spring Meeting, Orlando, 23-24 April', pp. 351–357.

Cosenza, P. & Ghoreychi, M. (1999), 'Effects of very low permeability on the long-term evolution of a storage cavern in rock salt', *Int. J. Rock. Mech. Min. Sci* **36**(4), 527 – 533.

Cristescu, N. (1987), 'Elastic viscoplastic constitutive equations for rock', *Int. J. Rock Mech. Min. Sci. & Geomech. Abstr.* **24**(5), 271–281.

Cristescu, N. (1993), 'A general constitutive equation for transient and stationary creep of rock salt', *Int. J. Rock Mech. Min. Sci. & Geomech. Abstr.* **30**(2), 125–139.

Cristescu, N. & Gioda, G. (1994), *Visco-Plastic Behaviour of Geomaterials*, Springer Verlag, Wien-New York.

Cristescu, N. & Hunsche, U. (1998), *Time Effects in Rock Mechanics*, John Wiley & Sons, Chichester.

Cristescu, N. & Paraschiv, I. (1995), The optimal shape of rectangular-like caverns, *in* 'Int. J. Rock. Mech. Min. Sci. & Geomech. Abstr.', Vol. 32, Elsevier, pp. 285–300.

Czaikowski, O. (2011), Laborative und rechnerische Untersuchungen zu geomechanisch-geohydraulischen Wechselwirkungen im Tongestein im Hinblick auf die Endlagerung radioaktiver Abfälle, PhD thesis, Fakultät für Energie- und Wirtschaftswissenschaften der Technischen Universität Clausthal.

Deng, J., Yang, Q. & Liu, Y. (2014), 'Time-dependent behaviour and stability evaluation of gas storage caverns in salt rock based on deformation reinforcement theory', *Tunn. Undergr. Sp. Tech.* **42**, 277 – 292.

Desai, C. (2016), 'Disturbed state concept as unified constitutive modeling approach', *J. Rock. Mech. Geotech. Eng.* **8**(3), 277–293.

Desai, C. & Salami, M. (1987), A constitutive model and associated testing for soft rock, *in* 'Int. J. Rock. Mech. Min. Sci. & Geomech. Abstr.', Vol. 24, pp. 299–307.

Desai, C. & Varadarajan, A. (1987), 'A constitutive model for quasi-static behavior of rock salt', *J. Geophys. Res.* **92**, 445–456.

Desai, C. & Zhang, D. (1987), 'Viscoplastic model for geologic material with generalized flow rule', *Int. J. numer. Anal. Met.* **11**, 603–627.

Desbois, G., Urai, J. L. & de Bresser, J. H. (2012), 'Fluid distribution in grain boundaries of natural fine-grained rock salt deformed at low differential stress (Qom Kuh salt fountain, central Iran): Implications for rheology and transport properties', *J. Struct. Geol.* **43**, 128 – 143.

DeVries, K. L., Mellegard, K. D., Callahan, G. D. & Goodman, W. M. (2005), Cavern roof stability for natural gas storage in bedded salt, Technical report, Prepared for United States Department of Energy, National Energy Technology Laboratory.

DeVries, K., Mellegard, K. & Callahan, G. (2000), Cavern design using a salt damage criterion: proof-of-concept research final report, *in* 'SMRI Spring Meeting, Houston', pp. 1–18.

Düsterloh, U. (2010), *Geotechnische Sicherheitsnachweise für Hohlraumbauten im Salinargebirge unter besonderer Berücksichtigung laborativer Untersuchungen: ein Beitrag zum Nachweis von Standsicherheit und Barrierenintegrität für untertägige Abfallentsorgungsanlagen und Hohlraumbauten des salinaren Berg-und Kavernenbaus*, Papierflieger-Verlag.

Duvant, G. & Lions, J. L. (2012), *Inequalities in mechanics and physics*, Vol. 219, Springer Science & Business Media.

Eickemeier, R. (2005), A new model to predict subsidence above brine fields, *in* 'Proceedings of Solution Mining Research Institute (SMRI) Fall 2005 Technical Meeting. Nancy, France: Solution Mining Research Institute (SMRI)', pp. 1–20.

Erdöl und Erdgas in der Bundesrepublik Deutschland 2015 (2016), Technical report, Landesamt für Bergbau, Energie und Geologie (LBEG), Hannover.

Evans, D., Reay, D., Riley, N., Mitchell, W. & Busby, J. (2006), Appraisal of underground energy storage potential in Northern Ireland, sustainable and renewable energy programme, Internal Report IR/06/095, Technical report, British Geological Survey.

Farmer, I. W. & Gilbert, M. J. (1984), Time dependent stregth reduction of rock salt, *in* 'Proceedings of the first conference on mechanical behavior of salt, Clausthal-Zellerfeld', Trans Tech Pub, pp. 3–18.

Fokker, P. A. & Orlic, B. (2006), 'Semi-analytic modelling of subsidence', *Mathematical geology* **38**(5), 565–589.

Fokker, P., Kenter, C. & Rogaar, H. (1993), The effect of fluid pressures on the mechanical stability of (rock) salt, *in* 'Proc. 7th symp. on salt, Elsevier Sci. Pub'.

Fossum, A., Munson, D., Chan, K. & Bodner, S. (1998), 'Constitutive basis of the MDCF model for rock salt', *Series on rock and soil mechanics* **22**, 235–248.

Frantziskonis, G. & Desai, C. (1987), 'Effects of very low permeability on the long-term evolution of a storage cavern in rock salt', *Acta. Mech.* **68**, 151 – 170.

Friedman, M., Dula, W., Gangi, A. & Gazonas, G. (1984), Structural petrology of experimentally deformed synthetic rocksalt, *in* 'First Conference on the Mechanical Behaviour of Rocksalt', Transtech Claustal-Zellerfeld, pp. 19–36.

Fuenkajorn, K. & Phueakphum, D. (2010), 'Effects of cyclic loading on mechanical properties of Maha Sarakham salt', *Eng. Geol.* **112**(1-4), 43–52.

Fuenkajorn, K., Sriapai, T. & Samsri, P. (2012), 'Effects of loading rate on strength and deformability of Maha Sarakham salt', *Eng. Geol.* **135-136**, 10–23.

Günther, R. (2009), Phänomenologisches Stoffmodell für duktile Salzgesteine zur Beschreibung primären, sekundären und tertiären Kiechens, PhD thesis, Fakultät für Geowissenschaften, Geotechnik und Bergbau der Technischen Universität Bergakademie Freiberg.

Günther, R.-M., Salzer, K., Popp, T. & Lüdeling, C. (2015), 'Steady-state creep of rock salt: Improved approaches for lab determination and modelling', *Rock. Mech. Rock. Eng.* **48**(6), 2603–2613.

Günther, R. & Salzer, K. (2007), A model for rock salt, describing transient, stationary, and accelerated creep and dilatancy., *in* '6th conference on the mechanical behavior of salt- SALTMECH6, Hannover , Germany, 22-25 May'.

Guo, C., Pan, L., Zhang, K., Oldenburg, C. M., Li, C. & Li, Y. (2016), 'Comparison of compressed air energy storage process in aquifers and caverns based on the Huntorf CAES plant', *Appl. Energ.* **181**, 342 – 356.

Guo, Y., Yang, C. & Mao, H. (2012), 'Mechanical properties of Jintan rock salt under complex stress paths', *Int. J. Rock. Mech. Min. Sci* **56**, 54–61.

Hampel, A. (2012), 'The CDM constitutive model for the mechanical behavior of rock salt: Recent developments and extensions', *Mechanical Behavior of Salt VII. Eds. Bérest, P., Ghoreychi, M., Hadj-Hassen, F., Tijani, M., Paris: CRC Press/Balkema* pp. 45–55.

Hampel, A. (2015), Description of damage reduction and healing with the CDM constitutive model for the thermo-mechanical behavior of rock salt, *in* 'Proc. of the 8th Conf. on the Mech. Behaviour of Salt (Eds.: Lance Roberts)', pp. 301–310.

Hampel, A., Gunther, R., Salzer, K., Minkley, W., Pudewills, A., Leuger, B., Zapf, D., Staudtmeister, K., Rokahr, R., Herchen, K. et al. (2010), Benchmarking of geomechanical constitutive models for rock salt, *in* '44th US Rock Mechanics Symposium and 5th US-Canada Rock Mechanics Symposium', American Rock Mechanics Association.

Hampel, A. & Schulze, O. (2007), The composite dilatancy model: A constitutive model for the mechanical behavior of rock salt, *in* '6th conference on the mechanical behavior of salt- SALTMECH6, Hannover , Germany, 22-25 May'.

Hansen, F. D., Mellegard, K. D. & Senseny, P. E. (1984), Elasticity and strength of ten natural rock salts, *in* '1st conference on the mechanical behavior of salt, Pennsylvania State University', pp. 71–83.

Heard, H. (1972), 'Steady-state flow in ploycrystalline halite at pressure of 2 Kilo bars. Flow and Fracture of Rocks', *Am. Geophys. Union* pp. 191–209.

Heemann, U. & Heusermann, S. (2004), Theoretical and experimental investigation on stresses and permeability in the BAMBUS project, *in* 'DisTec 2004, International Conference on Radioactive Waste Disposal', pp. 26–28.

Hein, H. (1991), Ein Stoffgesetz zur Beschreibung des thermo-mechanischen Verhaltens von Steinsalzgranulat, PhD thesis, RWTH Aachen.

Heusermann, S., Lux, K.-H. & Rokahr, R. (1983), *Entwicklung mathematisch-mechanischer Modelle zur Beschreibung des Stoffverhaltens von Salzgestein in Abhängigkeit von der Zeit und der Temperatur auf der Grundlage von Laborversuchen*

mit begleitenden kontinuumsmechanischen Berechnungen nach der Methode der finiten Elemente, Fachinformationszentrum Energie, Physik, Mathematik Karlsruhe.

Heusermann, S., Rolfs, O. & Schmidt, U. (2003), 'Nonlinear finite element analysis of solution mined storage caverns in rock salt using the LUBBY2 constitutive model', *Comput. Struct.* **81**, 629–638.

Hickman, H. S. & Evans, B. (1991), 'Experimental pressure solution in halite: the effect of grain/interphase boundary structure', *J. Geol. Soc* **148**, 549–560.

Hirth, J. P. & Lothe, J. (1982), *Theory of dislocations*, John Wiley & Sons.

Höfer, K. & Thoma, K. (1968), 'Triaxial tests on salt rocks', *Int. J. Rock. Mech. Min. Sci. & Geomech. Abstr.* **5**(2), 195 – 196.

Hou, Z. (2003), 'Mechanical and hydraulic behavior of rock salt in the excavation disturbed zone around underground facilities', *Int. J. Rock. Mech. Min. Sci* **40**, 725–738.

Hou, Z. & Lux, K. H. (1998), 'Ein neues Stoffmodell für duktile Salzgesteine mit Einbeziehung von Gefügeschädigung und tertiärem Kriechen auf der Grundlage der Continuum-Damage-Mechanik', *Geotechnik* **21**, 259–263.

Huang, X. & Xiong, J. (2011), 'Numerical simulation of gas leakage in bedded salt rock storage cavern', *Procedia engineering* **12**, 254–259.

Hunsche, U. (1984), Fracture experiments on cubic rock salt samples, *in* 'The Mechanical Behavior of Salt, Proc. of 1st Conf', pp. 169–179.

Hunsche, U. (1993), 'Strength of rock salt at low mean stress', *Geotechnik-Sonderheft, Glückauf, Essen* pp. 160–163.

Hunsche, U. (1994), Uniaxial and triaxial creep and failure tests on rock: experimental technique and interpretation, *in* 'Visco-Plastic Behaviour of Geomaterials', Springer, pp. 1–53.

Hunsche, U. E. (1992), *True Triaxial Failure Tests on Cubic Rock Salt Samples. Experimental Methods and Results*, Springer Berlin Heidelberg, Berlin, Heidelberg, pp. 525–536.

Hunsche, U. & Hampel, A. (1997), 'Rock salt- the mechanical properties of the host rock material for radio active waste', *Eng. Geol.* **52**, 271–291.

Hunsche, U. & Hampel, A. (1999), 'Rock salt- the mechanical properties of the host rock material for radio active waste repository', *Eng. Geol.* **52**, 271–291.

Hunsche, U. & Schulze, O. (1994), 'Das Kriechverhalten von Steinsalz', *Kali und Steinsalz* **11**(8/9), 238–255.

Hunsche, U., Schulze, O., Walter, F. & Plischke, I. (2003), Projekt Gorleben 9G2138110000, thermomechanisches Verhalten von Salzgestein., Technical report, BGR, Hannover.

Jafari, M. K., Brouard, B. & Bérest, P. (2011), Multi-cycle gas storage in salt caverns, *in* 'SMRI conference, York, UK, 3-4 October'.

Jeremic, M. L. (1994), *Rock mechanics in salt mining*, A.A.Balkema Publisher, Rotterdam, Brookfield.

Karimi-Jafari, M., Berest, P. & Brouard, B. (2008), Subsidence, sinkholes and craters above salt caverns, *in* 'Solution Mining Research Institute Spring Meeting, Porto, Portugal', Vol. 269.

Khaledi, K., Mahmoudi, E., Datcheva, M., König, D. & Schanz, T. (2016), 'Sensitivity analysis and parameter identification of a time dependent constitutive model for rock salt', *J. Comput. Appl. Math.* **293**, 128–138.

Khaledi, K., Mahmoudi, E., Datcheva, M. & Schanz, T. (2016*a*), 'Analysis of compressed air storage caverns in rock salt considering thermo-mechanical cyclic loading', *Environ. Earth. Sci.* **75**(15), 1149.

Khaledi, K., Mahmoudi, E., Datcheva, M. & Schanz, T. (2016*b*), 'Stability and serviceability of underground energy storage caverns in rock salt subjected to mechanical cyclic loading', *Int. J. Rock. Mech. Min. Sci.* **86**, 115–131.

Khaledi, K., Miro, S., König, M. & Schanz, T. (2014), 'Robust and reliable metamodels for mechanized tunnel simulations', *Comput. Geotech.* **61**, 1–12.

Khaledi, K., Schanz, T. & Miro, S. (2014), 'Application of metamodelling techniques for mechanized tunnel simulation', *J Theor Appl Mech* **44**(1), 45–54.

Kim, H.-M., Rutqvist, J., Ryu, D.-W., Choi, B.-H., Sunwoo, C. & Song, W.-K. (2012), 'Exploring the concept of compressed air energy storage (CAES) in lined rock caverns at shallow depth: A modeling study of air tightness and energy balance', *Appl. Energ.* **92**, 653 – 667.

Knabe, T., Schweiger, F. H. & T.Schanz (2012), 'Calibration of constitutive parameters by inverse analysis for a geotechnical boundary problem', *Can Geotech J* **49**, 170–183.

Krajcinovic, D., ed. (1996), *Damage Mechanics*, Vol. 41 of *North-Holland Series in Applied Mathematics and Mechanics*, North-Holland.

Kushnir, R., Dayan, A. & Ullmann, A. (2012), 'Temperature and pressure variations within compressed air energy storage caverns', *Int. J. Heat. Mass. Tran.* **55**(21-22), 5616 – 5630.

Langer, M. (1982), 'Geotechnical investigation methods for rock salt', *Bulletin of the International Association of Engineering Geology* **25**(1), 155–164.

Lestringant, C., Bérest, P. & Brouard, B. (2010), Thermo-mechanical effects in Compressed Air Storage (CAES)., *in* 'SMRI Fall Meeting, Leipzig', pp. 29–44.

Leuger, B., Staudtmeister, K., Yıldırım, S. & Zapf, D. (2010), Modeling of creep mechanism and damage of rock salt, *in* '7th European Conference on Numerical Methods in Geotechnical Engineering (NUMGE 2010), 02–04 June 2004, Trondheim/Norway', pp. 89–94.

Levasseur, S., Malecot, Y., Boulon, M. & Flavigny, E. (2008), 'Soil parameter identification using a genetic algorithm', *Int J Numer Anal Met* **32**, 189–213.

Li, M., Zhang, H., Xing, W., Hou, Z. & Were, P. (2015), 'Study of the relationship between surface subsidence and internal pressure in salt caverns', *Environ. Earth. Sci.* **73**(11), 6899–6910.

Li, S., Abe, S., Urai, J. L., Strozyk, F., Kukla, P. A. & van Gent, H. (2012), A method to evaluate long-term rheology of Zechstein salt in the tertiary, *in* '7th conference on the mechanical behavior of salt- SALTMECH7, Paris , France, 16-19 April'.

Liang, W., Yang, C., Zhao, Y., Dusseault, M. & Liu, J. (2007), 'Experimental investigation of mechanical properties of bedded salt rock', *Int. J. Rock. Mech. Min. Sci.* **44**(3), 400 – 411.

Liang, W., Zhang, C., Gao, H., Yang, X., Xu, S. & Zhao, Y. (2012), 'Experiments on mechanical properties of salt rocks under cyclic loading', *J. Rock. Mech. Geotech. Eng* **4**(1), 54–61.

Liang, W., Zhao, Y., Xu, S. & Dusseault, M. (2011), 'Effect of strain rate on the mechanical properties of salt rock', *Int. J. Rock. Mech. Min. Sci.* **48**(1), 161 – 167.

Liu, J., Xie, H., Hou, Z., Yang, C. & Chen, L. (2014), 'Damage evolution of rock salt under cyclic loading in unixial tests', *Acta Geotechnica* **9**, 153–160.

Lux, K.-H. (2009), 'Design of salt caverns for the storage of natural gas, crude oil and compressed air: Geomechanical aspects of construction, operation and abandonment', *Geological Society, London, Special Publications* **313**(1), 93–128.

Ma, H., Yang, C., Li, Y., Shi, X., Liu, J. & Wang, T. (2015), 'Stability evaluation of the underground gas storage in rock salts based on new partitions of the surrounding rock', *Environ. Earth. Sci.* **73**(11), 6911–6925.

Ma, L. J., Liu, X. Y., Fang, Q., Xu, H. F., Xia, H. M., Li, E. B., Yang, S. G. & Li, W. P. (2013), 'A new elasto-viscoplastic damage model combined with the generalized Hoek-Brown failure criterion for bedded rock salt and its application', *Rock. Mech. Rock. Eng.* **46**, 53–66.

Ma, L. J., Liu, X. Y., Wang, M. Y., Xu, H. F., Hua, R. P., Fan, P. X., Jiang, S. R., Wang, G. A. & Yi, Q. K. (2013), 'Experimental investigation of the mechanical properties of rock salt under triaxial cyclic loading', *Int. J. Rock. Mech. Min. Sci* **62**, 34–41.

Mahmoudi, E., Khaledi, K., Miro, S., König, D. & Schanz, T. (n.d.), 'Probabilistic analysis of a rock salt cavern with application to energy storage systems', *Rock. Mech. Rock. Eng.* **50**, 139–157.

Mahmoudi, E., Khaledi, K., von Blumenthal, A., König, D. & Schanz, T. (2016), 'Concept for an integral approach to explore the behavior of rock salt caverns under thermo-mechanical cyclic loading in energy storage systems', *Environ. Earth. Sci.* **75**(14), 1–19.

Martín, L. B., Rutqvist, J. & Birkholzer, J. T. (2015), 'Long-term modeling of the thermal–hydraulic–mechanical response of a generic salt repository for heat-generating nuclear waste', *Eng. Geol.* **193**, 198–211.

Matei, A. & Cristescu, N. (2000), 'The effects of volumetric strain on elastic parameters for rock salt', *Mech. Cohes. Frict. Mat.* **5**, 113–124.

Maton, J.-P., Zhao, L. & Brouwer, J. (2013), 'Dynamic modeling of compressed gas energy storage to complement renewable wind power intermittency', *Int. J. Hydrogen. Energ.* **38**(19), 7867 – 7880.

Meier, J., Moser, M., Datcheva, M. & Schanz, T. (2013), 'Numerical modeling and inverse parameter estimation of the large-scale mass movement Gradenbach in Carinthia (Austria)', *Acta Geotech* **8**, 355–371.

Meier, J., Rudolph, S. & Schanz, T. (2009), 'Effective algorithm for parameter back calculation–geotechnical applications', *Bautechnik* **86**(1), 86–97.

Minkley, M. & Muehlbauer, J. (2007), Constitutive models to describe the mechanical behavior of salt rocks and the imbedded weakness planes, *in* '6th conference on the mechanical behavior of salt- SALTMECH6, Hannover , Germany, 22-25 May'.

Miro, S., Hartmann, D. & Schanz, T. (2014), 'Global sensitivity analysis for subsoil parameter estimation in mechanized tunneling', *Comput Geotech* **56**, 80–88.

Moghadam, S. N., Nazokkar, K., Chalaturnyk, R. J. & Mirzabozorg, H. (2015), 'Parametric assessment of salt cavern performance using a creep model describing dilatancy and failure', *Int. J. Rock. Mech. Min. Sci.* **79**, 250 – 267.

Munson, D. (1997), 'Constitutive model of creep in rock salt applied to underground room closure', *Int. J. Rock. Mech. Min. Sci.* **34**(2), 233–247.

Munson, D. & Dawson, P. (1981), Salt-constitutive modeling using mechanism maps, Technical report, Sandia National Labs., Albuquerque, NM (USA); Cornell Univ., Ithaca, NY (USA). Dept. of Mechanical and Aerospace Engineering.

Munson, D. E. (1979), Preliminary deformation-mechanism map for salt (with application to WIPP), Technical report, SAND79-0076, Sandia National Laboratories, Albuquerque, NM.

Munson, D. E. (1998), Analysis of multistage and other creep data for domal salts, Technical report, Sandia National Labs., Albuquerque, NM (USA); Cornell Univ., Ithaca, NY (USA). Dept. of Mechanical and Aerospace Engineering.

Nazary, S., Mirzabozorg, H. & Noorzad, H. (2013), 'Modeling time-dependent behavior of gas caverns in rock salt considering creep, dilatancy and failure', *Tun. Undergr. Sp. Tech.* **33**, 171–185.

Nicolae, M. (1999), 'Non associated elasto viscoplastic models for rock salt', *Int. J. Eng. Sci.* **37**, 269–297.

Norton, F. H. (1929), *The creep of steel at high temperatures*, number 35, McGraw-Hill Book Company, Incorporated.

Olivella, S. & Gens, A. (2002), 'A constitutive model for crushed salt', *Int. J. Numer. Anal. Meth. Geomech.* **26**, 719–746.

Peach, C. J. (1991), Influence of deformation on the fluid transport properties of salt rocks, PhD thesis, Department of Geology, University of Utrecht, Netherlands.

Peach, C. J. & Spiers, C. J. (1996), 'Influence of crystal plastic deformation on dilatancy and permeability development in synthetic salt rock', *Tectonophysics* **256**(1), 101–128.

Perzyna, P. (1966), 'Fundamental problems in viscoplasticity', *Rec. Adv. Appl. Mech.* **9**, 243–377.

Pfeifle, T., Brodsky, N. & Munson, D. (1998), 'Experimental determination of the relationship between permeability and microfracture-induced damage in bedded salt', *Int. J. Rock. Mech. Min. Sci* **35**(4-5), 593 – 594. 3rd North American Rock Mechanics Symposium.

Popp, T. & Kern, H. (1998), 'Ultrasonic wave velocities, gas permeability and porosity in natural and granular rock salt', *Phys. Chem. Earth.* **23**(3), 373 – 378.

Popp, T., Kern, H. & Schulze, O. (2001), 'Evolution of dilatancy and permeability in rock salt during hydrostatic compaction and triaxial deformation', *J. Geophys. Res.* **106**, 4061–4078.

Popp, T., Wiedemann, M., Kansy, A. & Pusch, G. (2007), Gas transport in dry rock salt–implications from laboratory investigations and field studies, *in* 'The mechanical behavior of salt-Understanding of THMC processes in salt.-Taylor & Francis', pp. 17–26.

Pudewills, A. (2007*a*), Modeling of hydro-mechanical behavior of rock salt in the near field of repository excavation, *in* '6th conference on the mechanical behavior of salt-SALTMECH6, Hannover, Germany', pp. 22–25.

Pudewills, A. (2007*b*), Modellierung des mechanischen Verhaltens von Steinsalz: Vergleich aktueller Stoffgesetze und Vorgehensweisen, Technical report, Forschungszentrum Karlsruhe.

Pudewills, A. & Droste, J. (2003), 'Numerical modeling of the thermomechanical behavior of a large-scale underground experiment', *Comput. Struct.* **81**(8-11), 911 – 918.

Pudewills, A. & Krauss, M. (1999), 'Implementation of a viscoplastic model for crushed salt in the ADINA program', *Comput. Struct.* **72**(1), 293–299.

Raju, M. & Khaitan, S. K. (2012), 'Modeling and simulation of compressed air storage in caverns: A case study of the Huntorf plant', *Appl. Energ.* **89**(1), 474 – 481.

Roberts, L. A., Buchholz, S. A., Mellegard, K. D. & Düsterloh, U. (2015), 'Cyclic loading effects on the creep and dilation of salt rock', *Rock. Mech. Rock. Eng.* **48**(6), 2581–2590.

Saltelli, A., Andres, T. & Ratto, M. (2008), *Global Sensitivity Analysis.The Primer*, John Wiley & Sons Ltd.

Sambeek, L. L. V., Ratigan, J. L. & Hansen, F. D. (1993), 'Dilatancy of rock salt in laboratory tests', *Int. J. Rock. Mech. Min. Sci. & Geomech. Abstr.* **30**(7), 735 – 738.

Schulze, O., Heemann, U., Zetsche, F., Hampel, A., Pudewills, A., Günther, R., Minkley, W., Salzer, K., Hou, Z., Wolters, R. et al. (2007), Comparison of advanced constitutive models for the mechanical behavior of rock salt-results from a joint research project. i. modeling of deformation processes and benchmark calculations, *in* 'Proc. of the 6th Conf. on the Mech. Behaviour of Salt (Eds.: Wallner, M., Lux, K.-H., Minkley, W. & Hardy, Jr., HR), Hannover', pp. 77–88.

Schulze, O., Popp, T. & Kern, H. (2001), 'Development of damage and permeability in deforming rock salt', *Eng. Geol* **61**, 163–180.

Sedláček, R. & Blum, W. (2002), 'Microstructure-based constitutive law of plastic deformation', *Comput. Mater. Sci.* **25**(1), 200–206.

Senseny, P. & Fossum, A. (1998), 'Testing to estimate the Munson-Dawson parameters', *Series on rock and soil mechanics* pp. 263–276.

Senseny, P., Hansen, F., Russell, J., Carter, N. & Handin, J. (1992), 'Mechanical behaviour of rock salt: Phenomenology and micromechanisms', *Int. J. Rock. Mech. Min. Sci. & Geomech. Abstr.* **29**(4), 363–378.

Serbin, K., Ślizowski, J., Urbańczyk, K. & Nagy, S. (2015), 'The influence of thermodynamic effects on gas storage cavern convergence', *Int. J. Rock. Mech. Min. Sci* **79**, 166 – 171.

Sharifzadeh, M. & Ghasr, A. (2006), Numerical simulation of gas storage caverns in Qom region, *in* 'Rock Mechanics in Underground Construction: ISRM International Symposium 2006: 4th Asian Rock Mechanics Symposium, 8-10 November 2006, Singapore', World Scientific, p. 186.

Ślizowski, J. & Lankof, L. (2003), 'Salt-mudstones and rock-salt suitabilities for radioactive-waste storage systems: rheological properties', *Appl. Energ.* **75**(1-2), 137 – 144.

Song, R., Bai, Y.-M., Zhang, J.-P., Jing, D.-Y. & Yang, C.-H. (2013), 'Experimental investigation of the fatigue properties of salt rock', *Int. J. Rock. Mech. Min. Sci.* **64**, 68–72.

Spiers, C. J., Peach, C. J., Brzesowsky, R. H., Schutjens, P. M. T. M., Liezenberg, J. L. & Zwart, H. J. (1988), *Long term rheological and transport properties of dry and wet salt rocks, EUR 11848, prepared for Commission of the European Communities*, University of Utrecht, Utrecht, The Netherlands.

Spiers, C. J., Urai, J. L., Lister, G. S., Boland, J. N. & Zwart, H. J. (1986), *The influence of fluid-rock interaction on the rheology of salt rock*, Report EUR 10399 EN, Commission of the European Communities.

Sriapai, T., Walsri, C. & Fuenkajorn, K. (2012), 'Effect of temperature on compressive and tensile strengths of salt', *ScienceAsia* **38**, 166–174.

Sriapai, T., Walsri, C. & Fuenkajorn, K. (2013), 'True-triaxial compressive strength of Maha Sarakham salt', *Int. J. Rock. Mech. Min. Sci.* **61**, 256 – 265.

Staudtmeister, K. & Rokahr, R. (1997), 'Rock mechanical design of storage caverns for natural gas in rock salt mass', *Int. J. Rock. Mech. Min. Sci.* **34**(3), 300–12.

Stormont, J. (1997), 'In situ gas permeability measurements to delineate damage in rock salt', *Int. J. Rock. Mech. Min. Sci.* **34**(7), 1055–1064.

Stormont, J., Daemen, J. & Desai, C. (1992), 'Prediction of dilation and permeability changes in rock salt', *Int. J. Numer. Anal. Met.* **16**(8), 545–569.

Thomas, R. & Gehle, R. (2000), A brief history of salt cavern use, *in* 'Proceeding of 8^{th} world salt symposium', pp. 207–214.

Tryller, H. & Musso, L. (2006), Controlled cavern leaching in bedded salt without blanket in Timpa del Salto, *in* 'SMRI Spring Meeting, Brussels, Belgium, 30 April-3 May'.

Unteregger, D., Fuchs, B. & Hofstetter, G. (2015), 'A damage plasticity model for different types of intact rock', *Int. J. Rock. Mech. Min. Sci* **80**, 402 – 411.

Urai, J. L., Spiers, C. J., Peach, C. J., Franssen, R. & Liezenberg, J. L. (1987), 'Deformation mechanisms operating in naturally deformed halite rocks as deduced from microstructural investigations', *Geologie en Mijnbouw* **66**, 165–176.

Urai, J. L., Spiers, C. J., Zwart, H. J. & Lister, G. S. (1986), 'Weakening of rock salt by water during long-term creep', *Nature* **324**, 554–557.

Urai, J. & Spiers, C. (2007), The effects of grain boundary water on deformation mechanisms and rheology of rock salt during long-term deformation, *in* '6th conference on the mechanical behavior of salt- SALTMECH6, Hannover , Germany, 22-25 May'.

Verrall, R. A., Fields, R. J. & Ashby, M. F. (1977), 'Deformation mechanism maps for LiF and NaCl', *J. Am. Ceram. Soc.* **60**, 211–216.

Voyiadjis, G. Z., Ju, J. W. W. & Chaboche, J. L. (1998), *Damage Mechanics in Engineering Materials*, Elsevier.

Wang, T., Ma, H., Yang, C., Shi, X. & Daemen, J. (2015), 'Gas seepage around bedded salt cavern gas storage', *J. Nat. Gas. Sci. Eng.* **26**, 61 – 71.

Wang, T., Yan, X., Yang, H., Yang, X., Jiang, T. & Zhao, S. (2013), 'A new shape design method of salt cavern used as underground gas storage', *Appl. Energ.* **104**, 50 – 61.

Wang, T., Yang, C., Ma, H., Daemen, J. & Wu, H. (2015), 'Safety evaluation of gas storage caverns located close to a tectonic fault', *J. Nat. Gas. Sci. Eng.* **23**, 281 – 293.

Wang, T., Yang, C., Ma, H., Li, Y., Shi, X., Li, J. & Daemen, J. (2016), 'Safety evaluation of salt cavern gas storage close to an old cavern', *Int. J. Rock. Mech. Min. Sci.* **83**, 95–106.

Wang, Z. L., Li, Y. C. & Wang, J. (2007), 'A damage-softening statistical constitutive model considering rock residual strength', *Comput. Geosci.* **33**(1), 1 – 9.

Wawersik, W. R. & Hanuum, D. W. (1980), 'Mechanical behavior of New Mexico rock salt in triaxial compression up to 200 °C', *J. Geophys. Res.* **85**(B2), 891–900.

Wawersik, W. R. & Zeuch, D. H. (1984), *Creep and Creep Modeling of Three Domal Salts: A Comprehensive Update*, Vol. 84, Sandia National Laboratories.

Wei, L., Yinping, L., Chunhe, Y., Deyi, J., Daemen, J., Jie, C. & Junfeng, K. (2016), 'A new method of surface subsidence prediction for natural gas storage cavern in bedded rock salts', *Environ. Earth. Sci.* **75**(9), 1–17.

Weidinger, P., Hampel, A. Blum, W. & Hunsche, U. (1997), 'Creep behavior of natural rock salt and its description with the composite model', *Mater. Sci. Eng.* **A234-236**, 646–648.

Xia, C., Zhou, Y., Zhou, S., Zhang, P. & Wang, F. (2015), 'A simplified and unified analytical solution for temperature and pressure variations in compressed air energy storage caverns', *Renew Energ* **74**, 718 – 726.

Xiong, J., Huang, X. & Ma, H. (2015), 'Gas leakage mechanism in bedded salt rock storage cavern considering damaged interface', *Petroleum* **1**(4), 366 – 372.

Yahya, O., Aubertin, M. & Julien, M. (2000), 'A unified representation of the plasticity, creep and relaxation behavior of rocksalt', *Int. J. Rock. Mech. Min. Sci.* **37**(5), 787–800.

Yang, C., Jing, W., Daemen, J., Zhang, G. & Du, C. (2013), 'Analysis of major risks associated with hydrocarbon storage caverns in bedded salt rock', *Reliab. Eng. Syst. Safe.* **113**, 94–111.

Yang, C., Wang, T., Li, J., Ma, H., Shi, X. & Daemen, J. (2016), 'Feasibility analysis of using closely spaced caverns in bedded rock salt for underground gas storage: a case study', *Environ. Earth. Sci.* **75**(15), 1138.

Yang, C., Wang, T., Li, Y., Yang, H., Li, J., Qu, D., Xu, B., Yang, Y. & Daemen, J. (2015), 'Feasibility analysis of using abandoned salt caverns for large-scale underground energy storage in China', *Appl. Energ.* **137**, 467 – 481.

Zhang, C., Liang, W., Li, Z., Xu, S. & Zhao, Y. (2015), 'Observations of acoustic emission of three salt rocks under uniaxial compression', *Int. J. Rock. Mech. Min. Sci.* **77**, 19 – 26.

Zhang, G., Wu, Y., Wang, L., Zhang, K., Daemen, J. J. & Liu, W. (2015), 'Time-dependent subsidence prediction model and influence factor analysis for underground gas storages in bedded salt formations', *Eng. Geol.* **187**, 156–169.

Zhang, N., Ma, L., Wang, M., Zhang, Q., Li, J. & Fan, P. (2017), 'Comprehensive risk evaluation of underground energy storage caverns in bedded rock salt', *J. Loss. Prevent. Proc.* **45**, 264–276.

Schriftenreihe des Lehrstuhls für Grundbau, Boden- und Felsmechanik der Ruhr-Universität Bochum

Herausgeber: H.L. Jessberger

1 (1979) **Hans Ludwig Jessberger**
Grundbau und Bodenmechanik an der Ruhr-Universität Bochum

2 (1978) **Joachim Klein**
Nichtlineares Kriechen von künstlich gefrorenem Emschermergel

3 (1979) **Heinz-Joachim Gödecke**
Die Dynamische Intensivverdichtung wenig wasserdurchlässiger Böden

4 (1979) **Poul V. Lade**
Three Dimensional Stress-Strain Behaviour and Modeling of Soils

5 (1979) **Roland Pusch**
Creep of soils

6 (1979) **Norbert Diekmann**
Zeitabhängiges, nichtlineares Spannungs-Verformungsverhalten von gefrorenem Schluff unter triaxialer Belastung

7 (1979) **Rudolf Dörr**
Zeitabhängiges Setzungsverhalten von Gründungen in Schnee, Firn und Eis der Antarktis am Beispiel der deutschen Georg-von-Neumayer- und Filchner-Station

8 (1984) **Ulrich Güttler**
Beurteilung des Steifigkeits- und Nachverdichtungsverhaltens von ungebundenen Mineralstoffen

9 (1986) **Peter Jordan**
Einfluss der Belastungsfrequenz und der partiellen Entwässerungs-möglichkeiten auf die Verflüssigung von Feinsand

10 (1986) **Eugen Makowski**
Modellierung der künstlichen Bodenvereisung im grundwasserdurchströmten Untergrund mit der Methode der finiten Elemente

11 (1986) **Reinhard A. Beine**
Verdichtungswirkung der Fallmasse auf Lastausbreitung in nichtbindigem Boden bei der Dynamischen Intensivverdichtung

12 (1986) **Wolfgang Ebel**
Einfluss des Spannungspfades auf das Spannungs-Verformungsverhalten von gefrorenem Schluff im Hinblick auf die Berechnung von Gefrierschächten

13 (1987) **Uwe Stoffers**
Berechnungen und Zentrifugen-Modellversuche zur Verformungsabhängigkeit der Ausbaubeanspruchung von Tunnelausbauten in Lockergestein

14 (1988) **Gerhard Thiel**
Steifigkeit und Dämpfung von wassergesättigtem Feinsand unter Erdbebenbelastung

15 (1991) **Mahmud Thaher**
Tragverhalten von Pfahl-Platten-Gründungen im bindigen Baugrund,
Berechnungsmodelle und Zentrifugen-Modellversuche

16 (1992) **Rainer Scherbeck**
Geotechnisches Verhalten mineralischer Deponieabdichtungsschichten
bei ungleichförmiger Verformungswirkung

17 (1992) **Martin M. Bizialiele**
Torsional Cyclic Loading Response of a Single Pile in Sand

18 (1993) **Michael Kotthaus**
Zum Tragverhalten von horizontal belasteten Pfahlreihen aus langen Pfählen in Sand

19 (1993) **Ulrich Mann**
Stofftransport durch mineralische Deponieabdichtungen:
Versuchsmethodik und Berechnungsverfahren

20 (1992) **Festschrift anlässlich des 60. Geburtstages von**
Prof. Dr.-Ing. H. L. Jessberger
20 Jahre Grundbau und Bodenmechanik an der Ruhr-Universität Bochum

21 (1993) **Stephan Demmert**
Analyse des Emissionsverhaltens einer Kombinationsabdichtung im Rahmen der
Risikobetrachtung von Abfalldeponien

22 (1994) **Diethard König**
Beanspruchung von Tunnel- und Schachtausbauten in kohäsionslosem Lockergestein
unter Berücksichtigung der Verformung im Boden

23 (1995) **Thomas Neteler**
Bewertungsmodell für die nutzungsbezogene Auswahl von Verfahren zur Altlastensanierung

24 (1995) **Ralph Kockel**
Scherfestigkeit von Mischabfall im Hinblick auf die Standsicherheit von Deponien

25 (1996) **Jan Laue**
Zur Setzung von Flachfundamenten auf Sand unter wiederholten Lastereignissen

26 (1996) **Gunnar Heibrock**
Zur Rissbildung durch Austrocknung in mineralischen Abdichtungsschichten
an der Basis von Deponien

27 (1996) **Thomas Siemer**
Zentrifugen-Modellversuche zur dynamischen Wechselwirkung zwischen Bauwerken
und Baugrund infolge stoßartiger Belastung

28 (1996) **Viswanadham V. S. Bhamidipati**
Geosynthetic Reinforced Mineral Sealing Layers of Landfills

29 (1997) **Frank Trappmann**
Abschätzung von technischem Risiko und Energiebedarf bei Sanierungsmaßnahmen
für Altlasten

30 (1997) **André Schürmann**
Zum Erddruck auf unverankerte flexible Verbauwände

31 (1997) **Jessberger, H. L. (Herausgeber)**
Environment Geotechnics, Report of ISSMGE Technical Committee TC 5
on Environmental Geotechnics

Herausgeber: Th. Triantafyllidis

32 (2000) **Triantafyllidis, Th. (Herausgeber)**
Boden unter fast zyklischer Belastung: Erfahrung und Forschungsergebnisse (Workshop)

33 (2002) **Christof Gehle**
Bruch- und Scherverhalten von Gesteinstrennflächen mit dazwischenliegenden Materialbrücken

34 (2003) **Andrzej Niemunis**
Extended hypoplastic models for soils

35 (2004) **Christiane Hof**
Über das Verpressankertragverhalten unter kalklösendem Kohlensäureangriff

36 (2004) **René Schäfer**
Einfluss der Herstellungsmethode auf das Verformungsverhalten von Schlitzwänden in weichen bindigen Böden

37 (2005) **Henning Wolf**
Zur Scherfugenbänderung granularer Materialien unter Extensionsbeanspruchung

38 (2005) **Torsten Wichtmann**
Explicit accumulation model for non-cohesive soils under cyclic loading

39 (2008) **Christoph M. Loreck**
Die Entwicklung des Frischbetondruckes bei der Herstellung von Schlitzwänden

40 (2008) **Igor Arsic**
Über die Bettung von Rohrleitungen in Flüssigböden

41 (2009) **Anna Arwanitaki**
Über das Kontaktverhalten zwischen einer Zweiphasenschlitzwand und nichtbindigen Böden

Herausgeber: T. Schanz

42 (2009) **Yvonne Lins**
Hydro-Mechanical Properties of Partially Saturated Sand

43 (2010) **Tom Schanz (Herausgeber)**
Geotechnische Herausforderungen beim Umbau des Emscher-Systems
Beiträge zum RuhrGeo Tag 2010

44 (2010) **Jamal Alabdullah**
Testing Unsaturated Soil for Plane Strain Conditions: A New Double-Wall Biaxial Device

45 (2011) **Lars Röchter**
Systeme paralleler Scherbänder unter Extension im ebenen Verformungszustand

46 (2011) **Yasir Al-Badran**
Volumetric Yielding Behavior of Unsaturated Fine-Grained Soils

47 (2011) **Usque ad finem**
Selected research papers

48 (2012) **Muhammad Ibrar Khan**
Hydraulic Conductivity of Moderate and Highly Dense Expansive Clays

49 (2014) **Long Nguyen-Tuan**
Coupled Thermo-Hydro-Mechanical Analysis: Experimental and Back Analysis

50 (2014) **Tom Schanz (Herausgeber)**
Ende des Steinkohlenbergbaus im Ruhrrevier: Realität und Perspektiven für die Geotechnik
Beiträge zum RuhrGeo Tag 2014

51 (2014) **Usque ad finem**
Selected research papers

52 (2014) **Houman Soleimani Fard**
Study on the Hydro-Mechanical Behavior of Fiber Reinforced Fine Grained Soils,
with Application to the Preservation of Historical Monuments

53 (2014) **Wiebke Baill**
Hydro-Mechanical Behaviour of Clays - Significance of Mineralogy

54 (2014) **Qasim Abdulkarem Jassim Al-Obaidi**
Hydro-Mechanical Behavior of Collapsible Soils

55 (2015) **Veselin Zarev**
Model Identification for the Adaption of Numerical Simulation Models -
Application to Mechanized Shield Tunneling

56 (2015) **Meisam Goudarzy**
Micro and Macro Mechanical Assessment of Small and Intermediate Strain
Properties of Granular Material

57 (2016) **Oliver Detert**
Analyse einer selbstregulierenden interaktiven Membrangründung
für Schüttkörper auf geringtragfähigen Böden

58 (2016) **Yang Yang**
Analyses of Heat Transfer and Temperature-induced Behaviour in Geotechnics

59 (2017) **Alborz Pourzargar**
Application of Suction Stress Concept to Partially Saturated Compacted Soils

60 (2017) **Hanna Haase**
Multiscale Analysis of Clay-Polymer Composites for Geoenvironmental Applications

61 (2017) **Kavan Khaledi**
Constitutive Modeling of Rock Salt with Application to Energy Storage Caverns